MOLECULAR BEAM EPITAXIAL (MBE) GROWTH OF HIGH QUALITY InP and $Al_{0.48}In_{0.52}As$

A Thesis

submitted to the Faculty of Engineering

of the University of Glasgow

for the degree of

Doctor of Philosophy

by

TIN SUNG CHENG, B.Sc.

This thesis is dedicated to my family.

Acknowledgements

I wish to thank Professor J. Lamb for the provision of laboratory and computing facilities in the Department of Electronics and Electrical Engineering, University of Glasgow, and also my supervisor, Dr C.R. Stanley for his invaluable advice and guidance throughout this project.

I would also like to thank my industrial supervisor at BTRL, Dr D.R. Wood for his enthusiastic assistance and encouragement on the work described in the latter part of this thesis. I am indebted to many people at BTRL for their advice and help during my six months stay. These include Drs G.J. Davies, M.A.G. Halliwell, D.A. Andrews, E.G. Scott, D.C. Rogers, C.J. Allen and M.H. Lyons. Thanks are given to Dr S. Davey for performing the low temperature PL on the MOMBE InP and AlInAs discussed in chapters 6 and 7.

I like to express my gratitude towards Dr C. Sotomayor-Torres for her invaluable advice and encouragement in this work. I am grateful to Dr. I. Ferguson for performing the low temperature PL and photoluminescence excitation spectroscopy (PLE) on AlInAs described in chapter 8. Thanks are given to Dr T.P. Beales at STC, Harlow in Essex for taking the PL spectra at high pressures.

I sincerely thank my landlady, Miss R.P. MacLeod for her kindness and boundless patience shown to me during my stay in Glasgow and through whom I have the pleasure in knowing the generosity of many of her friends and relations from the highlands of Scotland.

Thanks are also due to all the technical staff in

the Department who provided assistance throughout this work. I would also like to thank all my fellow research students for making my stay in Glasgow so enjoyable. In particular, V.M Airaksinen, K.Y. Lee, R. Salahi, I. McIntyre, A.F. Jezierski, D. Halliday, J. Adams, K.T. Lee, M. Laughton and F. Laughton.

I like to thank Drs. D. Halliday and M. Henini of the University of Nottingham for proof-reading some of this thesis.

Last but not the least, I would like to thank my parents and sisters for their understanding and support during my years of study.

Financial support from the Science and Engineering Research Council (SERC) and from BTRL through a CASE award are gratefully acknowledged.

Abstract

This thesis concerns the growth and characterisation of InP grown by MBE and MOMBE; and AlInAs grown by MBE.

The growth of undoped InP epitaxial layers using solid sources was examined. The quality of the layers was assessed using the techniques of capacitance voltage electrochemical (CV) profiling, photoluminescence (PL) and Hall effect measurement. By controlling systematically the three growth parameters of substrate temperature, growth rate and flux ratio, materials of improved quality were produced as shown by narrower PL line-width, and higher Hall mobilities.

A thorough study of n-type doping in InP using sulphur generated from an electrochemical Knudsen source has been performed. The experimental results are explained in terms of a kinetic model of sulphur incorporation and desorption in conjunction with a thermodynamic analysis of the effect of substrate temperature and flux ratios. The results show that sulphur is a controllable dopant with well defined behaviour in InP.

An attempt has been made to produce p-type InP using magnesium doping. The electrical and optical properties of these doped layers were comparable to the undoped samples. However, the surface morphology of the doped samples was found to deteriorate as the magnesium flux was increased. However there was little effect on the electrical or optical characteristics.

Epitaxial InP layers grown by MOMBE at BTRL were also characterised. Magnesium, sulphur and silicon were found to be the residual shallow impurities present in these samples. Deep Level Transient Spectroscopy (DLTS) measurements shows that all electron traps observed in the MOMBE material have already been observed in InP grown by solid sources. Impurity band conduction exists in these samples which dominates the Hall measurements at low temperatures. The MOMBE samples have comparable electrical and optical properties to the best InP layers grown by solid source MBE.

The ternary compound of AlInAs grown lattice matched to InP was characterised. During growth it was observed that there is a region of substrate temperature which produces a rough surface. This region of rough surface growth was correlated with an increase in the PL line-width as well as the appearance of unique deep traps in the DLTS measurements. Growth at elevated temperatures led to an increase in the loss of indium leading to mismatched layers.

The thesis concludes with a study of PL recombination mechanisms associated with the observed emission spectrum from AlInAs. Using a Diamond Anvil Cell (DAC) the PL dependence on hydrostatic pressure was determined.

CHAPTER 1

Fundamental Processes and Principles of Molecular Beam Epitaxy (MBE)

1.1 Introduction

Since the original development of the three temperature vacuum evaporation technique by Gunther et al. [1.1] in the late fifties, molecular beam epitaxy (MBE) has become an indispensable technology for the preparation of both compound and alloy semiconductor materials. MBE is essentially a thin film deposition method performed in an ultra high vacuum environment in which the substrate is normally held at a constant temperature during growth. Compared with other epitaxial growth techniques such as Liquid Phase Epitaxy (LPE) and Metal-Organic Chemical Vapour Phase Deposition (MOCVD), MBE offers more precise control over layer thickness and alloy composition. Because of the nature of MBE, namely a slow growth rate (~1 monolayer per second) and low growth temperature, ultra thin layers with smooth and featureless surfaces having very high uniformity can readily be produced. Furthermore, through the precise control of the individual fluxes, complicated structures with atomically tailored compositions and pre-determined doping profiles may be fabricated with a high degree of reproducibility.

The growth of III-V materials by MBE was initially thought to be problematic because of the large differences in vapour pressures between the group III and V elements. However, Arthur [1.2] was able to show that in the case of GaAs, the sticking coefficient of As_2 (S_{As2}, defined as the fraction of the incident to

the incorporated flux) is dependent on the number of available Ga atoms on the growth surface; $S_{As2}=0$ in the absence of free Ga atoms and which increasing to unity in the presence of free Ga atoms. In MBE growth, the substrate is normally heated well above room temperature, e.g. to 580°C for GaAs and 500°C for InP. A critical point is reached, known as the congruent sublimation temperature T_{cs} beyond which evaporation of the group V atoms from the surface is far greater than the group III atoms, which ultimately lead to a metal rich surface. T_{cs} for a few of the common III-V semiconductors are listed in Table 1.1 . Stoichiometric single crystal films may be produced, therefore, as long as there is a sufficient number of group V atoms to offset the non-congruent effect and to provide an over-potential for epitaxial growth; the surplus of the group V flux simply evaporates off the growth surface.

The interest in the III-V compounds and alloys stems from their potential application to a variety of microwave and opto-electronics components. Many electronic devices have been fabricated using MBE layers. These include field effect transistors (FETs) [1.3,1.4], varactor diodes [1.5], IMPATT diodes [1.6], double heterostructure (DH) lasers [1.7] and high electron mobility transistors (HEMTs) [1.8]. In the area of optical communication, sources and detectors which operate in the 1.3-1.6μm wavelength region where silica-based optic fibres have low absorption loss and minimum dispersion [1.9-1.11], are required. This optical regime can be realised in the III-V family as shown in figure 1.1 where the wavelength (or energy gap) versus the lattice constant for different binary, ternary and quaternary systems is plotted. For example, InGaAsP scans the wavelengths between 1.65-0.92μm (0.75-1.35eV) when lattice matched to an InP substrate and between 0.87-0.65μm (1.42-1.91eV)

Table 1.1 The congruent sublimation (T_{cs}) and oxide removal (T_{ox}) temperatures for a few of the common III-V semiconductors.

Material system	T_{cs} (°C)	T_{ox} (°C)
GaAs	620	560
InP	365	500
GaP	670	580
InSb	-	400
InAs	370	-
AlAs	>860	-

Table 1.2 The approximate growth 'temperature window' for some of the III-V compounds and alloys.

Material system	Temperature window for growth (°C)
GaAs	485-640
InP	430-590
InAs	390-490
AlAs	650-760
InGaAs	500-600
AlInAs	520-660

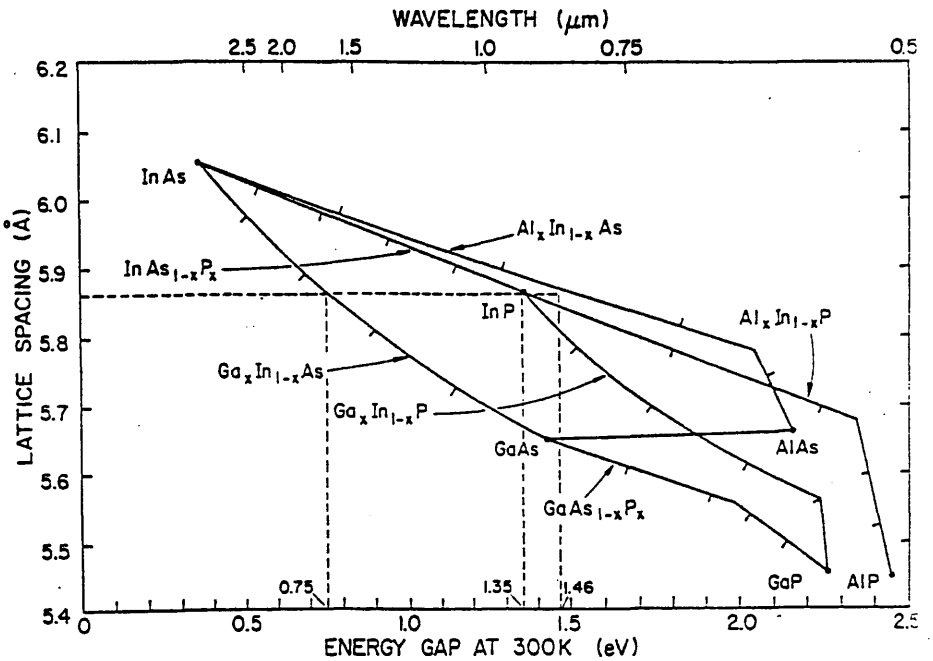

Figure 1.1 Diagram of the lattice constant as a function of the room temperature energy band gap for a range of the III-V semiconductors.

when lattice matched to a GaAs substrate.

The original purpose of the research described in this thesis was to study the InGaAsP material system with a view to fabricating opto-electronic devices operating at 1.3-1.55μm. In the first instance, it is important to establish control over the purity of epitaxial InP before commencing the growth of the ternary (InGaAs) and eventually the quaternary (InGaAsP) alloys. The former part of the work described in this thesis is therefore a continuation of earlier studies by Martin et al. [1.12] on the growth of InP, but aiming to optimize the growth parameters so as to achieve high quality epitaxial layers.

In June 1986, a fire destroyed many of the research laboratories in the Electrical and Electronics Engineering Department at the University of Glasgow, including the whole of the MBE facility. As a result, the research was continued at British Telecom Research Laboratory (BTRL) in Ipswich through the support of a CASE studentship. But the research was redirected away from MBE growth towards the characterisation of III-V compounds and alloys (InP & AlInAs) produced by MBE. The thesis is therefore divided into two parts; the first covers the growth of epitaxial InP produced in the Glasgow InP system (Chapters 2-4) and the second is concerned with the characterisation of InP grown by Metal-Organic Source MBE (Chapter 5) and AlInAs grown by MBE (Chapters 6-7). The optical and pressure measurements discussed in chapter 7 was undertaken in collaboration with the University of St. Andrews (the pressure measurements were taken by Dr. T. Beals at STL, Harlow in Essex).

The present chapter provides a brief introduction of the MBE processes. For a more complete and detailed review on the subject, references [1.13, 1.14] are to be recommended.

1.2 System Configuration

The concept of MBE is illustrated schematically in figure 1.2. A number of Knudsen cells are normally present which are located close to each other and are directed towards the substrate. For the growth of the AlGaAs/GaAs system, the cells required are Al, Ga and As depicted in the figure. In addition two dopant cells, usually Si and Be, are also present providing n- and p-type doping respectively. Shutters are situated in front of each cell to allow fast interrupt of the fluxes thus offering the potential for well controlled and sharp interfaces between layers of different composition and/or doping type. Figure 1.3 shows a schematic diagram of a commercial MBE system manufactured by VG Semicon. It has three UHV chambers: the sample loading chamber commonly known as the "load-lock", the preparation/analysis chamber and the main growth chamber. The three chambers are isolated from each other by gate-valves. The load-lock is the only chamber routinely exposed to atmosphere and is designed to have a small volume so that it may be pumped down quickly after substrate loading. Commercial systems are normally designed to take several wafers (e.g. 6 two inches wafers) at any one time. After the fast entry load-lock has reached a good vacuum ($\leq 10^{-7}$mbar), the substrate is moved into the preparation chamber where it is normally heated to above 200°C on a heater stage to remove any residual moisture on the surface of the substrate and its holder. The pressure in this section is kept at $\leq 10^{-9}$mbar by an ion pump. In-situ surface analysis such as Auger electron spectroscopy (AES) may be performed in this section of the system to determine the chemical state of the surface before and/or after growth. The growth chamber, being pumped by an ion pump or a turbomolecular pump, is kept in an UHV

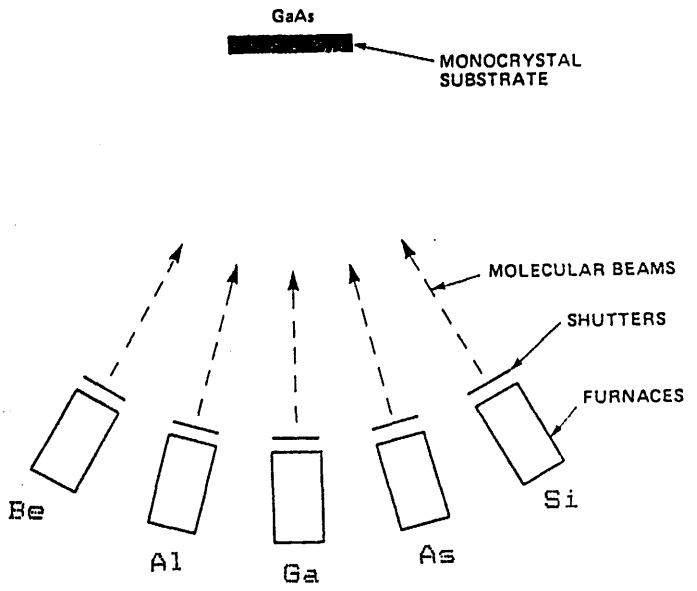

Figure 1.2 Schematic diagram of the basic concept of MBE for growing (Ga,Al)As. The mechanical shutter in front of each furnaces provides a quick interruption of the beam flux, thus gives a precise control of the material composition and doping profile.

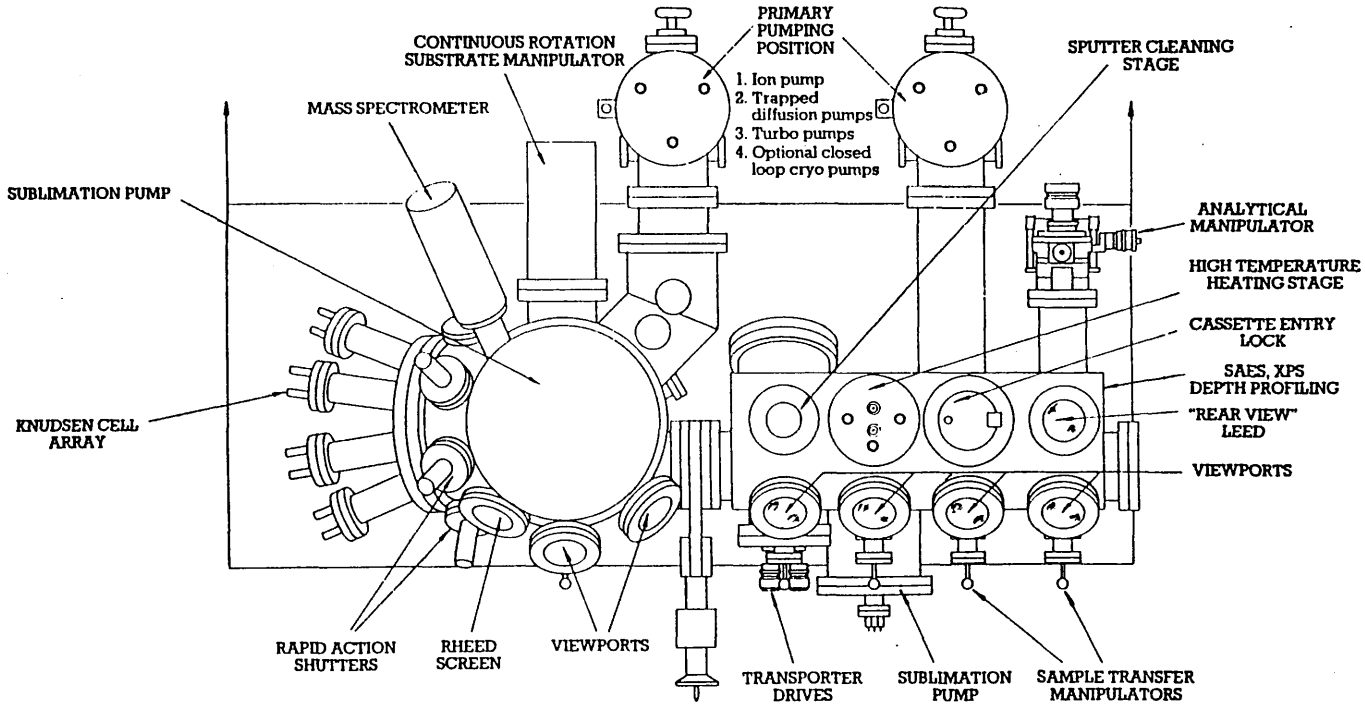

Figure 1.3 Schematic diagram of a commercial MBE system manufactured by VG Semicon.

condition continuously (with pressure $<10^{-10}$mbar) except when the Knudsen cells are empty and source reloading is necessary. After the growth chamber has been to atmosphere (either for source recharging or for repair) the system is baked at about 200°C for a prolong period (e.g. a week) in order to restore good UHV conditions. The Knudsen cells (Al,Ga,As etc.) in the growth chamber are resistively heated to temperatures which yield the elemental vapour pressures desired for growth. Since the operating temperatures of the cells are normally high, the unwanted impurities that evolves from the construction materials can be significant. To ensure a low level of accidental doping of the epitaxial layers, it is therefore imperative that the uncontrolled fluxes of atoms reaching the substrate are as weak as possible. Therefore, boron nitride (pBN) is the preferred crucible material used in MBE growth since it combines a low rate of outgassing with a weak chemical activity up to temperatures of the order of 1500°C. Cryogenic screening around the space of the substrate is essential to minimize stray fluxes of atoms or molecules from the wall of the chamber and from the heated parts of the system. This is achieved by continuously flowing liquid nitrogen (LN_2) through a cryopanel.

The group V and the group III cells used in MBE are similar in construction except in some systems where an additional section known as the 'cracker' is fitted in front of the group V cell. The cracker is basically a high temperature zone operated at ≈900°C and its function is to convert tetramers molecules (e.g. As_4) from the Knudsen cell into a flux of dimers (As_2), which has been shown to have a simpler incorporation chemistry (see section 1.4 below).

The molecular beam fluxes are monitored by an ion gauge situated at the back of the substrate holder.

The gauge may be rotated through 180° to intercept the incident fluxes and provide a beam equivalent pressure (BEP) measurement, which in the case of the group III BEP relates directly to the growth rate. The substrate is normally rotated continuously during growth to achieve good lateral uniformity of the layer [1.15]. The substrate temperature can either be measured by an infrared pyrometer or simply by a thermocouple located at the back of the substrate. The composition of the epitaxial layer is controlled by the presence of shutters which can be used to interrupt the incident molecular beams.

The equipment for various UHV-compatible analytical techniques can be incorporated into the MBE system. Some of these provide an in-situ surface probe to facilitate a good understanding of the growth processes, consequently resulting in better control over the quality of the epitaxial layers. Probably the most important of these is reflection high energy electron diffraction (RHEED) which provides information on the changes in the surface structure of the outermost atomic layers. For example, the RHEED pattern at the heat cleaning stage of the substrate prior to epitaxial growth appears diffuse and spotty. However after the thermal treatment, the observed pattern becomes sharp and streaky with either an As-stabilised (2x4) or Ga-stabilised (4x2) RHEED pattern depending on the magnitude of the incident arsenic flux and the substrate temperature, indicating that the native oxide on the substrate surface has been removed and the existence of a flat surface. It is particularly important to control precisely the composition and the thickness of the layers in the case of growing the III-V alloys, quantum wells and superlattice structures. The oscillations in the intensity of the specularly reflected spot in the RHEED pattern may be used to determine accurately the

growth rate and hence the thickness (to within a monolayer) and composition of the layers [1.16]. Auger electron analyzer (AES) is another in-situ surface probe which determines the chemical composition of the outer-most atomic layers. It may be used to provide information on the residual surface contaminants of a chemically cleaned substrate prior to and after epitaxial growth. Surface segregation effects can also be studied using AES [1.17].

Prior to epitaxial growth, it is crucial to ensure the MBE system has an acceptable low level of impurity gas species such as CO, CO_2 and H_2O to minimise contamination from the background. The pressures of these gases may be detected by a quadrupole mass spectrometer which allows the initial state of the system to be assessed.

Auxiliary equipment, such as secondary ion mass spectroscopy (SIMS) and surface profiling AES, can also be found in some of the more sophisticated MBE systems. As well as being a thin film growth system, the MBE provides an excellent tool for the study of surface physics.

1.3 Flux Generation

The beam flux (F) from the group V or III sources arriving at the substrate are determined by the Knudsen equation as

$$F = \frac{1.118\times10^{22} \times AxP\cos\theta}{l^2(MT)^{1/2}} \text{ molecules/cm}^2\text{s} \quad \ldots\ldots\ldots (1.1)$$

where P is the equilibrium vapour pressure of the element in Torr,

A is the area of aperture of the cell orifice in cm^2,

l is the distance between the substrate and the tip of the crucible in cm,

M is the molecular weight of the element in a.m.u's,

T is the absolute temperature in Kelvin, &

θ is the angle between the beam and the substrate surface normal.

The above equation holds if the cell aperture is less than the mean free path of the vapour molecules within the cell. Beams generated from the group III source are atomic in nature while those from the group V cell consist of molecules. Typical fluxes used in MBE are : ~10^{15} atoms/cm^2s for group III elements, ~10^{16} molecules/cm^2s for group V elements and 10^9-10^{11} atoms/cm^2s for the dopants.

Thus far, the sources used in MBE are in elemental form although recently there have been much activity in using gaseous sources. For instance the group III flux, normally generated from a metallic element (such as solid gallium or indium), may be obtained using metal alkyls such as triethylindium (TEIn) or trimethylindium (TMIn). The group V fluxes may be generated via three different routes:

(a) from a compound source, e.g polycrystalline GaAs or InP, which generates predominately a dimeric beam (As_2 or P_2 respectively). However, it should be noted that a group III flux (Ga or In) is also produced which cannot be measured directly by the ion gauge. This affects the overall growth rate of the epitaxial layer. The additional flux is particularly undesirable in the growth of ternary or quaternary alloys since control over the material composition becomes extremely difficult.

(b) from an elemental solid source, which can be obtained with a higher purity than the compound

source. The flux generated is primarily tetrameric which can be converted into group V dimers by the cracker. The generation of group V fluxes from elemental solid sources has now become the most widely method used in MBE.

(c) from a gas source (the group V hydrides). The hydrides have the advantage of being an essentially 'infinite' supply source, i.e. replenishment can be undertaken outside the MBE system. The flow of the gases are controlled by a set of precision valves. Epitaxial layers grown using gas sources exhibit very good optical and electrical properties (see chapter 5).

1.4 Growth Mechanisms of Dimers versus Tetramers

Growth using dimers has been shown to improve both the optical and electrical properties of epitaxial GaAs layers [1.18,1.19], through a decrease in the deep level concentrations [1.20]. A simple kinetic model has been proposed by Joyce et al. to explain the observed behaviour [1.21]. Figure 1.4(a) and 1.4(b) depict schematically the processes involved in the growth of GaAs using As_4 and As_2 respectively. In the case of As interacting with Ga on a Ga stabilised surface, the As_2 molecule is adsorbed in a precursor state and migrates freely with a finite surface lifetime. There are three different reaction paths for the molecule. Firstly, the As_2 molecule can dissociatively chemisorbed when it encounters two adjacent unbonded Ga atoms. The second reaction path is the desorption of As_4 when two As_2 molecules encounter and interact with one another. Thirdly, the As_2 molecule can simply evaporate off the semiconductor surface without any interaction. The sticking

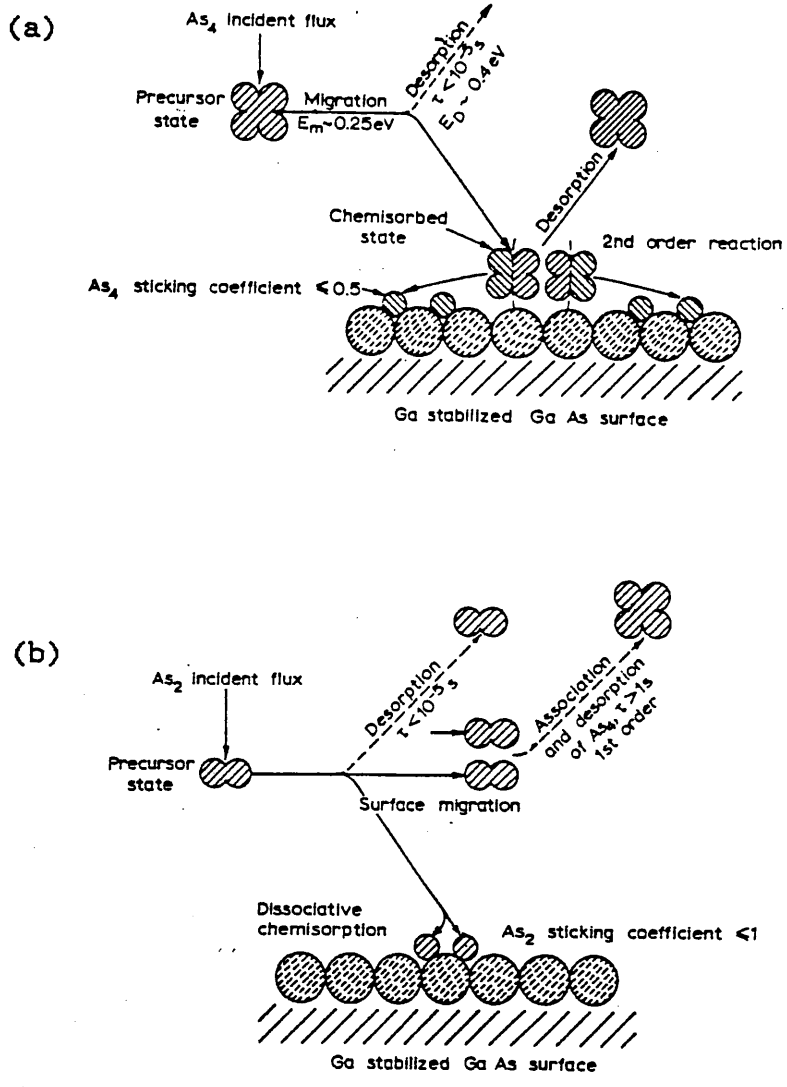

Figure 1.4 Schematic diagram of the growth mechanisms of GaAs using (a) As_4 and (b) As_2 species, as given in reference [1.21].

coefficient of As_2 on GaAs, therefore, is ≤ 1. In contrast, the kinetics of As_4 on GaAs are more complex. The arsenic atoms in this case are incorporated via a pair-wise dissociative chemisorption process, i.e. for any two As_4 molecules encountering two pairs of neighbouring unbonded Ga atoms, four As atoms are incorporated and the other four atoms just desorb as a As_4 molecule. The sticking coefficient of As_4 on GaAs is therefore ≤ 0.5. This is a second order reaction and the arsenic coverage is much less compared to that for As_2. In these circumstances, it is much more likely for native related defects to be incorporated into the crystal lattice when using As_4 for growth.

The need to use dimers is more important in the case of InP than GaAs because of the high vapour pressure of white phosphorus, which cannot be pumped away efficiently, leading to an undesirable high background pressure in the system. It has also been shown that the use of P_4 as the growth species produce inferior epitaxial layers [1.22]. Consequently, phosphorus dimers (P_2) produced by cracking the tetramers are the preferred species for the growth of the phosphorus compounds and alloys.

P_4 molecules condensed to

1.5 Growth of binary compounds, ternary and quaternary alloys

The growth of binary compounds, e.g. GaAs and InP is relatively simple compared to the growth of the alloys. The growth rate is controlled only by the magnitude of the incident group III flux since the sticking coefficient of the group III element is unity and that of the group V element is dependent on the presence of excess of the group III elements [1.2]. Epitaxial growth of binary compounds may therefore be produced by simply supplying an excess amount of group

V flux onto the growth surface. The group V flux should be sufficient to replace those group V atoms lost by non-congruent evaporation and also to provide an over potential for growth. Those group V species that are not used will simply desorb from the surface.

The growth of the ternary alloys are much more involved, in particular the type II alloys [i.e. those contain two group V elements (As & P)]. For the type I alloy [those containing two group III elements (Ga & In)], e.g $In_xGa_{1-x}As$, the composition of the alloy is normally a function of the relative arrival rates of In and Ga. The alloy composition x is given by

$$x = \frac{F_{In}}{F_{In} + F_{Ga}} \qquad \ldots\ldots\ldots\ldots\ldots\ldots\ldots\ldots\ldots\ldots (1.2)$$

The equation is valid as long as there is negligible desorption of the group III element at the growth temperature used. If the desorption is not negligible then the indium flux must be increased to offset the loss and hence maintain the required composition.

Type II ternary alloys such as $GaAs_yP_{1-y}$ and $InAs_yP_{1-y}$ are difficult to grow due to the inter-dependence of the sticking coefficients of As and P . Using modulated molecular beam techniques, Foxon et al. measured the sticking coefficient of As_4 (P_4) as a function of P_4 (As_4) at a fixed growth rate [1.23]. They found that the incorporation of As molecules is much higher than that for P molecules and the group III element does not affect the composition. It is then possible to grow these type II alloys with predetermined compositions by limiting the more reactive species, in this case arsenic, relative to the group III flux and supply an excess flux of the other group V element. Since the sticking coefficients of the group III elements are unity under normal MBE growth conditions, the growth of quaternary alloys

would therefore be similar to the growth of the ternary alloys.

1.6 Substrate Temperature Effects

The quality of the epitaxial layer depends strongly on the temperature at which it is grown. A limited growth temperature window exists in which it is possible to produce material with both good electrical and optical properties. The temperature range of this window is governed by a low (T_{lo}) and a high (T_{hi}) temperature. T_{lo} is associated with the temperature below which oxygen related species are stable on the growth front and consequently oxygen related defects will be incorporated into the crystal lattice of the epitaxial layer. As a result of the oxygen incorporation, deep states within the forbidden energy band gap will be formed which act as traps for carriers thus degrading the electrical and optical properties of the semiconductor. Similarly growth at temperatures above T_{hi} should be avoided since the concentration of native defects (e.g. group V vacancies) will become substantial. It should be noted that T_{lo} and T_{hi} are not unique but depend on factors such as the level of CO, CO_2 and H_2O in the growth system, the group III to V flux ratio and the material system considered. Table 1.2 shows the approximate growth temperature 'windows' for some of the compounds and alloys in the III-V family. It can be seen that InAs and AlAs are grown at the lowest and highest temperatures respectively. Growth involving Al is especially difficult because aluminium oxides are stable and requires high temperatures for dissociation and desorption. For instance, to avoid oxygen incorporation in AlInAs, growth should be performed at T_s>660°C. Unfortunately, above 600°C the desorption

loss of indium becomes significant resulting in a measurable change of the composition. This would lead to a lattice mismatch between the layer and the substrate and consequently the introduction of strain and dislocations in the epitaxial layer.

1.7 Flux Ratio

The arrangement and population of atoms and molecules on the surface of a semiconductor substrate during growth may be varied by changing the ratio of group III to V flux ratio. RHEED can be used to reveal the surface stoichiometry through the difference in surface reconstructions under varying growth conditions. For example, a gallium stabilised surface on (100)GaAs surface has a 4x2 reconstructed pattern while an arsenic stabilised surface on (100)GaAs shows a 2x4 reconstructed pattern when monitored along the [110] direction. The flux ratio of Ga to As has been shown to have significant influence on the concentration of certain deep traps [1.24]. Furthermore the dopant site occupancy may be affected; for example, in the case of Ge in GaAs, p or n type material may be produced by varying the $Ga:As_4$ flux ratio forcing the Ge to occupy either the arsenic or the gallium lattice sites respectively [1.25].

Careful control of the group V:III flux ratio can also ensure negligible desorption of dopants when the epitaxial growth is performed at high substrate temperatures. For instance, Andrew et al. have shown that the concentration of both sulphur and selenium impurity atoms in GaAs can be decreased with an increase of the As_4:Ga flux ratio [1.26,1.27].

1.8 Dopants

In order to fabricate useful devices, both n and p type dopants are required. The most commonly used n-type dopants in MBE are the group IV (Si, Ge and Sn) and VI (S, Se and Te) elements. Theoretically, the group IV elements are amphoteric, i.e. they can either occupy a group III or a group V lattice site. In practice, however, only Ge shows a marked amphoteric behaviour in GaAs [1.25]. With its complicated incorporation behaviour, Ge is therefore an unattractive choice for doping. Si and Sn, on the other hand, occupy only the group III lattice site preferentially and therefore act predominantly as n-type dopants. Si has a unity sticking coefficient and shows negligible diffusion, but it requires a high operating temperature and consequently increases the probability of incorporating unwanted impurities [1.28]. Sn also has a unity sticking coefficient on GaAs [1.29] but it shows substantial surface segregation effects [1.30] and therefore it is impossible to grow structures with sharp carrier concentration profiles.

Doping with the group VI elements was first thought to be problematic because of their high vapour pressures. The group VI dopant in its elemental form would deplete in a very short time during bakeout. To overcome these problems, captive sources such as PbS, PbSe [1.31] and SnTe [1.32,1.33] have been used. Negligible lead was found in the grown layers. An alternative doping method has been demonstrated by Davies et al. [1.34] who used a sulphur electro-chemical Knudsen cell which proved to be a very promising n-type dopant source as evidenced in subsequent studies in GaAs [1.26] and InP [1.35].

Compared to n-type dopants, p-type elements with good characteristics are limited and a near ideal dopant is yet to be found. A number of workers have investigated

the dopants such as Mn, Zn, Be and Mg. However, Mn forms a deep level in GaAs [1.36], resulting in incomplete ionisation at room temperature. Zn, on the other hand, has a very low sticking coefficient at growth temperatures normally used in MBE. Be is probably the most widely used p-type dopant despite its associated toxic nature. It forms a shallow level in both GaAs [1.37] and InP [1.38] and layers can be doped to $10^{19}cm^{-3}$ or higher although it is sometimes unpredictable [1.39]. As an alternative dopant to Be, Mg was used in the growth of GaAs [1.40] but it was found to have a relatively low sticking coefficient. Consequently, in order to achieve a reasonable doping level, a Mg flux comparable to the gallium flux is required which changes the stoichiometry of the growth front and thus affects the properties of the layer.

1.9 Thesis Outline

The work described in the first part of this thesis is a continuation of research into the growth of InP which extends back over several years [1.12]. The investigations have identified the principal contaminant in InP as sulphur which originates from the red phosphorus charge, which accounts for the universal n-type character of uninadvertently doped InP grown by MBE. From secondary ion mass spectroscopy (SIMS) studies Mn, Fe, Mg and Ca acceptors have also been found in the undoped InP samples. However a systematic study of the influence of the growth conditions on the properties of InP has not been previously performed. Since sulphur is the dominant donor species in the epitaxial layers, it is intended that by systematically varying the growth parameters such as the substrate temperature, the growth rate and the group V:III flux ratio, the net free carrier

concentration (N_D-N_A) may be minimised and thus increasing the mobility of the layer.

In chapter 2, the optimum growth conditions for the growth of inadvertently doped InP are identified. Many characteristic features (electrical and optical) of the epitaxial InP layers are discussed in relation to the growth parameters.

The role of sulphur in InP is discussed in chapter 3. The sulphur used to dope the epitaxial layers was generated by an electrochemical Knudsen cell first described by Davies et al. [1.26]. The experimental results are explained in terms of thermodynamics and using the kinetic model proposed by Wood et al. [1.40].

Chapter 4 discusses an attempt to use Mg as a p-type dopant in InP grown under the optimum conditions as described in chapter 2. It is shown that the concentration of Mg in the doped samples is of comparable level to the undoped samples. Consequently it is concluded that Mg is unsuitable as an alternative dopant to Be.

The work carried at BTRL is presented in chapters 5 and 6. Chapter 5 is concerned with the characterisation of InP grown by the MOMBE technique. It is found that the material properties of the layer grown by this technique are of higher quality than its solid source grown InP counterpart. In chapter 6 the growth and characterisation of the ternary alloy AlInAs lattice matched to InP are described. It is shown that good quality material can be obtained by careful control of the growth parameter, in particular the substrate temperature.

A detailed optical investigation on AlInAs is described in chapter 7. This work was performed in collaboration with the University of St.Andrews. In addition, the dependence of the photoluminescence (PL) of AlInAs on hydrostatic pressure is studied, which

allows band structure to be examined.

Finally, the thesis concludes in chapter 8 with a discussion on the future work for the growth and characterisation of InP and AlInAs.

1.10 References

[1.1] K.G. Gunther, Z. Naturforsch., 13a, 1081 (1958).

[1.2] J.R. Arthur, J. Appl. Phys., 39, 4032 (1968).

[1.3] A.Y. Cho, J.V. DiLorenzo, B.S. Hewitt, W.C. Niehaus, W.O. Schlosser and C. Radice, J. Appl. Phys., 48, 346 (1977).

[1.4] C.E.C. Wood, Appl. Phys. Lett., 29, 746 (1976).

[1.5] A.Y. Cho and F.K. Reinhart, J. Appl. Phys., 45, 1812 (1974).

[1.6] A.Y. Cho, C.N. Dunn, R.L. Kuvas and W.E. Schroeder, Appl. Phys. Lett., 25, 224 (1974).

[1.7] B.I. Miller, J.H. McFee, R.J. Martin and P.K. Tien, Appl. Phys. Lett., 33, 44 (1978).

[1.8] D. Delagebeaudeuf and N.T. Linh, IEEE Trans. Electron. Devices, ED-29, 955 (1982).

[1.9] M. Horiguchi and H. Osansi, Elect. Lett., 12, 310 (1976).

[1.10] H. Tsuchiya and N. Imoto, Elect. Lett., 15, 476 (1979).

[1.11] T. Miya, Y. Terunuma, T. Hosaka and T. Miyashita, Elect. Lett., 15, 106 (1979).

[1.12] T. Martin and A. Iliadis, studies on the growth of InP at the University of Glasgow, 1982-1985.

[1.13] K. Ploog, "Crystals: Growth Properties and Applications, Vol.3, Springer, Berlin (1980).

[1.14] C.T. Foxon and B.A. Joyce, "Current Topics in Materials Science", ed. E. Kaldis, Vol.7, Chapter 1, North-Holland, Amsterdam (1981).

[1.15] A.Y. Cho and K.Y. Cheng, Appl. Phys. Lett., 38, 360 (1981).

[1.16] J.L. Lievin and C.G. Fonstad, Appl. Phys. Lett., 51, 1173 (1987).

[1.17] K. Ploog and A. Fischer, J. Vac. Sci. Technol., 15, 255 (1978).

[1.18] H. Kunzel and K. Ploog, Appl. Phys. Lett., 37, 416 (1980).

[1.19] H. Kunzel, J. Knecht, H. Jung, K. Wunstel and K. Ploog, Appl. Phys. A, 28, 167 (1982).

[1.20] J.H. Neave, P. Blood and B.A. Joyce, Appl. Phys. Lett., 36, 311 (1980).

[1.21] C.T. Foxon and B.A. Joyce, Surf. Sci., 50, 433 (1975).

[1.22] T. Kerr, PhD thesis, University of Glasgow (1984).

[1.23] C.T. Foxon, B.A. Joyce and M.T. Norris, J. Cryst. Gr., 49, 132 (1980).

[1.24] T. Hayakawa, M. Kondo, T. Suyama, K. Takahashi, S. Yamamoto, S. Yano and T. Hijikata, Appl. Phys. Lett., 49, 788 (1986).

[1.25] K. Ploog, A. Fischer and H. Kunzel, Appl. Phys., 18, 353 (1979).

[1.26] D.A. Andrews, R. Heckingbottom and G.J. Davies, J. Appl. Phys., 54, 4421 (1983).

[1.27] D.A. Andrews, M.K. Yong, R. Heckingbottom and G.J. Davies, J. Appl. Phys., 55, 841 (1984).

[1.28] E.H.C. Parker, R.A. Kubiak, R.M. King and J.D. Grange, J. Phys. D14, 1853 (1981).

[1.29] C.E.C. Wood and B.A. Joyce, J. Appl. Phys., 49, 4854 (1978).

[1.30] A.Y. Cho and J.R. Arthur, Prog. Solid State Chem., 10, 157 (1975).

[1.31] C.E.C. Wood, Appl. Phys. Lett., 33, 770 (1978).

[1.32] D.M. Collins, Appl. Phys. Lett., 35, 67 (1979).

[1.33] D.M. Collins, J.N. Miller, Y.G. Chai and R. Chow, J. Appl. Phys., 53, 3010 (1982).

[1.34] G.J. Davies, D.A. Andrews and R. Heckingbottom, J. Appl. Phys., 52, 7214 (1981).

[1.35] A. Iliadis, K.A. Prior, C.R. Stanley, T. Martin and G.J. Davies, J. Appl. Phys., J. Appl. Phy., 60, 213 (1986).

[1.36] Y. Kawamura, H. Asahi and H. Nagai, J. Appl. Phys., 54, 841 (1983).

[1.37] G.B. Scott, G. Duggan, P. Dawson and G. Weiman, J. Appl. Phys., 52, 6888 (1981).

[1.38] H. Asahi, Y. Kawamura, M. Ikeda and H. Okamoto, Jpn. J. Appl. Phys, 20, L187 (1981).

[1.39] C.R. Stanley, R.F.C. Farrow and P.W. Sullivan, The Technology and Physics of Molecular Beam Epitaxy, edited by E.H.C. Parker, Plenum Press, New York (1985), p275.

[1.40] C.E.C. Wood, D. Desimone, K. Singer and G.W. Wicks, J. Appl. Phys., 53, 4230 (1982).

CHAPTER 2

Growth of Unintentionally Doped InP by Solid Sources MBE

2.1 Introduction

Considerable interest has been shown towards the InP/InGaAsP material system for microwave and optoelectronic applications. As pointed out in the previous chapter, the quaternary alloy InGaAsP is important in the area of optical communication in the 1.3 to 1.6μm wavelength region. Compared to GaAs, InP has a larger Γ-L valley energy separation (0.6eV), a higher threshold field velocity and a larger peak to valley velocity ratio in its field characteristics. Superior transferred electron devices having a lower noise and better frequency characteristics may therefore be obtained [2.1]. Consequently, it is important to study systematically the growth parameters which govern the growth of epitaxial layers containing phosphorus, so that layers with good electrical and/or optical properties may be produced.

At present, InP grown using solid source MBE is much "inferior" in quality compared with material produced by other techniques such as LPE and metal-organic chemical vapour deposition (MOCVD). In contrast to GaAs, MBE growth of the phosphorus compounds using solid sources is problematical. For instance, the use of red phosphorus results in a high system background pressure which necessitates an effective pumping configuration. This high background pressure is caused primarily by the formation of white phosphorus species by the condensation of P_4 molecules on the cryopanel walls. Using a specially designed system to cope with

the pumping of phosphorus, Tsang et al. reported the growth of InP epitaxial layer at high substrate temperatures (≈580°C) with PL linewidths at 5K of less than 1meV [2.2]. However, electrical data for these layers were not given and the layer compensation therefore cannot be deduced.

Although Tsang's report indicates the viability of obtaining high optical quality InP by solid source MBE, the problem associated with controlling the composition of InGaAsP still remains. However, this may be circumvented by using gas sources instead of solid sources [2.3]. Indeed, InP grown by gas sources has been shown to exhibit 77K mobilities of ≈200,000 $cm^2V^{-1}s^{-1}$ [2.4]; the properties of homoepitaxial InP layers grown with gas sources will be described and discussed in chapter 5.

In the present chapter, the properties of unintentionally doped InP grown using solid sources (indium and red phosphorus) as a function of the substrate temperature (T_s), the P_2:In flux ratio and the growth rate (G_r) are reported. It will be shown that by systematically optimising the different growth parameters, epitaxial layers with good electrical and optical characteristics may be obtained. Many of the typical features found in InP will be illustrated through the assessment of the epitaxial layers by various analytical techniques such as the Hall effect measurement, low temperature photoluminescence (PL), C-V carrier concentration profiling and deep level transient spectroscopy (DLTS).

2.2 Experimental Procedure

The MBE system used for this work has briefly been described by Martin et al. [2.5], and is shown schematically in figure 2.1. The system was built at

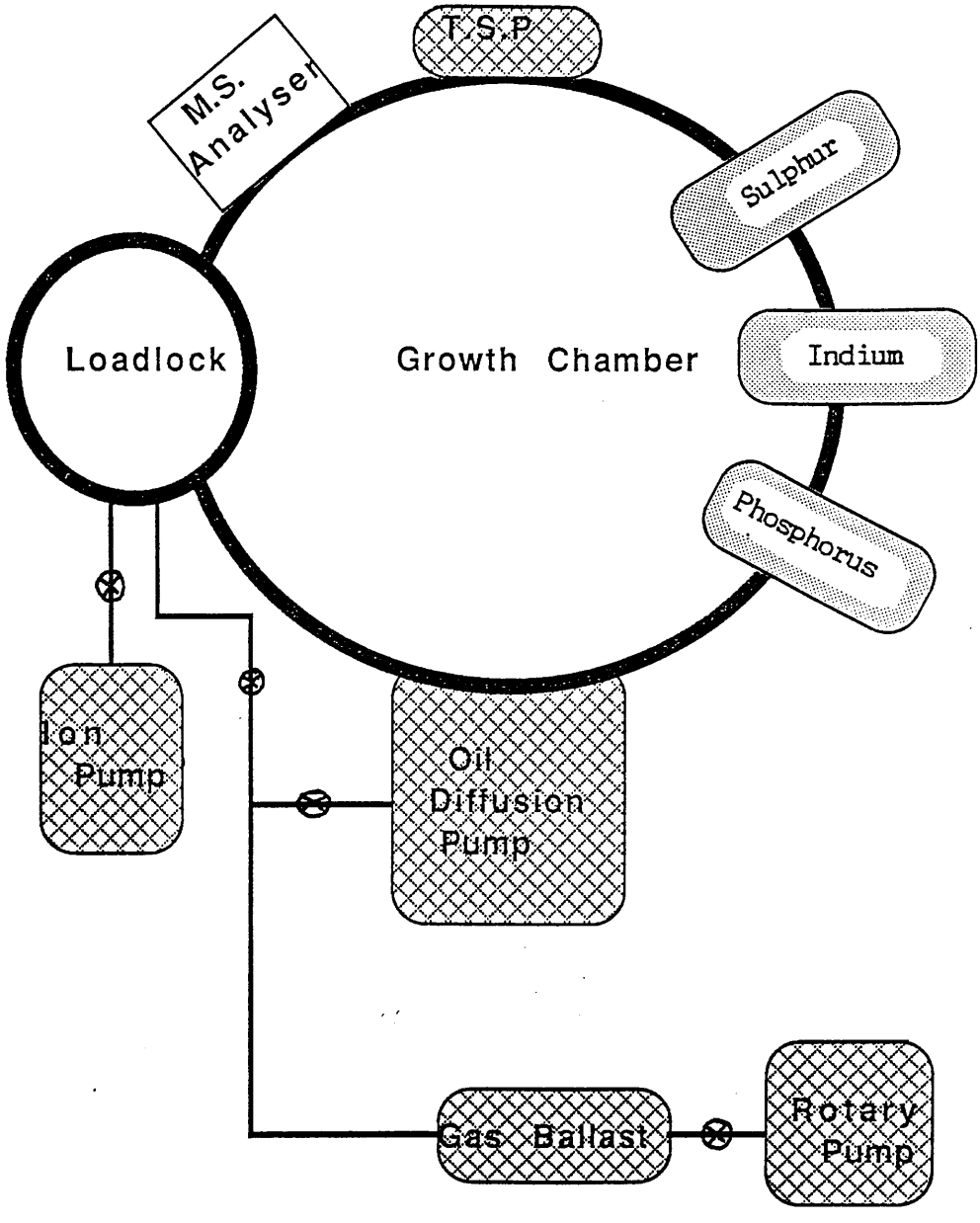

Figure 2.1 Schematic diagram of the MBE system used for growing InP.

the University of Glasgow and consisted of two chambers; a fast entry load-lock and a main UHV chamber. The load-lock and the growth chamber were pumped by an ion pump and a liquid nitrogen trapped oil-diffusion pump respectively. Additional pumping for the growth chamber was provided by a water cooled titanium sublimation pump (TSP). The gas load extracted from the chamber was collected into a ballast tank situated next in line to the diffusion pump. Once the pressure in the tank reached a pre-set value of about 10^{-3}mbar, the gas was expelled into the backing line via a magnetically operated valve. This prevents back-streaming of gases into the system and ensures the growth chamber is oil-free.

Because of the extreme reactivity of the phosphorus species with hydrocarbons, the inner parts of the rotary pump became heavily coated with a tar like substance which caused occasional seizure of the pump. To overcome this problem, an activated carbon filter was fitted in the backing line to reduce the amount of volatile phosphorus compounds entering the rotary pump. In addition, the rotary pump was ballasted with the boil off nitrogen gas from a liquid nitrogen dewar to minimise phosphorus reacting with oxygen species and condensing in the pump oil. Also, the rotary pump oil was continuously passed through an external oil filter unit. All these precautions added considerably to the servicing interval of the rotary pump.

The internal parts of the growth chamber were surrounded by liquid nitrogen-cooled panels. All of the Knudsen cells (In,P and S) were also cooled individually by water jackets. The partial pressures of all residual gases in the growth chamber, with the exception of hydrogen and the phosphorus species P_n (n=1-4), were typically $5x10^{-11}$mbar with the cryopanels cooled and the indium cell at operating temperature. Phosphorus dimers (P_2) generated by thermal cracking of

P_4 were used in all the growth runs which caused the system background pressure to rise to around 10^{-9}mbar. The beam equivalent pressures (BEP's) of the beam fluxes from the Knudsen cells containing indium (6N) and red phosphorus (6N) were measured by a movable ion gauge situated at the back of the substrate holder. The substrate temperature was measured by a thermocouple located in close proximity to the back of the substrate. The temperature was calibrated using the known eutectic points of Si-Al (577°C) and Ge-Al (423°C). The ion gauge as well as the quadrupole mass spectrometer were usually switched off before growth to avoid unwanted contaminants such CO and CO_2.

Both semi-insulating Fe- and n+ S-doped (100)InP substrates, purchased from Mining and Chemical Products (MCP) were used in the growth runs. The substrates were first polished in a solution of 0.5% bromine in methanol, degreased in organic solvents (Trichloroethane, Acetone, Methanol and Propanol), etched in a solution of $H_2SO_4:H_2O_2:H_2O$ (10:1:1) for 15-20 seconds, rinsed thoroughly with 18MΩ de-ionised water and blown dry using filtered nitrogen. The temperature of the etch was kept at or below 70°C before the etching was performed. The substrate was subsequently mounted onto a molybdenum holder using pure metallic indium and immediately introduced into the system, where the surface oxide was removed by heating for three minutes at ≈530°C in an excess flux of P_2 [2.6].

2.3 Growth Rate Calibration

The growth rate, G_r, is an essential parameter which requires to be established so the thicknesses of the epitaxial layers can be controlled precisely. At normal MBE growth temperatures (where desorption of

the group III species is negligible), G_r is directly proportional to the incident group III flux. There are two different methods for measuring G_r; using a shadow mask [2.7] or measuring the RHEED intensity oscillations [2.8]. The period of RHEED oscillations corresponds precisely to the growth of a mono-layer of material. However, the former technique was used in our system to determine G_r. Here the shadow mask made from a small piece of tantalum foil (welded on the sample block) shields part of the substrate to the incident indium flux to form a step whose height gives a direct measure of G_r corresponding to the particular indium flux used. The height of this step is measured using a Taly-step instrument. Figure 2.2 shows the experimental data of the indium BEP as a function of G_r. It is clear from the graph that a linear relationship exists between the indium BEP (measured by the ion gauge) and the growth rate G_r. For a typical growth rate of 1.5μm/hr the corresponding indium BEP is 4×10^{-7}mbar. This calibration graph is used to set the indium flux for subsequent growth runs to obtain the required growth rate. The experimental points in the graph show some degree of scatter, which is probably due to the non-uniformity of the samples, the position and the state of the ion gauge.

2.4 Desorption of P_2 and In from InP

Langmuir (free) and Knudsen (equilibrium) evaporation of InP have been investigated by Farrow et al. [2.9]. InP is shown to have a congruent sublimation temperature T_{cs}=365°C. For temperatures up to T_{cs}, InP decomposes according to the equilibrium reaction: $InP = In + \frac{1}{2}P_2$. Above T_{cs}, i.e. in the non-congruent regime, phosphorus desorbs at a much faster rate leading ultimately to an indium rich surface.

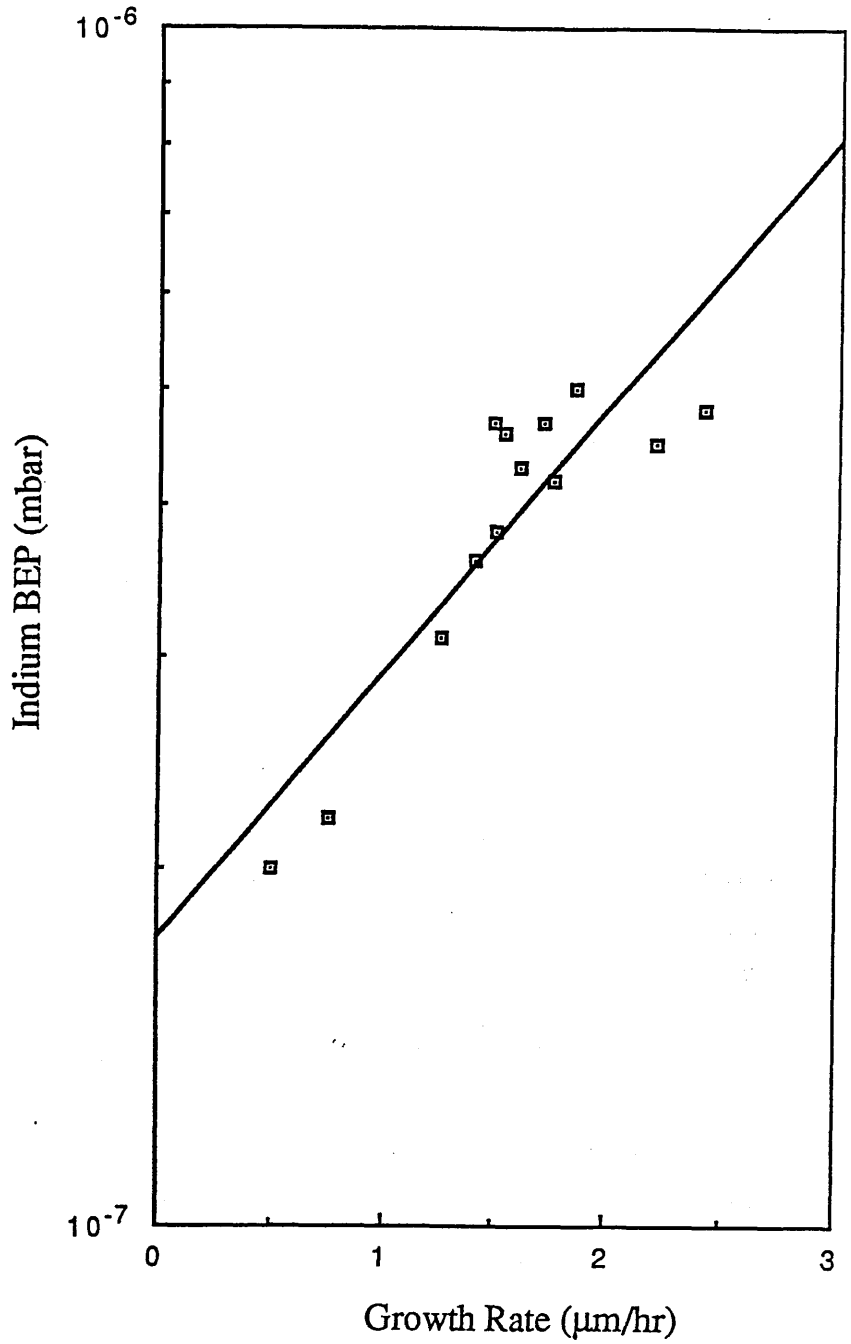

Figure 2.2 Calibration of the indium BEP as a function of the growth rate G_r. The indium BEP varies linearly with G_r. The scatter in the graph is associated with the non-uniformity of the samples, the position and the state of the ion gauge.

Since epitaxial InP is normally grown at ~150°C above T_{cs}, an excess of P_2 flux must be supplied to replace the lost molecules to maintain a phosphorus stabilised surface. The P_2 molecules that are not incorporated will simply evaporate off the surface because of their zero sticking coefficient in the absence of any free indium atoms.

The quality of unintentionally doped InP grown by MBE has been shown to be limited by residual sulphur (donor concentration $\approx 10^{16} cm^{-3}$) associated with the phosphorus flux [2.5]. Therefore, it becomes necessary to use a minimum P_2 flux in the growth of InP to ensure the lowest level of sulphur incorporation. To determine the magnitude of the P_2 flux required, the stabilisation and evaporation of phosphorus on InP were investigated. A number of InP epitaxial layers were grown separately and with different P_2 overpressures. For each layer, the substrate temperature (T_s) was increased in step of two degrees and the growth at each T_s was allowed to proceed for two to five minutes while visual inspection of the surface was made. This procedure was continued until indium droplets were visible. Figure 2.3 shows the experimental results for the growth rate of 1.4μm/hr. Included in the figure is the equilibrium of P_2 flux over InP deduced by Farrow [2.9]; the experimental data can be seen to lie close to it in the high temperature region. The curve in the graph may be explained by a simple flux conservation model which states that the overall P_2 flux supplied to the growth surface is equal to the flux taken up for growth plus the flux desorbed from the surface, i.e

$$F_{total}(P_2) = F_{growth} + F_{desorb}(P_2) \quad \ldots\ldots\ldots\ldots\ldots\ldots (2.1)$$

At the metal rich transition temperature T_{mt}, i.e., the point at which the surface becomes metal rich,

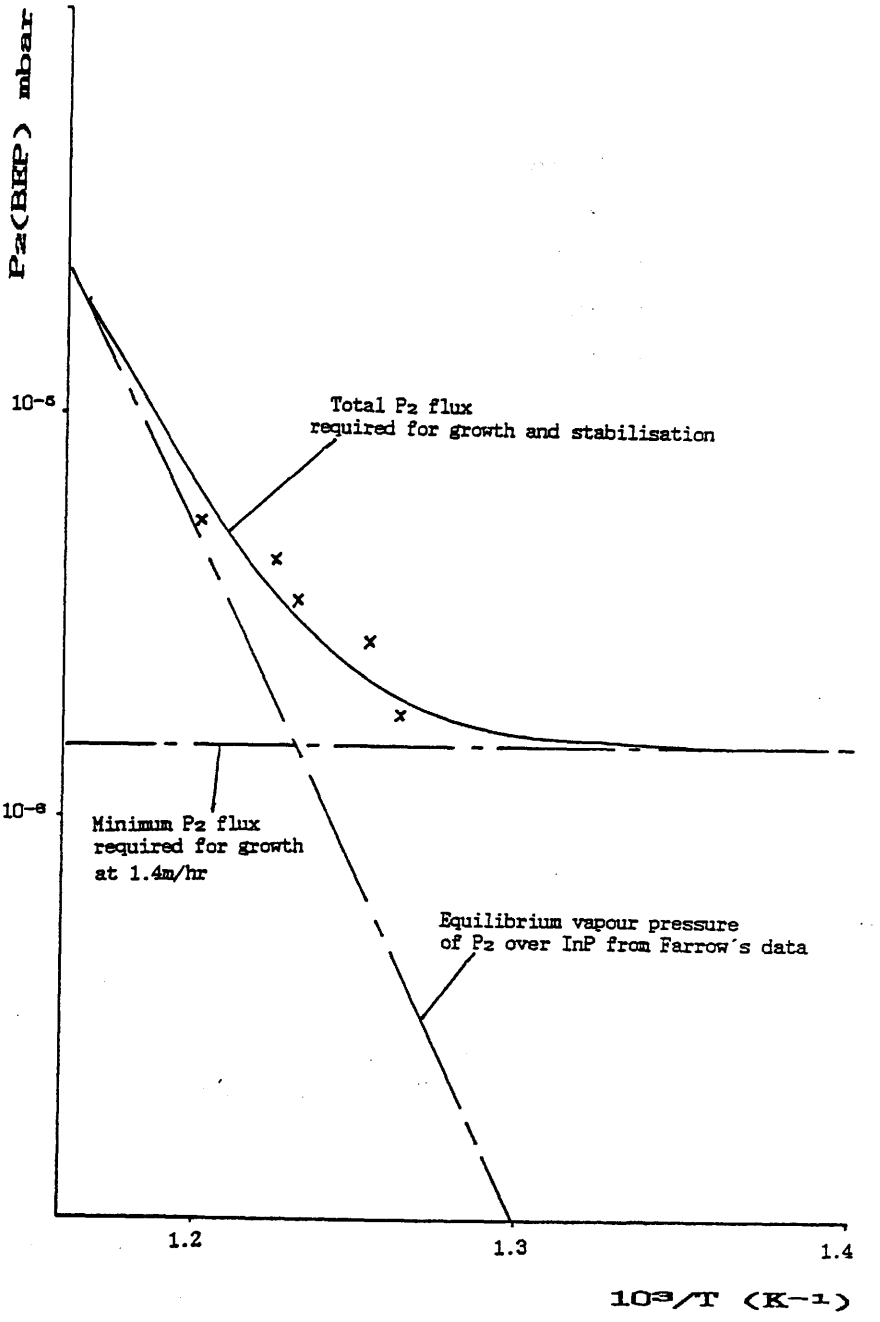

Figure 2.3 The results for the indium rich transition experiment. The dotted lines are the minimum P_2 flux required for growth at 1.4μm/hr and the equilibrium vapour pressure of P_2 over InP obtained by Farrow [2.9]. The solid line is the total P_2 flux for growth and stabilisation, which gives good agreement with the experimental data.

equation 2.1 reduces to

$$F_{total}(P_2) \approx F_{desorb}(P_2) \quad \ldots\ldots\ldots\ldots\ldots\ldots\ldots\ldots\ldots\ldots (2.2)$$

Therefore at T_{mt}, the BEP pressure of P_2 is simply the equilibrium vapour pressure of phosphorus as found by Farrow. Also shown in figure 2.3 is the minimum BEP of P_2 for the growth rate of 1.4μm/hr. The solid line in the figure is the sum of the vapour pressure of P_2 over InP plus the minimum P_2 required for growth. There is excellent agreement between the experimental data and the theory, considering the simplicity of the model.

Gallium is known to desorb from the surface of GaAs when the growth temperature is above 650°C [2.10], resulting in a reduced growth rate. Similarly, one would expect indium to desorb from InP surface at high substrate temperatures. Our main concern is to establish whether a substantial amount of indium desorbs at 460°C< T_s<560°C, the temperature region for our growth. The desorption rate may be estimated using a mass action analysis proposed by Heckingbottom [2.11]. Using such analysis the normalised growth rate as a function of the temperature is computed and the results are shown in figure 2.4 for InP, InAs and GaAs. It can be seen that there is negligible desorption of indium at temperatures up to 560°C, which has been confirmed experimentally [2.7].

2.5 Reduction of (N_D-N_A) in undoped InP

A low level of background free-carrier concentration in InP is required for device structures, so that control of intentional dopants may be obtained with the required electrical and/or optical properties. It

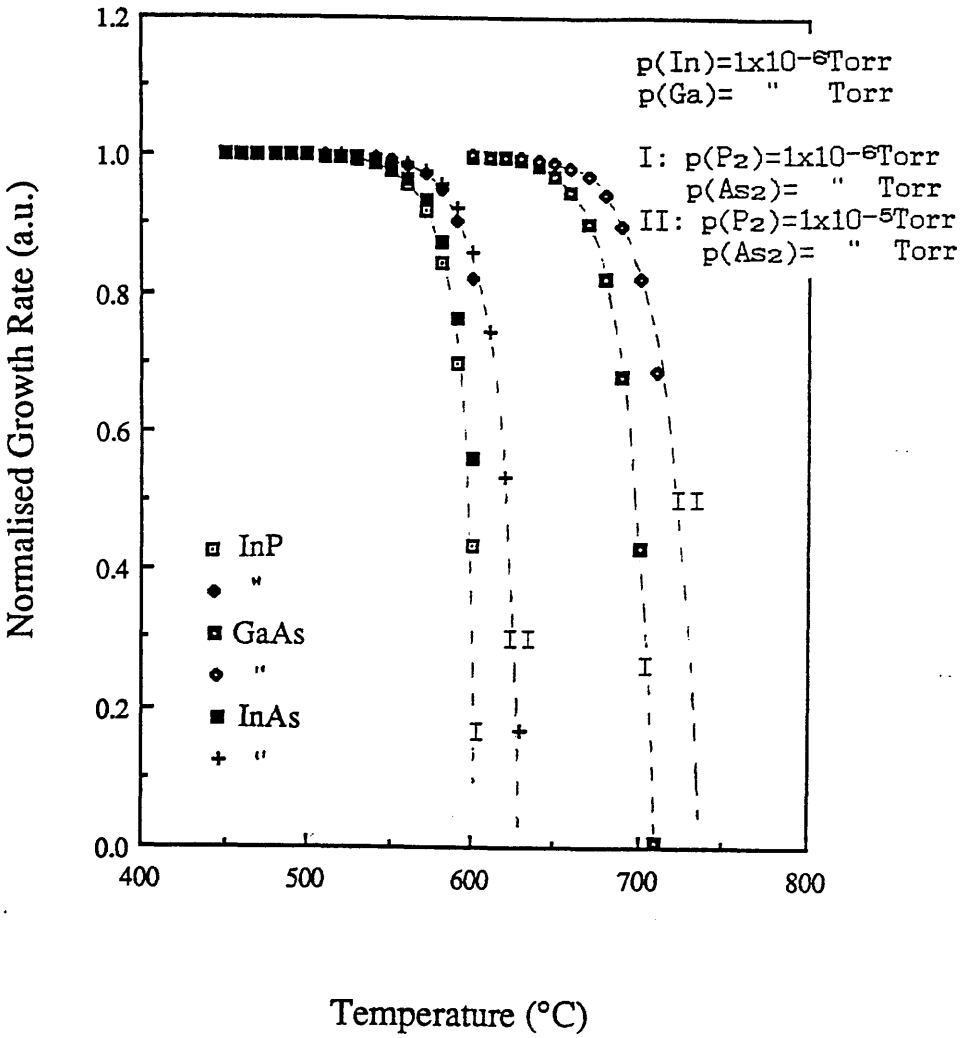

Figure 2.4 Dependence of the normalised growth rate on the temperature calculated following the analysis given by Heckingbottom [2.11]. The material system considered are InP, GaAs and InAs. At T_s<560°C, negligible desorption of indium is predicted for InP and InAs. In comparison, negligible desorption of gallium is predicted at T_s<660°C.

is possible to minimise (N_D-N_A) and thus increase the mobility by carefully controlling the three basic growth parameters: the substrate temperature T_s, the group V/III flux ratio and the growth rate G_r.

2.5.1 Effect of P_2:In flux ratio

To obtain the lowest level of (N_D-N_A) in the growth of undoped InP a minimum phosphorus flux, i.e. flux required for growth plus that for stabilisation, should be used as mentioned previously. The effect of the P_2:In flux ratio on the free-carrier concentration was investigated. An undoped InP sample was grown by using three different P_2 overpressure while the indium flux was kept constant (growth rate of 1.4μm/hr) and T_s=480°C. As shown in figure 2.5, the BEP flux ratio of P_2:In used was in the range 3-30. (N_D-N_A) has a low value ~$5x10^{15}cm^{-3}$ which increases to around $2x10^{16}cm^{-3}$ for P_2:In>15. This increase in (N_D-N_A) is associated with an increase of the sulphur flux in the P_2 beam, whose magnitude can be measured indirectly as will be shown in section 2.5.3. Free-carrier concentration in the low $10^{15}cm^{-3}$ range can routinely be achieved at T_s=480°C with a P_2:In flux ratio of <10. Most of the subsequent growth runs were performed under these growth conditions.

2.5.2 Effect of substrate temperature T_s

As will be discussed in the next chapter, sulphur desorbs from the surface of InP in the form of a compound of sulphide at temperatures beyond 500°C. Therefore, by growing InP at T_s>500°C it is possible to increase the rate of the sulphur desorption, leading to a reduction in (N_D-N_A). However, this necessitates a high incident P_2 flux to offset the increase of non-congruent evaporation rate of P_2. This in turn means an increase in the incident unintentional sulphur flux, which is undesirable. To

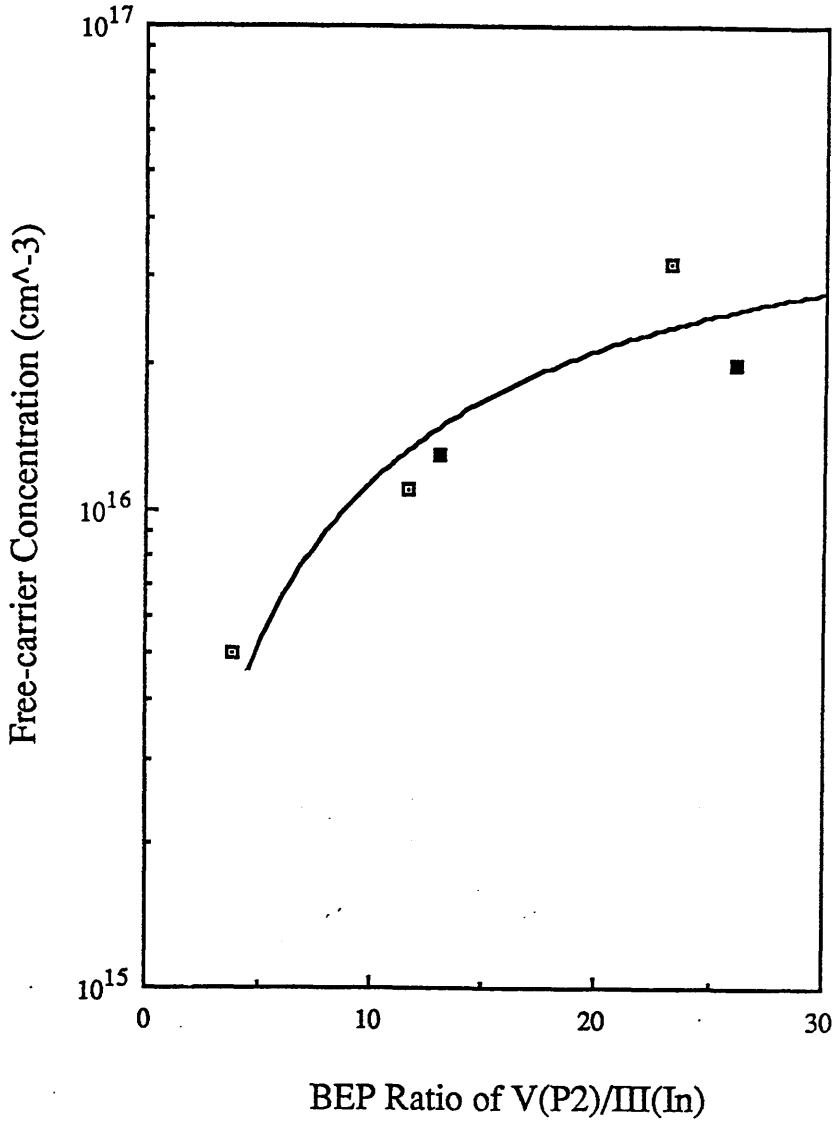

Figure 2.5 Dependence of (N_D-N_A) on the BEP ratio of P_2:In. Free-carrier concentration $<10^{16}cm^{-3}$ can be obtained with a BEP(P_2:In) < 10, and for 10<BEP(P_2:In)<30, (N_D-N_A) has a value between 1-$3x10^{16}cm^{-3}$.

determine if the desorption of sulphur is more significant than the increase of sulphur flux in the P_2 beam, an undoped InP was grown with T_s varying between 480° to 540°C. The BEP of P_2 used was $6x10^{-6}$ mbar. About an order of magnitude decrease in the free carrier concentration from $1.3x10^{16}$ to $3x10^{15}cm^{-3}$ was obtained when T_s was increased to 540°C. The free carrier concentration as a function of the inverse temperature is plotted in figure 2.6. The data (#174) obtained by Iliadis et al. [2.12] is also included in the figure and can be seen to follow the approximately the same behaviour.

The compensation ratio (N_A/N_D) at 77K for a number of undoped InP were measured as a function of T_s and the results are shown in figure 2.7. The temperature range investigated lies between 420° to 560°C. The data point at 560°C in the graph is from reference [2.12]. From the figure, it can be seen that layers grown at both high and low T_s have a high compensation ratio whilst layers grown at $460°C<T_s<530°C$ have N_A/N_D ~0.3 compensation. The high compensation at low T_s can be associated with an increase in the concentration of deep traps N_S. On the other hand, growth at $T_s>530°C$ would result in an increase in the concentration of intrinsic defects such as phosphorus vacancy complex.

2.5.3 Effect of Growth Rate G_r

Since the concentration of dopants N_D is proportional to $1/G_r$, N_D can be controlled by varying G_r. An undoped InP structure consisting of four regions was grown corresponding to four different growth rates (0.5, 0.7, 0.9 and 1.5μm/hr). The experiment was performed at a constant P_2 flux and T_s while the indium flux was varied. (N_D-N_A) decreased significantly for the high growth rate as found by CV measurements. For free-carrier concentrations above $10^{16}cm^{-3}$, the level of sulphur (N_D) in the sample has been found approximately

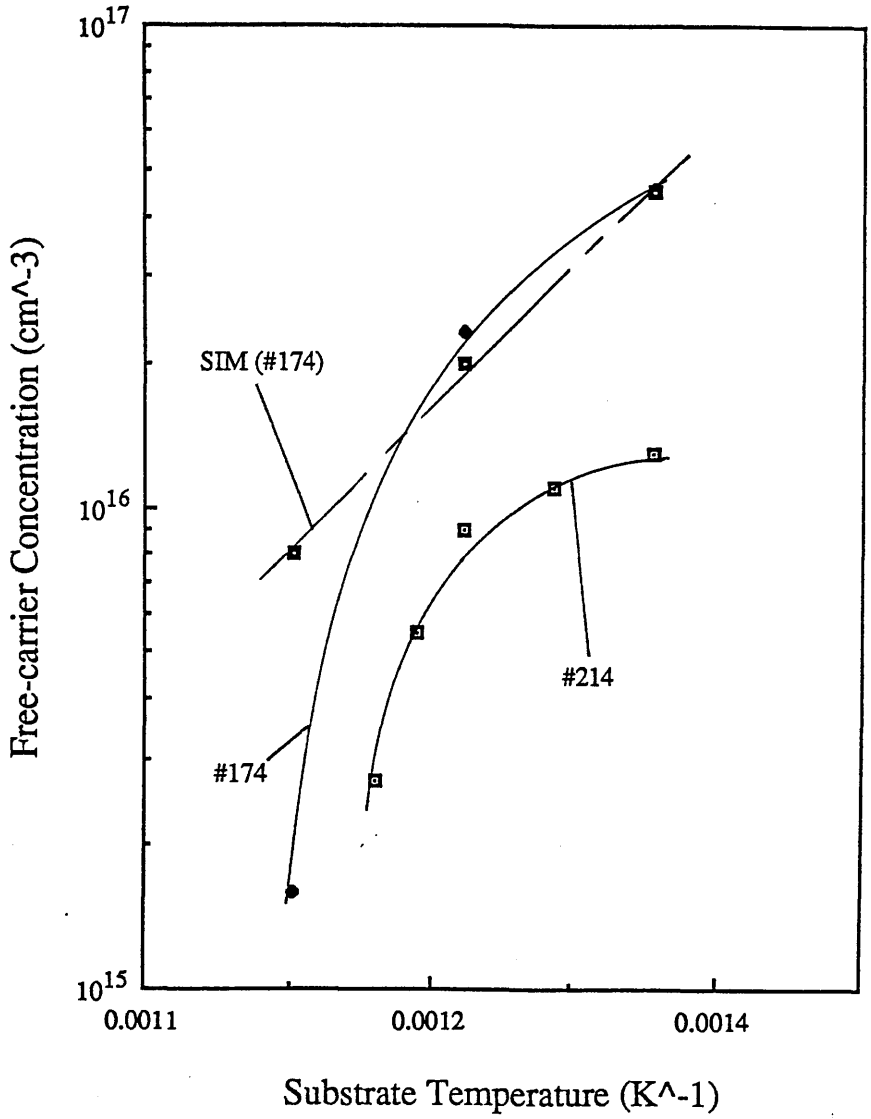

Figure 2.6 The experimental results of (N_D-N_A) versus the inverse of the substrate temperature T_s for sample #214. Included in the figure is the results obtained by Iliadis et al. in reference [2.13] for comparison.

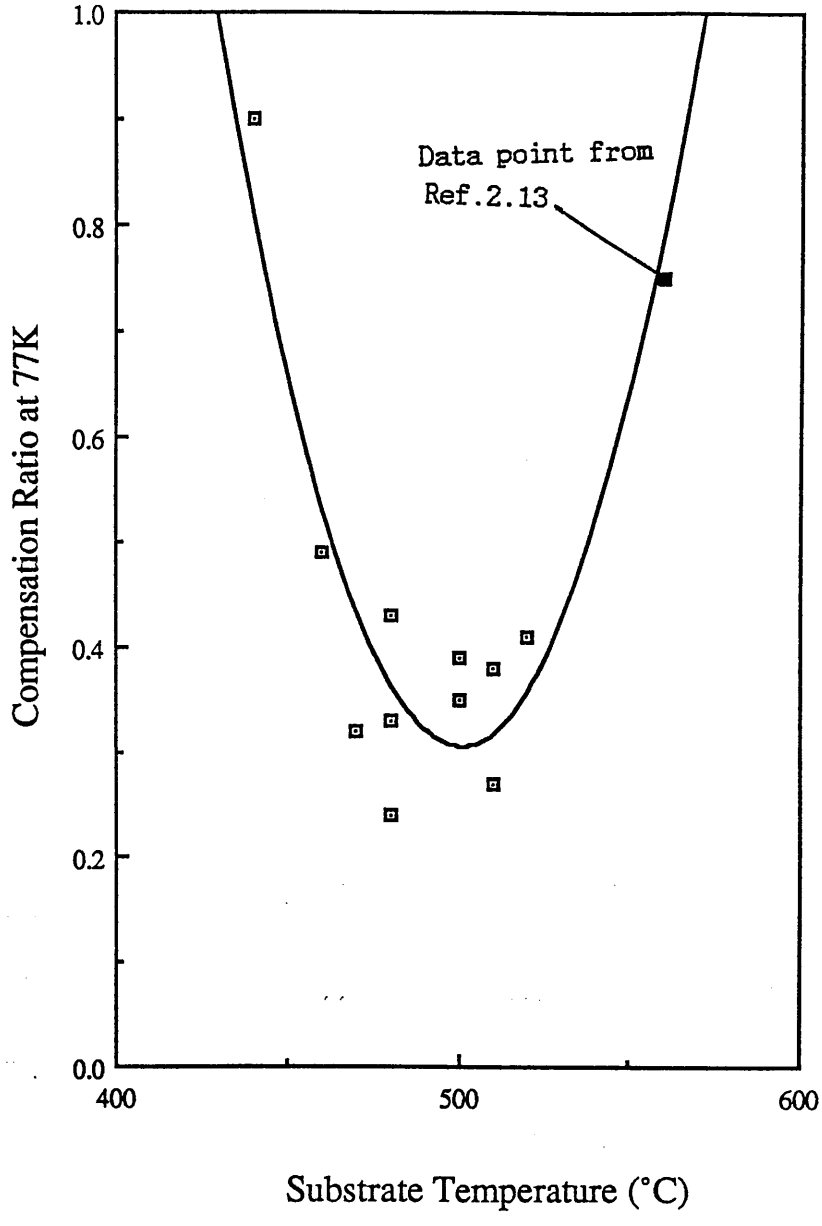

Figure 2.7 Dependence of the carrier compensation ratio on the substrate temperature. The high temperature data point is from reference [2.13].

equal to (N_D-N_A) [2.13]. Hence, it is possible to calculate an associated dopant flux if a plot of $1/(N_D-N_A)$ versus G_r is made (see also chapter 3). Such plot has been carried out as shown in figure 2.8 where the slope of the graph gives the sulphur flux from the red phosphorus. For the growth conditions used, i.e $BEP(P_2)=3x10^{-6}$mbar and $T_s=480°C$, the sulphur flux is found to be $2x10^8 cm^{-2}s^{-1}$.

It should be noted that the surface morphology of the epitaxial InP deteriorates as G_r increases. The surface defects are primarily of the 'oval' type which is probably associated with indium cell spitting analogous to gallium spitting in GaAs [2.14]. A compromise therefore should be made between the electrical and morphological characteristics when growing InP.

2.6 Hall Effect Measurements

The mobility and resistivity measurements were performed on $6mm^2$ specimens. Ohmic contacts were formed with tin dots and annealed at 430°C for about 30s in an inert gas atmosphere (N_2). Before carrying out the contacting procedure the tin dots were etched in HCl to remove surface oxide(s). Any residual indium remaining on the back of the InP substrate was removed in concentrated nitric acid to give a better thermal contact for annealing.

2.6.1 Hall measurements at 300 and 77K

The electrical properties of InP epitaxial layers grown were routinely measured by the Hall effect technique at both 77 and 300K. The carrier compensation ratio (θ) is calculated using the tables

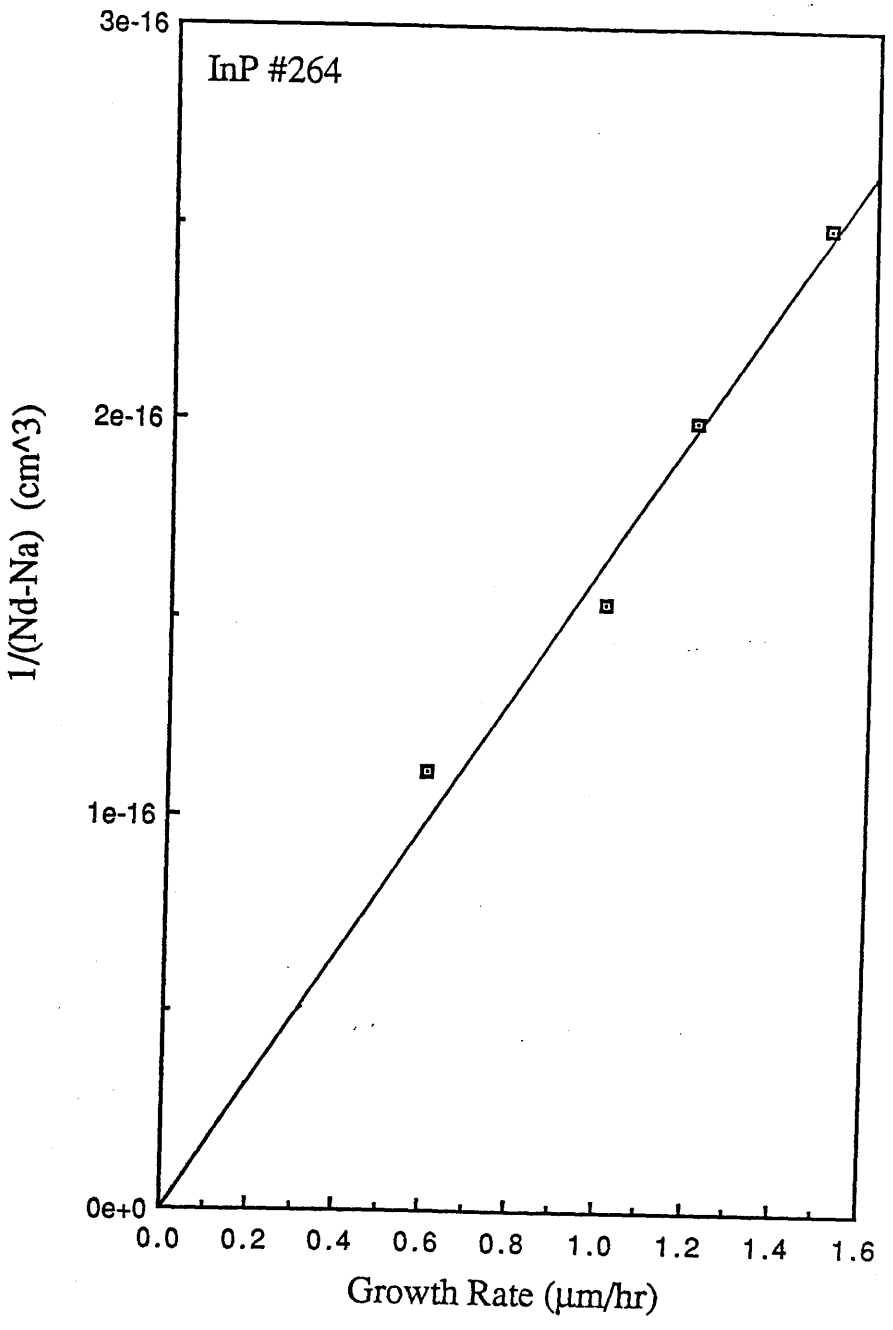

Figure 2.8 A plot of the inverse free-carrier concentration versus the growth rate. From the slope of the graph, the associated sulphur flux from the phosphorus cell is calculated to be $2 \times 10^{8} cm^{-2} s^{-1}$.

given by Walukiewicz for InP [2.15]. It should be noted that the measured Hall mobility and free carrier concentration should be converted to their drift values when using Walukiewicz's tables. The relationship between the Hall and drift mobilities and carrier concentrations are as follows [2.16]:

$$u_{(drift)} = 1/r_H \times \mu_{(hall)} \quad \ldots\ldots\ldots\ldots\ldots\ldots\ldots\ldots (2.3)$$

$$n_{(drift)} = r_H \times n_{(hall)} \quad \ldots\ldots\ldots\ldots\ldots\ldots\ldots\ldots (2.4)$$

where r_H is the Hall scattering factor which takes a value of 1.25 and 1.1 at 300 and 77K respectively [2.17].

An estimate of the total concentration of acceptors in the layer may be calculated from the compensation ratio θ. Table 2.1 shows the experimental results for the undoped samples. θ is deduced using the data measured at 77K to avoid errors introduced by deep donor levels [2.16] and also the uncertainty of r_H at room temperature [2.17].

2.6.2 Variable temperature measurements of mobility and (N_D-N_A)

Hall measurements as a function of temperature were made on specimens #203 and #249. These undoped samples were grown under different growth conditions to give different electrical behaviour. The experimental results are plotted in figure 2.9, 2.10. The samples show the general trend in the μ versus T curves in which μ increases from low T and reaches a maximum at about 80K and finally decreases as T increases. The behaviour of the μ(T) curve may be explained by taking into account the various scattering mechanisms: polar phonon scattering (OP), ionised impurity scattering (II), acoustic deformation potential scattering (DP)

Table 2.1 Hall measurements at 300K and 77K for some of the InP samples grown.

Sample No.	300K $n(cm^{-3})$ $\mu(cm^2/Vs)$	77K $n(cm^{-3})$ $\mu(cm^2/Vs)$	T_s (°C)	N_D (cm^{-3})	N_A (cm^{-3})
231	8.2×10^{15}	3.2×10^{15}	500	4.9×10^{15}	1.7×10^{15}
	2650	2.5×10^{4}			
236A	2.1×10^{16}	4.7×10^{15}	520	8×10^{15}	3.3×10^{15}
	1920	1.8×10^{4}			
235	4.3×10^{15}	2.4×10^{15}	510	3.3×10^{15}	9.3×10^{14}
	2720	3.32×10^{4}			
234	8.2×10^{15}	3.9×10^{15}	470	5.7×10^{15}	1.8×10^{15}
	2750	2.36×10^{4}			
233	6.8×10^{15}	3.4×10^{15}	480	5.1×10^{15}	1.7×10^{15}
	2410	2.5×10^{4}			
232	7.4×10^{15}	3.4×10^{15}	510	4.7×10^{15}	1.3×10^{15}
	2780	2.9×10^{4}			
203	2.1×10^{15}	1.6×10^{15}	480	2.1×10^{15}	5.1×10^{14}
	4400	4.25×10^{4}			
237B1	1.6×10^{16}	5.5×10^{15}	460	1.1×10^{16}	5.3×10^{15}
	2160	1.4×10^{4}			
237D1	1.7×10^{16}	2×10^{15}	440	1.9×10^{16}	1.7×10^{16}
	2600	5200			

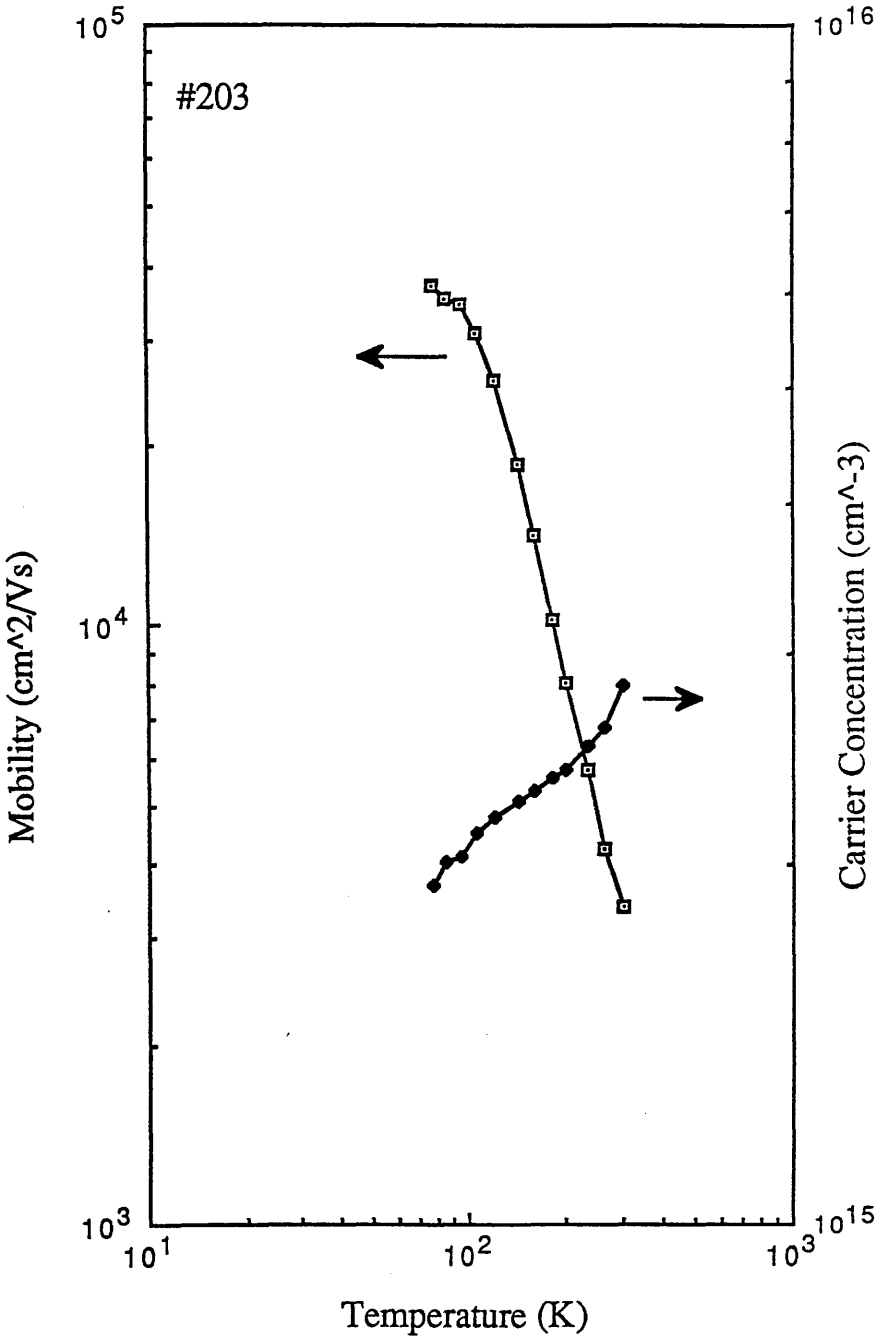

Figure 2.9 Carrier concentration and mobility for the undoped InP #203 in the temperature range of 77-300K.

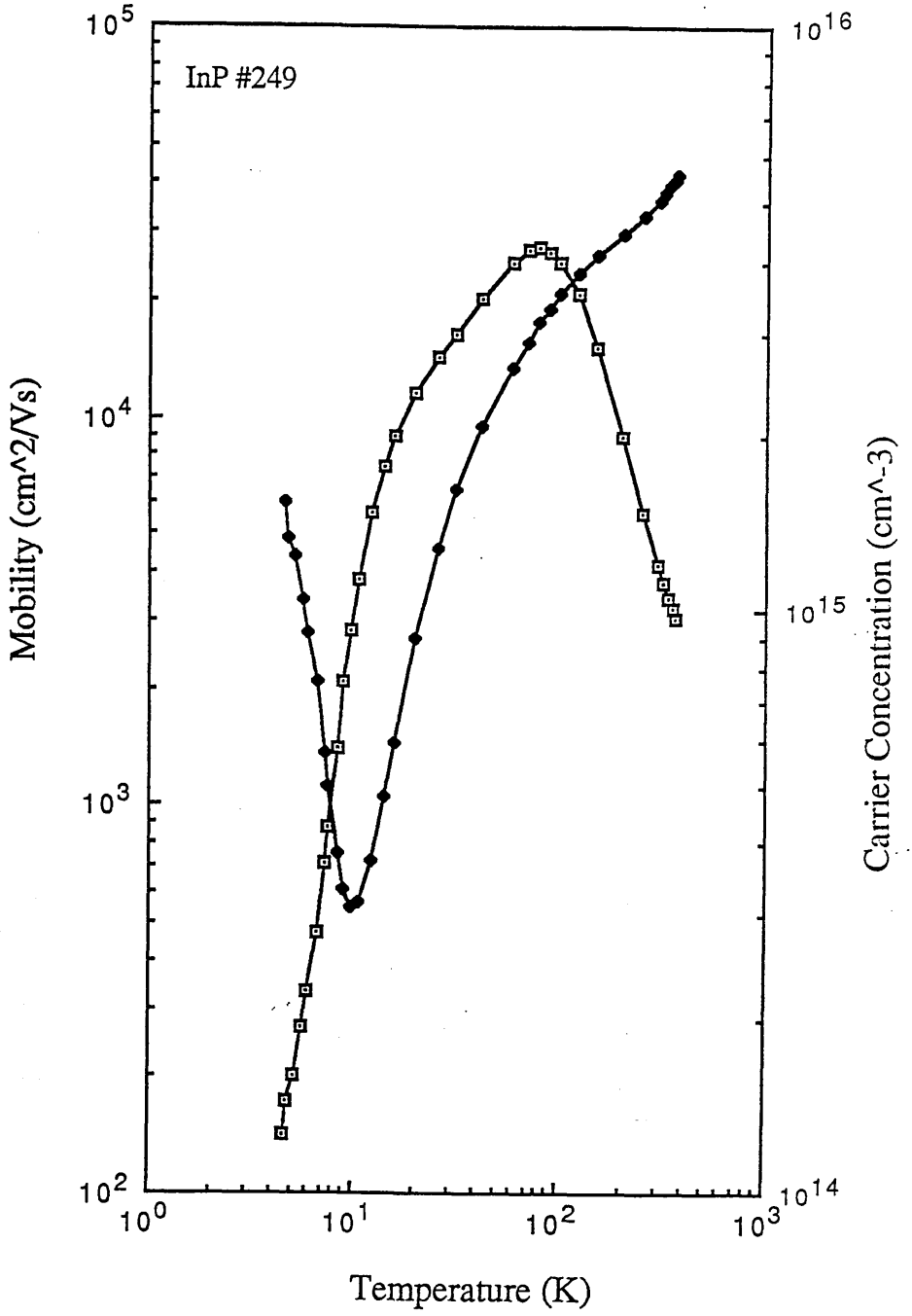

Figure 2.10 Behaviour of the carrier concentration and mobility as a function of temperature in the range of 4-300K. The presence of a minimum in the carrier concentration at ~10K clearly demonstrates the existence of impurity band conduction.

and piezoelectric scattering (PE). Assuming each of these four scattering process may be described by a scattering time constant , the total mobility may be calculated by the so called Mathiessen's rule [2.18]:

$$1/\mu_{(total)} = 1/\mu_{(op)}+1/\mu_{(ii)}+1/\mu_{(pe)}+1/\mu_{(dp)} \quad \ldots\ldots\ldots\ldots (2.5)$$

This theoretical approximation has been computed for sample #203. If a deformation potential of 13eV is used, a close fit to the experimental data is obtained as shown in figure 2.11 (contributions of the different scattering mechanisms are also included). At high temperatures (T>200K), the mobility is dominated by optical phonon scattering while at low temperatures (T<100K) it is dominated by ionised impurities. At the intermediate temperature region (100<T<200K), the acoustic deformation potential scattering has some effect on the total mobility. At the lowest temperatures (T<10K), the conduction is dominated by impurity band conduction, which is characterised by a minimum in the (N_D-N_A) versus temperature graph as shown in figure 2.10. Impurity band conduction at low temperatures has also been observed for other semiconductors, e.g. InSb [2.19] and InAs [2.20]. The onset of impurity band conduction depends both on the carrier concentration and the compensation ratio, and which is discussed in more details in chapter 5.

2.6.3 Possible Source of Errors in the Hall Effect Calculation

Despite the relative ease of provision of electrical data from the Hall effect measurement, care should be exercised when calculating the 'true' mobility and carrier concentration from the raw experimental data. In some cases, substantial errors may be introduced if

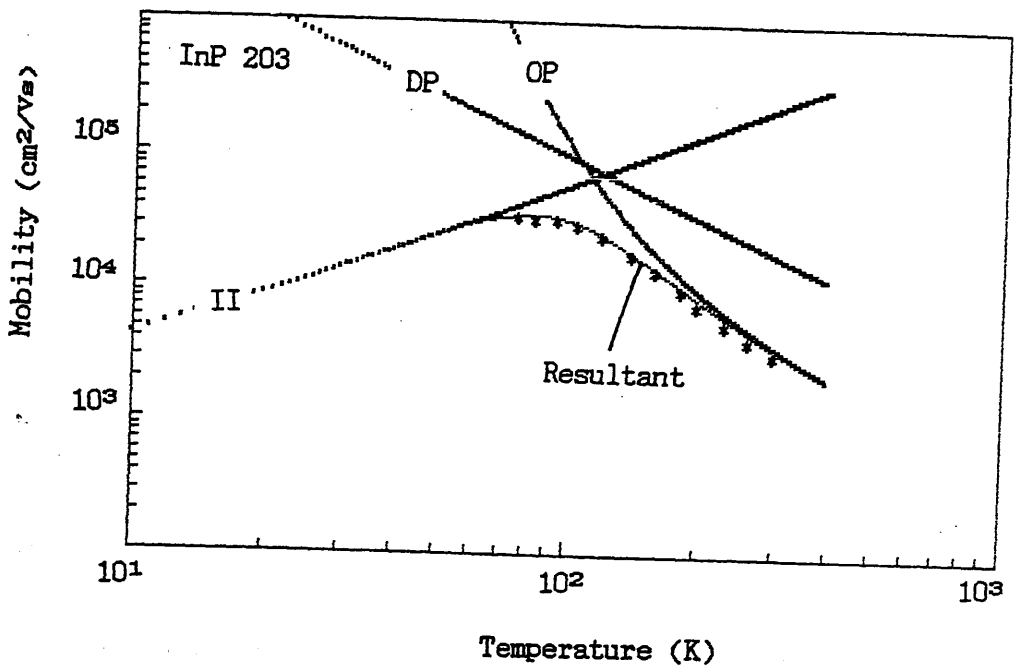

Figure 2.11 A theoretical fit to the mobility versus temperature data using Mathiessen's rule. Included are the separate scattering mechanisms considered.

the following factors are not considered:

(a) Surface and Interface Depletion Effects

Surface depletion arises from the Fermi level at the semiconductor surface being pinned at a fixed position by the presence of deep states. Similarly, at the interface between an n-type epitaxial layer and a semi-insulating substrate the carriers diffuse into vacant states in the substrate. The extent to which such diffusion occurs depends on the concentration of deep traps available and therefore the width of depletion. Calculations of the depletion width as a function of (N_D-N_A) have been performed on GaAs by Chandra *et al.*[2.21]. Using the same method, the corresponding relationships for InP have been calculated, which are shown in figures 2.12(a) and 2.12(b) for the surface and interface depletion respectively. Here a potential of 0.5 and 0.6eV is assumed for the surface and interface regions. From these figures, it is seen that depletion becomes important for materials with low (N_D-N_A). Hence for very low doped samples, the 'electrical' thickness of the layer can significantly differ from the physical one. If the correction is not made when calculating (N_D-N_A), then an overestimate of the compensation ratio would result.

(b) Interfacial Spike

Often, an accumulation of impurities is found at the interface when undoped epitaxial InP is grown on a semi-insulating substrate. The buildup of impurities at the interface has been attributed to an increase in the sulphur concentration [2.5], and which manifests itself as a spike in the free-carrier concentration versus depth profile. Studies on the growth interruption in InP under different conditions were performed to investigate the effect of this impurity

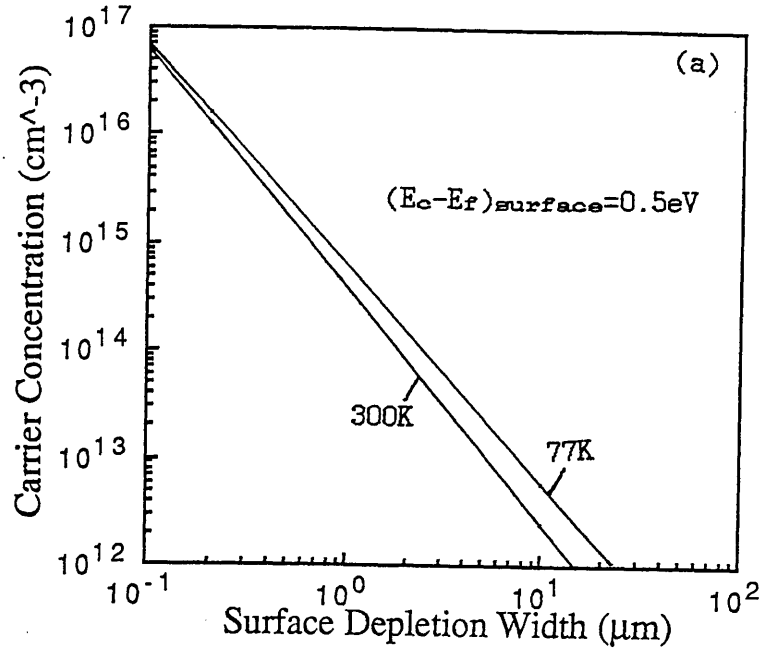

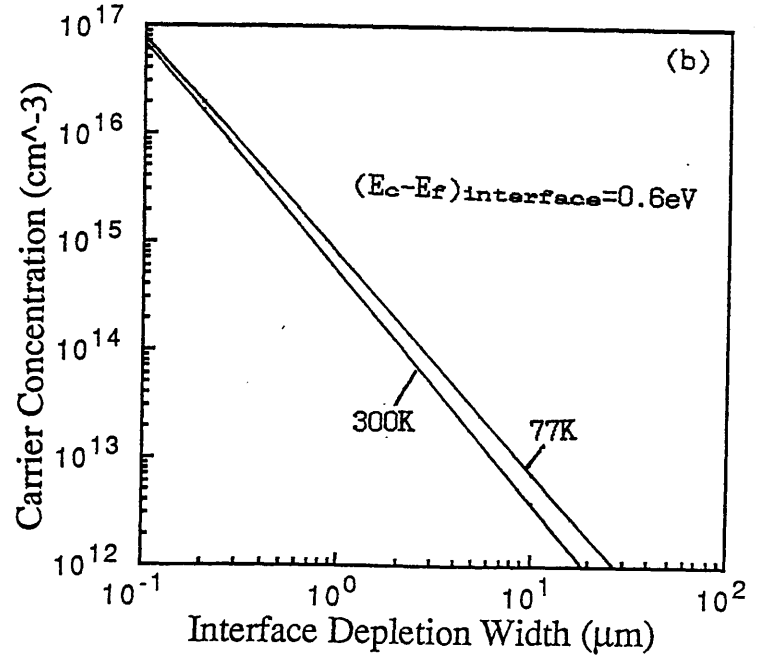

Figure 2.12 Depletion widths as a function of the carrier concentration for InP calculated following the analysis given in reference [2.21].

spike. An undoped InP epitaxial layer was grown in which two growth interrupts were made during growth at T_s=480°C, $p(P_2)=2\times10^{-6}$mbar and $p(In)=4\times10^{-7}$mbar. The first interruption was made by shutting off both the indium and the phosphorus fluxes for a period of 15mins. In this case the phosphorus background pressure was sufficient to stabilise the growth surface. The second interruption was introduced by closing off only the indium flux for the same duration. Figure 2.13 shows the plot of carrier concentration depth profile. At the first growth interrupt, the (N_D-N_A) is at the same level as the background concentration at $1\times10^{16}cm^{-3}$. At the second growth interrupt, a spike is found to be present, suggesting that the increase in (N_D-N_A) is associated with the incident P_2 flux. Sulphur contamination at the substrate of GaAs has been shown to originate from the wet etching step prior to epitaxial growth [2.22]. This would also be expected to occur for InP substrates. Consequently, the observed interfacial spike in InP is believed due to two different sources:- from the sulphur impurities in the P_2 flux and from the sulphuric acid etch used prior to growth.

The existence of the sulphur accumulation at the interface would mean the Hall technique measures an average conductivity from two active layers, so that a two-layer conductivity model is appropriate [2.23]:

$$(N_D-N_A)_{exp}=(n_1\mu_1d_1 + n_2\mu_2d_2)^2/[(d_1+d_2)(n_1d_1\mu_1^2 + n_2d_2\mu_2^2)] \quad \ldots\ldots\ldots\ldots\ldots\ldots (2.6)$$

$$\mu_{exp} = (n_1d_1\mu_1^2 + n_2d_2\mu_2^2)/(n_1\mu_1d_1 + n_2\mu_2d_2) \quad \ldots\ldots\ldots\ldots\ldots\ldots (2.7)$$

where subscripts 1 and 2 denote the two respective layers, (i) the 'normal' epitaxial layers, and (ii) the layer associated with the effectively δ-doped interface.

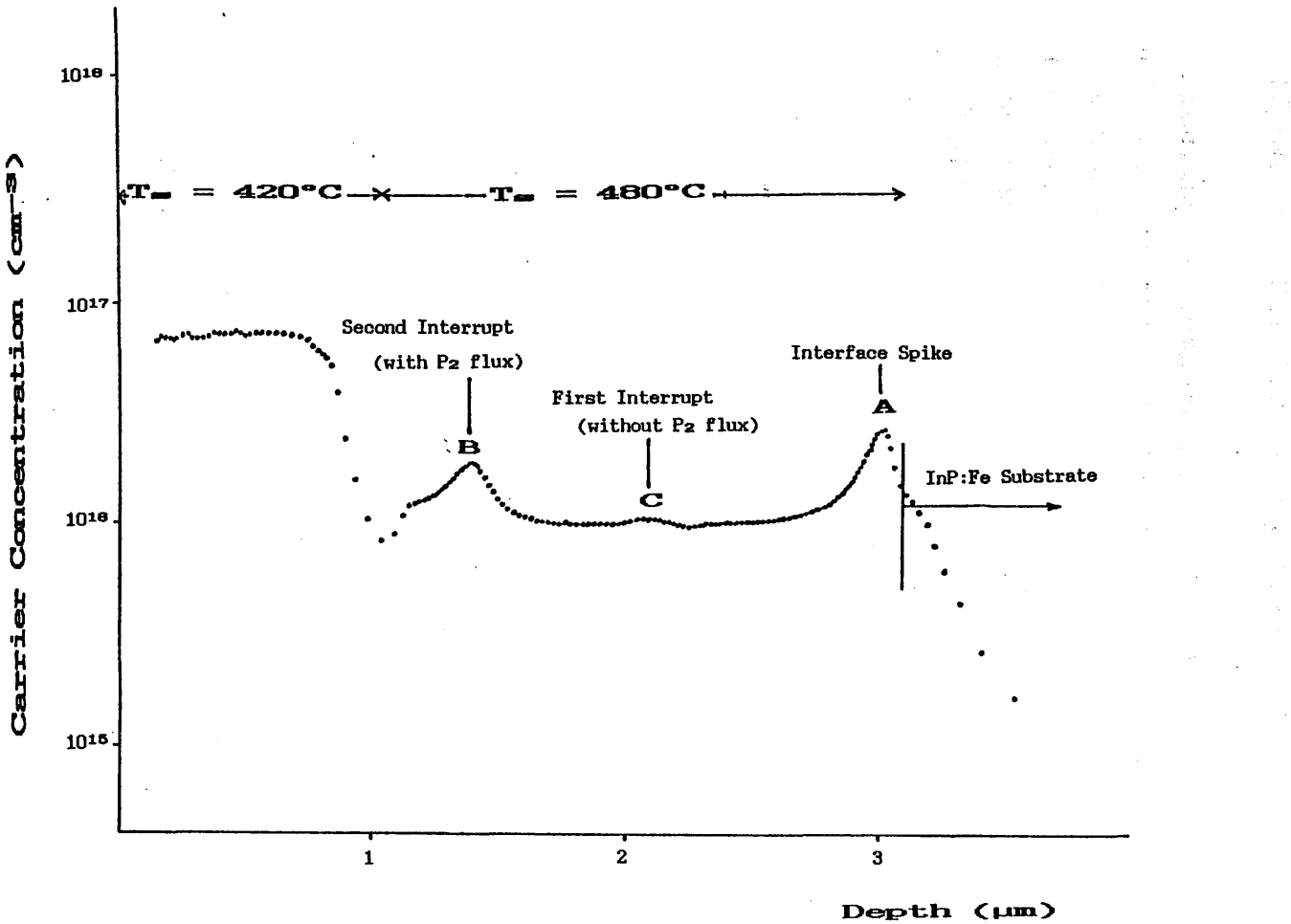

Figure 2.13 C-V profile for the growth interruption experiment which shows impurity accumulation in different regions.

Figure 2.14 shows a C-V plot of an undoped InP with a high interfacial spike relative to the concentration of the background level. The Hall effect measurement at room temperature gave

$(N_D-N_A) = 1.3x10^{16}cm^{-3}$ and $\mu=2,200cm^2V^{-1}s^{-1}$

Assuming a compensation of 0.4 and 0.8 for the epilayer and the interfacial layer respectively, and with the following values:

$n_1=4.5x10^{15}cm^{-3}$ $n_2=1.8x10^{17}cm^{-3}$

$\mu_1=4100cm^2V^{-1}s^{-1}$ $\mu_2=1000cm^2V^{-1}s^{-1}$

$d_1=2.1\mu m$ $d_2=0.3\mu m$

The estimated $(N_D-N_A)=1.9x10^{16}cm^{-3}$ and $\mu=2200cm^2V^{-1}s^{-1}$, agree well with the measured values considering the approximation made to the interfacial layer.

2.7 Deep Level Transient Spectroscopy (DLTS) Measurement

Details such as the energy position, the concentration and the capture cross-section of impurities lying deep (>100meV) within the forbidden energy gap can be obtained by the deep level transient spectroscopy technique (DLTS). Deep levels act mostly as non-radiative recombination centers thus quenching the PL emission efficiency. The electrical behaviour of the epitaxial layer is degraded because carriers are trapped by these deep centers. The DLTS technique provides a unique signature for each individual trap and may in some cases identify the species involved by comparing the detected DLTS signal to those already measured for known impurities.

The deep levels in an unintentionally doped InP layer grown on a n+ substrate were investigated. A Schottky diode is required to study the majority

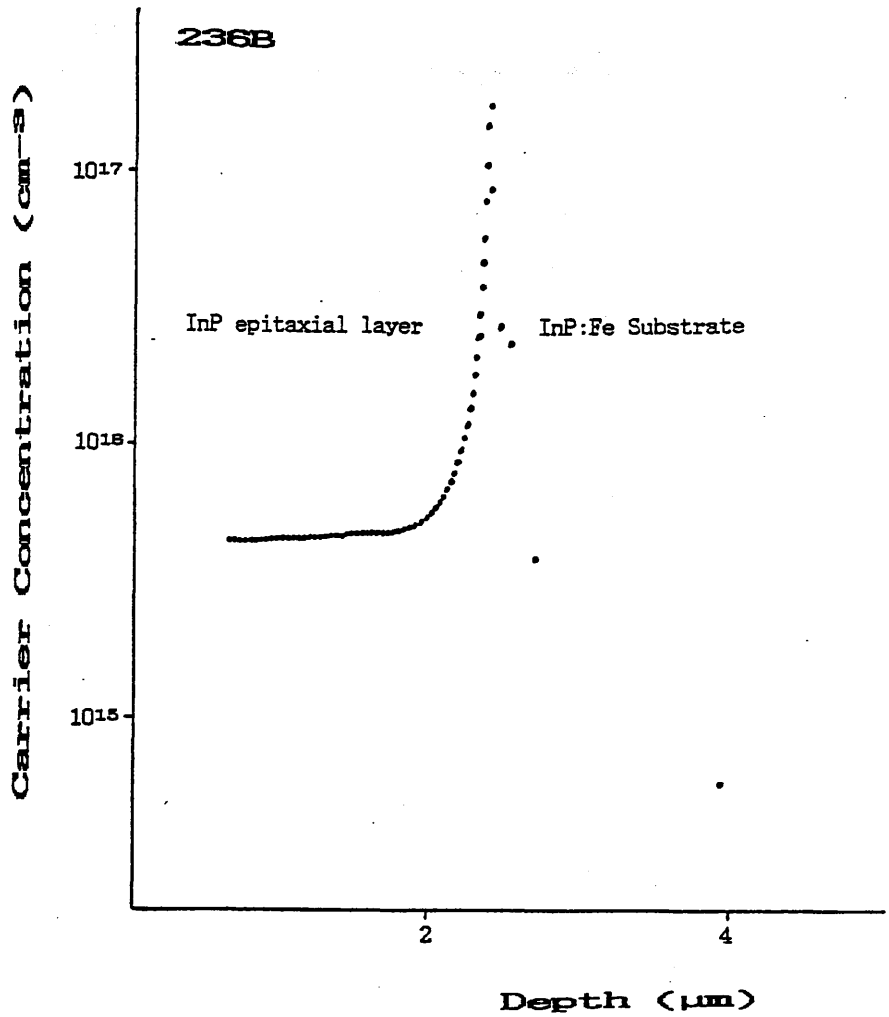

Figure 2.14 Free-carrier concentration profile as a function of depth from CV measurement, showing a substantial interfacial spike. If the spike is not taken account in the Hall effect measurement calculations, an incorrect (N_D-N_A) would result leading to a higher compensation ratio (see text).

carrier traps using DLTS. Since the sample was grown on a conducting substrate, the substrate was used to form the ohmic contact while the Schottky contact was made to the surface of the epitaxial layer. The ohmic contact was formed by using an alloy of Au/Ge/Ni and annealed at 420°C for 20s. The Schottky contact was achieved by simply depositing a layer of Au (about 2500Å) through a mechanical mask.

The I-V characteristic of the fabricated diode is shown in figure 2.15(a). At a reverse bias of -2V the dark current is about 0.1mA which is adequately low for the DLTS measurement. The commercial DLTS system manufactured by Polaron was used for the measurement, which is capable of scanning the temperature range between 77-400K. Figure 2.15(b) shows a typical DLTS spectrum for sample 296A at rate windows of 1000/s and 400/s. The peaks in the DLTS spectrum depends on the rate window used; the higher the rate window, the higher the temperature position of the peak. Four peaks, labelled EDT1, EDT2, EDT3 and EDT4, are clearly resolved with corresponding activation energies of 432, 269, 281 and ~100meV as shown in figure 2.16. Table 2.2 lists the observed electron traps together with their estimated concentrations N_S and capture cross-sections σ. Traps EDT1, EDT2 and EDT3 correspond to the three respective electron traps, E1 ,E2 and E3 observed by Asahi et al. [2.24] in MBE grown InP grown using solid sources. The electron trap EDT1 may correspond to the IE1 trap observed in VPE materials by Bremond et al., which they believed to be associated with Fe impurities outdiffused into the epitaxial layer from the substrate [2.25]. However, SIMS measurements provide no evidence for Fe outdiffussing from the substrate in our samples.

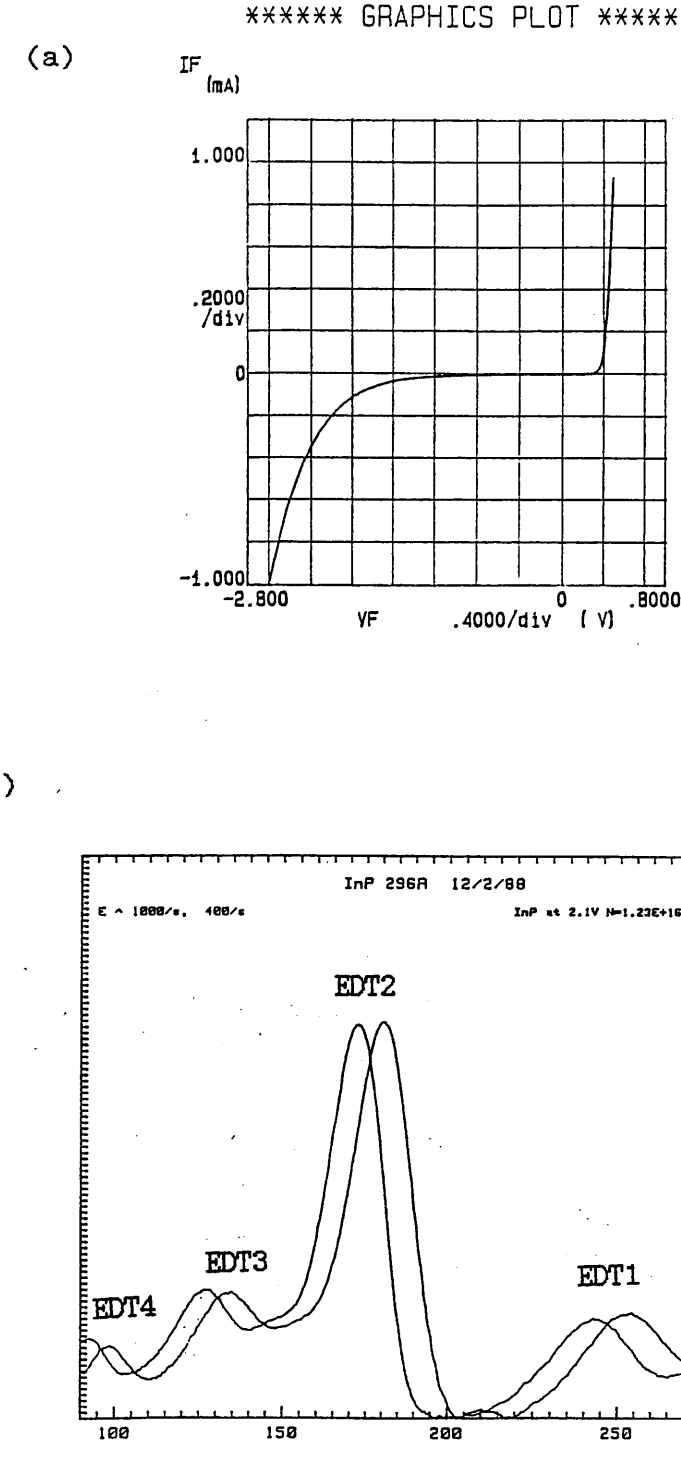

Figure 2.15 (a) I-V characteristic of the Schottky diode fabricated on an undoped InP. (b) DLTS spectrum showing the four observed electron traps EDT1, EDT2, EDT3 and EDT4.

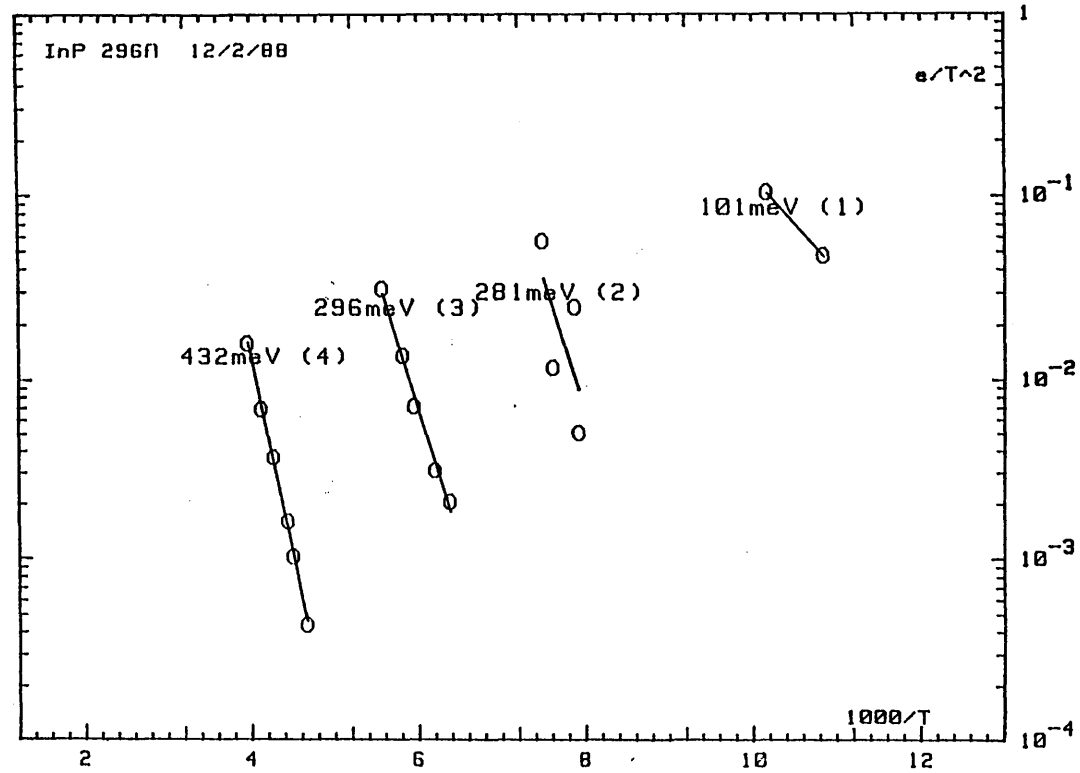

Figure 2.16 Arrhenius plot of the four observed electron traps in undoped InP grown by solid source MBE.

Table 2.2 Observed electron traps in InP grown by solid source MBE.

Trap	E_a(meV)	N_S(cm^{-3})	σ(cm^{-2})
EDT1	432	$4x10^{14}$	$2.7x10^{-14}$
EDT2	296	$1.65x10^{15}$	$2.4x10^{-14}$
EDT3	281	$5x10^{14}$	$2.3x10^{-14}$
EDT4	100?	$3.5x10^{14}$	?
	N_S(total) =	$2.9x10^{15}cm^{-3}$	

2.8 Photoluminescence at low temperatures

When incident light of energy greater than the band gap energy is directed onto a semiconductor, the photons are absorbed creating free electrons and holes. These then relax through many different recombination processes resulting in emitted photons of different energies [2.26]. The photoluminescence (PL) then provides an identification of the likely recombination paths involved.

The PL system used in this work consisted of a He-Ne laser operating at 633.2nm, a 1m monochromator and Ge p-i-n photodetector. The samples were cooled in a 15K optical cryostat cooled by recirculating He. PL signals were detected with the usual lock-in techniques to reduce the noise. Higher resolution PL at 2K was also performed at the University of St. Andrews using a system with a liquid helium cooled immersion cryostat (more detailed of this system can be found in reference 2.27).

A typical PL spectrum of an undoped epitaxial InP sample grown by MBE is shown in figure 2.17. Principally, there are three different emission regions; near band edge recombination (labelled A), a donor-to-acceptor pair transition (labelled B) and the 1.36eV emission with its phonon replicas at the lower energies (labelled C). These three regions are discussed separately below.

2.8.1 Near band edge emission

The PL spectrum of the InP is dominated by the recombination of bound excitons which yield a linewidth of ~4meV indicating high quality material. Table 2.3 lists the observed emission peaks with their appropriate assignments. The peak at 1.417eV is assigned to an exciton bound to a neutral shallow donor (D°-X) and the lower energy shoulder at 1.415eV

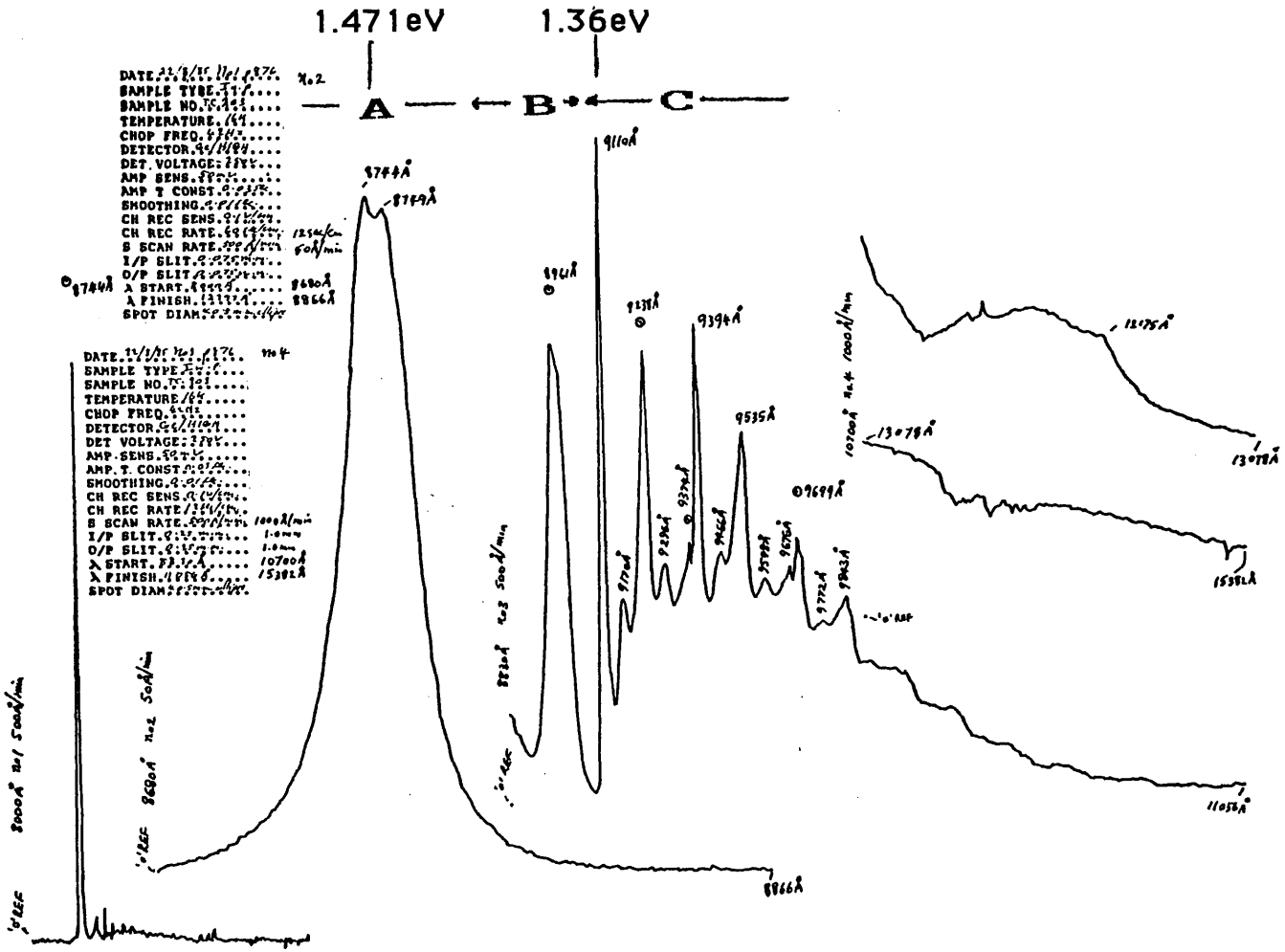

Figure 2.17 16K PL of an undoped InP with the emission regions A, B and C corresponding to the near band edge recombination, the donor-to-acceptor pair transition and the 1.36eV emission plus its phonon side band respectively.

Table 2.3 PL emission peaks from an InP sample and with the possible assignment to the individual peaks.

peak (eV)	Assignment
1.4183	X, free exciton
1.4175	(D°-X), exciton bound to neutral donor
1.4165	(D°-X)', 1st state of exciton bound to donor
1.4160	(D°-h), donor-valence band transition
1.3835	(e-A°), free to bound transition associated with magnesium
1.3785	(D°-A°), donor-acceptor transition associated with magnesium
(1.3785)	(e-A°), free to bound transition associated with carbon
1.3758	(D°-A°), donor-acceptor transition associated with carbon
1.3600	exciton bound to a deep donor associated with a phosphorus vacancy

to an exciton bound to an ionised donor (D^+-X). The temperature dependence of the (D°-X) emission has been measured. The experimental result is shown in figure 2.18. The normalised intensity of the peak decreases as the temperature is increased. In the high temperature region, the curve approximately follows an exponential decay law with an thermal activation energy of 10meV. This value agrees well with the donor activation energy measured by Chamberlain et al. using far infrared techniques [2.28].

2.8.2 Donor-Acceptor pair transition

The intensity of the D-A pair transition is low compared with the (D°-X) emission for most of the undoped samples. For undoped InP, the donor to acceptor pair emission may be resolved into two distinct peaks, see figure 2.19. The peak at 1.380eV and 1.3786eV are the free to bound (e-A°) and the donor to acceptor (D°-A°) pair transitions respectively. Comparison with the emissions peaks for different impurities in implanted InP samples given by Skromme et al. [2.29] suggests that the observed (e-A°) and (D°-A°) peaks are associated with magnesium impurities (also see chapter 4).

2.8.3 Emission at 1.36eV and its phonon replica

The PL emission peak at 1.36eV was a consistent feature of nominally undoped InP grown in the present MBE system. The same transition has also been detected in polycrystalline InP [2.30], heat treated LEC InP [2.31] and MOCVD InP [2.32]. It has been assigned to excitonic recombination at a deep neutral donor associated with a phosphorus vacancy [2.31,2.32]. In this section, results obtained from measuring the dependence of the emission peak on the sample temperature and laser excitation intensity further supports this assignment. In figure 2.20, the 1.36eV

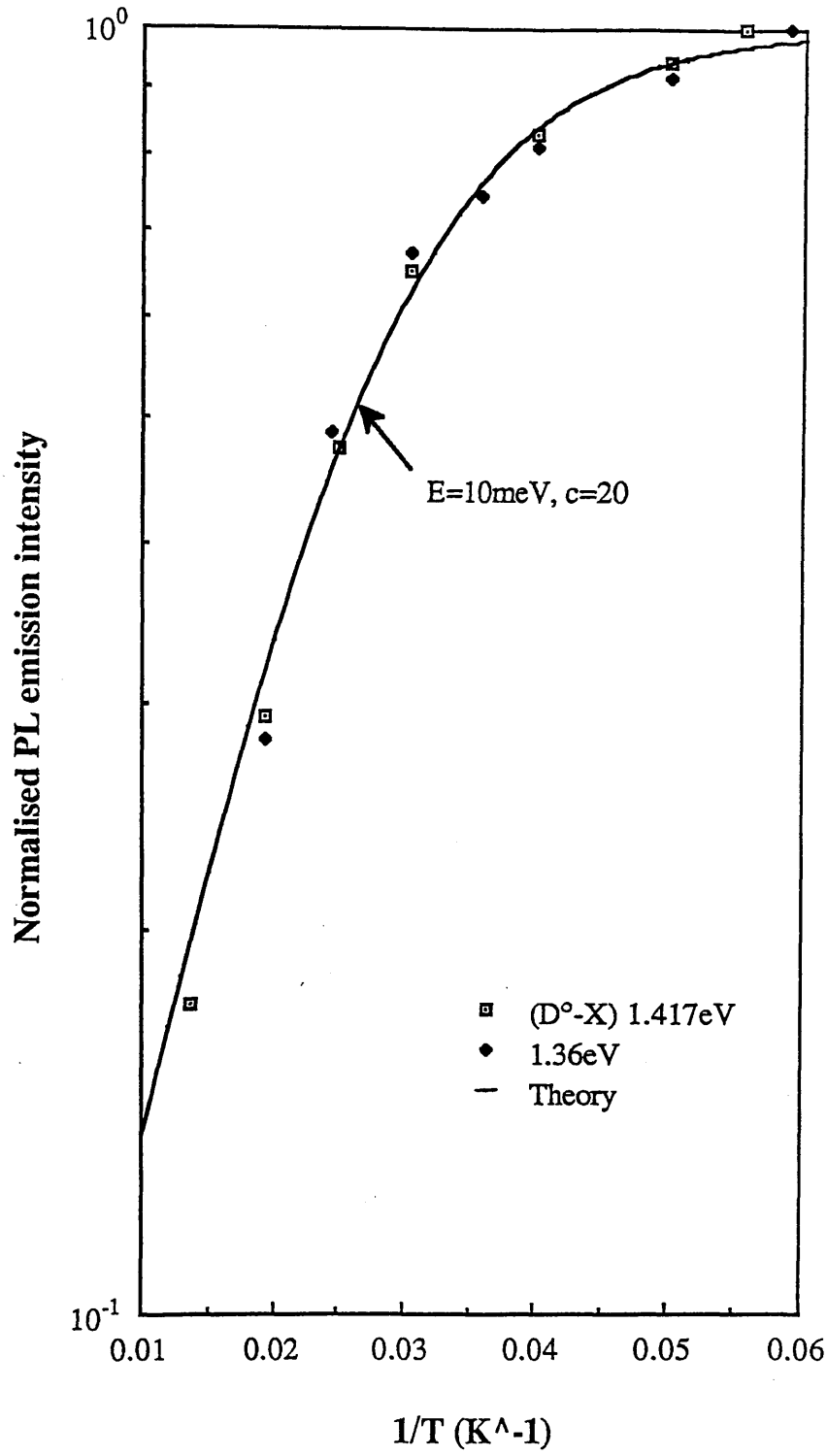

Figure 2.18 Normalised PL intensity of the (D°-X) and the 1.36eV line as a function of inverse temperature. Both emissions exhibit the same temperature dependence and have an activation energy of 10meV.

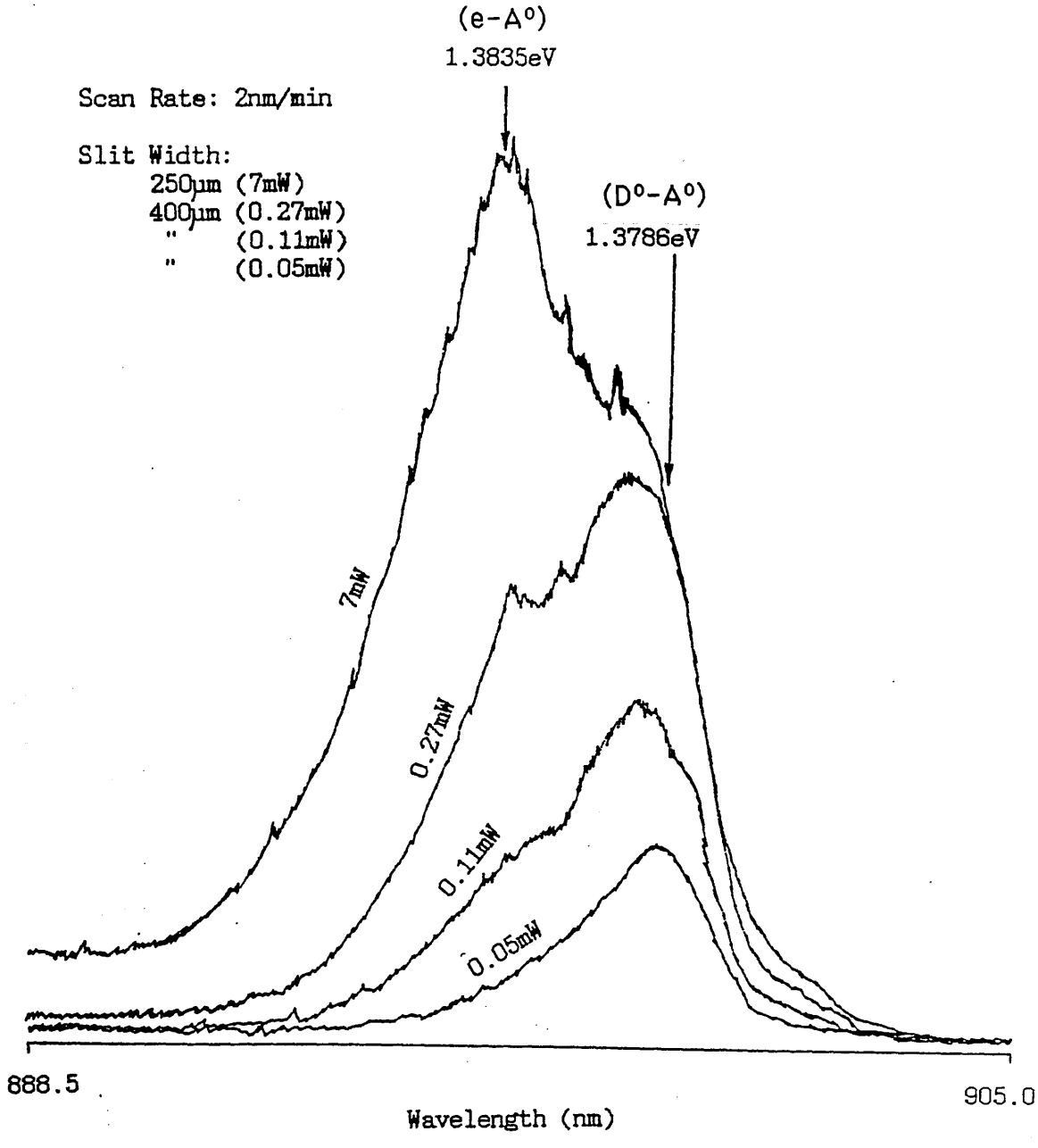

Figure 2.19 Low temperature PL in the ~1.38eV emission region. The emission peaks at 1.3830 and 1.3786eV are identified as the (e-A°) and (D°-A°) transitions associated with magnesium respectively.

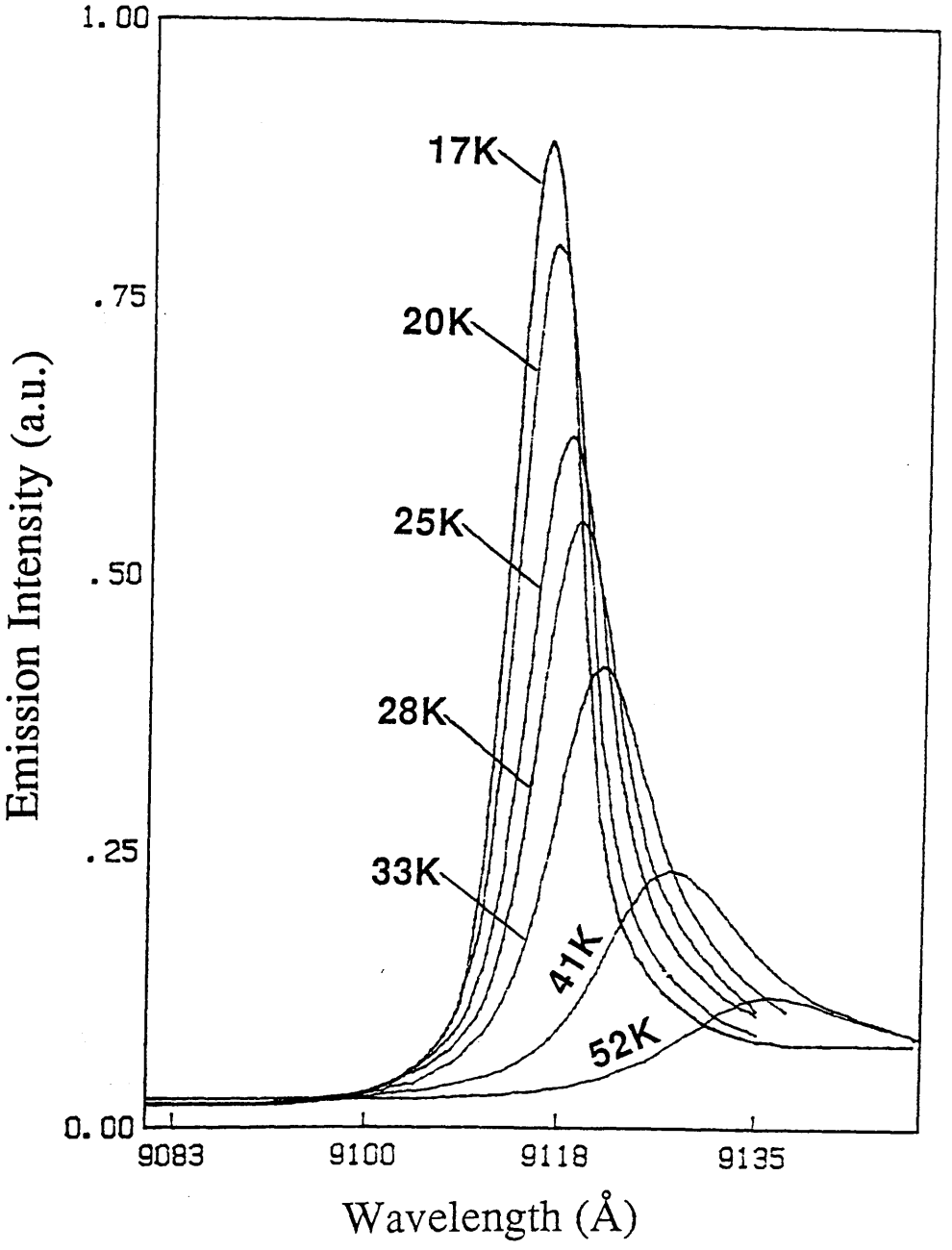

Figure 2.20 PL emission at ~1.36eV region as a function of the sample temperature.

emission spectra as a function of the sample temperature is illustrated. It has a half-width of 1.1meV at 17K, increasing to 1.4meV at 25K due solely to k_BT broadening. The position of the peak also shifts to a lower energy as the temperature is increased, the decrease follow closely the temperature dependence of the fundamental energy gap [2.33] as shown in figure 2.21. The solid line in the figure is the temperature dependence of the energy gap shifted downwards by 63meV to allow comparison with experimental data for the 1.36eV line.

The dependence of the peak intensity of the 1.36eV emission on the laser excitation intensity is shown in figure 2.22 and may be described by

$$I(1.36eV) = KP^n \quad \ldots\ldots\ldots\ldots\ldots\ldots\ldots\ldots (2.8)$$

where I(1.36eV) is the emission intensity at 1.36eV, P is the excitation intensity of the laser at 633nm, K is a constant and n takes a value between 1 and 2 depending on the recombination mechanism involved [2.34]. From figure 2.22, it is seen that n has a value close to 1 at low excitation intensities (<1.5 Wcm^{-2}) while at high intensities (>1.5 Wcm^{-2}) the emission begins to saturate, indicating that the 1.36eV is associated with the recombination of bound excitons.

The integrated emission intensity of the 1.36eV line as a function of temperature is shown in figure 2.18. The normalised PL intensity as a function of temperature for an exciton bound to a neutral donor is given by the equation [2.35]

$$\frac{I(T)}{I(0)} = \frac{1}{[\ 1 + c\ \exp(-E/k_BT)\ ]} \quad \ldots\ldots (2.9)$$

where E is the thermal activation energy, I(T) is the

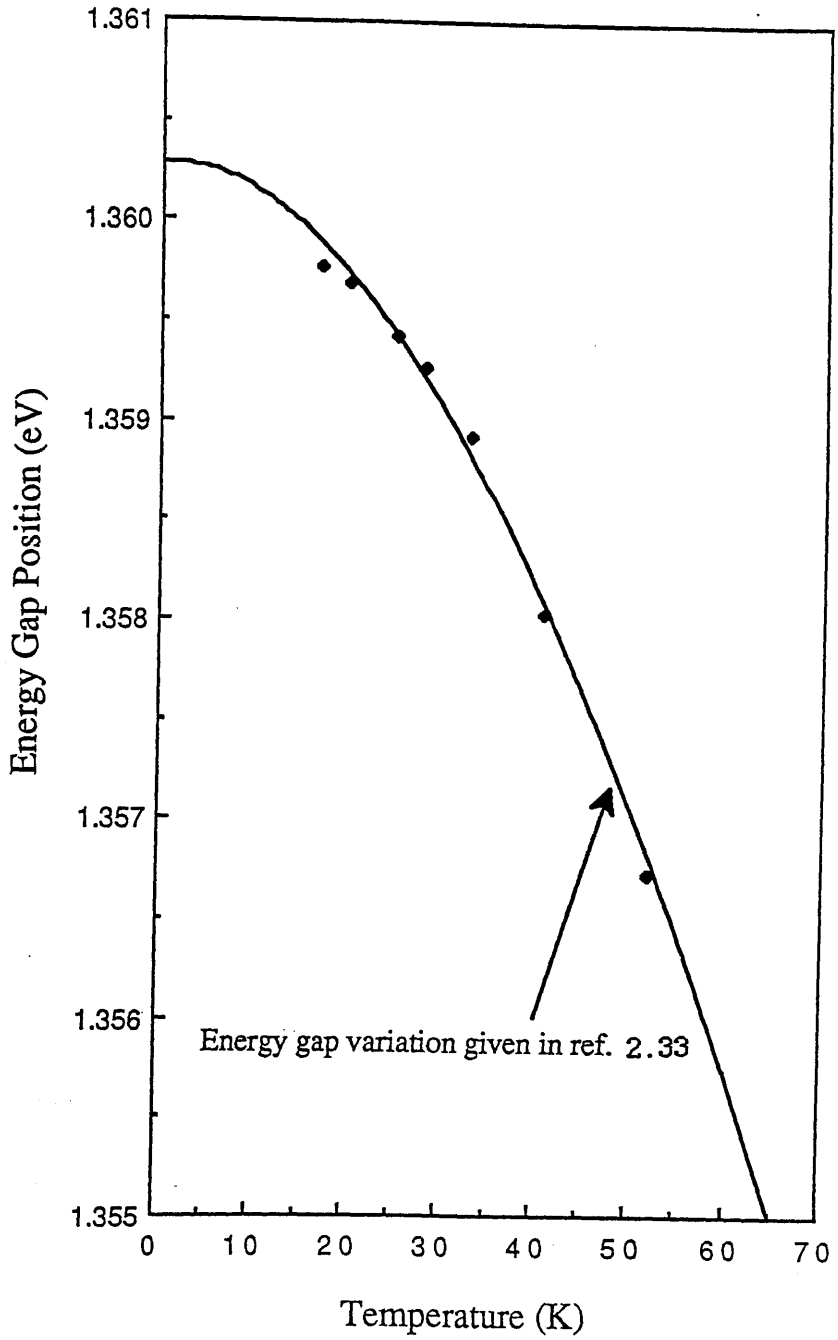

Figure 2.21 A plot of the energy peak of the 1.36eV line against the sample temperature. The energy shift of the peak closely follows the temperature dependence of the fundamental energy band gap (solid line) which has been lowered by 63meV to allow comparison with the experimental data.

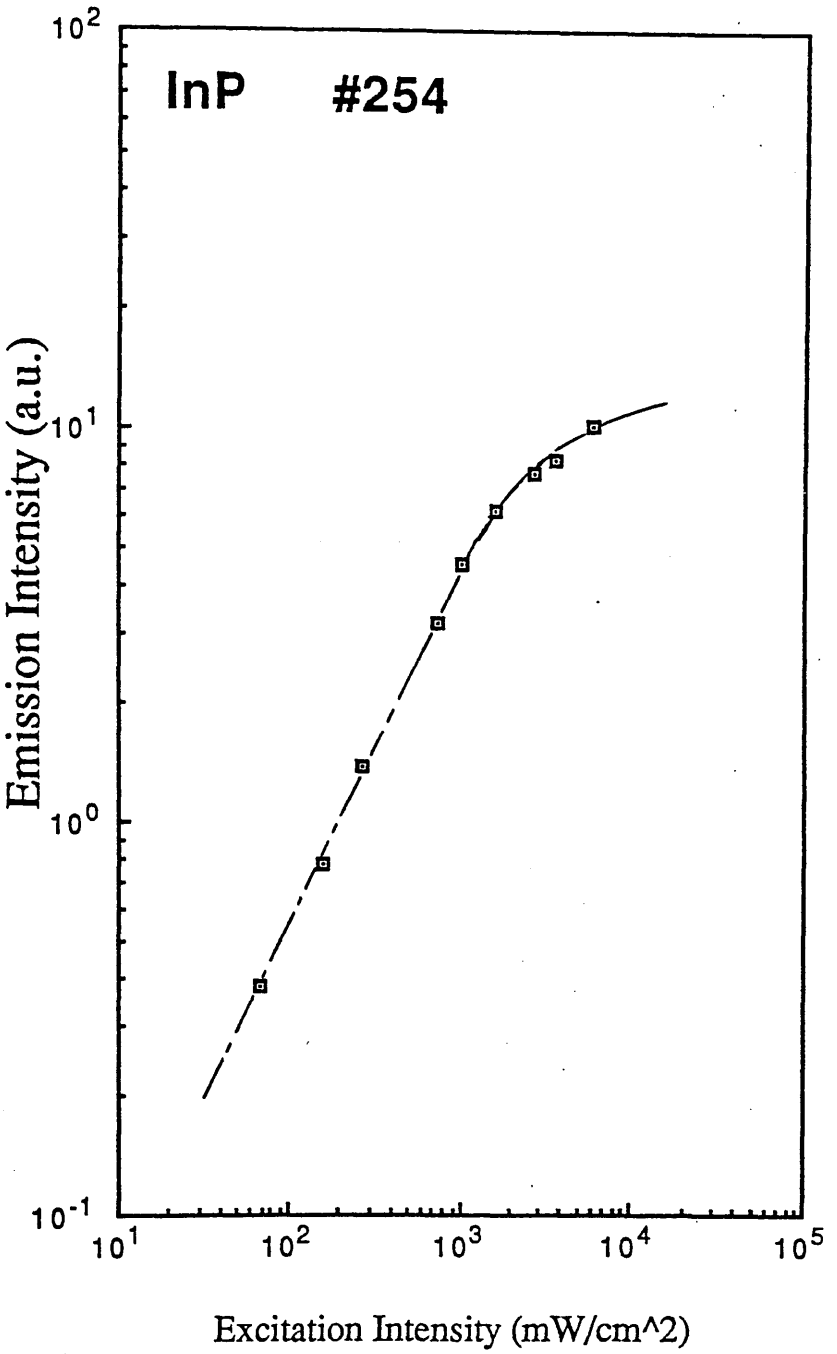

Figure 2.22 Dependence of the PL emission intensity of the 1.36eV peak as a function of excitation intensity. For low laser excitation ($<1.5 Wcm^{-2}$), the slope of the graph is unity, while at higher excitation ($>1.5 Wcm^{-2}$) the emission intensity begins to saturate, suggesting the recombination process involves bound excitons.

intensity of the peak at temperature T and c is a constant. A best fit to the experimental results yields c=20 and E=10±1 meV. In addition, it is seen from figure 2.18 that the experimental data for the (D°-X) transition at 1.417eV also shows the same temperature dependence. An interesting point to note is the difference between the energy gap and the 1.36eV emission peak is 60meV which is a factor of six larger than the value for the thermally activated process. This could indicate significant lattice relaxation, resulting in a large Frank-Condon shift although no other experimental data is available to support this conjecture.

The emission intensity of the 1.36eV transition as a function of P_2/In flux has also been studied. The experiment was performed with a constant indium flux whilst the P_2 flux was varied over an order of magnitude. Figure 2.23 shows the ratio of the intensity of the 1.36eV transition to the emission intensity of the (D°-X) line as a function of the BEP of P_2:In. Included in the figure is the result obtained by Ovadia et al. [2.36]. It can be seen that the 1.36eV line is almost quenched completely at high BEP(P_2:In). This again is in line with the assignment of a phosphorus vacancy complex since at high BEP(P_2:In) the concentration of phosphorus would greatly be reduced.

The emission intensity of the 1.36eV peak was investigated as a function of the substrate temperature. Contrary to that observed by Kerr [2.37] and Wakefield et al. [2.32], the emission intensity of the 1.36eV line was found to be substantially decreased for InP layers grown at high substrate temperature (>530°C). Figures 2.24 (a) and (b) show the PL spectra around the 1.36eV emission at T_s=480°C and T_s=540°C respectively. The 1.36eV emission intensity can be seen to decreased almost completely

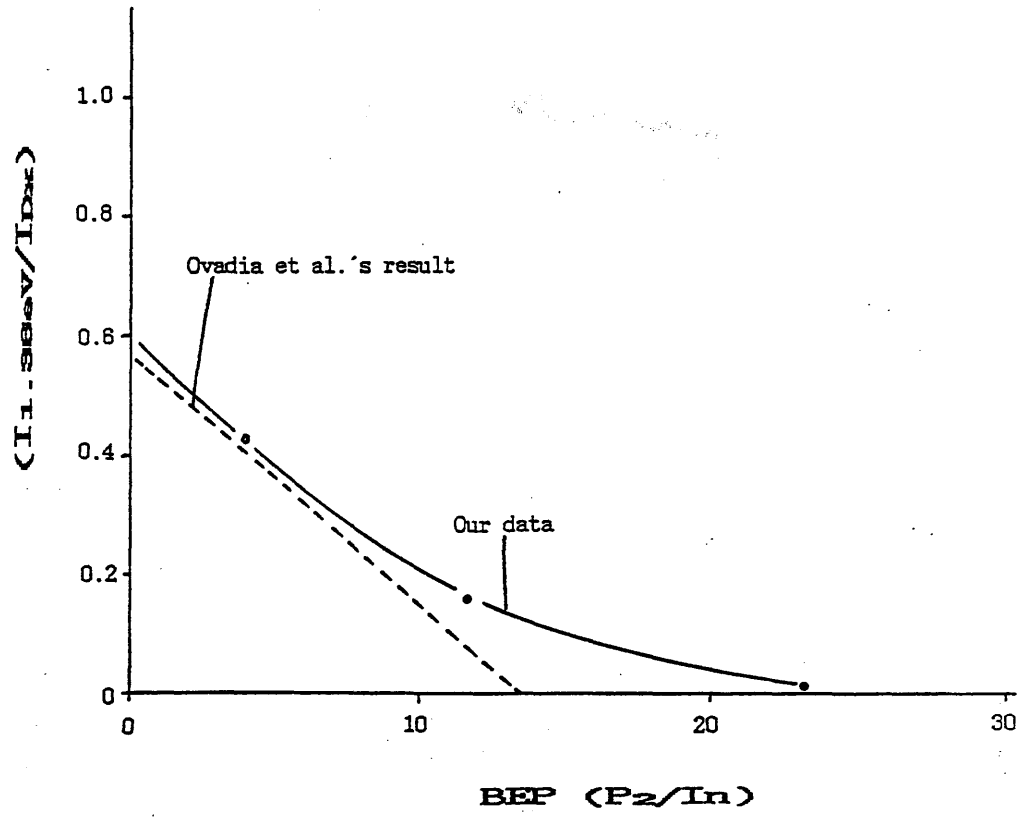

Figure 2.23 Dependence of $(I_{1.36eV}/I_{D^0-X})$ on the ratio of BEP(P_2/In). The solid line is the result found by Ovadia et al. [2.36].

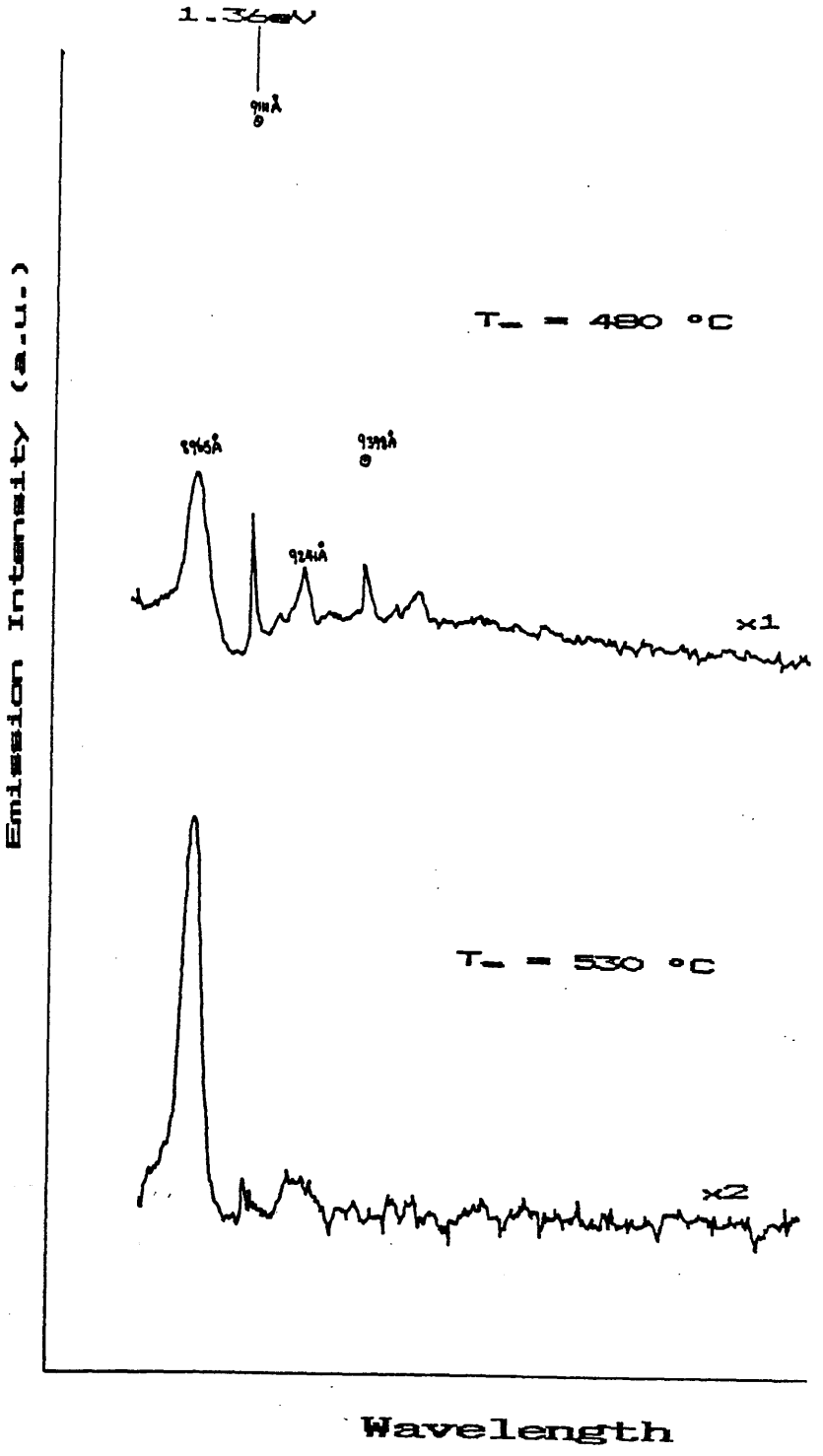

Figure 2.24 PL emission spectra at around 1.36eV for an InP sample grown at T_s=480°C and T_s=530°C.

for the layer grown at 540°C. The experimental results lead to speculation that of the complex involved might be associated with the oxygen species. The sharp emission of the 1.36eV is similar to the PL emission lines of oxygen observed in GaP [2.38]. In addition, Cheng et al. have found that oxygen on a (100) InP substrate is removed at temperatures >500°C [2.39]. Hence, it is tentatively be concluded that the complex associated with the 1.36eV emission consists of oxygen and phosphorus vacancy even though its exact composition is not known at present.

A small emission peak at slightly higher energy (~1meV) than the 1.36eV has been detected. This higher energy shoulder was found to be removable by changing the adhesion substance to the cryostat sample holder from Air Product grease to Bostick No.1 glue. Figure 2.25 shows the PL spectra obtained using Air Product grease as the adhesion medium; the high energy peak (~1.3613eV) is present for the excitation point where the semiconductor was in contact with the cryostat head. The insert in the figure shows the different excitation points. The high energy peak is absent at the free-standing excitation point. Figure 2.26 shows the PL spectra obtained using Bostick No.1 glue as the adhesion medium; the high energy peak is absent at all the excitation points shown in the insert. This indicates that the higher energy emission peak is not associated with impurity in the semiconductor but is a consequence of external stress effects induced by the adhesion substance. Ovadia et al. [2.36] has also observed this emission line which they believed to be due to internal strain present in the crystal lattice.

The low energy side band (below 1.36eV) is associated with the emission of phonons related to the 1.36eV peak. Table 2.4 lists the energy of the individual energy peak positions and their possible assignment following from that given in reference

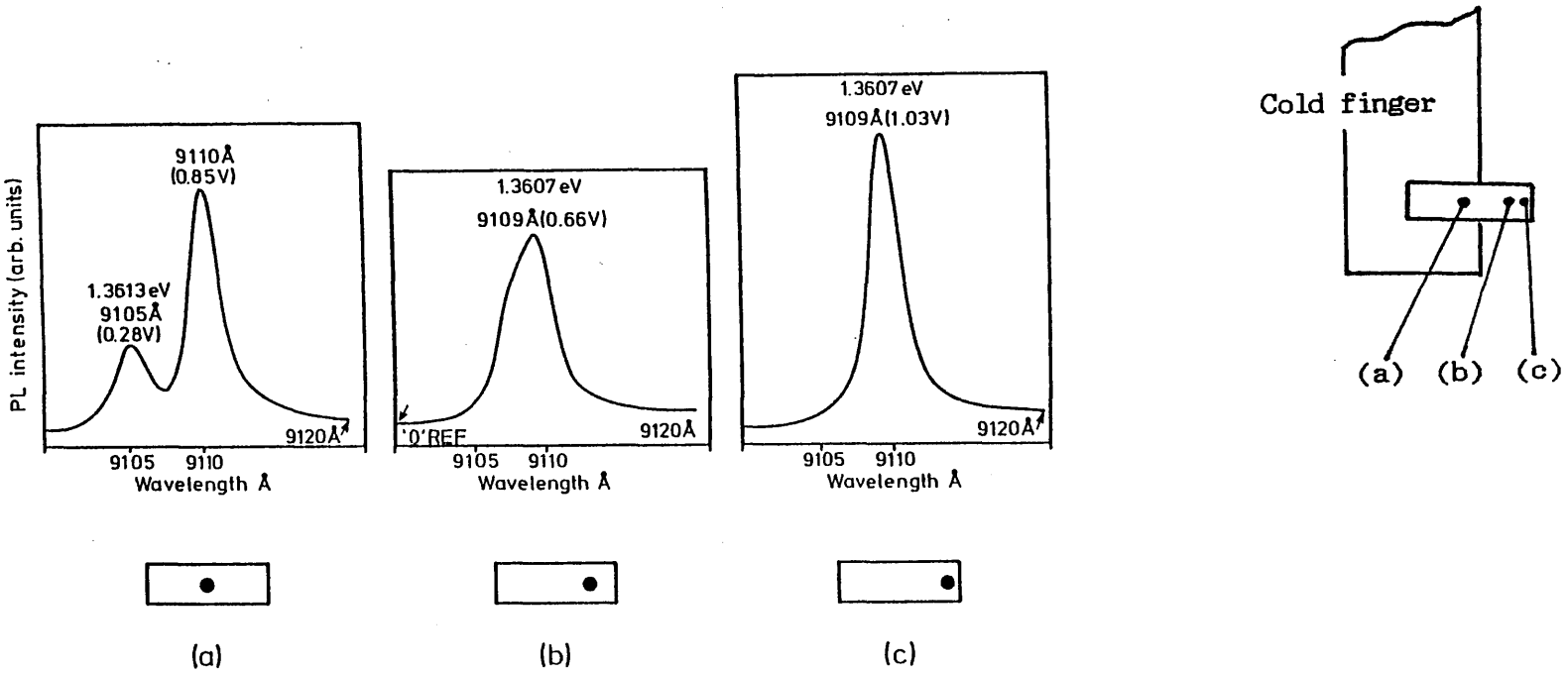

Figure 2.25 Spectra showing the effect of induced external strain caused by using Air Product grease, giving rise to the high energy peak at 1.3613eV.

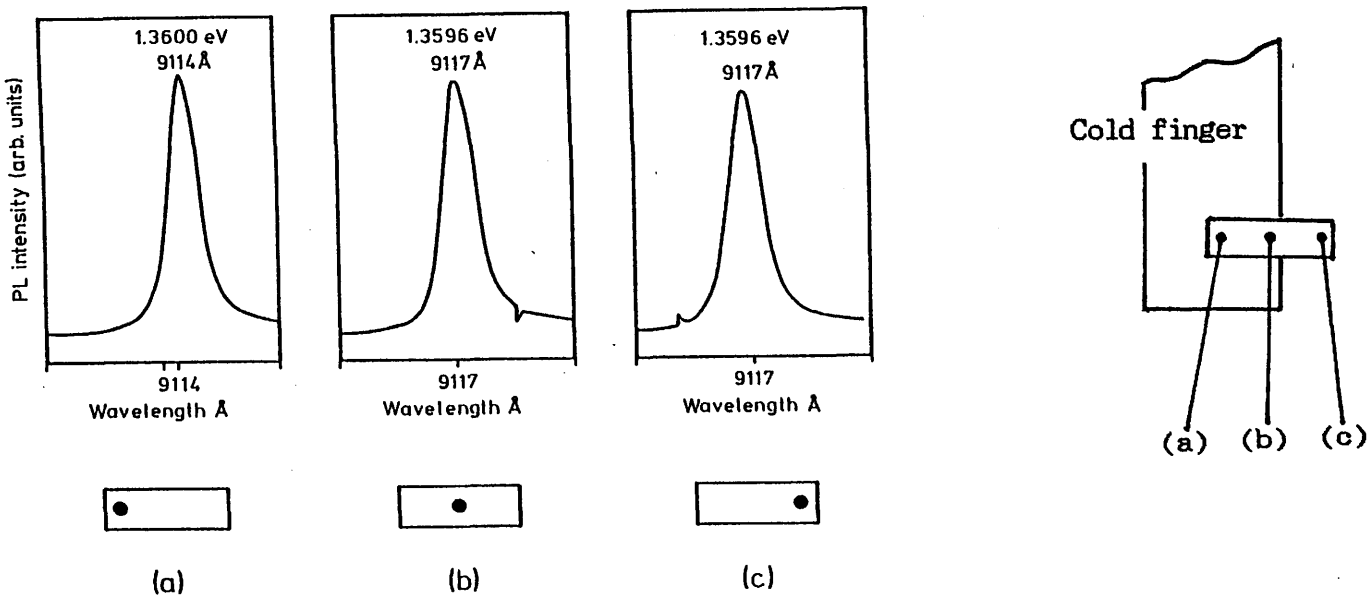

Figure 2.26 Spectra obtained at different excitation points when the adhesion medium was changed to Bostick No.1 glue; the emission line at 1.3613eV is absent.

Table 2.4 The energy peak positions of the individual transitions in the observed phonon sideband. The assignment of the peaks is in accordance with that given in reference 2.32.

Line	Energy (eV) [Å]	Energy difference from A (meV)	Assignment
	1.3833 [8961]	-	D-A pair
A	1.3607 [9111]	-	$D^{\circ}X$
B	1.3519 [9170]	8.8	$D^{\circ}X_{-TA}$
C	1.3418 [9239]	18.9	$D^{\circ}X_{-LA}$
D	1.3339 [9294]	-	D-A $pair_{-LO}$
E	1.3229 [9371]	37.8	$D^{\circ}X_{-TO}$
F	1.3193 [9397]	41.4	$D^{\circ}X_{-LO}$
G	1.3094 [9468]	51.3	$D^{\circ}X_{-TA-local}$
H	1.3003 [9534]	60.4	$D^{\circ}X_{-LA-local}$
I	1.2915 [9599]	-	D-A $pair-2LO$
J	1.2813 [9676]	79.4	$D^{\circ}X_{-TO-local}$
K	1.2779 [9701]	82.8	$D^{\circ}X_{-2LO}$
L	1.2686 [9773]	92.1	$D^{\circ}X_{-2TA-local}$
M	1.2594 [9844]	101.3	$D^{\circ}X_{-2LA-local}$

2.32. The existence of the well structured phonon side band would indicate that the impurity associated with the 1.36eV line strongly coupled to the crystal lattice.

2.9 Conclusion

A systematic study on the dependence of the growth parameters on the quality of the epitaxial layers grown by MBE has been performed. It is shown that by varying the three growth parameters, namely the group V to III flux ratio, the growth rate and the substrate temperature, the free-carrier concentration in the layer may be reduced with an increase in the carrier mobility. The optimum growth conditions for growing unintentionally doped InP having a 77K mobility greater than $15000 cm^2V^{-1}s^{-1}$ with a compensation of about 0.3 were found as P_2:In<10, growth rate of 1.5μm/hr and $T_s \approx 500°C$. The highest quality layer achieved to date has the following electrical properties at 77K:

$(N_D-N_A)=2.5x10^{15}cm^{-3}$ and $\mu=42,500 cm^2V^{-1}s^{-1}$

These results are poor compared with InP grown by other techniques such as MOCVD for which mobilities in excess of $1x10^5 cm^2V^{-1}s^{-1}$ can be obtained. Even though the mobility of InP may be increased by controlling the different growth parameters (growth temperature, growth rate and flux ratios), the ultimate limiting factor must be the purity of the starting material [2.5].

It is noted that although Hall effect measurement provide a quantitative measure on the electrical property of the epitaxial layer, care should be taken when calculating the carrier concentration and mobility since errors may be introduced from the

surface depletion effect and the interface impurity spike. Deep level measurement using the DLTS technique has revealed four majority carrier traps with activation energy of 432, 290, 281 & ~100meV below the conduction band. These electron traps are the same as observed by Asahi et al. [2.24] in InP grown using P_4 and solid indium, suggesting these traps are specific to the growth using solid sources.

The PL spectra for the InP samples grown here exhibit the commonly observed peaks. PL at low temperature is dominated by the exciton bound to donors recombination (D°-X) with FWHM$\leq$5meV. Assignment of the various emissions have been made following that published in the literature. The persistent emission at 1.36eV has been investigated, whose excitonic nature is further verified. The origin of this 1.36eV emission is thought to be associated with a complex involving oxygen and phophorus vacancy.

2.10 References

[2.1] C. Hilsum and H.D. Rees, Elect. Lett. 6, 277-278 (1970).

[2.2] W.T. Tsang, R.C. Miller, F. Capasso and W.A. Bonner, Appl. Phys. Lett., 41, 467 (1982).

[2.3] M.B. Panish and S. Sumski, J. Appl. Phys., 55, 3571 (1984).

[2.4] Y. Kawaguchi, H. Asahi and H. Nagai, Inst. Phys. Conf. Ser. No. 79:Chapter 2, GaAs and Related Compounds, Karuizawa, Japan, 1985.

[2.5] T. Martin, C.R. Stanley and A. Iliadis, C.R. Whitehouse and D.E. Sykes, Appl. Phys. Lett., 46, 994 (1985).

[2.6] V.M. Airaksinen, T.S. Cheng and C.R. Stanley, J. Cryst. Growth, 81, 332 (1987).
[2.7] V.M. Airaksinen, PhD Thesis, University of Glasgow (1987).

[2.8] J.J. Harris, B.A. Joyce and P.J. Dobson, Surf. Sci., 103, L90 (1981).

[2.9] R.F.C. Farrow, J.Phys. D, 7, 2436 (1974).

[2.10] J.M. Van Hove and P.I. Cohen, Appl. Phys. Lett., 47, 726 (1985).

[2.11] R. Heckingbottom, J.Vac.Sci.Technol. B3, 572 (1985).

[2.12] A. Iliadis and C.R. Stanley, University of Glasgow, private communication.

[2.13] A. Iliadis, K.A. Prior, C.R. Stanley, T. Martin and G.J. Davies, J. Appl. Phys., 60, 213 (1986).

[2.14] C.E.C. Wood, L. Rathbun, H. Ohno and D. Desimone, J. Cryst. Growth, 51, 299 (1981).

[2.15] W. Walukiewicz, J. Appl. Phys., 51, 2659 (1980).

[2.16] P. Blood and J.W. Orton, J. Phys. C: Solid State Phys., 7, 893 (1974).

[2.17] D.L. Rode, Phys. Stat. Sol. (b), 55, 687 (1973).

[2.18] "GaInAsP Alloy Semiconductors", edited by T.P. Pearsall, John Wiley & Son, 1982, page 194.

[2.19] R.F. Broom and A.C. Rose-Innes, Proc. Phys. Soc. (London), B69, 1269 (1956).
[2.20] J.R. Dixon, J. Appl. Phys., 30, 1413 (1959).

[2.21] A. Chandra, C.E.C. Wood, D.W. Woodward and L.F. Eastman, Solid State Elect., 22, 645 (1979).

[2.22] Y.G. Chai, Appl. Phys. Lett., 47, 1327 (1985).

[2.23] D.J. Ashen, D.A. Anderson, N. Apsley and M.T. Emeny, J. Cryst. Growth, 60, 225 (1982).

[2.24] H. Asahi, Y. Kawamura, M. Ikeda and H. Okamoto, J. Appl. Phys., 52, 2852 (1981).

[2.25] G. Bremond, A. Nouailhat and G. Gillot, Gallium Arsenide and Related Compounds 1981 (Inst. Phys. Conf. Ser. No. 63) p239.

[2.26] P.J. Dean, Prog. Crystal Growth Charact., 5, 89 (1982).

[2.27] I. Ferguson, PhD Thesis, University of St. Andrews (1989).

[2.28] J.M. Chamberlain, H.B. Ergun, K.A. Gehring and R.A. Stradling, Solid State Comm., 9, 1563 (1971).

[2.29] B.J. Skromme, G.E. Stillman, J.D. Oberstar and S.S. Chan, J. Electron. Mater., 13, 463 (1984).

[2.30] D. Barthruff, K.W. Benz and G.A. Antypas, J. Electron. Mater., 4, 485 (1979).

[2.31] K.R. Duncan, L.Eaves, A. Ramdane, W.B.Roys, M.S. Skolnick and P.J. Dean, J. Phys. C: Solid State Phys., 17, 1233 (1984).

[2.32] B. Wakefield, L.Eaves, K.A. Prior, A.W. Nelson and G.J.Davies, J. Phys. D: Appl. Phys., 17, L133 (1984).

[2.33] Y.P Varshni, Physica, 34, 149 (1967).

[2.34] Xu Zhongying, Xu Jizong, Ge Weikun, Zheng Baozhen, Xu Junying and Li Yuzhang, Solid State Comm., 61, 707 (1987).

[2.35] P.J. Dean, Phys. Rev., 157, 655 (1967).

[2.36] S. Ovadia and A. Iliadis, Proceeding SPIE International Society of Optical Engineers, 822, 40 (1987).

[3.37] T. Kerr, PhD thesis, University of Glasgow (1984).

[2.38] P.J. Dean, C.H. Henry and C.J. Frosch, Phys. Rev., 168, 812 (1968).

[2.39] K.Y. Cheng, A.Y. Cho, W.R. Wagner and W.A. Bonner, J. Appl. Phys., 52, 1015 (1981).

CHAPTER 3

Behaviour of Sulphur in Intentionally Doped InP Grown by MBE

3.1 Introduction

As pointed out in the previous chapter, sulphur is the dominant, electrically active donor species present in undoped InP grown by MBE. It also appears as a universal impurity in InP grown by other epitaxial growth techniques such as VPE and LPE [3.1,3.2]. Even though sulphur (a group VI element in the periodic table) has a higher vapour pressure compared to the group IV elements such as Si and Ge, its interaction with the host lattice of a III-V semiconductor is sufficiently strong to ensure effective doping as shown theoretically by Heckingbottom [3.3]. Unlike the intrinsic amphoteric behaviour of the group IV elements, sulphur acts as an n-type impurity regardless of its site occupancy, which is generally believed to be in the group V site because of the smaller size difference between sulphur and the group V atom compared to sulphur and the group III atom [3.4].

Andrew et al. have investigated the intentional sulphur doping in both GaAs [3.5] and AlGaAs [3.6] as a function of growth parameters. The sulphur flux was generated by an electrochemical Knudsen cell which circumvented the problems associated with the use of elemental sulphur. They showed that the incorporation of sulphur was greatly influenced by the growth temperature, T_s, and the As_4:Ga flux ratio. In the case of sulphur in GaAs, the free-carrier concentration, (N_D-N_A) decreased substantially when the epitaxial

layers were grown at T_s>590°C but was relatively constant when grown below 590°C. The decrease of (N_D-N_A) at high substrate temperatures was found to mirror exactly the decrease in the sulphur concentration as detected by SIMS. Subsequently, they used a thermodynamic analysis to show that desorption of the volatile species Ga_2S was the cause of decrease of the sulphur concentration. At T_s<590°C, a kinetic barrier was present which hindered the desorption of Ga_2S resulting in a relatively constant (N_D-N_A). The loss of sulphur at high temperatures could also be partially offset by increasing the As_4:Ga overpressure, thus decreasing the population of the gallium atoms available to form Ga_2S as a result of the increased number of surface arsenic atoms. Similar incorporation and desorption behaviour was also found for selenium in GaAs [3.7]. The desorption of Ga_2S and Ga_2Se have a comparable activation energies of ≈3eV. However, desorption of Ga_2Se only becomes significant above ≈620°C, i.e. ≈30° higher than for Ga_2S. Consequently, selenium may be considered a more suitable dopant species for GaAs in the technologically important growth temperature region.

The properties of sulphur in InP have been partially investigated by Iliadis et al. [3.8], who found that (N_D-N_A) in the epitaxial layer could similarly be reduced at high T_s. Applying a similar thermodynamic analysis to that used for sulphur in GaAs, they concluded that either InS or In_2S desorption was the cause of the decrease of sulphur concentration in the layer. In this chapter, a detailed and systematic study of the influence of the growth conditions on the intentional incorporation of sulphur into InP grown by MBE is presented. This provides an understanding of the role played by the unintentional doping of sulphur in InP and the possibility of control over the quality of the epitaxial layers.

3.2 Experimental Method

The MBE system used in this work has been described in the previous chapter. The doping of InP was performed with an electrochemical Knudsen cell based on the design of Davies et al. [3.9]. The electrochemical cell is essentially a solid state cell consisting of Ag/AgI/Ag_2S sandwiched between two platinum electrodes, and the whole is enclosed within a conventional Knudsen cell structure as shown in figure 3.1. The application of an external EMF to the cell results in a change of the chemical potentials, hence the activities of both silver and sulphur atoms in the Ag_2S and consequently the equilibrium vapour pressure of sulphur over the solid state cell. This type of cell may be heated to well above the typical bake-out temperature (≈100-200°C) encountered in MBE, thus avoiding the problems associated with the high vapour pressure of elemental sulphur. Another advantage of the cell is its fast response time (≈1s). Complicated and sharp dopant profiles can be achieved which would otherwise be impossible with a conventional thermal Knudsen source. The operating temperature of the electrochemical cell is kept constant (e.g. at 200°C). The flux of sulphur species S_n (n=2, 3,..., 8) emerging from the cell is given by

$$F_{Sn}=C(T)\exp(2nEF/RT) \quad \ldots\ldots\ldots\ldots\ldots\ldots\ldots\ldots (3.1)$$

where

$$C(T)=\frac{1.118\times10^{22}\times A\times P^{\circ}_{Sn}\times \exp(-2nE^{*}F/RT)}{l^{2}(MT)^{1/2}} \quad ,$$

P°_{Sn} is the equilibrium partial pressure of sulphur molecules S_n over sulphur,

E is the external applied EMF,

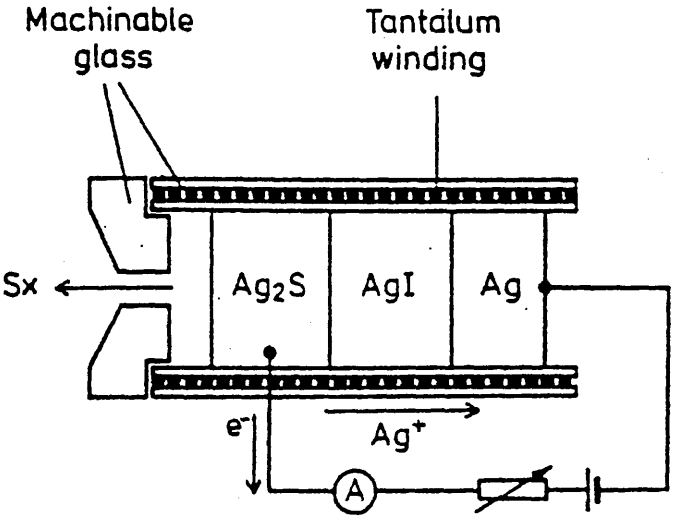

Figure 3.1 Schematic diagram from reference [3.9] showing the basic construction of the sulphur electrochemical cell.

E* is the EMF of the cell in equilibrium with liquid sulphur (measured as 230mV at 473K & 243mV at 573K)

F is Faraday's constant,

R is the gas constant, and

T is the operating temperature of the cell in Kelvin.

The epitaxial layers discussed in this chapter were grown with the electrochemical Knudsen cell kept at 200°C and the applied EMF varied up to 190mV. Under these conditions, the incident sulphur species is predominantly dimers with a flux at least three orders of magnitude larger than the next most abundant species S_3 [3.9]. Thus, in the remaining discussion, the sulphur flux from the cell is regarded to consist of only S_2 molecules, i.e. F_{S2}.

InP epitaxial layers were grown by varying any one of the growth parameters, such as the substrate temperature T_s or the growth rate G_r, while keeping all the others constant. The concentration of the incorporated sulphur (C_B) in the sample was then determined from the free-carrier concentration versus depth profile measured using the electrochemical C-V profiler, since it has been shown from extensive SIMS analyses of S-doped MBE InP layers that C_B and (N_D-N_A) are approximately equal for $(N_D-N_A) \geq 10x^{16}cm^{-3}$ [3.8].

3.3 Results and Discussion

3.3.1 Dependence of the Concentration of Incorporated Sulphur (C_B) on Incident Sulphur Flux (F_{S2})

For the growth of device structures with fixed levels of carrier concentrations, the dependence of

C_B on F_{S2} is required. To achieve a desired concentration of sulphur in the epitaxial layer, an external EMF is applied to the electrochemical Knudsen cell. A linear relationship has been found to exist between the concentration of sulphur incorporated in the layer and the incident sulphur flux for both GaAs [3.9] and InP [3.8] at low T_s where desorption of dopant is negligible. This relationship is then used as a calibration for the required doping level in subsequent design of epitaxial layer structures.

InP epitaxial layers were grown at low T_s (desorption is negligible), defined as temperatures below 500°C (will be shown in the next section), and high T_s (>500°C). The concentration of the incorporated sulphur in the structures as a function of the electrochemical cell EMF were measured by CV profiling. The results are shown in figure 3.2. Samples #201 and #207 were grown at T_s=480°C, while sample #218 and #198 were grown at T_s=540°C. Samples #207 and #218 were S-doping 'staircases' obtained by changing the EMF of the electrochemical cell in discrete steps. The growth rate and the P_2:In flux ratio were kept constant at 1.5μm/hr and 10:1 respectively during the growth runs. At low T_s (480°C), a linear relationship is obtained which is comparable to that reported in reference [3.9]. A similar relationship can also be seen to be present at high T_s (540°C). This observed behaviour will be shown in section 5.4 to imply that both the incorporation and desorption rates have equal kinetic orders.

3.3.2 Dependence of C_B on T_s

When an epitaxial layer is grown at a high substrate temperature, C_B will be reduced due to an increase in the dopant desorption rate. The value of C_B will

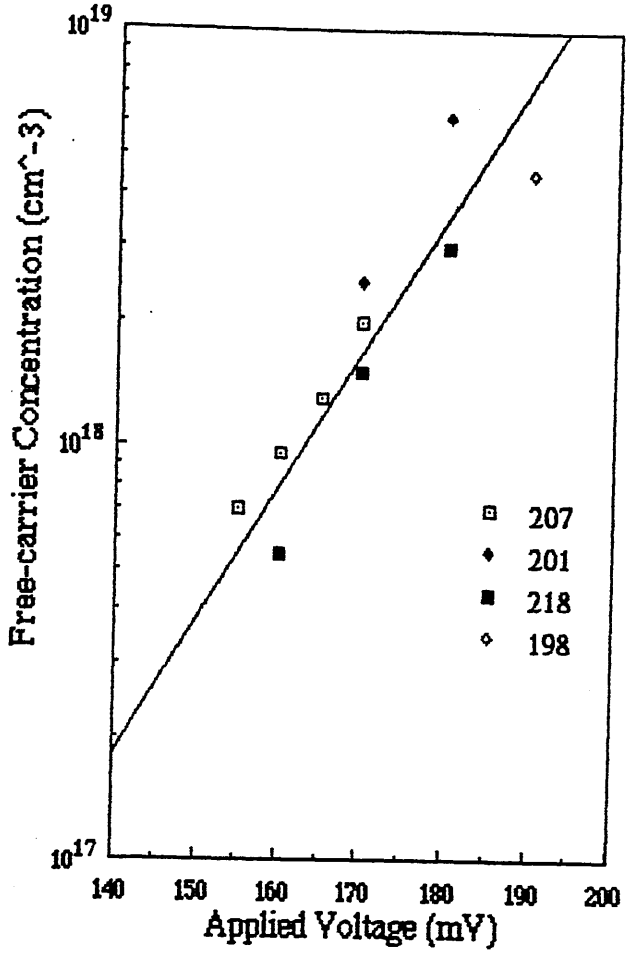

Figure 3.2 Free-carrier concentration as a function of the electrochemical cell EMF. Samples #201 and #207 were grown at T_s=480°C and sample #218 and #198 at T_s=540°C, both showing a linear relationship.

therefore be different for growth at low and high T_s. This difference is required to be known for designed structures grown at different temperatures with predetermined carrier concentrations. The concentration of sulphur (C_B) in InP as a function of T_s was investigated. Three samples (#191, #196 & #198) were grown, all at a constant doping flux with the electrochemical cell set at 190mV. The same growth rate of 1.5μm/hr was used for all the samples, while phosphorus BEPs of 4.7×10^{-6} mbar (#191) and 6.5×10^{-6}mbar (#196 & #198) were used. A typical CV plot is shown in figure 3.3(a). C_B is seen to decrease as a function of T_s. The dependence of C_B on T_s of a number of samples are plotted in a graph of $\ln(C_B)$ against $1/T_s$, which is shown in figure 3.3(b). Two distinct temperature regions can clearly be seen to exist at below and above 500°C, analogous to that for sulphur in GaAs [3.5]. An activation energy for the desorption species may be estimated from the high temperature region of the curve in figure 3.3(b), and is found to be 4.5eV. This is ~1.5eV higher than that measured for S and Se in MBE grown GaAs.

3.3.3 Dependence of C_B on G_r

The study of the relationship between C_B and G_r can provide information about the kinetics of dopant incorporation and desorption. This will give an understanding of the role of sulphur in InP. The incorporation and desorption of sulphur as a function of G_r were investigated. Three layers were grown at substrate temperatures T_s=480°C, 520°C and 540°C, i.e. they were grown at a low, intermediate and high temperatures respectively. The incident sulphur flux and the phosphorus overpressure were kept constant for each of the growth runs. Figure 3.4 shows schematically the

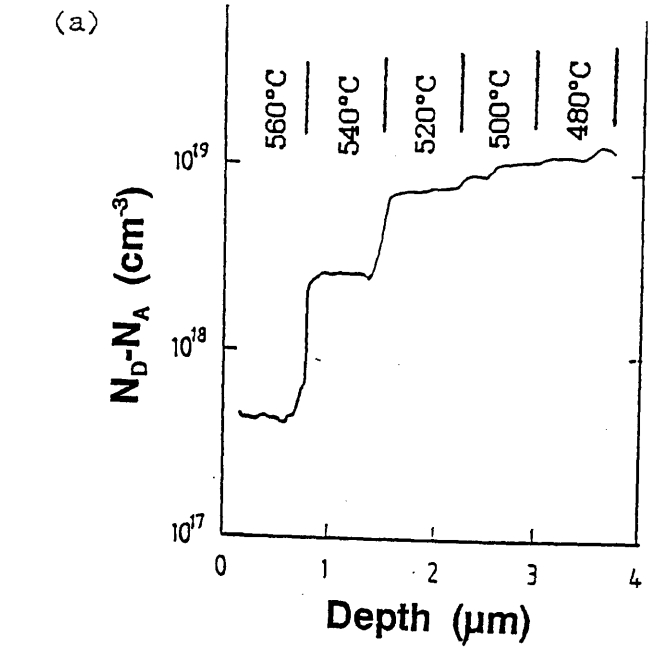

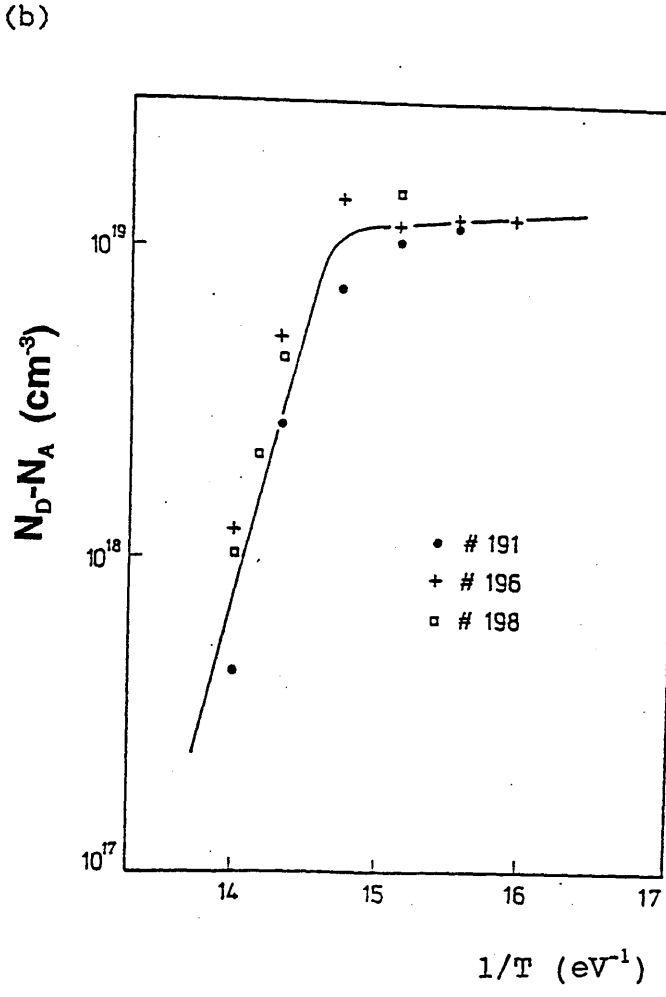

Figure 3.3 **(a)** A typical C-V depth profile of a **sulphur** doped sample as a function of T_s (500-560°C). **(b)** Dependence of C_s on the inverse of T_s. The growth conditions used are: EMF=190mV, G_r=1.5μm/hr, p(P_2)={4.7x10^{-6}mbar (#191), 6.5x10-6mbar (#196 & #198)}. An activation energy of 4.5eV for desorption is deduced from the high T_s portion of the graph.

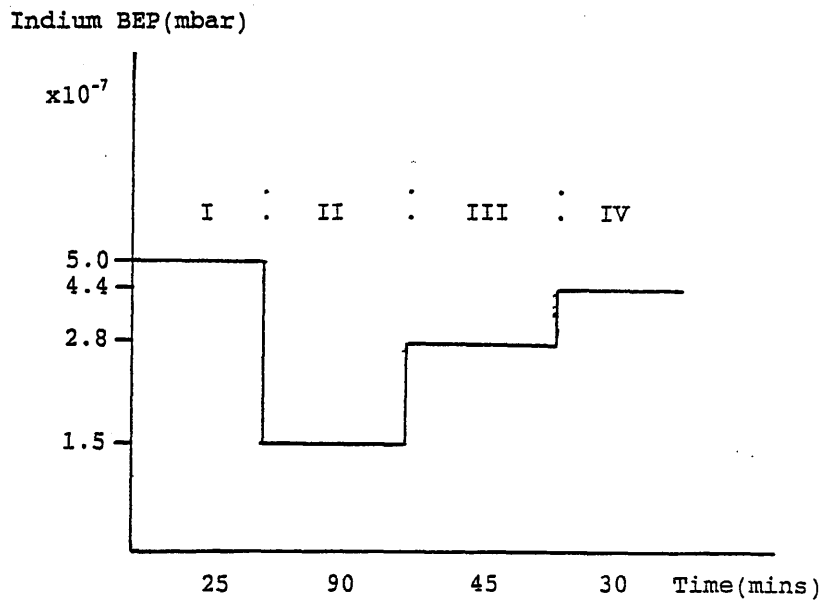

Figure 3.4 Schematic diagrams of the growth sequence for the sample #188 (T_s=480°C), #224 (T_s=520°C) and #217 (T_s=540°C) as a function of G_r.

growth sequence of the three layers. Regions I to IV correspond to different indium BEP used. Figure 3.5(a) shows the C-V profiles recorded for the layers grown at T_s=480°C (sample #188) and 520°C (sample #224). In figure 3.5(b), the experimental data for #188 and #224 have been converted to a plot of $F_{s2}/(N_D-N_A)$ against G_r, where F_{s2} has been calculated using equation (3.1). For the low temperature grown sample (#188), the graph is a straight line passing through the origin, while for the intermediate temperature grown sample (#224) the graph is again a straight line but intercepts the y-axis at a point ≈1μm/hr above the origin. For the high temperature grown sample T_s=540°C, however, the dopants incorporated in the layer does not appear to vary as G_r changes which is shown in figure 3.6 (sample #217). The experimental results at the three different growth temperatures used are explained using the kinetic model proposed by Wood et al. [3.10] and is discussed in section 3.4.

3.3.4 Dependence of C_B on P_2:In Flux Ratio

At high substrate temperatures, the carrier concentration in InP epitaxial layers has been found to be substantially reduced (section 3.3.2) caused by an increase in the dopant desorption rate. One may lower this desorption rate and thus increase the carrier concentration in the layer by increasing the group V to III flux ratio, which has been shown experimentally in GaAs [3.5]. For S in InP, the effect of the flux ratio of P_2 :In on C_B was investigated in the high substrate temperature regime. The proposed structure of the epitaxial layers is illustrated in figure 3.7(a) in which the uncorrected BEP flux ratio p(P_2:In) is to be varied between 10 and 30; the incident indium flux is to be kept constant throughout

(a)

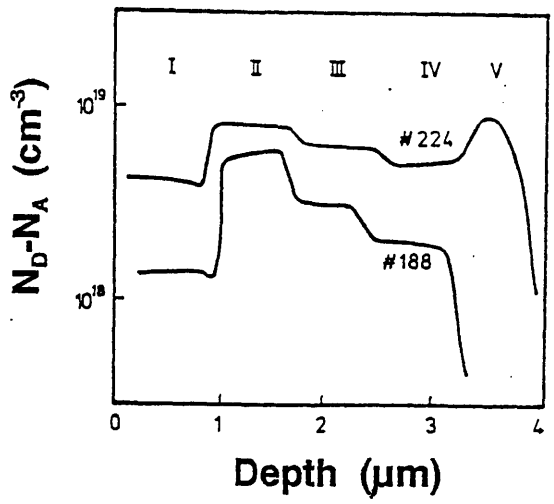

(b)

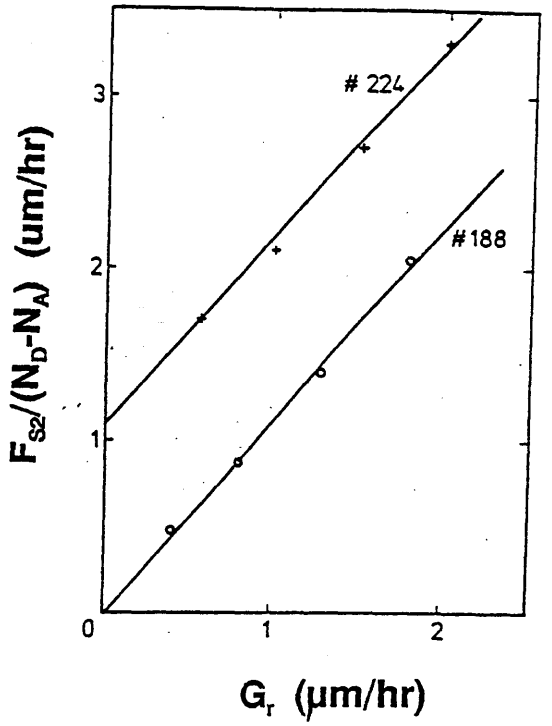

Figure 3.5 (a) C-V plot for samples #188 and #224. (b) The ratio of the incident sulphur flux to the concentration of incorporated sulphur plotted against the growth rate for the corresponding two samples.

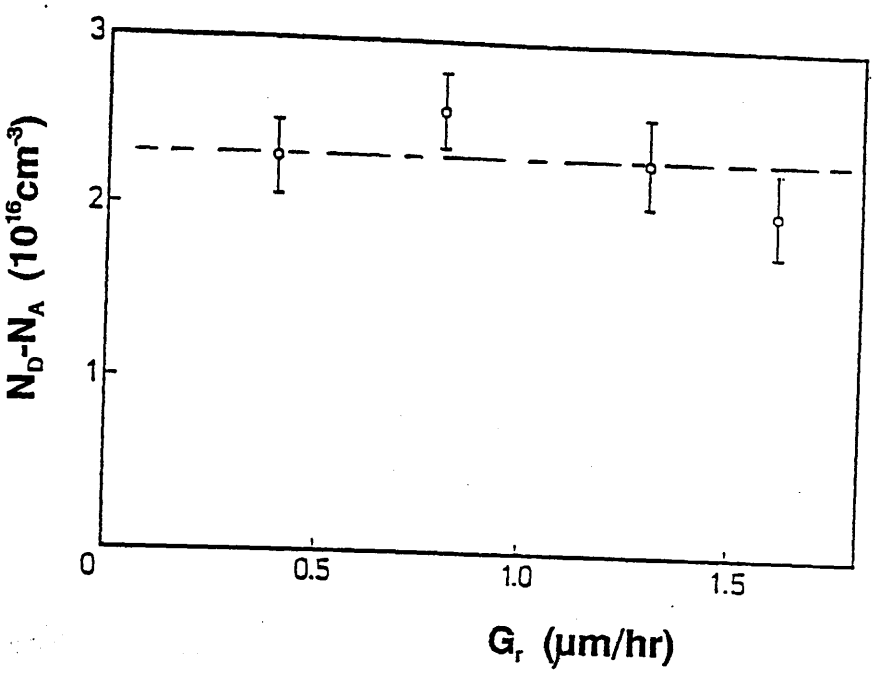

Figure 3.6 Experiment data of the concentration of incorporated sulphur as a function of the growth rate for sample #217 grown at T_s=540°C.

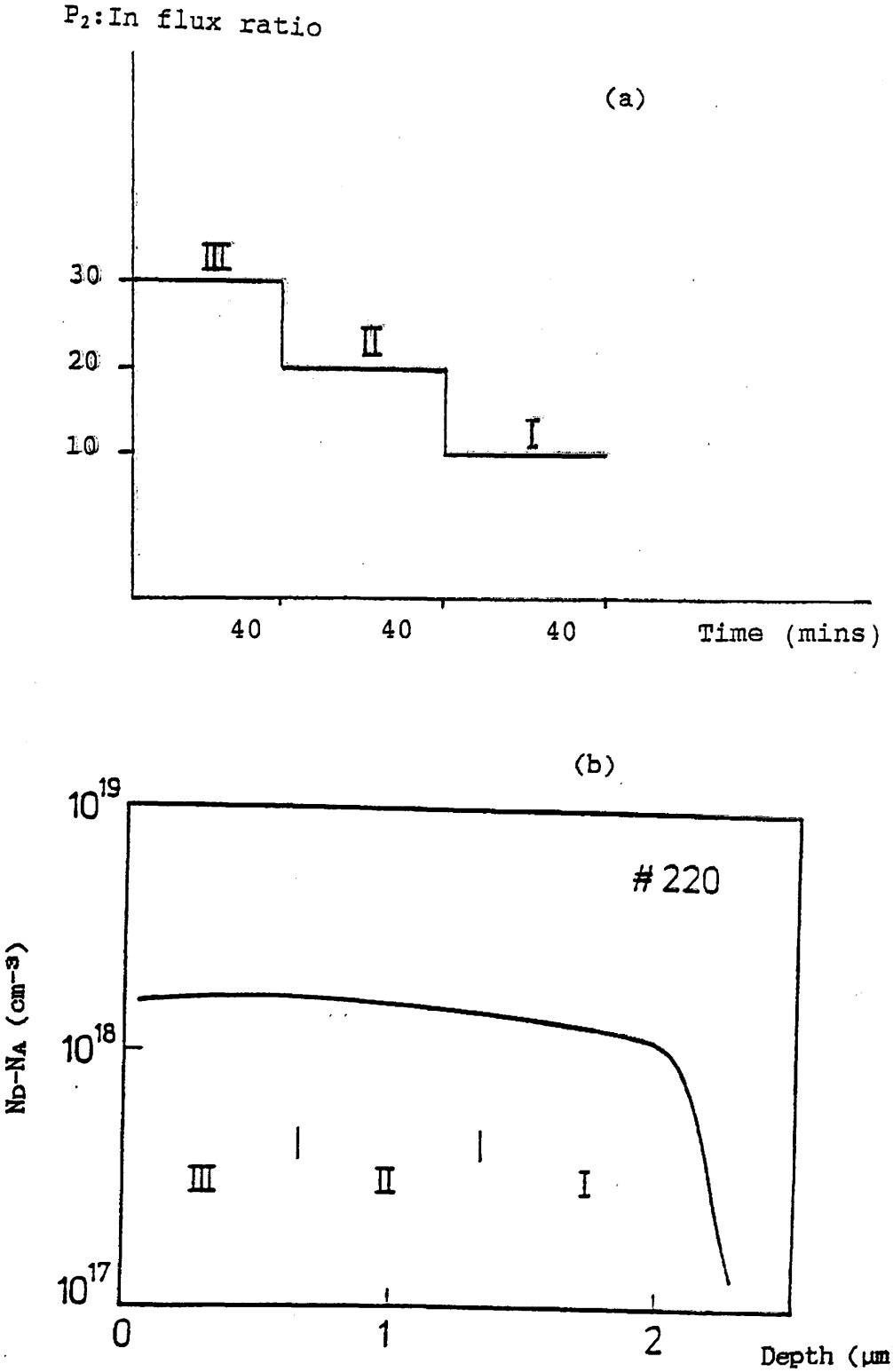

Figure 3.7 (a) Schematic diagram of the growth sequence for sample #220. (b) C-V plot for sample #220 with regions I, II, III correspond to P_2:In BEP of 10, 20 and 30 respectively.

the growth while the phosphorus flux was changed. The sample was grown on a semi-insulating Fe-doped substrate and at a growth temperature T_s=540°C with an indium BEP of $4.5x10^{-7}$mbar (growth rate of 1.5μm/hr).

Figure 3.7(b) shows the recorded C-V profile plot of the sample grown, where regions I, II and III correspond to $p(P_2:In)$=10, 20 and 30 respectively; the thickness of each region is approximately 0.6um. Increasing the P_2 overpressure did not appear to have a significant effect on the carrier concentration in the sample, thus indicating that the desorption of sulphur is changed only slightly and the effect is very much weaker than that observed for sulphur in GaAs [3.5]. The overpressure behaviour of S in InP, S & Se in GaAs and S in AlGaAs are shown in figure 3.8 for comparison. The experimental data for GaAs and AlGaAs are taken from reference [3.5,3.7] and [3.6] respectively. For GaAs and AlGaAs, the carrier concentration is seen to be directly proportional to $p(As_4:Ga)$ in direct contrast to the insensitivity of sulphur in InP.

3.4 Growth Model

The kinetic model proposed by Wood et al. [3.10] forms the basis of the growth model described below which accounts for the observed behaviour discussed in the earlier sections. In this model, the dopants are considered to be incorporated into the bulk of the crystal from a surface layer. The rate equation from reference [3.10] for the concentration of sulphur atoms is given by

$$dC_s/dt = F_{s2} - F_{des} - F_{inc} \quad \ldots\ldots\ldots\ldots\ldots\ldots (3.2)$$

where C_s is the concentration of sulphur atoms in the

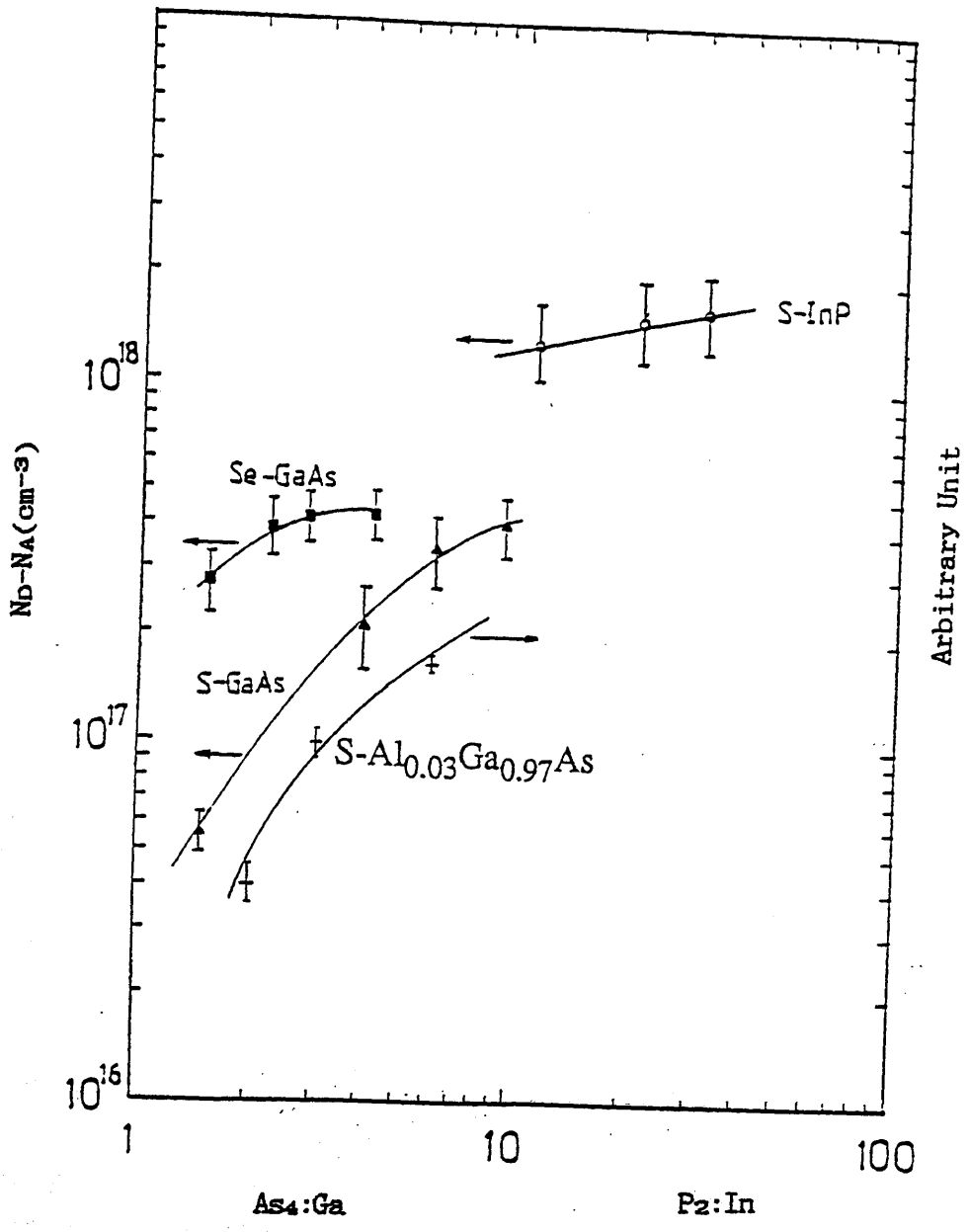

Figure 3.8 The concentration of incorporated dopants plotted against the group V:III flux ratio for sulphur in InP, GaAs, AlGaAs and selenium in GaAs.

surface layer,

F_{s2} is the incident flux of sulphur species,

F_{inc} is the incorporated sulphur flux,

F_{des} is the desorbed sulphur flux.

Strictly, there should be another flux term on the right hand side of this equation, which is associated with the flux coming out from the bulk of the crystal. However, it is normally very small and therefore has been neglected.

If the respective kinetic orders of incorporation and desorption are assumed to be m and n, at steady state, equation (3.2) becomes

$$F_{s2} = F_{inc} + F_{des}$$

$$= KC_s^m + DC_s^n \quad \ldots\ldots\ldots\ldots\ldots\ldots\ldots\ldots (3.3)$$

where K and D are the rate constants of incorporation and desorption respectively.

At high T_s, $F_{inc} \ll F_{des}$, and equation (3.3) can be simplified to

$$F_{s2} \approx F_{des} \quad \ldots\ldots\ldots\ldots\ldots\ldots\ldots\ldots (3.4)$$

Assuming the measured dopant concentration C_B is proportional to some power k of the incident flux in this high temperature region, i.e.,

$$C_B \propto F_{s2}^k$$

$$= NF_{s2}^k \quad \ldots\ldots\ldots\ldots\ldots\ldots\ldots\ldots (3.5)$$

where N is a function which depends on T_s, the growth rate G_r and the group V flux.

Now C_B and G_r are related through the expression:

$$C_B = F_{inc}/G_r \quad \ldots\ldots\ldots\ldots\ldots\ldots\ldots\ldots (3.6)$$

Substituting equations (3.5) and (3.6) into (3.4) gives

$$F_{des} = (F_{inc}/NG_r)^{1/k} \quad \ldots\ldots\ldots\ldots\ldots\ldots\ldots\ldots (3.7)$$

i.e. the kinetic order of the desorption reaction is 1/k times the kinetic order of the incorporation reaction at high temperature. As shown in figure 3.2, C_B is found to be directly proportional to the incident sulphur flux in both the high and the low desorption regime:

$$C_B \propto F_{s2} \quad \ldots\ldots\ldots\ldots\ldots\ldots\ldots\ldots\ldots\ldots\ldots\ldots (3.8)$$

Therefore k=1 and the incorporation and desorption of sulphur are of equal kinetic orders relative to C_s. The simplest assumption to explain this is that both rates of reaction are of first order i.e., m=n=1, similar to Sn in GaAs [3.11]. This implies that the desorbing species at high T_s contains only one sulphur atom. Therefore one would expect the desorbing compound to be In_xS (x=1,2,..). The likely desorbing species will be discussed below.

When both the kinetic orders of incorporation and desorption are of first order, equation (3.3) becomes:

$$F_{s2} = (K + D)C_s \quad \ldots\ldots\ldots\ldots\ldots\ldots\ldots\ldots (3.9)$$

Now, from equation (3.6)

$$C_B = F_{inc}/G_r$$
$$= KC_s/G_r$$

$$\text{i.e. } C_s = C_B G_r/K \quad \ldots\ldots\ldots\ldots\ldots\ldots\ldots\ldots (3.10)$$

Substitute equation (3.10) into (3.9) yields

$$F_{s2} = (1 + D/K) C_B G_r \quad \ldots\ldots\ldots\ldots\ldots\ldots\ldots\ldots (3.11)$$

Assuming the incorporation rate constant is directly proportional to the growth rate [3.10], i.e., $K=K'G_r$. Equation (3.11) is then given by

$$F_{s2}/C_B = (G_r + D/K') \quad \ldots\ldots\ldots\ldots\ldots\ldots\ldots\ldots (3.12)$$

At low growth temperatures, $D \ll K'$ and equation (3.12) reduces to

$$F_{s2}/C_B = G_r \quad \ldots\ldots\ldots\ldots\ldots\ldots\ldots\ldots\ldots\ldots (3.13)$$

At intermediate growth temperatures, $D \approx K'$ and equation (3.12) becomes

$$F_{s2}/C_B = G_r + 1 \quad \ldots\ldots\ldots\ldots\ldots\ldots\ldots\ldots\ldots (3.14)$$

At high growth temperatures, $D \gg K'$, equation (3.12) can be written as

$$F_{s2}/C_B = D/K' \quad \ldots\ldots\ldots\ldots\ldots\ldots\ldots\ldots\ldots\ldots (3.15)$$

The experimental evidence broadly confirms the main features of the model for sulphur in InP. Namely, the results shown in figure 3.5(b) are found to confirm equations (3.13) and (3.14) at low (T_s=480°C) and intermediate (T_s=520°C) temperatures respectively. Comparison of equation (3.15) with the experimental results obtained at high T_s (540°C) as shown in figure 3.6 agrees well with equation (3.15). This implies that the desorption rate constant D is also not a function of the growth rate G_r. Consequently, the desorption rate of sulphur from InP is independent of the incident indium flux F_{In}, while the incorporation rate is directly proportional to F_{In}.

The concentration of incorporated sulphur in InP as a function of T_s can be obtained by considering that the desorption rate constant (D) and the incorporation rate constant (K) to be exponentially dependent on T_s:

$$D \propto \exp\{-E_{des}/k_B T_s\} \quad \ldots\ldots\ldots\ldots\ldots\ldots\ldots\ldots (3.16)$$

and

$$K \propto \exp\{-E_{inc}/k_B T_s\} \quad \ldots\ldots\ldots\ldots\ldots\ldots\ldots\ldots (3.17)$$

where E_{des} is the activation energy for desorption,
E_{inc} is the activation energy for incorporation, and
k_B is Boltzmann's constant.

For high growth temperatures where desorption is important, the concentration of incorporated sulphur is given by equation (3.15). Substituting equations (3.16) and (3.17) into (3.15) gives

$$C_B \propto \{\exp[(E_a/k_B T_s]\} \quad \ldots\ldots\ldots\ldots\ldots\ldots\ldots\ldots (3.18)$$

where $E_a = (E_{inc}-E_{des})$

Hence, plotting $\ln(C_B)$ against the reciprocal growth temperature, should yield a straight line whose slope equals is proportional to $(E_{inc}-E_{des})$. The net activation energy has experimentally been found to be 4.5eV as shown in figure 3.3.

The results from the growth rate dependence indicate that kinetic effects are relatively unimportant at high substrate temperatures where dopant desorption is significant. In this regime, a description of the reaction rates based on thermodynamics is appropriate, which has also been applied successfully to S in GaAs [3.5]. In reference [3.5], it was concluded that Ga_2S is the likely desorbing molecules at high substrate

temperature (>590°C). At lower substrate temperatures, a kinetic barrier is assumed to be present which prevents the desorption. For S in InP, Iliadis et al. have considered the reactions which give rise to the formation of the volatile sulphide InS and In_2S [3.8]. These reactions were

$$4InP(s) + S_2(g) = 2In_2S(g) + 2P_2(g) \quad \ldots\ldots\ldots (3.19)$$

and

$$2InP(s) + S_2(g) = 2InS(g) + P_2(g) \quad \ldots\ldots\ldots (3.20)$$

Under typical MBE growth conditions, the pressure of In_2S estimated from equation (3.19) is large (10^{-2} to 10^{-3} Torr) for T_s=450-550°C and a kinetic barrier is again assumed to be operative. The desorption of InS via equation (3.20) only becomes important when the loss via equation (3.19) is constrained by the large kinetic barrier.

According to Heckingbottom, the incident species for MBE growth acquire the substrate temperature very quickly [3.14]. Consequently the surface concentration of dopant species may be considered to be in equilibrium with the bulk of the crystal rather than the vapour phase. The possible reactions for sulphur desorption are then given by

$$In_{In} + S_p = InS(g) \quad \ldots\ldots\ldots\ldots\ldots\ldots (3.21)$$

and

$$2In_{In} + 2P_p + S_p = In_2S(g) + P_2(g) \quad \ldots\ldots\ldots (3.22)$$

It should be noted that InS and In_2S are only two of the many compounds of In_xS (x=1,2,...) considered for the desorption process. At first sight, equation (3.21) appears to be the required reaction since a change in the phosphorus overpressure would not affect the rate of sulphur desorption. If Heckingbottom's approach is used to estimate the level of

incorporation of sulphur in MBE materials from VPE data, then the desorbing flux of InS in equation (3.21) can be calculated for a given C_B. For typical MBE growth conditions : T_s=560°C, G_r=1.7μm/hr, $p(P_2)$ =10^{-6}mbar, $p(S_2)$=8x10^{-9}mbar, C_B=$10^{17}cm^{-3}$, the partial pressure of the volatile compounds InS would be 10^{-17}mbar which is about 8 orders of magnitude smaller than the value required to account for the observed desorption rate. Conversely, if VPE data are again used for the reaction of equation (3.22), the In_2S pressure estimated would be 4x10^{-12}mbar. Considering the approximate nature of the thermodynamic data used in the calculations, the pressure of In_2S can be regarded as realistic. At low substrate temperatures (<500°C), the desorption of In_2S is assumed to be hindered by the presence of a kinetic barrier.

The enthalpy for the desorption of sulphur can further be obtained from equation (3.22). The concentration of the incorporated chalcogen $[S_p]$ is given in terms of the corresponding enthalpy and entropy H and S as

$$[S_p] = p(In_2S)[p(P_2)] \exp[(H/k_BT)-(S/k_B)] \quad \ldots\ldots\ldots (3.23)$$

The pressure of the desorbing sulphide $p(In_2S)$ is nearly constant in the high desorption regime so that if the pressure of the group V element $p(P_2)$ is also constant, the slope of the $\ln[S_p]$ versus $1/k_BT$ plot is the enthalpy H (found to be 4.5eV from the experimental result since $[S_p]=C_B$) which can be calculated from the enthalpies given in table 3.1 in which the H_a, H_b, .., H_e are the enthalpies for the different reactions shown. The values in table 3.1 are from experimental results except for H_a which is estimated from the substitution energy of S in InP calculated by Kraut and Harrison [3.15]. The result

Table 3.1 Experimental values of enthalpy for the reactions in InP and in GaAs.

Reaction	ENTHALPY (eV) InP	GaAs	Reference
$Sp+P(g) \rightleftharpoons S(g)+Pp$	$H_a=0.37$	-	[3.15]
$S(g) \rightleftharpoons S(s)$	$H_b=-3.0$	-	[3.16]
$\frac{1}{2}P_2(g) \rightleftharpoons P(g)$	$H_c=2.6$	-	[3.17]
$In_{In}+Pp \rightleftharpoons In(s)+\frac{1}{2}P_2(g)$	$H_d=1.63$	-	[3.18]
$2In(s)+S(s) \rightleftharpoons In_2S(g)$	$H_e=1.6$	-	[3.16]
$Sp+As(g) \rightleftharpoons S(g)+As_{As}$	-	$H_a=-0.44$	[3.19]
$S(g) \rightleftharpoons S(s)$	-	$H_b=-3.0$	[3.16]
$\frac{1}{2}As_2(g) \rightleftharpoons As(g)$	-	$H_c=2.0$	[3.20]
$Ga_{Ga}+As_{As} \rightleftharpoons Ga(s)+\frac{1}{2}As_2(g)$	-	$H_d=1.9$	[3.21]
$2Ga(s)+S(s) \rightleftharpoons Ga_2S(g)$	-	$H_e=0.2$	[3.16]

is $H=H_a+H_b+H_c+H_d+H_e=4.8eV$, compares well with the experimentally measured value.

Similarly, the desorption reaction for sulphur in GaAs would be analogous to equation (3.22):

$$2Ga_{Ga} + 2As_{As} + S_{As} \rightleftharpoons Ga_2S(g) + As_2(g) \quad \ldots\ldots\ldots (3.24)$$

The substitution energy of S in GaAs is not available, but it is expected to be comparable to the substitution energy of Te [3.19], i.e. $H_a=-0.44eV$. The other enthalpies are also given in table 3.1. The enthalpy for the overall reaction described by equation (3.24) then becomes $H=2.6eV$, which is again in good agreement with the experimental result [3.5]. The same calculation for Se and Te can be expected to produce similar results, i.e. ~3eV.

Thus far, the experimental results are explained satisfactorily by the theory for both GaAs and InP. In the case of InP, the mostly likely desorbing reaction is equation 3.22 which is dependent on the phosphorus pressure. However the experimental data indicate that the concentration of incorporated sulphur in InP is practically independent of the phophorus overpressure. It is possible to explain this anomaly as follows: If dopant desorption is significant, a change in the flux of the group V element usually affects the incorporation and desorption rates due to a change in the surface stoichiometry of the growing crystal. Consider the desorption and incorporation rate constants be proportional to some powers t and u respectively of the group V pressure p(V), i.e.,

$$D = D_o\, p(V)^t \quad \ldots\ldots\ldots (3.25)$$
$$K = K_o G_r p(V)^u \quad \ldots\ldots\ldots (3.26)$$

C_B can then be solved by using equations (3.15), (3.25) and (3.26) to give

$$C_B = K_o F_{S2} p(V)^{u-t}/D_o \quad \ldots\ldots\ldots\ldots\ldots\ldots\ldots (3.27)$$

From this equation, it can be seen that the group V pressure affects both the incorporation and desorption reactions, hence the observed behaviour of C_B. For instance, increasing the group V flux would result in a decrease in the number of available group V lattice sites to accommodate the surface dopant atoms and therefore lead to a reduction of the rate of dopant incorporation. However, increasing the group V flux would at the same time decrease the number of group III atoms available to form the volatile dopant compound such as Ga_2S in the case of GaAs. Consequently the desorption rate of dopant is again reduced. From the experimental results shown in figure 3.7 for S-doped InP, it may then be concluded that these two processes must almost balance each other out, hence giving a constant sulphur concentration as found by C-V measurement. In another word, u=t for S in InP. For S and Se-doped GaAs, however, one or both of the effects must be kinetically different as can be inferred from figure 3.8, i.e. $u \neq t$.

For S in GaAs, the appropriate desorption reaction for the surface adatoms (*) is given by

$$2Ga^* + S^* = Ga_2S(g) \quad \ldots\ldots\ldots\ldots\ldots\ldots\ldots (3.28)$$

where (g) denotes the vapour phase. The effect of the group V overpressure on the desorption rate may be determined by considering the kinetic model proposed by Foxon and Joyce as described in chapter 1. According to the model, the reaction may be described as

$$2Ga* + As_4* = 2GaAs + \tfrac{1}{2}As_4(g) \quad \ldots\ldots\ldots\ldots\ldots (3.29)$$

If a mass action relationship is assumed to exist, then the following relationship is obtained

$$[Ga^*]^2 \sim [p(As_4)]^{-½} \quad \ldots\ldots\ldots\ldots\ldots\ldots\ldots\ldots (3.30)$$

Therefore $t=-½$ and so $u=-1½$ since $(u-t)$ is measured to be unity. This indicates that both the dopant incorporation and desorption are inversely related to the arsenic overpressure but with different power dependences.

The situation for S in InP is quite different since the concentration of incorporated dopants is found to be insensitive to the change in the P_2 overpressure. Again using Foxon and Joyce's model, one may deduce that $t=-1$. Thus $u=1$ since $(u-t)=0$. Consequently, the incorporation rate of sulphur is directly proportional to the phosphorus overpressure, while its desorption rate is inversely proportional to the phosphorus overpressure, i.e. the incorporation rate dependence is in direct contrast to that for sulphur in GaAs.

3.5 Conclusion

The incorporation and desorption behaviour of sulphur in InP has been investigated as a function of the adjustable growth parameters, namely the substrate temperature, the growth rate and the group V pressure. It is shown that sulphur desorbs from the surface of InP at substrate temperatures >500°C while for T_s<500°C the desorption is assumed to be prevented by the presence of a kinetic barrier. The dependence of the sulphur concentration C_B incorporated in the epitaxial layer was found to be directly proportional to the incident sulphur flux even at the high substrate temperature regime. Both the incorporation and

desorption rates are shown to have first order kinetics similar to Sn in GaAs [3.11].

The dependence of C_B on the growth rate G_r was found to have a linear relationship at $T_s \leq 520°C$. At high growth temperature, i.e. $T_s=540°C$, C_B was found to be independent of G_r. These results are explained using the kinetic model of Wood et al. [3.10]. The desorption rate is shown to be independent of the incident indium flux F_{In} and that the incorporation rate is directly proportional to F_{In}. This indicates that kinetic effects are relatively unimportant at high substrate temperatures and that the situation is more inclined towards the thermodynamic equilibrium phase.

At the high desorption regime, C_B was found to be a very weak function of the group V pressure, $p(P_2)$, unlike sulphur in GaAs where it was found that C_B was directly proportional to the arsenic pressure [3.5]. It is shown that either one or both of the processes (incorporation and desorption) of sulphur in InP must be different from that of sulphur in GaAs. Thermodynamic analysis has shown that the desorbing species of sulphur in InP is the compound indium sulphide In_2S rather than InS. It is pointed out that sulphur is probably much nearer thermodynamic equilibrium with the bulk of the crystal rather than the vapour phase as assumed by Iliadis et al. [3.8]. The desorption reaction is then given by equation (3.22), with an enthalpy estimated to be 4.8eV, in good agreement with the experimental result of 4.5eV. Similarly, the desorption reaction for Ga_2S in GaAs should be as given in equation (3.24). The enthalpy for equation (3.24) is found to be 2.6eV, again in close agreement with the experimental result of 3eV reported by Andrews et al. [3.5].

3.6 References

[3.1] P.J. Dean, M.S. Skolnick and L.L Taylor, J. Appl. Phys., 55, 957 (1984).

[3.2] M.S. Skolnick, P.J. Dean, S.H. Groves and E. Kuphal, Appl. Phys. Lett., 45, 962 (1984).

[3.3] R. Heckingbottom, C.J. Todd and G.J. Davies, J. Electrochem. Soc., 127, 444 (1980).

[3.4] L. Pauling, "The Nature of the Chemical Bond", 3rd edition, Cornell University Press, 1960.

[3.5] D.A. Andrews, R. Heckingbottom and G.J. Davies, J. Appl. Phys., 54, 4421 (1983).

[3.6] D.A. Andrews, R. Heckingbottom and G.J. Davies, J. Appl. Phys., 60, 1009 (1986).

[3.7] D.A. Andrews, M.Y. Kong, R. Heckingbottom and G.J. Davies, J. Appl. Phys., 55, 841 (1984).

[3.8] A. Iliadis, K.A. Prior, C.R. Stanley, T. Martin and G.J. Davies, J. Appl. Phys., 60, 213 (1986).

[3.9] G.J Davies, D.A. Andrews and R. Heckingbottom, J. Appl. Phys., 52, 7214 (1981).

[3.10] C.E.C. Wood and B.A. Joyce, J. Appl. Phys., 49, 4854 (1978).

[3.11] J.J. Harris, D.E. Ashenford, C.T. Foxon, P.J. Dobson and B.A. Joyce, Appl. Phys. A33, 87 (1984).

[3.12] S.S. Iyler, R.A. Metzger, F.G. Allen, in: VLSI Science and Technology 1984, Proc. 2nd Intern. Symp. on Very Large Scale Integration Science and Technology (Electrochemical Society, 1984), p473.

[3.13] J.M. Van Hove and P.I. Cohen, Appl. Phys. Lett., 47, 726 (1985).

[3.14] R. Heckingbottom, G.J. Davies and K.A. Prior, Surf. Sci., 132, 375 (1983).

[3.15] E.A. Kraut and W.A. Harrison, J. Vac. Sci. Technol., B2, 409 (1984).

[3.16] K.C. Mills, Thermodynamic Data for Inorganic Sulphides, Selenides and Tellurides (Butterworths, London, 1974).

[3.17] O. Kubaschewski and C.B. Alcock, Metallurgical Thermochemistry, 5th ed. (Pergamon, Oxford, 1975).

[3.18] R.F.C. Farrow, J. Phys., D7, 4236 (1974).

[3.19] E.A. Kraut, private communication, 1986.

[3.20] Thermodynamic Properties of the Elements, Advances in Chemistry Series No. 18 (American Chemical Society, Washington, DC, 1956).

[3.21] C. Pupp, J.J. Murray and R.F. Pottle, J. Chem. Thermodynamics, 6, 123 (1974).

CHAPTER 4

An Investigation of Magnesium in Indium Phosphide grown by Molecular Beam Epitaxy

4.1 Introduction

Both n- and p-type dopants having well behaved characteristics are essential for the fabrication of devices. In comparison to the available n-type dopants, there does not appear to be an impurity with well defined p-type doping characteristics in MBE grown InP. Kawamura et al. [4.1] have studied the possibility of using manganese (Mn) but the position of the Mn acceptor energy level was found to be influenced by the phosphorus overpressure. Under high ($\approx 2.4 \times 10^{-6}$ Torr) and low ($\approx 7 \times 10^{-7}$ Torr) phosphorus fluxes, the Mn acceptors formed levels at 280meV and 40meV respectively above the valence band. In a later report, Asahi et al. [4.2] discussed the use of beryllium (Be) as an alternative p-type dopant. They found that Be acceptors form a shallow level ($\approx$14meV above the valence band) and that InP could be doped up to $\approx 6 \times 10^{18}$ cm^{-3} without the morphology deteriorating. However, other authors have reported that the behaviour of Be in InP is sometimes unpredictable [4.3]. Another route to produce p-type material is to post-diffuse with dopants such as Zn and Cd [4.4]. However, complicated structures cannot be formed by this method and a more reliable and possibly less toxic impurity having good characteristics is therefore required for doping during growth.

In a follow-up study to their work on residual donors in nominally undoped InP, Iliadis et al. [4.5] identified four principal acceptor impurities by

secondary ion mass spectrometry (SIMS), namely Mg, Ca, Mn and Fe. The former two impurities are shallow acceptors whereas the latter are deep acceptors. Mg and Ca are two potential candidates as p-type dopants, although Ca doping of GaAs from Ca_2As_3 has proved unsatisfactory [4.6]. On the other hand, there are two factors which may favour the use of Mg as a p-type dopant in InP. Firstly, the presence of $\leq 10^{15}cm^{-3}$ Mg atoms in nominally undoped MBE-grown InP, as reported by Iliadis et al., indicates the ease with which Mg can be incorporated in the crystal lattice from unidentified background sources. Secondly, both Mg-doped GaAs and AlGaAs grown by metal-organic chemical vapour deposition (MOCVD) and MBE have been reported [4.7,4.8]. Although the authors in reference [4.8] have shown that Mg has a very low sticking coefficient (10^{-5}) on GaAs grown at 560°C, InP is generally grown at a much lower temperature. Consequently Mg can be expected to have a higher sticking coefficient on InP and hence a better incorporation behaviour. Indeed, magnesium has been successfully doped in InP up to a concentration of $10^{18}cm^{-3}$ by MBE using sources of P_4 and solid indium [4.9]. In this chapter, the properties of InP grown with an incident Mg flux under conditions which produce inadvertently doped layers with good electrical and optical characteristics are presented [4.10].

4.2 Experimental Procedure

The MBE system was the same as used for growing undoped InP and has been described in chapter 2. Phosphorus dimers (P_2) generated by thermal cracking of P_4 were used in all the growth runs. Semi-insulating Fe-doped (100)InP substrates were used, which were cleaned and degreased in organic solvents and etched

for 15s in a solution of H_2SO_4:H_2O_2:H_2O (10:1:1). The substrate mounted onto a Mo block with metallic indium was then immediately transferred into the vacuum system in which the surface oxide was removed by heating to 530°C for 3mins in a phosphorus stabilising flux.

The growth conditions used were nominally identical for all the samples, with BEPs of 2-3x10^{-6}mbar for P_2 and 4x10^{-7}mbar for In, equivalent to a growth rate of 1.5μm/hr. The substrate temperature used was ≈500°C which was the temperature required to obtain high quality undoped material with 77K residual electron concentrations of ≈2x$10^{15}$$cm^{-3}$ and mobilities up to 42,500$cm^2V^{-1}s^{-1}$, corresponding to a compensation ratio $_h$, defined as N_A/N_D, of ≈0.25 (see Chapter 2). These results are comparable to the values reported by Roberts et al. for unintentionally doped InP grown in a commercial MBE system [4.11].

The measurement techniques used to characterise the grown layers included the Hall effect measurement, C-V profiling, low temperature PL and secondary electron microscopy (SEM).

4.3 Magnesium Doping

The magnesium cell was equipped with a p-BN crucible and was operated at temperatures between 130 to 300°C. It was found that the Mg flux could be detected by the ion gauge for the highest cell temperature used; at T_{Mg}=300°C, the BEP of Mg was ≈1x10^{-9}mbar. Following the analysis of Wood et al. [4.6], the doping concentration of Mg may be written in terms of BEPs of the fluxes as

$$N_{Lg} = 1.11\times10^{22} \times \frac{BEP_{Mg} \times \aleph_{In} \times (T_{Mg} \times M_{In})^{1/2}}{BEP_{In} \times \aleph_{Mg} \times (T_{In} \times M_{Mg})^{1/2}} cm^{-3} \quad ..(4.1)$$

where M is the atomic mass of the element under consideration,

T is the temperature of the cell in degrees Kelvin,

$\aleph$ is the ionization coefficient of the BEP gauge for a particular species and is given by

$$\frac{\aleph}{\aleph(N_2)} = \frac{0.4Z}{14} + 0.6 \quad .....(4.2)$$

where $\aleph(N_2)$ is the ionization coefficient for nitrogen and Z is the atomic number of the species.

Hence, if Mg is assumed to be incorporated into InP with a unity sticking coefficient, the expected range of doping concentrations would be between $\approx1\times10^{15}$ and $1\times10^{20}cm^{-3}$ for the cell temperatures used in this work.

4.4 Results and Discussion

4.4.1 Electrical Properties

Samples grown in a Mg-flux were found to be n-type in character instead of the expected p-type behaviour from both Hall effect and C-V measurements. Table 4.1 summaries the free-carrier concentration (N_D-N_A) and mobility at 300K and 77K for a number of samples grown in a Mg flux, together with two nominally undoped samples. A carrier compensation ratio $\theta=N_A/N_D$ between 0.2-0.4 is obtained for the "Mg-doped" material based

Table 4.1 Electrical data for both Mg-doped and undoped InP grown by MBE. Samples #252, #253 and #255 were grown in a Mg flux while layers #203 and #232 were not intentionally doped.

Sample No.	n_{300k} x10^{15} (cm^{-3})	μ_{300k} ($cm^2V^{-1}s^{-1}$)	n_{77k} x10^{15} (cm^{-3})	μ_{77k} ($cm^2V^{-1}s^{-1}$)	θ (N_A/N_D)
252	3.9	3160	2.4	28000	~0.4
253	4.6	2600	-	-	-
255	3.0	3700	1.9	32000	~0.35
232	7.4	2800	3.4	29000	~0.30
203	2.1	4400	1.6	42500	~0.25

on the theoretical data given by Walukiewicz [4.12], comparable to the compensation ratio for the unintentionally doped material. No allowance has been made for possible two layers conductivity effects associated with the presence of accumulated impurities at the substrate-epilayer interface often observed in InP as described in chapter two. This can result in an under estimate of μ and over estimate of (N_D-N_A) for the epitaxial layer. Therefore, the values of θ quoted in table 4.1 represent upper limits. The total concentration of shallow acceptors N_A is estimated to be $\leq 1x10^{15}cm^{-3}$, correlating well with the low emission levels related to shallow acceptors observed in the PL spectra discussed in section (4.4.3).

The lack of evidence from the electrical data for a reduction in mobility at 77K caused by additional ionised impurity scattering with the corresponding increase in θ due to the presence of Mg in the lattice suggests that the sticking coefficient of Mg on InP at T_s=500°C is very low in marked contrast to the result for GaAs [4.6].

4.4.2 Surface Morphology

The surface morphology of samples #252, #258 and #261 was examined by secondary electron microscopy (SEM). The specimens were tilted during recording to produce better imaging of the defects. The relative defect densities of these three samples are as follows; #252 ($5x10^5cm^{-2}$) < #258 ($6.5x10^5cm^{-2}$) < #261 ($1x10^6cm^{-2}$). The highest surface defect concentration occurred in the presence of the highest magnesium flux. The flux originating from the magnesium cell therefore aided the formation of the defects which were of different sizes and shapes, indicating that they were being created continuously as the growth

proceeded. Figure 4.1(a) and 4.1(b) are SEM micrographs for an undoped and a "Mg-doped" sample. The majority of the surface defects are the 'classical' oval defects which can be clearly seen in figure 4.1(a) to align themselves in the [0$\bar{1}$1] orientation. Terraced dislocation defects were also present in some of the samples (not shown in the micrographs). Furthermore, pair defects were also observed which might have nucleated as a result of sulphur contamination associated with the substrate preparation in the H_2SO_4:H_2O_2:H_2O etch [4.13].

4.4.3 Photoluminescence at the Near Band Edge and in the 1.38eV region

An indication of the quality of epitaxial layers may be conveniently obtained by photoluminescence spectroscopy. Figure 4.2 shows PL spectra for an unintentionally doped and a "Mg-doped" sample. Both spectra have similar features, being dominated by neutral donor-bound exciton transitions (D°-X) at 1.417eV. The experimental results obtained for the half-width of the (D°-X) transitions and the ratio between the peak heights of the band-acceptor (e-A°) pair and (D°-X) transitions for the samples investigated are given in Table 4.2. Less than 5% of the total integrated emission intensity is associated with the shallow acceptor impurities. The average half-width for the (D°-X) line is 4.0meV, confirming good sample quality.

A detailed study of the PL emission around 1.38eV was performed in order to compare the various emission peaks with those produced by known chemical impurity species in InP. The observed emission peaks are listed in table 4.3 and their appropriate designations given. Three distinct peaks were observed in the "Mg-doped"

(a)

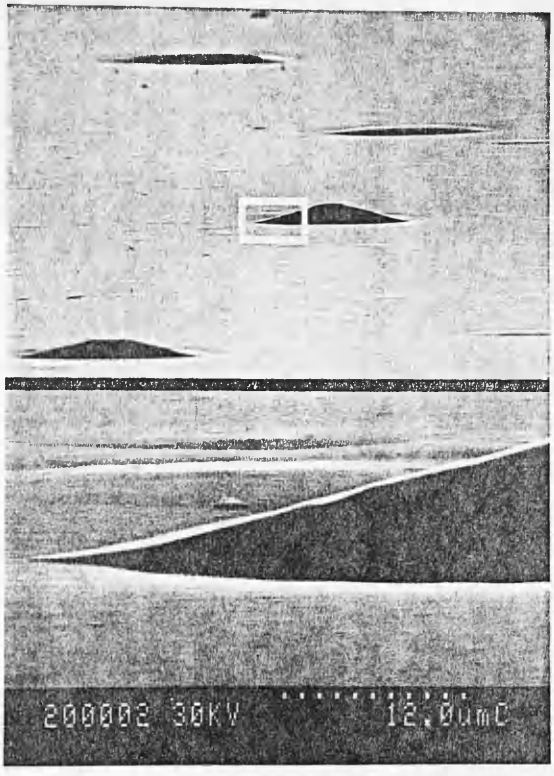

(b)

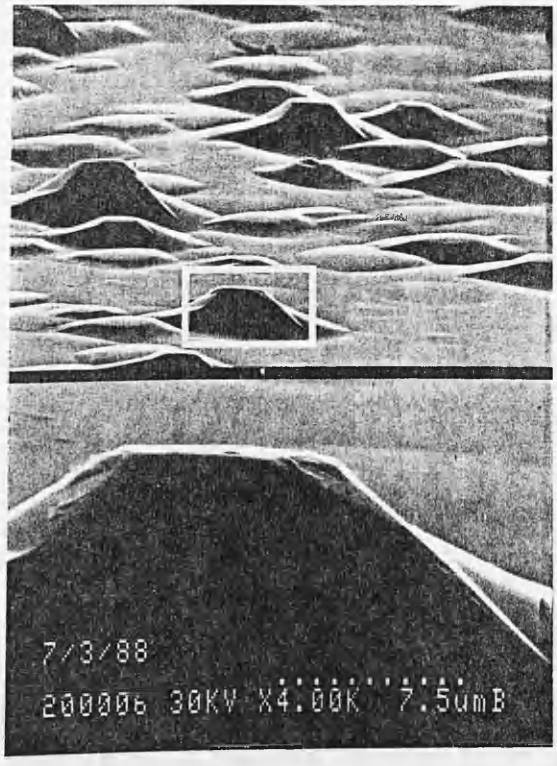

Figure 4.1 Scanning electron micrographs to illustrate typical defects observed on (100)InP grown by MBE; (a) undoped sample and (b) Mg-doped sample.

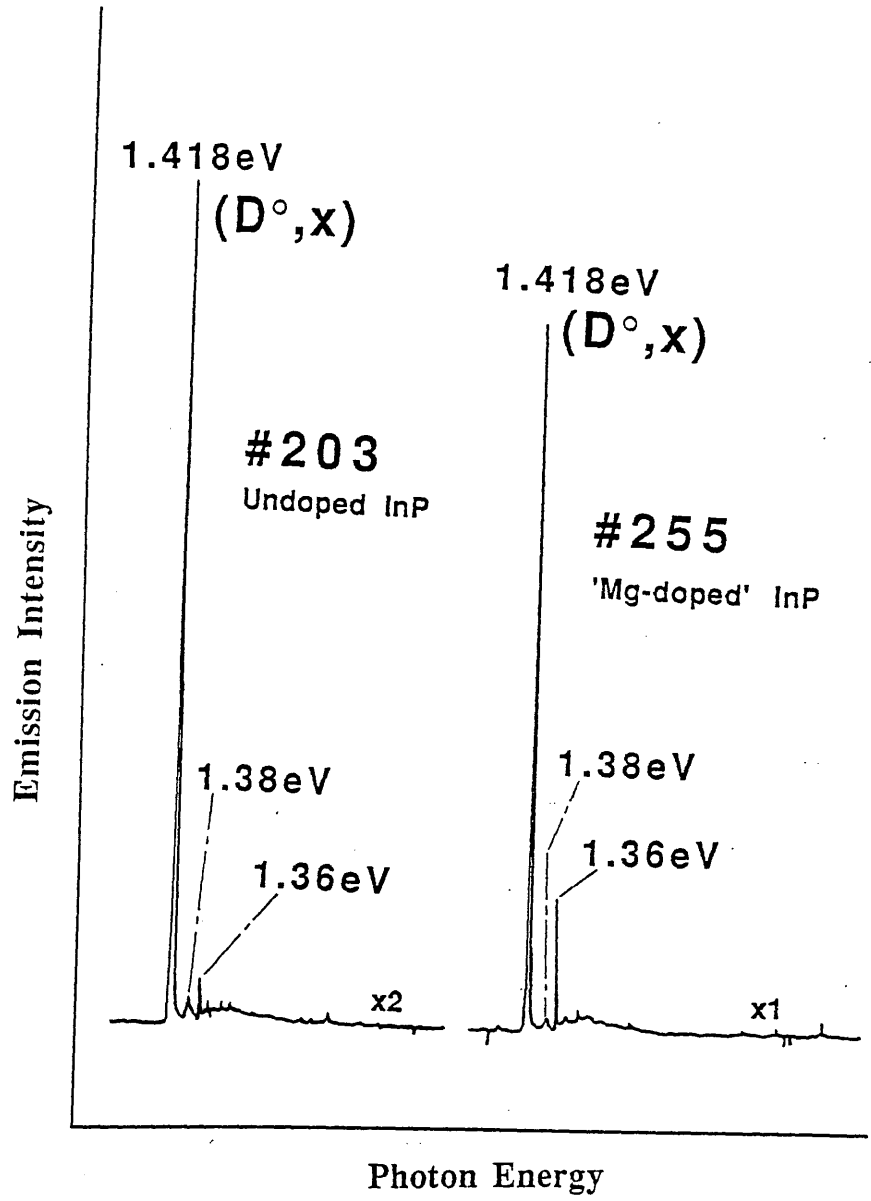

Figure 4.2 17K PL spectra of MBE-grown undoped InP (#203) and Mg-doped InP (#255) for an excitation intensity at 633nm of ~10Wcm^{-2}.

Table 4.2 17K PL data for the Mg-doped InP samples. The full widths at half maximum for the (D°-X) transitions lie within 3-5meV and the ratio of the (B-A°) emission at 1.38eV to the (D°-X) excitonic line at 1.417eV, I(B-A°)/I(D°-X), is $\leq$5% for all samples.

Sample No.	T_{Mg} (°C)	FWHM (D°-X) (meV)	I(B-A°)/I(D°-X) %
252	130	3.6	5.0
253	140	4.2	4.6
254	150	3.8	2.9
255	160	4.1	3.3
258	200	4.1	4.6
259	260	4.3	2.1
261	300	3.6	3.5

Table 4.3 Energies of the (D-A°) and (B-A°) transitions assigned to the shallow acceptor impurities C, Mg, Be, and Zn in InP (reference 4.12). The principal emission peaks determined here for MBE-grown InP are a (D°-A°) transition at 1.3800eV and a (B-A°) line at 1.3835eV identified with magnesium, and a (D°-A°) transition at 1.3758eV associated with carbon.

	C	Mg	Be	Zn	
(B-A°)	1.3796	1.3832	1.3829	1.3781	Ref.4.12
	(1.3800)	1.3835	-	-	Our data
(D°-A°)	1.3755	1.3785	1.3782	1.3732	Ref.4.12
	1.3758	1.3800	-	-	Our data

InP but only two peaks were discernible in the undoped samples at 2K (see figure 4.3). Comparing their energies with published data, the peaks at 1.3835 and 1.3800eV may be assigned to conduction band to acceptor (e-A°) and donor-acceptor (D°-A°) transitions respectively involving shallow Mg states [4.14]. This agrees with the observation of T. Martin who found that the level of magnesium vary directly with the intensities of these transitions [4.15]. The third distinct peak at 1.3758eV found here in Mg-InP is caused by (D°-A°) transitions involving carbon acceptors [4.14]. The (e-A°) transitions associated with carbon overlap the (D°-A°) peak of Mg and are not fully resolved since the energy difference between a (e-A°) and a (D°-A°) transition is ≈4-5meV.

The activation energies of Mg and C may be calculated using the expression derived by Eagles [4.16]:

$$E_A = E_g(T) - E(e\text{-}A^\circ) + \tfrac{1}{2}k_B T_e \quad \ldots\ldots\ldots\ldots\ldots\ldots (4.3)$$

where $E_g(T)$ is the band gap energy for a sample temperature T,

$E(e\text{-}A^\circ)$ is the peak energy of the free to bound transition,

k_B is Boltzmann's constant, and

T_e is the temperature of carriers in degrees Kelvin.

Taking E_g=1.4233eV at T=2K and an electron temperature of 25K [4.17], the activation energies for Mg and C are calculated to be 40.9 and 44.4±0.3meV respectively, in good agreement with the published data given in reference 4.12 for low-dose ion-implanted InP. In addition, from the energy difference between the (e-A°) and (D°-A°) emissions, an estimate of the donor binding energy may be

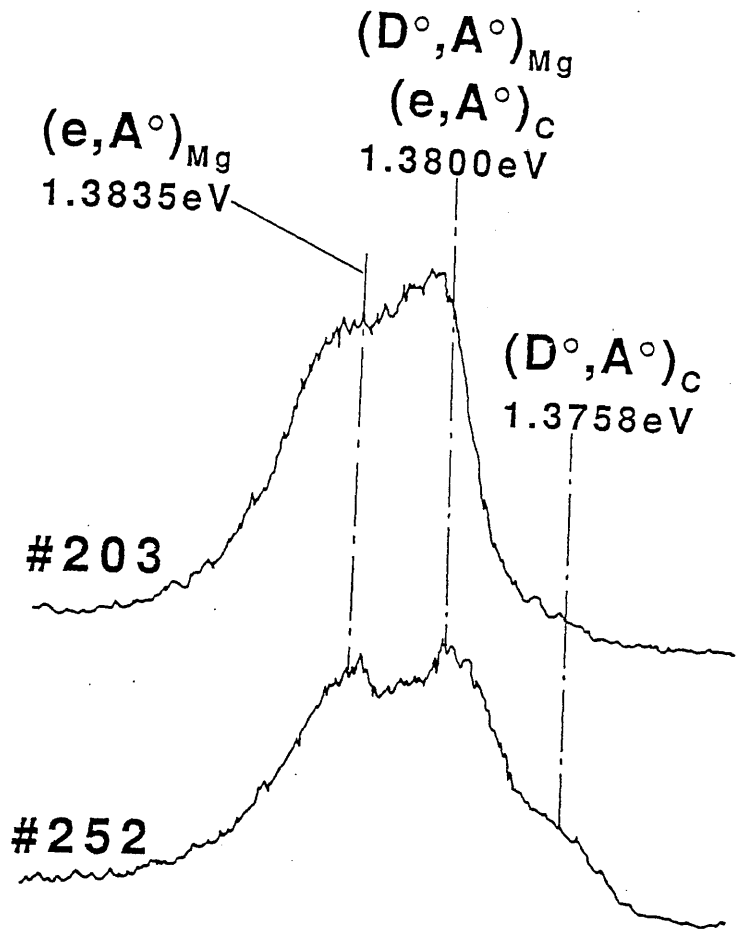

Figure 4.3 PL spectra around 1.38eV for undoped and Mg-doped InP. Three distinct peaks are present in the Mg-doped sample while two peaks are recorded in the undoped epitaxial layer. The transitions at 1.3835 and 1.3800eV are related to magnesium and the line at 1.3758eV is associated with carbon. The excitation intensity was ~10mWcm^{-2}.

obtained from [4.17]

$$E_D = E(e\text{-}A^\circ) - E(D^\circ\text{-}A^\circ) + e^2/(4\pi\epsilon_0\epsilon_r R) - \tfrac{1}{2}k_B T_e \quad .....(4.4)$$

where ϵ_r is the dielectric constant of the semiconductor and R is the average distance between the donors and the acceptors. Taking a value of $E(e\text{-}A^\circ)-E(D^\circ\text{-}A^\circ)$ = 3.5meV from the experimental results, R = 300A [4.18] and T_e = 25K, the calculated value for E_D is 6.29meV which is in reasonable agreement with 7.65meV found by Chamberlain et al. [4.19].

The experimental data has been compared with a model based on Eagle's theory for the $(e\text{-}A^\circ)$ transition and a Lorentzian lineshape for the $(D^\circ\text{-}A^\circ)$ transition; the result is shown in figure 4.4 (a) and (b). Figure 4.4 (a) is a fit using a carrier temperature T_e of 10K; it is clear that the fit does not match the experimental spectrum at the high energy side. However, if a carrier temperature of 25K was used, a close fit is obtained as seen in figure 4.4 (b), which was the value used by Fischbach et al. [4.17]. An alternative interpretation for the 1.3835eV line has been offered by Burkhard et al. [4.18] who argued that the transition is associated with an excited state of the $(D^\circ\text{-}A^\circ)$ line rather than a $(e\text{-}A^\circ)$ transition. Both the $(D^\circ\text{-}A^\circ)$ and the $(D^{\circ+}\text{-}A^\circ)$ peaks then have a Lorentzian lineshape. However, it is not possible to fit two Lorentzians to the experimental data discussed here. Figure 4.5 shows the best attempt in fit the experimental spectrum with two Lorentzian curves; fair agreement is present except at the high energy side of the spectrum. The experimental spectrum has been investigated both as a function of the sample temperature and the incident laser power. Figure 4.6 shows the former dependence. When the temperature is increased from 2K to 24K, the spectrum is dominated by the emission at 1.3835eV $(e\text{-}A^\circ)$. This is associated

(a)

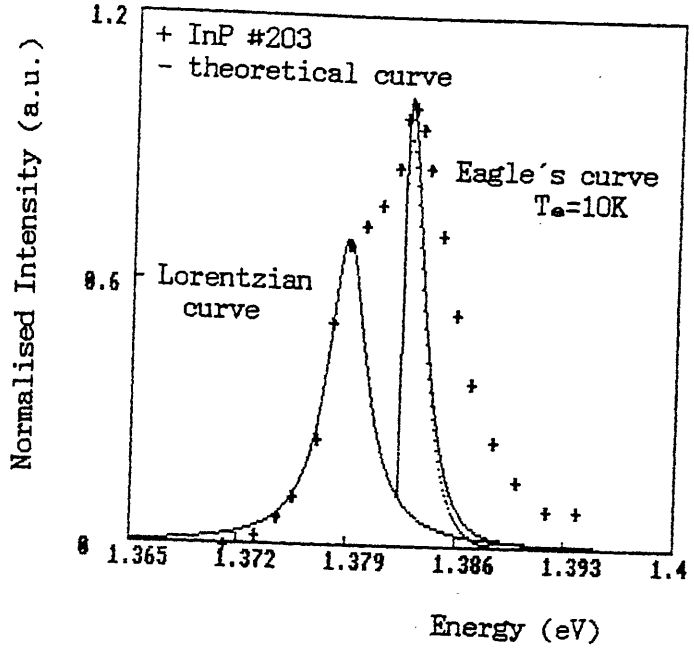

(b)

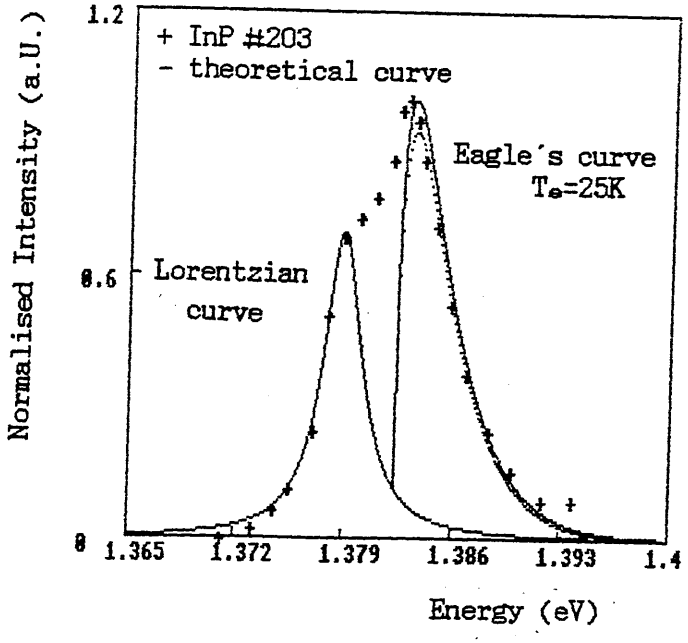

Figure 4.4 A theoretical fit to the emission lines at 1.3835 and 1.3800eV using Eagle's model and a Lorentzian curve respectively with (a) a carrier temperature of 10K and (b) with a carrier temperature of 25K.

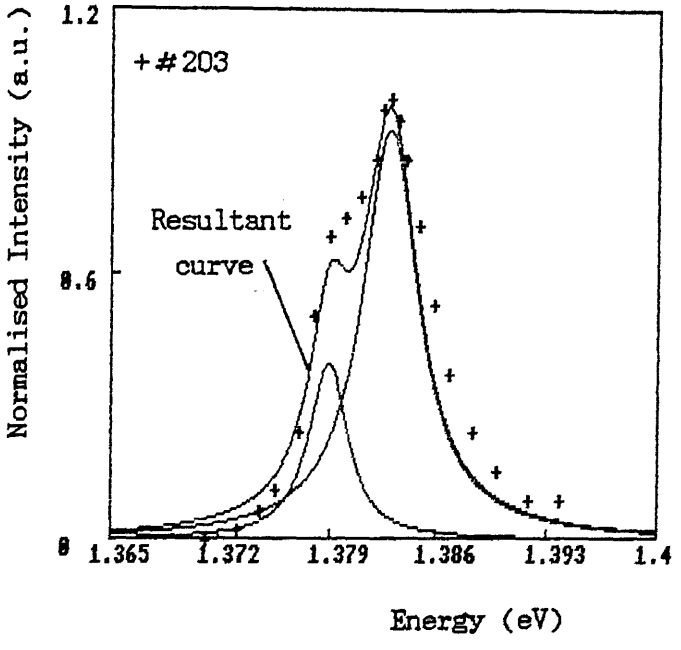

Figure 4.5 The emission lines at 1.3835 and 1.3800eV fitted using two Lorentzian curves. The resultant curve is in fair agreement with the experimental result except at the high energy side.

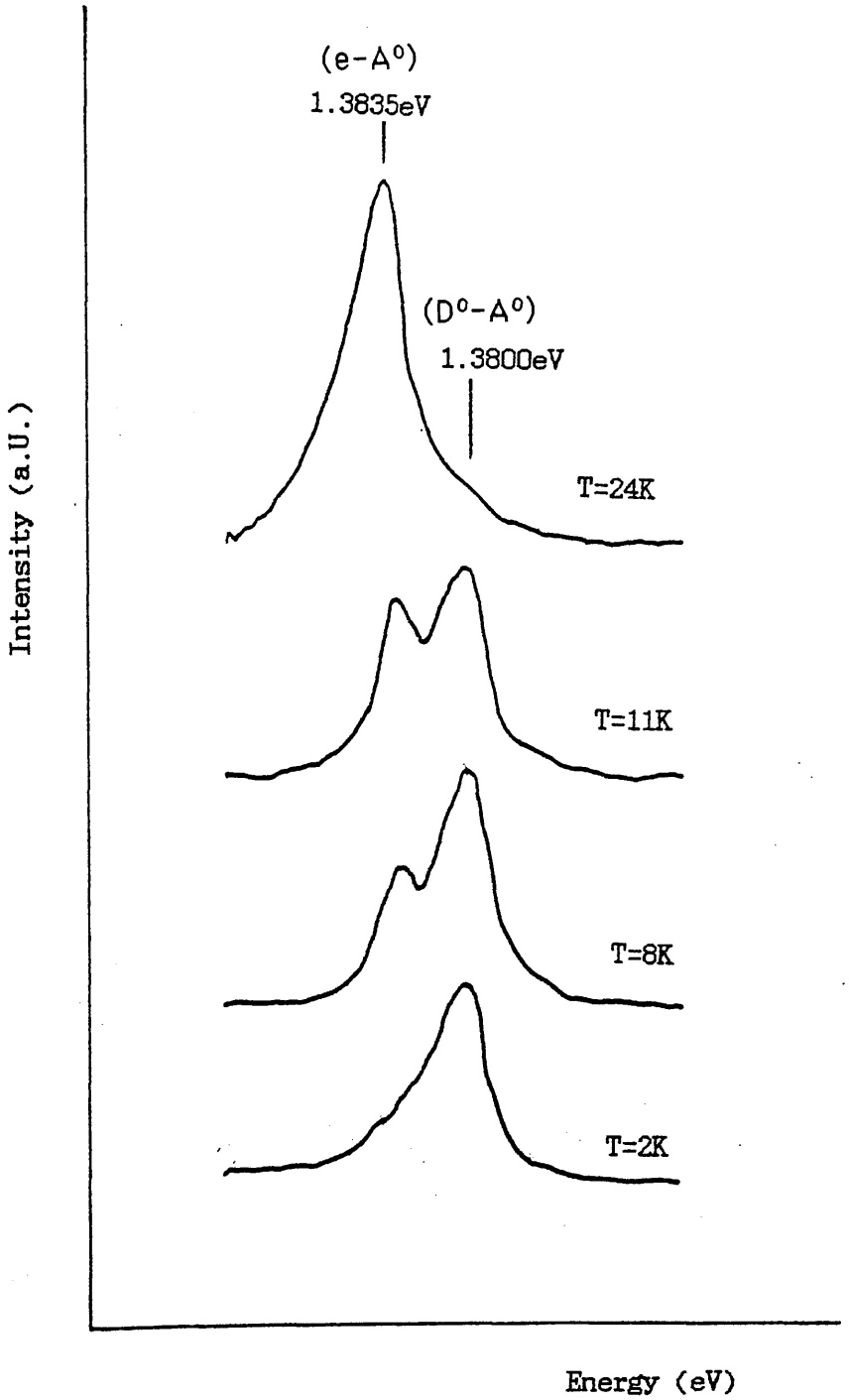

Figure 4.6 The behaviour of (e-A°) and (D°-A°) as a function of the sample temperature between 2 and 25K.

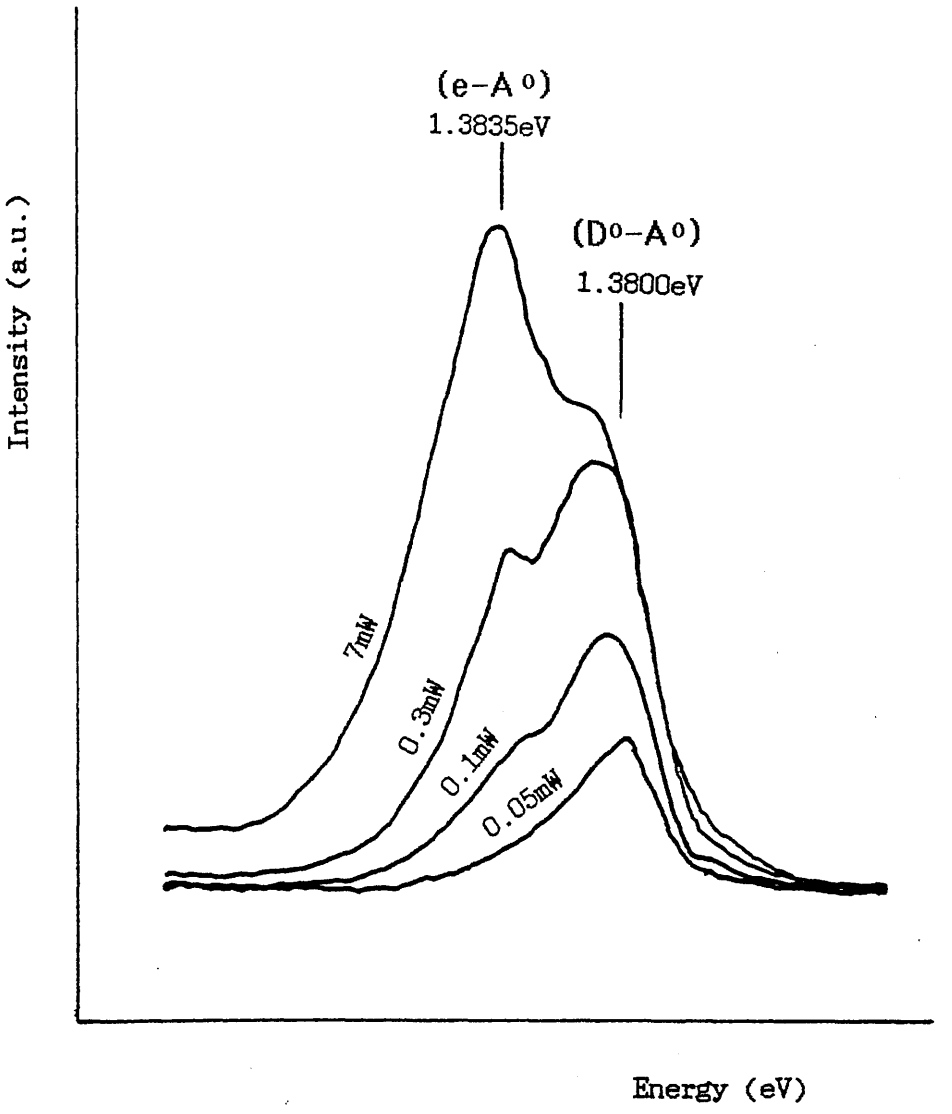

Figure 4.7 The behaviour of (e-A°) and (D°-A°) as a function of the incident laser power.

with the donors being thermally ionized. As a result, the population of free electrons is increased relative to the bound electrons and therefore giving a much stronger (e-A°) emission than the (D°-A°). In figure 4.7 the behaviour of the (e-A°) and (D°-A°) as a function of the laser power is shown. At low laser power (0.05mW), the overall spectrum is dominated by the (D°-A°) emission at 1.3800eV and at high laser power (7mW) the spectrum is dominated by the (e-A°) transition at 1.3835eV. The concentration of photo-excited carriers are increased as the laser excitation was increased. This gives increased screening and therefore reduces the effective donor binding energy, thus leading to a gradual transition from the (D°-A°) to (e-A°) as the excitation intensity is increased.

The excitonic emission centred at 1.36eV observed in undoped InP layers is also a consistent feature in the "Mg" doped InP discussed here. The magnitude of the intensity of this peak is comparable between the samples grown with and without a Mg flux, indicating that the presence of Mg atoms has little influence on the formation of the deep donor complex associated with the 1.36eV transition.

4.4 Conclusion

An investigation of Mg in InP grown by molecular beam epitaxy from solid sources has revealed two apparently different incorporation mechanisms depending on whether the incoming Mg is from a "background" source or as an elemental flux from a Knudsen cell. On the one hand, magnesium appears to be incorporated from what is assumed to be a low level background source in a relatively facile manner. Of the two impurities detected by SIMS in unintentionally

doped InP [4.5] which potentially can act as shallow acceptors, Mg rather than Ca is the principal electrically-active species at a concentration $\leq 10^{15}cm^{-3}$. No detectable incorporation of carbon is found in the inadvertently doped layers. In contrast, there is no evidence from both electrical data and low temperature PL spectra for measurable incorporation of Mg over and above the concentration derived from the background source when InP is grown at a substrate temperature of 500°C in a flux of Mg atoms generated by a Knudsen source. However, a small trace of carbon has been detected in the PL spectra from the "Mg-doped" samples. The optical activation energies for Mg and C are 40.9 and 44.4 ± 0.3meV respectively in excellent agreement with previously published data for low dose ion-implanted InP samples [4.14]. A donor binding energy of 6.29meV has been estimated from the results discussed above, compared with the value of 7.65eV obtained by Chamberlain et al. [4.19] using far infrared techniques. Although the intentional introduction of Mg into InP from an elemental flux has not been systematically investigated at growth temperatures «500°C, no evidence has been found from extensive studies of inadvertently doped InP for a significant dependence of Mg incorporation on substrate temperature between 350°C to >500°C. The origin of the background magnesium is unknown at present. However, it is anticipated that it is unlikely to come from the group III source considering the high vapour pressure of magnesium at the operating temperature of the group III cell. The magnesium would deplete completely in a very short time if it was from the indium source. In GaAs, magnesium has been shown successfully to incorporate in epitaxial layers using the compound Mg_2As_3 [4.6]. Therefore, in the case of InP, a probable source for the background magnesium could be the compound Mg_2P_3 originated from the

phosphorus source. However, there is no concrete evidence for this speculation and further experiments are required to elucidate this. An obvious experiment would be grow an epitaxial layer at different phophorus cell temperatures and performing SIMS measurement on the grown structure. One would expect the level of magnesium in the sample to vary as a function of the phophorus cell temperature if Mg_2P_3 is the culprit.

The surface morphology of the grown InP samples was found to depend strongly on the intentional Mg flux; the total density of surface defects increasing from $1x10^5cm^{-2}$ for undoped layers to $\geq 1x10^6cm^{-2}$ for samples grown in the highest Mg flux. Surprisingly, the high concentration of surface defects has little effect on the electrical and optical properties of the "Mg-doped" material. SEM observations of the morphology indicate that Mg somehow assists the nucleation of defects, in particular oval defects, but is not itself incorporated into the epitaxial layer. However, the exact mechanisms involved are at present not understood.

Finally, it is concluded that the negligible concentrations of Mg incorporated from an elemental flux into InP makes it unsuitable as a p-type dopant in MBE growth under the conditions discussed here.

4.5 References

[4.1] Y. Kawamura, H. Asahi and H. Nagai, J. Appl. Phys., 54, 841 (1983).

[4.2] H. Asahi, Y. Kawamura, M. Ikeda and H. Okamoto, Jpn. J. Appl. Phys., 20, L187 (1981).

[4.3] C.R. Stanley, R.F.C. Farrow and P.W. Sullivan, The Technology and Physics of Molecular Beam Epitaxy, edited by E.H.C. Parker, Plenum Press, New York (1985), p275.

[4.4] B.I. Miller, J.H. McFee, R.J. Martin and P.K. Tien, Appl. Phys. Lett., 33, 44 (1978).

[4.5] A. Iliadis, C.R. Stanley and D.E. Sykes, Proc. Mat. Res. Soc. (Europe), Symposium No.3, "Semiconductor Quantum Structures and Superlattices", Strasbourg, p167 (1985).

[4.6] C.E.C. Wood, D. Desimone, K. Singer and G.W. Wicks, J. Appl. Phys., 53, 4230 (1982).

[4.7] K. Tamamura, T. Ohhata, H. Kawai and C. Kojima, J. Appl. Phys., 59, 3549 (1986).

[4.8] A.Y. Cho and M.B. Panish, J. Appl. Phys., 43, 5118 (1972).

[4.9] K.J. Bachmann, E. Buehler, B.I. Miller, J.H. McFee and F.A. Thiel, J. Cryst. Growth, 39, 137 (1977).

[4.10] T.S. Cheng, V.M. Airaksinen and C.R. Stanley, J. Appl. Phys., 64, 6662 (1988).

[4.11] J.S. Roberts, P.A. Claxton, J.P.R. David and J.H. Marsh, Electron. Lett., 22, 506 (1986).

[4.12] W. Walukiewicz, J. Appl. Phys., 51, 2659 (1980).

[4.13] Y.G. Chai, Appl. Phys. Lett., 47, 1327 (1985).

[4.14] B.J. Skromme, G.E. Stillman, J.D. Oberstar and S.S. Chan, Appl. Phys. Lett., 44, 319 (1984).

[4.15] T. Martin, R.S.R.E.(Malvern), Private Communication.

[4.16] D.M. Eagles, J. Phys. Chem. Solids, 16, 76 (1960).

[4.17] J.U. Fischbach, G. Benz, N. Stath and M.H. Pilkuhn, Solid State Comm., 11, 725 (1972).

[4.18] H. Burkhard, E. Kuphal, F. Kuchar and R. Meisels, Proc. Inter. Conf. on GaAs and Related Compounds (1980), Inst. Phys. Conf. Ser. No.56: Chapter 8, p659.

[4.19] J.M. Chamberlain, H.B. Ergun, K.A. Gehring and R.A. Stradling, Solid State Comm., 9, 1563 (1971).

CHAPTER 5

Electrical and Optical Characterisation of InP Grown by Metal-organic Source MBE (MOMBE)

5.1 Introduction

Molecular Beam Epitaxy (MBE) and metal-organic chemical vapour deposition (MOCVD) are two well established methods for preparing high quality single crystals, especially III-V compounds and alloys. Each of these techniques has advantages over the other but often they are complementary. By combining them, a new form of thin film preparation method known as metal-organic molecular beam epitaxy (MOMBE) has emerged which has advantages over both MOCVD and MBE. MOMBE is essentially a thin film growth process performed in a conventional MBE system with the solid sources replaced by gases [e.g. phosphine (PH_3), triethylindium (TEIn)]. The main advantages of MOMBE are (a) convenient source replenishment without disturbing the integrity of the UHV environment in the growth system and (b) constant control of fluxes giving rise to accurate compositions in the growth of type II alloys [5.1]. However, an obvious drawback in MOMBE is the toxicity of the hydrides (AsH_3, PH_3) used as the group V sources. This requires stringent safety measures to be enacted. Alternatively, the group V alkyls [e.g. trimethylarsine (TMAs) and triethylphosphine (TEP)] may be used to reduce the hazards [5.2]. In MOMBE, an efficient pumping arrangement is necessary to cope with the removal of large quantity of hydrogen generated through cracking of the group V hydrides in the UHV chamber during growth. The high level of

hydrogen molecules has been shown to have a beneficial effect on the quality of the material [5.3]. Epitaxial GaAs [5.4] and InP [5.5] layers of exceptional quality have been achieved by MOMBE. Kawaguchi et al. in reference 5.5 reported undoped InP with a 77K mobility of 105,000 $cm^2V^{-1}s^{-1}$, comparable to the ultra-pure materials grown by MOCVD [5.6] and VPE [5.7]. This should be contrasted with the highest 77K mobility of 50,000 $cm^2V^{-1}s^{-1}$ reported for undoped InP grown by solid sources [5.8]. The superior quality of material obtainable by MOMBE has stimulated interest amongst research workers and as a result the existing conventional MBE systems in many laboratories have been converted to cope with gaseous sources.

In this chapter, the optical and electrical properties of InP grown by MOMBE will be discussed. The layers were grown by D.A. Andrews at BTRL using phosphine and three different three different indium sources; solid indium, triethylindium (TEIn) and trimethylindium (TMIn). The quality of the samples will be shown to depend on the indium source used. To assess the samples, low temperature PL, Hall effect measurement, DLTS and SIMS were used.

5.2 Growth Details

The system used for growth was a commercial V80H unit manufactured by VG Semicon and has been described elsewhere by Andrews et al. [5.9]. The system comprised of three chambers; a fast entry loadlock, a preparation and a main growth chamber. Phosphine fed into the system was thermally decomposed into hydrogen and phosphorus molecules in a low pressure («1 Torr) tantalum filled pBN cracker which was heated to 1000°C. Under the conditions used, the phosphine cracking efficiency was found to be greater than 95%

and the phosphorus molecules were predominantly P_2 relative to P_4. The high background pressure ($\sim 10^{-5}$torr) in the system during growth, containing mostly H_2 molecules generated through cracking of phosphine, was pumped continuously by an oil diffusion pump. The group III alkyls were introduced into the system via leak valves and effusion tubes directed towards the substrate. The elemental indium flux was generated by a Knudsen effusion cell.

A total of nine epitaxial layers of InP (MG59, MG70, MG76, MG78, MG80, MG84, MG86, MG229 and MG230) have been grown using phosphine with different indium sources (solid In, TEIn, TMIn) under nominally similar growth conditions. The growth rate for all the layers was approximately 1μm/hr except MG78 which was grown at 4μm/hr. MG59 was grown using elemental indium before the metal-alkyls were introduced into the system for the very first time. MG70 was also grown using elemental indium except that it was produced after a few MOMBE growth runs. MG76, MG229 and MG230 were grown using TMIn while MG78, MG84 and MG86 were grown using TEIn. Table 5.1 summaries the detail of the sample growth, their thicknesses and the electrical data obtained from C-V and Hall measurements.

5.3 Photoluminesecence Measurement at 4K

The PL spectra described in this section were recorded by S.T. Davey at BTRL using an argon ion laser operating at 514.5nm and a 0.5m monochromator together with a conventional lock-in amplifier for signal detection. Measurements were performed at 4K on four of the samples: MG59, MG70, MG76 and MG78. Figure 5.1 shows their PL spectra recorded with an incident power density of approximately 0.1 Wcm^{-2}. Each of the

Table 5.1 InP samples grown using different indium sources, together with their C-V and Hall data.

Sample	Indium Source	Thickness (μm)	Carrier Concentration ($\times 10^{16}$ cm^{-3}) C-V	Hall	Mobility ($cm^2V^{-1}s^{-1}$)	Compensation ratio θ
MG59	solid	2.8	2.0	3.2 (B)	3,800	
				3.2 (RT)	3,700	
				2.2 (77)	9,400	
				3.0 (CL,RT)	4,050	
				2.0 (CL,77)	10,000	0.30
MG70	solid	1.0	2.0	4.5 (B)	2,550	
				4.5 (RT)	2,300	
				2.7 (77)	4,550	0.56
MG76	TMI	3.8	0.2	0.27 (B)	4,400	
				0.31 (RT)	4,000	
				0.27 (77)	36,900	0.16
MG78	TEI	12.0	0.2	0.28 (B)	4,500	
				0.24 (RT)	4,800	
				0.18 (77)	46,500	0.11
MG80	TEI	5.0	0.8-4.0	2.2 (B)	3,800	
				2.2 (RT)	3,800	
				1.2 (77)	13,800	0.26
MG84	TEI	1.5	0.7	0.45 (RT)	4,100	
				0.30 (77)	21,250	0.45
MG86	TEI	3.5	1.0	3.3 (B)	3,600	
				3.2 (RT)	3,750	
				1.7 (77)	12,500	0.23
MG229	TMI	4.0	0.6	1.7 (B)	3,660	
				2.1 (RT)	3,080	
				1.0 (77)	15,040	0.27
MG230	TMI	2.0	0.4	0.59 (B)	4,020	
				0.73 (RT)	3,330	
				0.49 (77)	19,990	0.34

(B) : Blast contacts.
(RT) : Au/Sn contacts, squared sample at room temperature.
(77) : Au/Sn contacts, squared sample at 77K.
(CL,RT) : Au/Sn contacts, clover leaf patterned sample at room temperature.
(CL,77) : Au/Sn contacts, clover leaf patterned sample at 77K.

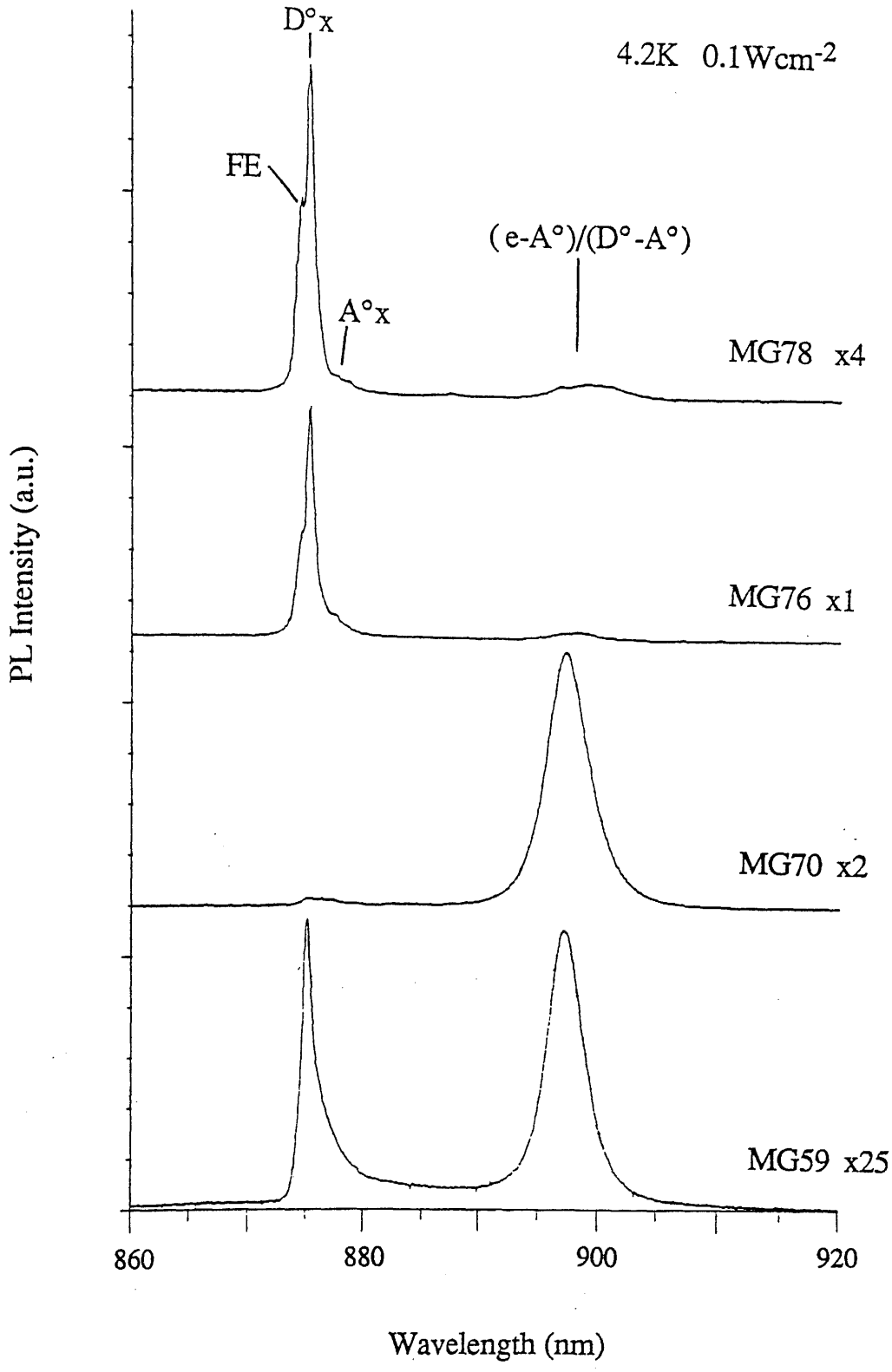

Figure 5.1 PL spectra of the InP grown using phosphine and different indium sources; TEIn (MG78), TMIn (MG76) and solid indium (MG70 & MG59).

spectra consists of two principal emission regions, characteristic of InP grown by other techniques; the near band edge bound exciton emission and the acceptor related transition at around 875 and 900nm respectively. Emission at longer wavelengths was not detected, suggesting a low ~ of radiative deep level in the material. concentration

The good quality of the MOMBE samples is demonstrated by the narrow linewidth of the (D°-X) emission ≈3meV for MG78. Comparison of the spectra shown in figure 5.1 indicates that the two layers grown with TEIn and TMIn have better optical properties compared with the samples grown using elemental indium. This is evidenced by the appearance of well resolved structure at the near band edge region for MG78 and MG76 as shown in figure 5.2. Much less structures are present for the other samples (MG70 and MG59) under the same excitation conditions. Designations of the various peaks around 875nm shown in the figure are in accordance with that used in chapter two. The presence of the FE shoulder at 1.4180eV is a strong indication of the high quality of the MOMBE material since it is associated with a low level of impurity defects. Substantial impurity defects present in the crystal tend to produce random electric fields which dissociate the excitons and hence FE emission would not be observed in the PL. Free excitons are therefore a very sensitive probe of the crystal quality.

The PL of the acceptor emission at ~1.38eV has been investigated as a function of both temperature and excitation intensity in an attempt to identify the shallow acceptors involved. Figure 5.3 shows the PL spectrum for sample MG78 at around 1.38eV, which clearly shows the existence of three separate peaks, namely P_1, P_2 and P_3 at energies of 1.3834, 1.3787 and 1.3757eV respectively. With an excitation intensity of

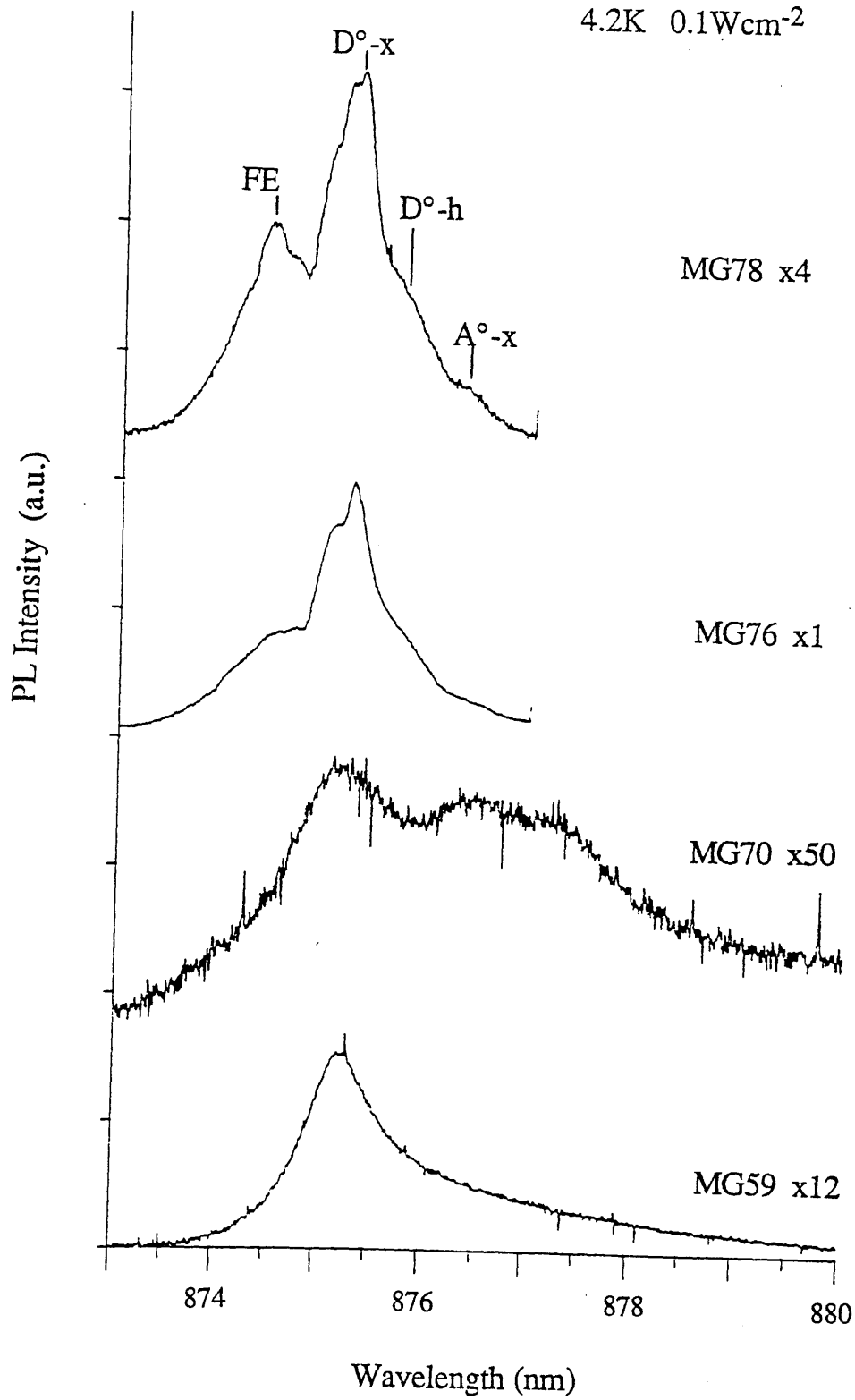

Figure 5.2 PL spectra of the MOMBE InP at the near band edge emission region. The assignment of the various peaks are the same as used in Chapter 2.

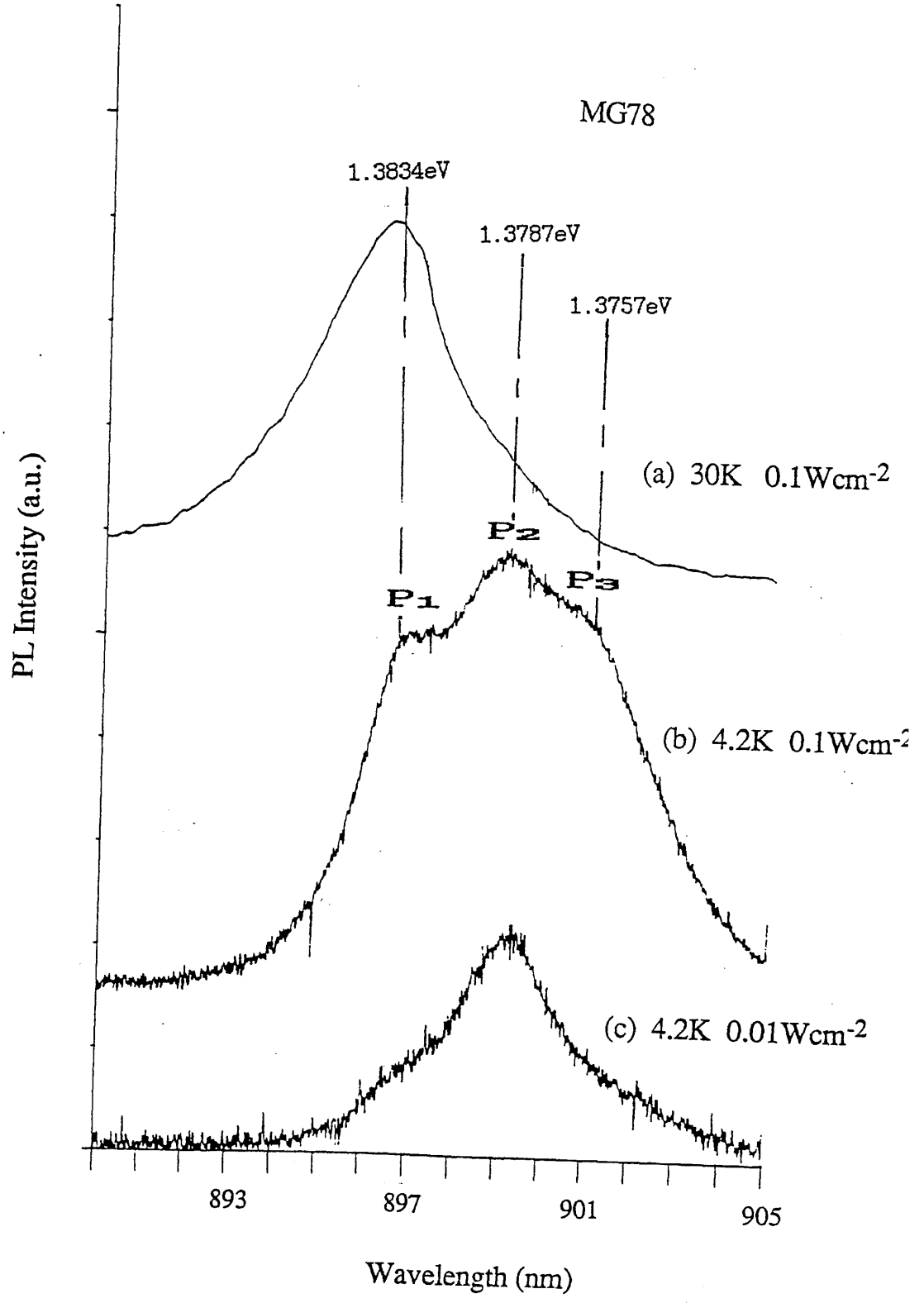

Figure 5.3 PL spectra of a MOMBE InP at the 1.38eV emission region as a function of the sample temperature and excitation intensity. Three peaks are resolved: P_1, P_2 and P_3, which are identified as the (e-A°), (D°-A°) emissions related to magnesium and the (D°-A°) emission associated with carbon respectively.

$0.1Wcm^{-2}$ and a temperature of 4.2K, the observed spectrum consists of emission peaks P_1, P_2 and P_3. When the temperature is increased from 4.2K to 30K but with the excitation intensity constant, peaks P_2 and P_3 quench relative to P_1 and eventually the overall spectrum becomes dominated by P_1, which is characteristic of a free to bound transition (e-A°). On the other hand, if the temperature is held at 4.2K and the excitation intensity reduced to $0.01Wcm^{-2}$, then the spectrum is dominated by peak P_2 which is related to donor to acceptor recombinations (D°-A°). The temperature and intensity dependence of the (e-A°) and (D°-A°) transitions have also been discussed in Chapter 4. Comparison of the energies of the peaks with those given by Skromme et al. [5.10] allow the identification of the impurity involved (see Chapter 4). The emission peaks are identified as follows:

Emission P_1 at 1.3834eV: free to bound transition associated with magnesium $(e\text{-}A°)_{Mg}$

Emission P_2 at 1.3787eV: donor to acceptor recombination related to magnesium $(D°\text{-}A°)_{Mg}$

Emission P_3 at 1.3757eV: donor to acceptor recombination involving carbon $(D°\text{-}A°)_C$

From the energetic position of the (e-A°) peak, an activation energy for the acceptor impurity involved has been calculated using equation (4.3) given in the previous chapter and is found to be 41meV, which compares favourably with Skromme's result for magnesium [5.11]. The designation of peak P_3 is to the donor to acceptor emission involving carbon $(D°\text{-}A°)_C$, again by comparison with Skromme's result. Emission associated with the $(e\text{-}A°)_C$ transition overlaps the $(D°\text{-}A°)_{Mg}$ line. Again using equation (4.3), the activation energy of carbon is found to be 45meV. It is interesting to note that the level of carbon

detected in the MOMBE samples is surprisingly low considering the large quantity of carbon related molecular species present in the growth chamber. This confirms the result of the thermodynamic analysis performed by Prior et al. [5.12] who show that carbon incorporation from species such as CO_2 is unlikely.

The 1.36eV emission line observed in the solid source grown InP discussed in Chapter two was not detected in any of the MOMBE samples. This suggests that one or more of the impurities/defects responsible for the formation of the complex is missing.

5.4 Hall Effect Measurements

The temperature variation of the Hall coefficient and resistivity in the range 4-350K has been measured for a number of samples. All the measurements were performed on square samples rather than the conventional clover-leaf pattern, except for specimen MG59 which was measured for both square and clover-leaf shapes. The mobility data presented here are therefore approximately 10-15% lower than the actual values. The clover-leaf pattern was formed by photolithography techniques and chemical etching. The etch solution used was H_2O:HNO_3:HCl (1:1:1) with an etch rate of 0.7μm/min. This particular etch was adequate for thin samples having thicknesses less than 2um. For thicker samples, however, the etch was found to be detrimental to the integrity of the epilayer as evident from the undercutting of the sample. A good wet etch having reasonable etch rate which does not undercut has still to be found for InP. The sand blasting techniques for forming the Hall pattern is therefore preferred in InP.

The mobility, carrier concentration and compensation ratio at room temperature and 77K are shown in table

5.1. The mobility value at 300K it ranges from 3,000 to ~5,000 $cm^{-2}V^{-1}s^{-1}$ while at 77K ranges from 10,000 to ~47,000 $cm^{-2}V^{-1}s^{-1}$. The compensation is calculated at liquid nitrogen temperature according to reference [5.13]. The mobility as a function of carrier concentration at 300K and 77K have been plotted and shown in figure 5.4(a) and 5.4(b) respectively. A value for the hall scattering factor r_H of 1.25 has been used for the data at 300K while r_H=1 was used at 77K [5.14]. The solid lines shown in figure 5.4 (a) and (b) are the theoretical values as given in reference [5.13]. An average compensation ratio of 0.6 and 0.4 are deduced for 300K and 77K respectively, which are comparable to that found for InP grown by solid sources.

5.4.1 Mobility versus temperature

The temperature behaviour of the Hall mobility has been measured for samples MG59, MG70, MG76, MG78 and MG84. The results are shown in figure 5.5. Sample MG78 exhibits a maximum mobility peak of 46,0000 $cm^2V^{-1}s^{-1}$ at 60K. The peak position shifts to a higher temperature as the compensation of the material increases, as can be seen for MG70, the most heavily compensated sample. The temperature behaviour of the mobility can be explained by considering the various scattering processes mentioned in chapter 2. In the high temperature regime, polar optical phonon scattering is the dominant mechanism, while at low temperatures, ionised impurity scattering becomes important. It is seen that the mobility curves follows approximately a T^{-2} power law in high temperatures (150-400K), typical of lattice phonon scattering as has been shown by Glicksman and Weiser [5.15]. Conversely, the mobility at low temperatures is

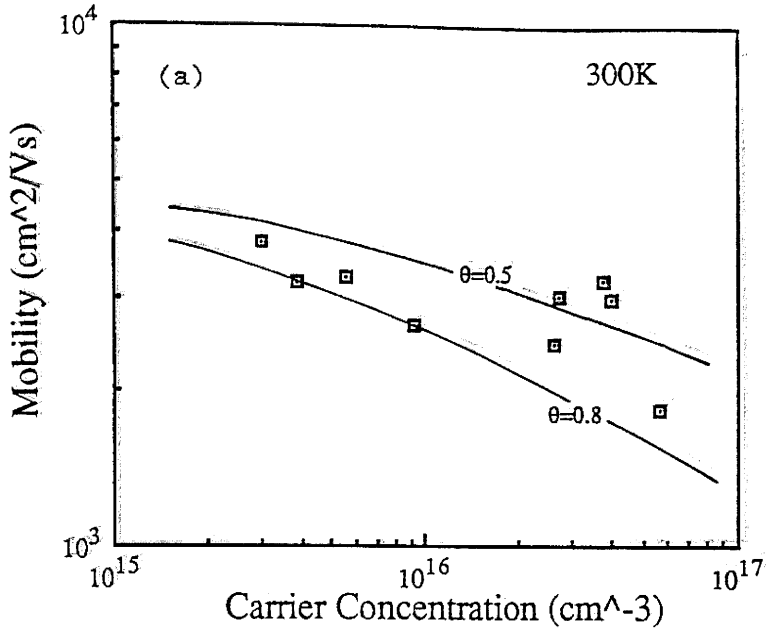

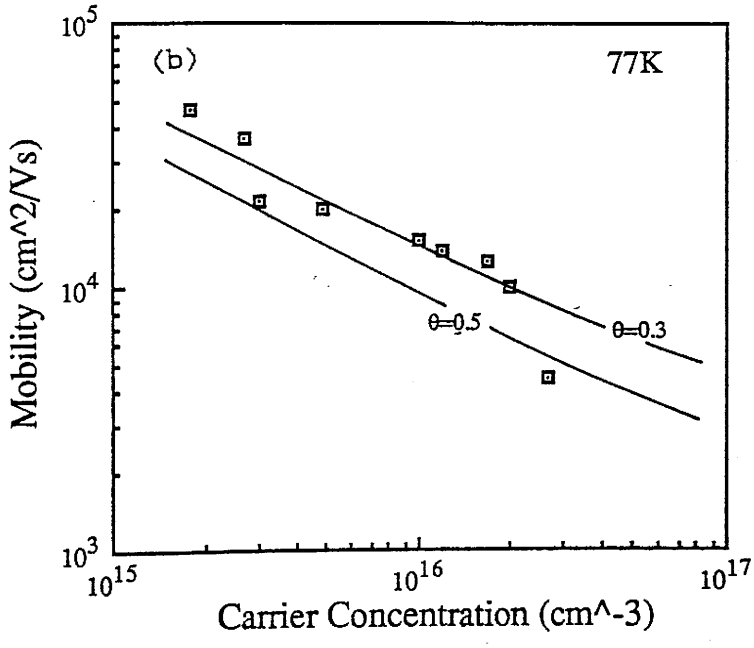

Figure 5.4 Dependence of the mobility on the free-carrier concentration at (a) 300K and (b) 77K.

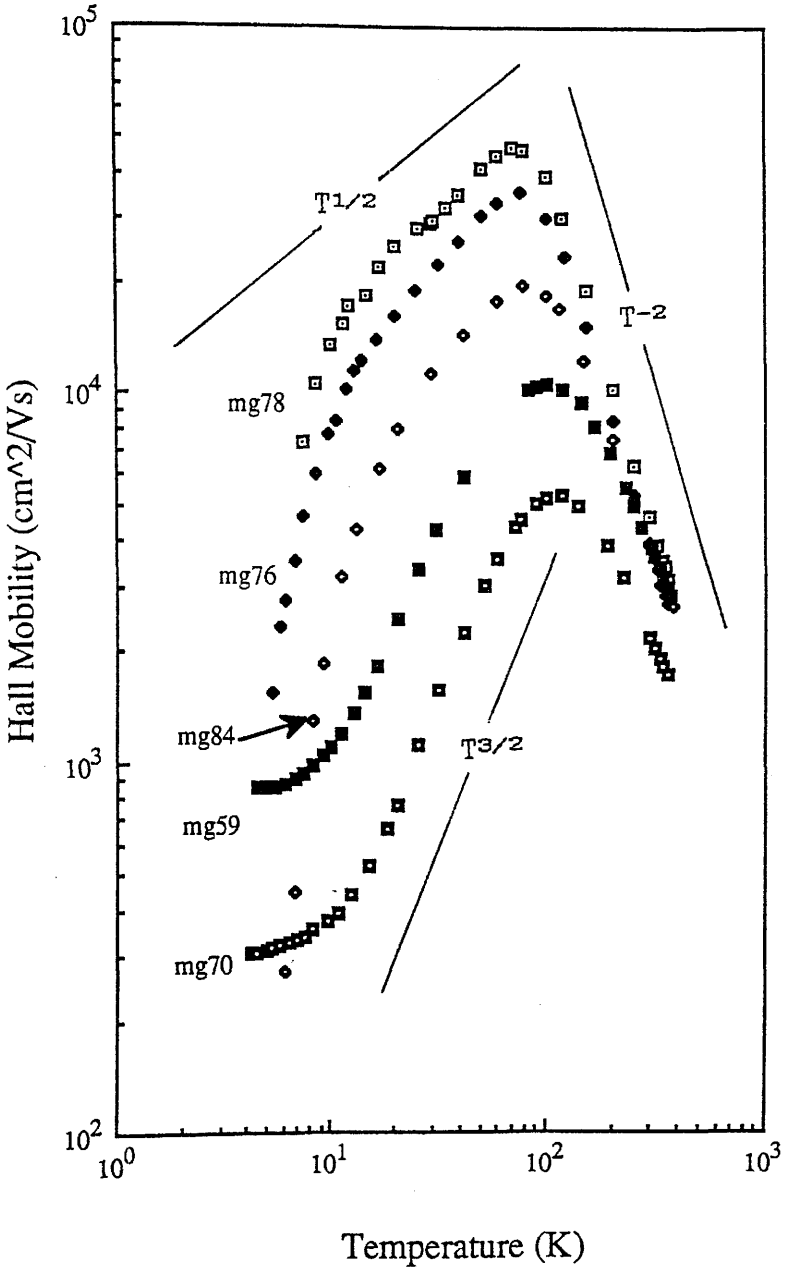

Figure 5.5 The Hall mobility as a function of temperature in the range of 4-350K.

controlled predominantly by ionised impurity scattering and is proportional to $T^{3/2}$. The more compensated materials follow such power law closely except at temperatures below ~10K. On the other hand, the mobility behaviour for the purer samples appears to have a $T^{1/2}$ variation, consistent with a lower compensation. At temperatures below 10K, the mobility for samples MG59 and MG70 becomes essentially temperature independent, signifying the dominant role played by conduction via impurity bands which will be discussed in more details in section 5.4.3.

5.4.2 Carrier concentration versus temperature

The carrier concentration as a function of reciprocal temperature for samples MG78 and MG84 is shown in figure 5.6. The most prominent feature in these curves is a minimum at ~10K for MG84, and at about 50K for MG59 & MG70 (not shown in the figure). At first sight, it is tempting to explain such behaviour with a change in the Hall scattering factor r_H as a function of temperature since $n=r_H/(qR_H)$. However, r_H has been calculated to be very close to unity at temperatures below 100K [5.14]. The characteristic dip in the carrier concentration is believed to be associated with impurity band conduction which will be discussed in the next section. For the present, it is sufficient to note that samples grown with solid indium show strong impurity band conduction while layers which were grown with only gaseous sources do not.

Substantial carrier freeze out occurs as the temperature is lowered. It is very pronounced for the samples grown with gaseous sources (MG84, MG76 and MG78). The activation energy of the shallow donors involved may be deduced from the low temperature

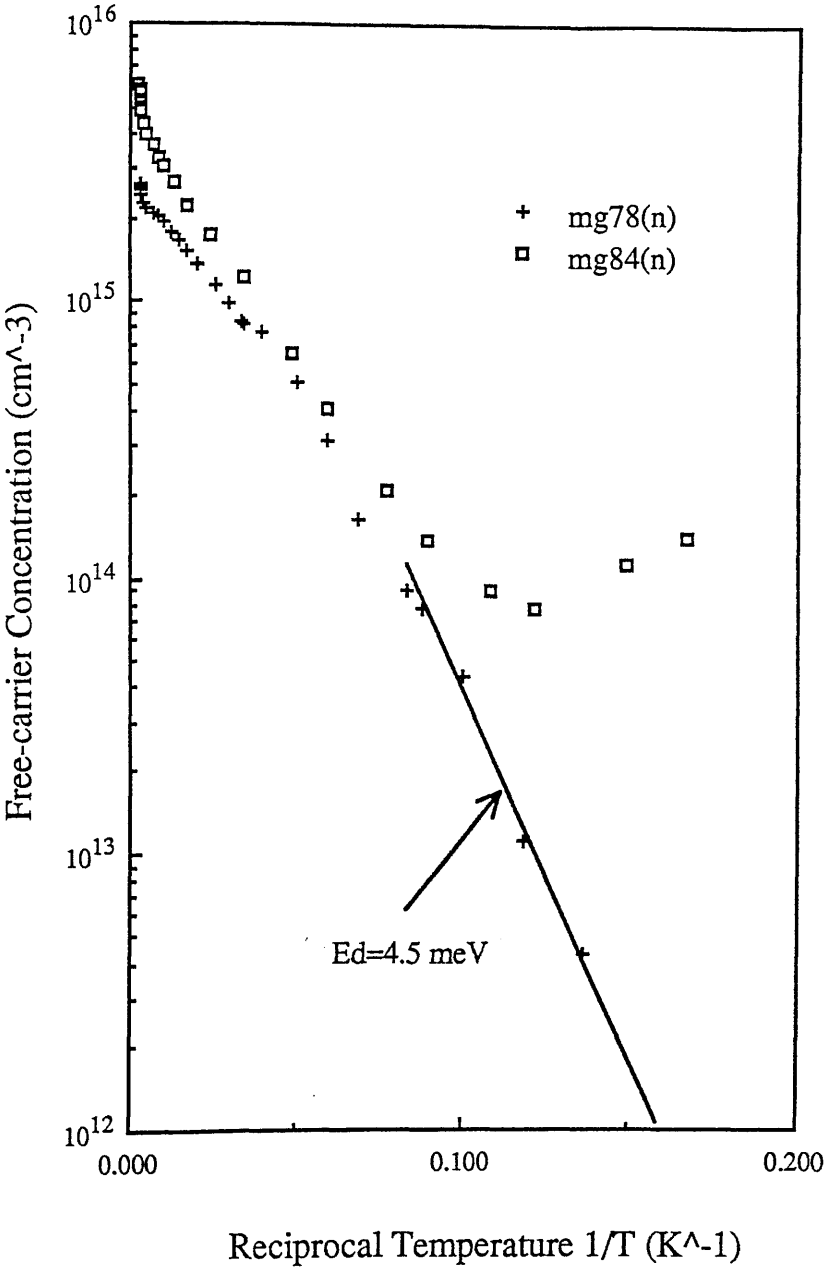

Figure 5.6 Dependence of the carrier concentration on the inverse of temperature.

region of the graph by assuming that the concentration of the carriers is proportional to $\exp\{-E_d/k_BT\}$. Table 5.2 lists the results obtained together with the values calculated using the expression $E_d=7.2\{1-3x10^{-6}(N_D-N_A)\}$ as given by Leloup [5.16]. Good agreement is seen between our results and that deduced using Leloup's expression, in particular for sample MG78. The values of E_d for samples MG84 and MG76 are approximately 1.2meV lower than predicted by Leloup, which is most likely caused by the presence of impurity band conduction. The impurity band conduction is so dominant (indicated by the dip in the carrier concentration at about 50K) that E_d could not be estimated for MG70 and MG59.

Another method of estimating E_d is to curve fit the experimental results of n(T) using the expression

$$\frac{n(T)[n(T)+N_A]}{N_D-N_A-n(T)} = gN_c \exp(-E_d/k_BT) \quad \ldots\ldots\ldots\ldots\ldots\ldots (5.1)$$

where N_c is the effective density of states in the conduction band and is given by $N_c=2[(2\pi m^*k_BT)/h^2]^{3/2}$ and g is the degeneracy factor.

Using g=1/2 and m*=0.077, the experimental results for MG78 has been fitted by varying the three input parameters N_D, N_A and E_d (see figure 5.7). It is found that the best fit is obtained for $N_D=2x10^{15}cm^{-3}$, $N_A=2x10^{14}cm^{-3}$ and $E_d=4.5$meV, which agrees well with the values previously deduced.

However the accuracy of the calculated value of E_d is such that it is not possible to discriminate between the different shallow donors e.g. S, Si, Se and Te. In spite of this, S and/or Si are expected to be present in the MOMBE samples since these two impurities are constantly seen in fairly high concentrations in InP grown by other techniques. SIMS and CV measurements which were undertaken to establish whether these

Table 5.2 The activation energy E_d of the shallow impurities deduced from the low temperature portion of the (N_D-N_A) versus temperature graph. Theoretical results of E_d calculated from reference 5.15 are included for comparison.

sample No.	E_d(meV)	E_d(meV) calculated from reference [5.15]
MG84	3.4	4.6
MG76	3.2	4.4
MG78	4.5	4.7
MG70	-	2.3
MG59	-	1.9

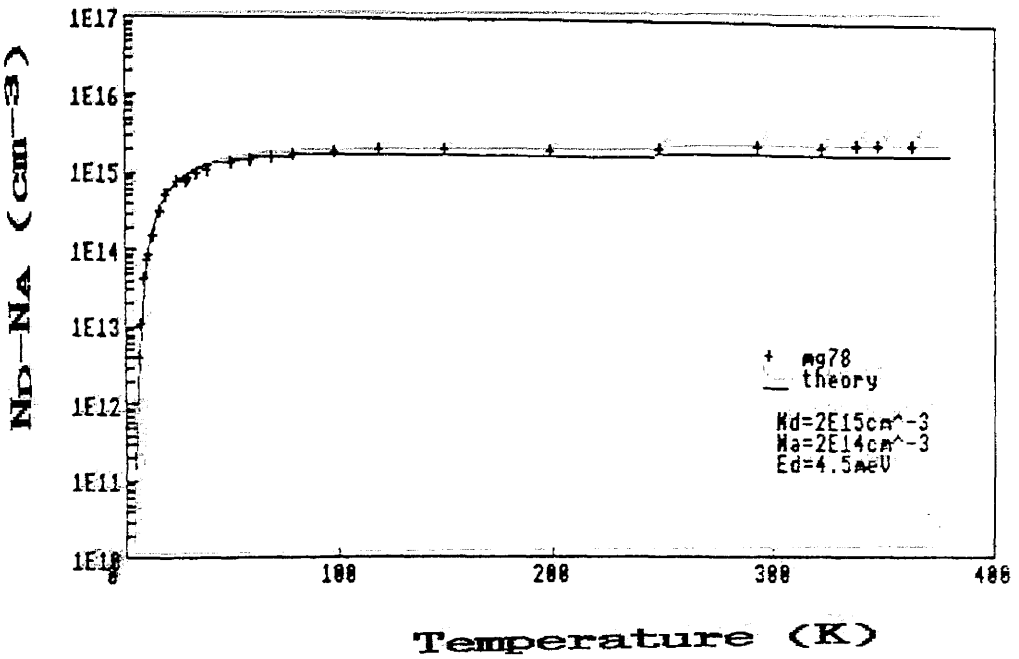

Figure 5.7 A theoretical fit to the temperature dependence of the carrier concentration for MG78.

impurities were incorporated into the samples are discussed in section 5.5.

5.4.3 Impurity band conduction

The electrical properties of InP at low temperatures are dominated by impurity band conduction. A typical temperature at which impurity band conduction becomes important is below ~20K for $(N_D-N_A)=5x10^{15}cm^{-3}$. However, this critical temperature depends strongly on both the impurity concentration and compensation ratio [5.17]. The characteristic feature of the presence of impurity band conduction is a distinct maximum in $\ln(R_H)$ versus T graph, see figure 5.8. A similar behaviour was first observed in Ge by Hung in 1950 who associated it with conduction involving two bands, namely the conduction band and the impurity band [5.18]. The problem associated with the presence of impurity band conduction is the introduction of uncertainties in the estimation of E_d using the n(T) versus T graph. The critical temperature T_c at which the maximum occurs in the Hall coefficient plot varies linearly as a function of $N_D^{1/3}\theta^{2/3}$ [5.17], where θ is defined as N_A/N_D. The experimental data have been plotted and found to confirm such a relationship as shown in figure 5.9. Included in the figure are the experimental data given in references [5.19,5.20] for comparison. This indicates that conduction occurs through a hopping process between impurity centers. From figure 5.9, it is possible to deduce T_c as a function of the free carrier concentration (N_D-N_A) for a given θ. The result is shown in figure 5.10 in which the compensation ratios of 0.3, 0.6 and 0.9 have been considered. For an (N_D-N_A) of $5x10^{15}cm^{-3}$ and θ of 0.3, T_c occurs at ~10K.

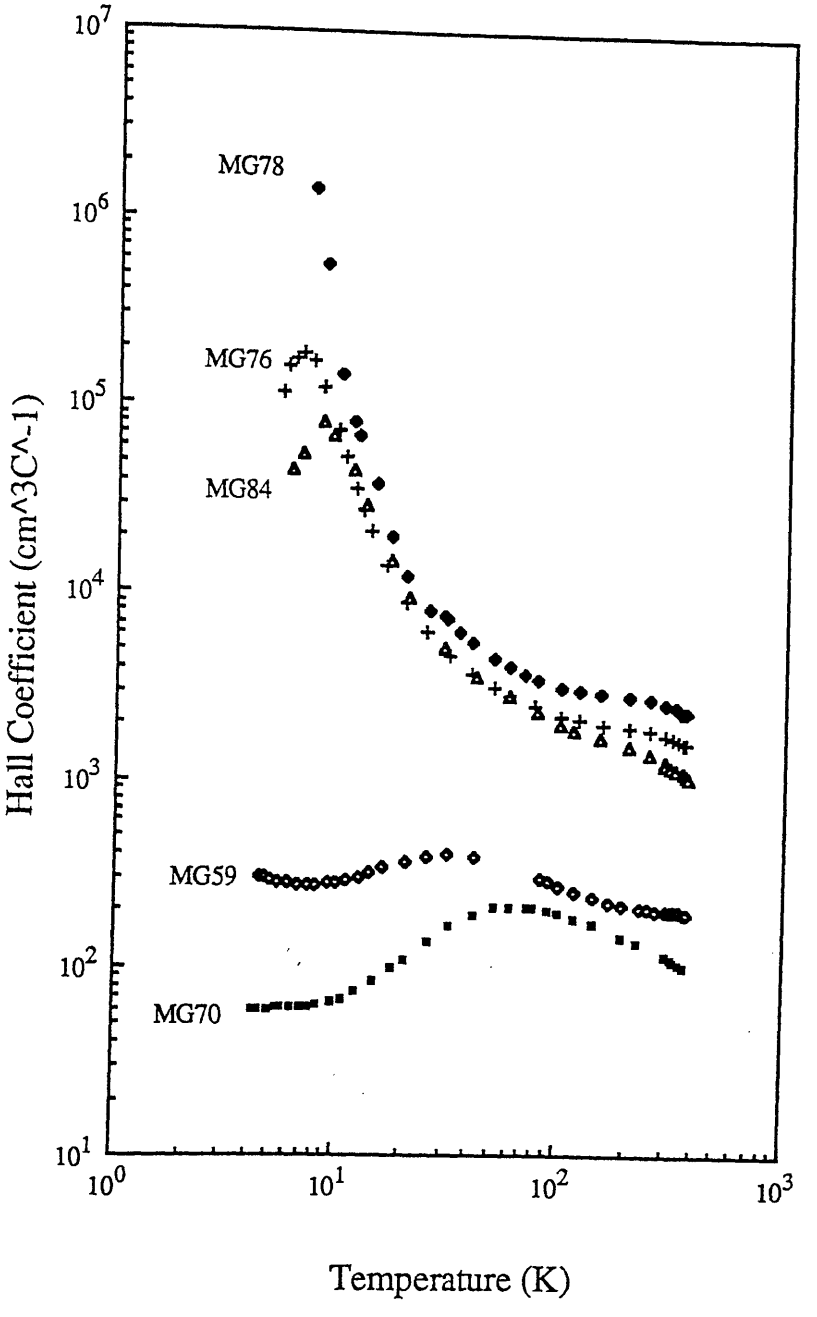

Figure 5.8 The Hall coefficient as a function of temperature. The maximum in the graph for each sample is associated with impurity band conduction.

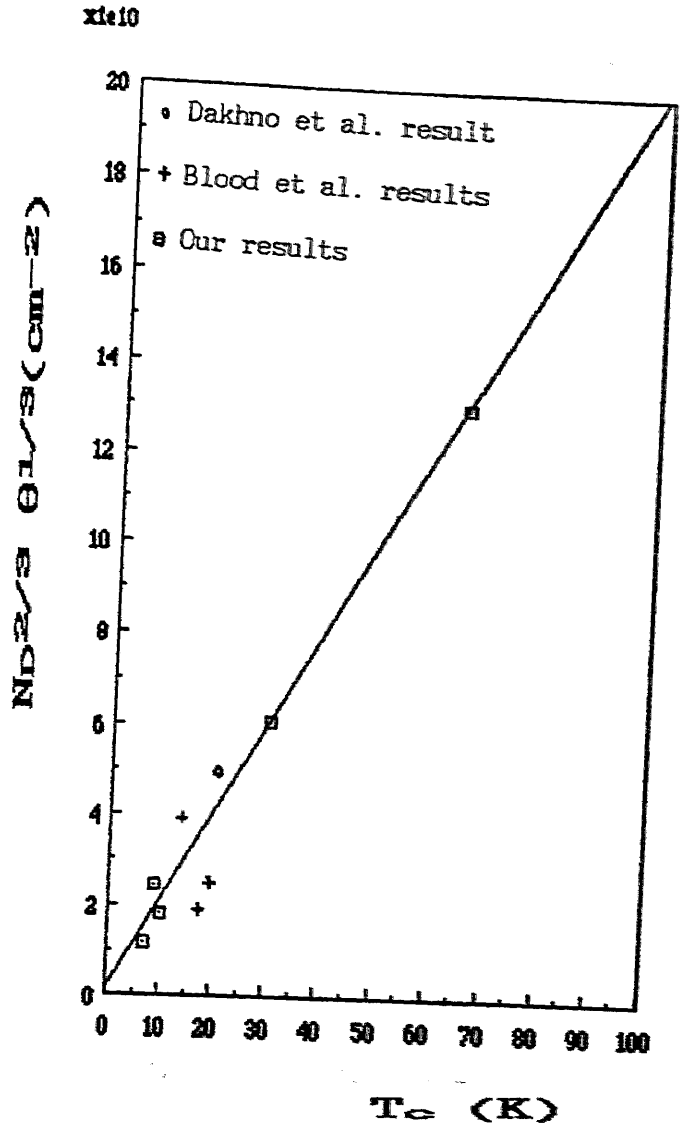

Figure 5.9 The critical temperature T_c at which impurity band conduction becomes important plotted against the product of the carrier concentration and compensation. Included in the figure are some of the experimental results found in the literature.

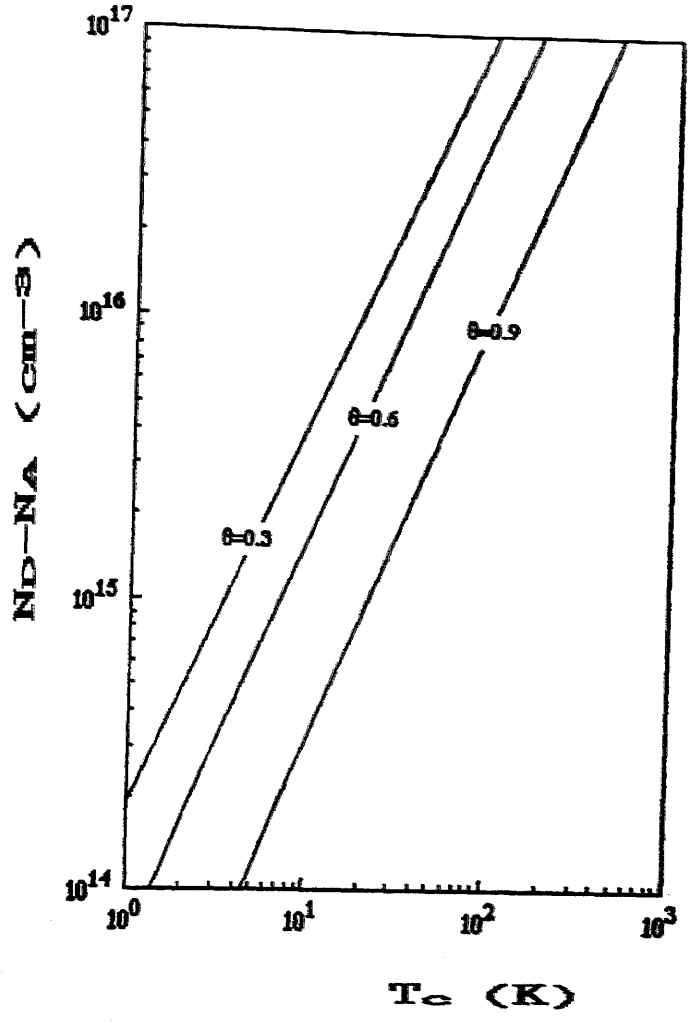

Figure 5.10 Free-carrier concentration as a function of T_e at compensations of 0.3, 0.6 and 0.9 deduced from the graph in figure 5.9.

5.5 Secondary Ion Mass Spectroscopy (SIMS) Measurements

In section 5.4.2, although the activation energy of the shallow impurities was estimated, the identity of the impurities in the samples could not be determined. It is known that sulphur and/or silicon are the two shallow donors dominant in InP grown by VPE [5.21], LPE [5.22] and MBE [5.23]. To determine whether these impurities are present in epitaxial InP grown by gas sources, two structures were designed. The first sample was grown by varying the flow rate of phosphine in steps of 1cc/min while keeping all other growth parameters constant (T_s at 600°C indicated, growth rate at 0.8μm/hr and the temperature of the cracker T_{crk} at 1000° C). The measured SIMS spectrum for this sample is shown in figure 5.11. It is seen that the concentration of Si (mass 28/30) is constant throughout the epilayer. On the other hand, the concentration of S (mass 34) decreases as the flow rate of phosphine decreases. This suggests that sulphur originates from the phosphine, either as a molecule or a compound.

The second sample was grown by varying the substrate temperature and the temperature of the cracker while the other growth parameters were kept constant (phosphine flow rate=3cc/mim, growth rate=0.85μm/hr). The substrate temperature was varied from 550 to 625°C and the temperature of the cracker was kept at 950°C except for the outermost layer which was grown with T_{crk} at 1000°C. The SIMS spectrum of Si and S levels found in the sample is shown in figure 5.12. The concentration of sulphur is seen to decrease from ~$1x10^{17}cm^{-3}$ to ~$5x10^{16}cm^{-3}$ as T_s was changed from 550° to 625°C, while the level of silicon remained essentially the same at ~$8x10^{16}cm^{-3}$. It should be noted that the substrate temperature is indicated values only and the

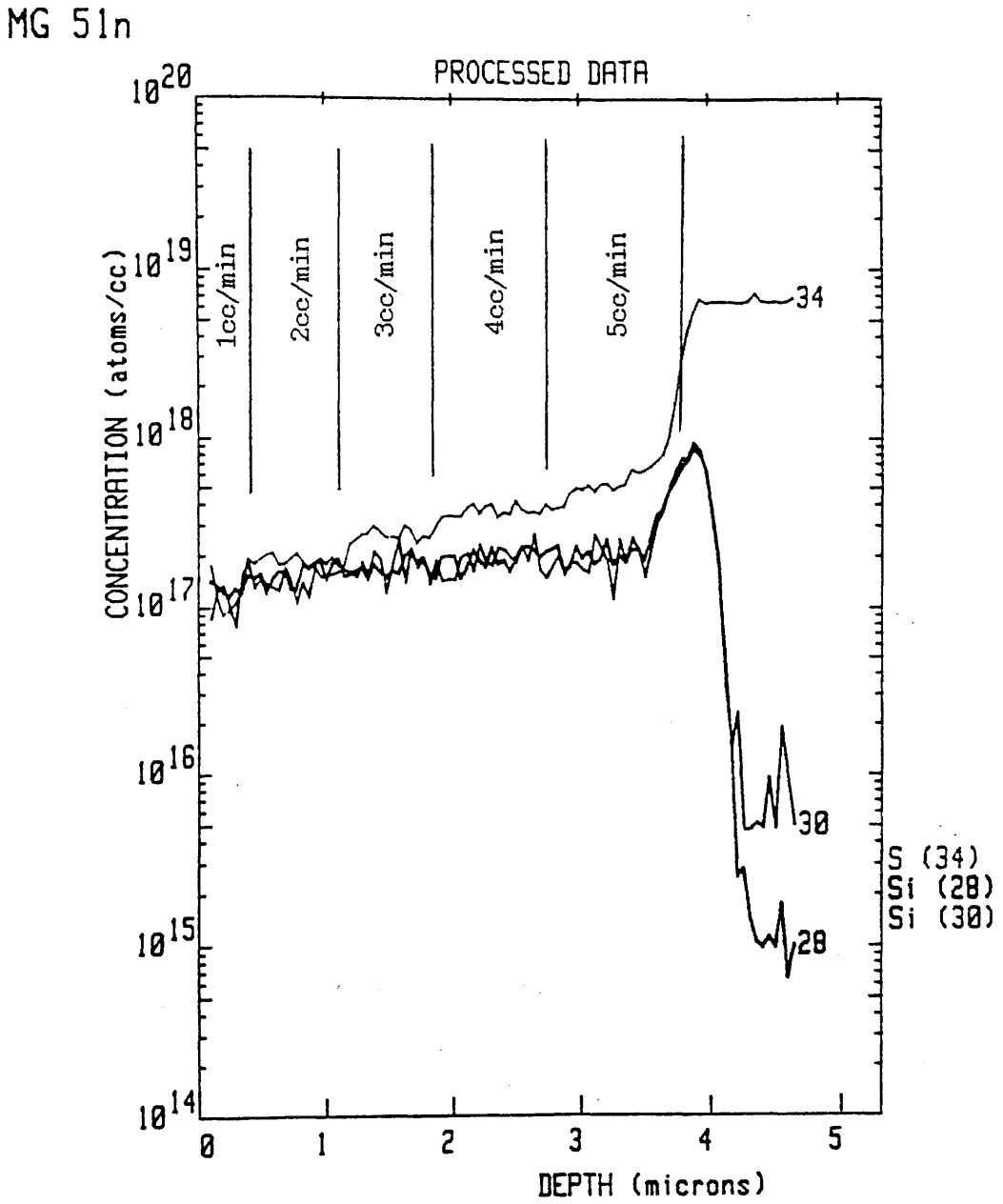

Figure 5.11 SIMS plot of the sulphur and silicon levels as a function of the phosphine flow rate for an InP grown with gas sources.

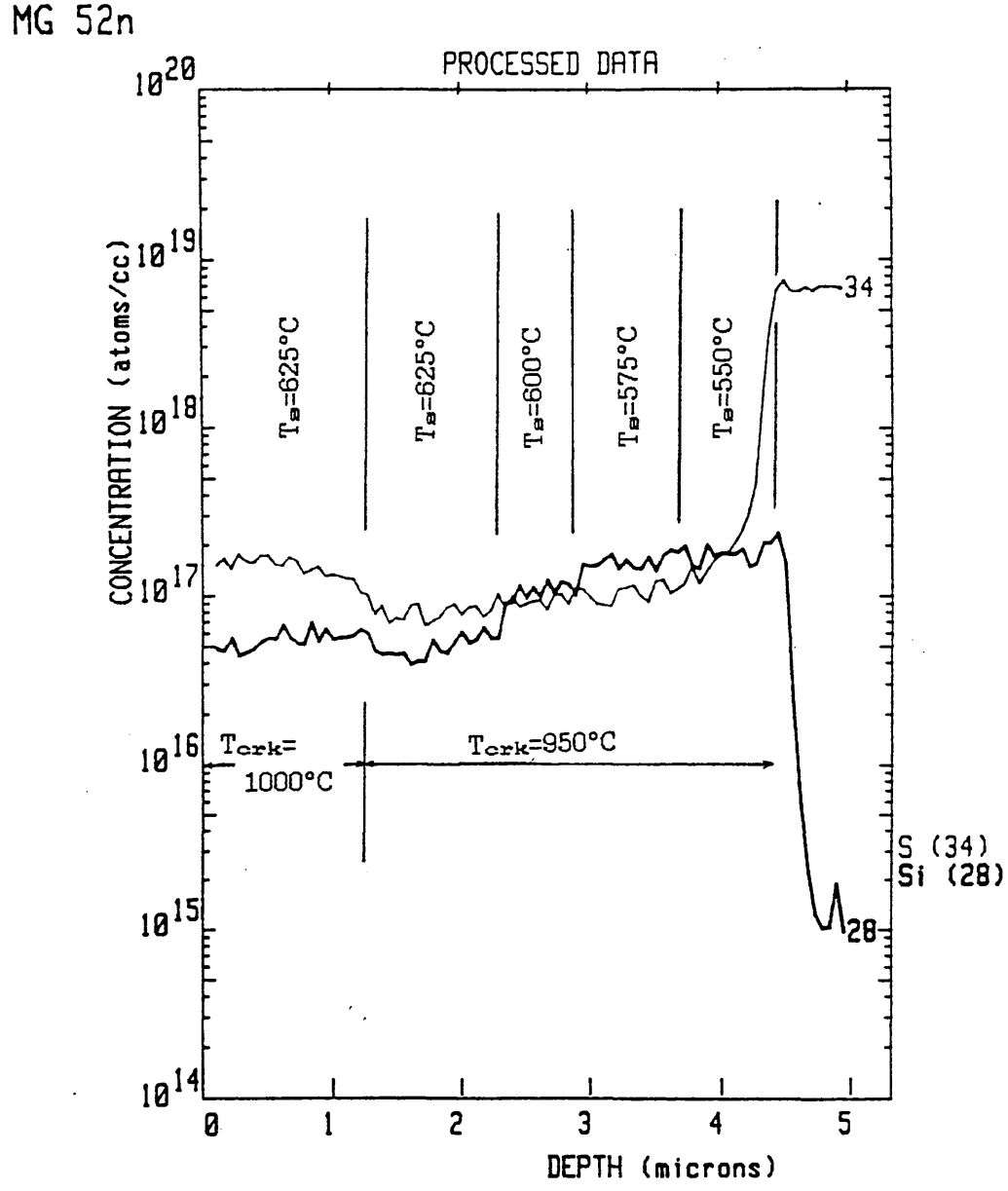

Figure 5.12 SIMS plot of the sulphur and silicon levels for an InP grown with gas sources at different substrate temperatures and cracker temperatures.

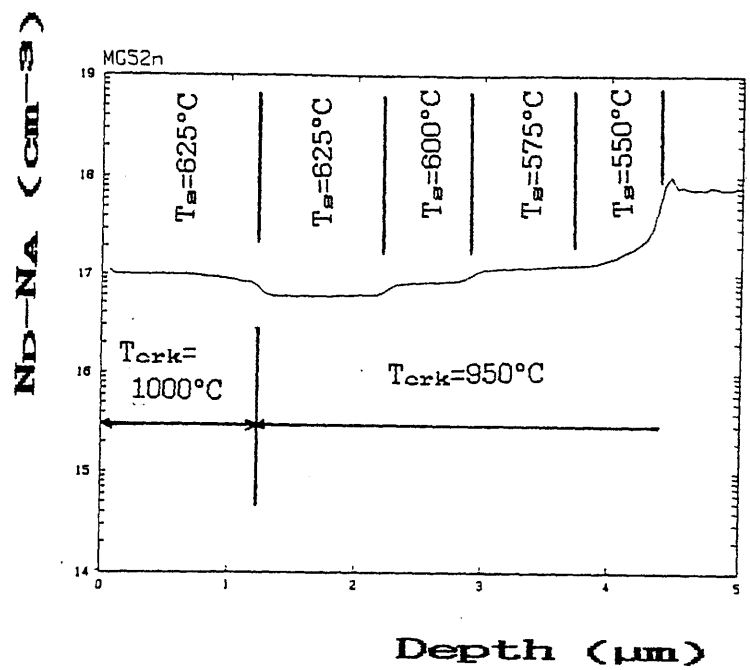

Figure 5.13 C-V profile for the InP sample with the SIMS spectrum shown in figure 5.12. The free-carrier concentration agrees well with the sum of sulphur and silicon concentrations found in figure 5.12, indicating these two impurities are electrical active species in the semiconductor.

Table 5.3 The deep traps observed in the MOMBE samples with their corresponding activation energies and concentrations. These traps are comparable to those observed in InP grown by other techniques, indicating there is no unique trap associated with the MOMBE growth process. Note that the total concentration of traps are significantly lower in the samples grown with only gas sources.

	E_a(meV)	MG59	MG70	MG76	MG78	Trap Comparison
ET1	670	-	-	3.9×10^{13}	1×10^{13}	E2[a], MBE2[b]
ET2	550	8×10^{13}	1.9×10^{14}	-	-	MBE3[b], V[c]
ET3	460	-	-	3.9×10^{13}	1×10^{13}	E4[a], MBE4[b]
ET4	320	1×10^{14}	1.3×10^{14}	-	-	E6[a], MBE7[b]
ET5	290	8×10^{13}	1.5×10^{14}	-	1×10^{13}	E7[a], MBE8[b], D2[d] IE4[e]
ET6	210	-	-	-	1.5×10^{13}	E8[a], MBE9[b], D1[d]
ET7	160	-	-	-	9.9×10^{12}	MBE10[b]
ET8	130	-	-	-	6×10^{12}	E9[a], MBE11[b], Y[c]
Total		2.6×10^{14}	6×10^{14}	7.8×10^{13}	6.1×10^{13}	
C-V		2×10^{16}	2×10^{16}	2×10^{15}	2×10^{15}	

References

(a) D.J. Nicholas, D. Allsopp, B. Hamilton, A.R. Peaker and S.J. Bass, J. Gryst. Growth, 68, 326 (1984).
(b) D. Halliday, PhD thesis, University of Nottingham (1987).
(c) P.R. Tapster, J. Phys., C16, 4173 (1983).
(d) H. Asahi, Y. Kawamura, M. Ikeda and H. Okamoto, J. Appl. Phys., 52, 2852 (1981).
(e) G. Bremond, A. Nouailhat and Guillot, Inst. Phys. Conf. Ser. No. 63, 239 (1981).

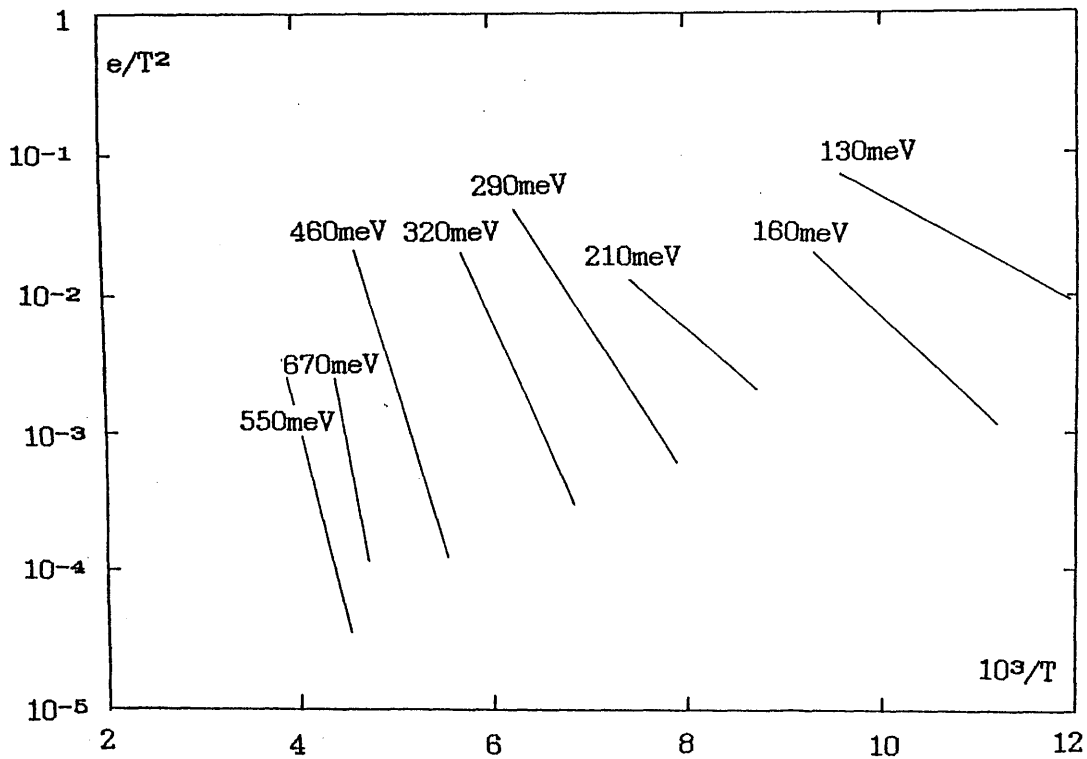

Figure 5.14 An Arrhenius plot of the traps detected in the MOMBE materials.

be very promising for producing device materials.

5.7 Conclusion

Good optical and electrical characteristics have been measured for InP epitaxial layers grown by gaseous source MBE. The best sample (MG78) has a 4.2K (D°-X) PL linewidth of 3meV and a peak mobility of 46,000$cm^2V^{-1}s^{-1}$ with a compensation ratio of 0.11. The mobility of this layer is much lower (~ factor of 2) than that reported by Kawaguchi et al. [5.5]. A possible reason for this is because the layer was amongst the first produced in the MOMBE system. DLTS measurements of the samples reveal the total concentration of electron traps to be low (in the mid $10^{13}cm^{-3}$ range), which is about an order of magnitude lower than the specimens grown with solid sources. The detected electron traps have all been observed by other workers in InP grown by other techniques and there are no unique traps that can be associated with the MOMBE growth process.

Low temperature PL (4.2K) as a function of both the excitation intensity and the sample temperature performed on the specimens has identified the presence of the shallow acceptor impurities Mg and C, their activation energies being 41 and 45meV respectively. However, the concentration of carbon is relatively low compared to the concentration of magnesium. Based on the results in this chapter, it may be concluded that Mg is a universal inadvertent shallow acceptors in InP. The origin of Mg is still not known although it may come from the group V source.

Hall effect versus temperature measurements on a number of the MOMBE samples reveal the existence of impurity band conduction at low temperatures, which

appears as a maximum in the Hall coefficient R_H versus temperature graph. The temperature at which R_H is a maximum, T_c, has been found to be proportional to $N_D^{1/3}\theta^{2/3}$. The presence of impurity band conduction results in an under-estimate of the shallow donor activation energy E_d deduced from the temperature dependence of free-carrier concentration graph. For a sample in which impurity band conduction was absent (MG78), E_d was found to be 4.5meV for a room temperature $(N_D-N_A)=2.4\times10^{15}cm^{-3}$.

The dominant shallow donor impurities in the MOMBE InP are sulphur and silicon as is the case with solid source InP. These two inadvertent contaminants are electrically active in the epitaxial layers. The origin of sulphur is believed to be associated with the phosphine gas source. On the other hand, the likely origin of silicon is from the cracker (since Si has a high vapour pressure) or from the phosphine in the form of a silicon compound which could either be dissociated at the cracker or at the growth surface.

5.8 References

[5.1] M.B. Panish, J. Electrochem. Soc.: Solid State Science & Technology, 127, 2729 (1980).

[5.2] W.T. Tsang, Appl. Phy. Lett., 45, 1234 (1984).

[5.3] A.R. Calawa, Appl. Phys. Lett., 33, 1020 (1978).

[5.4] A.R. Calawa, Appl. Phys. Lett., 38, 701 (1981).

[5.5] Y. Kawaguchi, H. Asahi and H. Nagai, Inst. Phys. Conf. Ser. No. 79: Chapter 2. GaAs and Related Compounds, page 79 (1985).

[5.6] M.A. Di Forte-Poisson, C. Brylinski and J.P. Duchemin, Appl. Phys. Lett., 46, 476 (1985).

[5.7] L.L. Taylor and D.A. Anderson, J. Cryst. Growth, 64, 55 (1983).

[5.8] J.S. Roberts, P.A. Claxton, J.P.R. David and J.H. Marsh, Electron. Lett., 22, 506 (1986).

[5.9] D.A. Andrews, S.T. Davey, C.G. Tuppen, B. Wakefield and G.J. Davies, Appl. Phys. Lett., 52, 816 (1988).

[5.10] B.J. Skromme, G.E. Stillman, J.D. Oberstar and S.S. Chan, J. Electron. Mater., 13, 463 (1984).

[5.11] B.J. Skromme, G.E. Stillman, J.D. Oberstar and S.S. Chan, Appl. Phys. Lett., 44, 319 (1984).

[5.12] K.A. Prior, G.J.Davies and R. Heckingbottom, J. Crystal Growth, 66, 55 (1984).

[5.13] W. Walukiewicz, J. Appl. Phys., 51, 2659 (1980).

[5.14] D.L. Rode, Phys. Stat. Sol. (b), 55, 687 (1973).

[5.15] M. Glicksman and K. Weiser, J. Electrochem Soc., 105, 728 (1958).

[5.16] J. Leloup, H. Djerassi, J.H. Albany and J.B. Mullin, J. Appl. Phys., 49, 3359 (1978).

[5.17] B.I. Shklovsky and A.L. Efros, "Electronic properties of doped semiconductors", Springer Series in Solid State Sciences, Vol.45, (1984).

[5.18] C.S. Hung, Phys. Rev., 79, 727 (1950).

[5.19] A.N. Dakhno, O.V. Emalyanenko, T.S. Lagunova and S.P. Staroseltseva, Sov. Phys. Semicond. 13, 1039 (1979).

[5.20] P. Blood and J.W. Orton, J. Phys. C: solid State Phys., 7, 893 (1974).

[5.21] P.J. Dean, M.S. Skolnick and L.L. Taylor, J. Appl. Phys., 55, 957 (1984).

[5.22] M.S. Skolnick, P.J. Dean, S.H. Groves and K. Kuphal, Appl. Phys. Lett., 45, 962 (1984).

C.R. Stanley and D.E. Sykes

[5.23] T. Martin, C.R. Stanley and A. Iliadis, Appl. Phys. Lett., 46, 994 (1985).

[5.24] S. Misawa, H. Okumura and S. Yoshida, J. J. Appl. Phys., 26, 1088 (1987).

[5.25] N. Putz, H. Heinecke, M. Heyen and P. Balk, J. Cryst. Growth, 74, 292 (1986).

CHAPTER 6

Electrical and Optical Properties of $Al_{0.48}In_{0.52}As$ grown by MBE

6.1 Introduction

The ternary alloy $Al_{1-x}In_xAs$ is technologically important in the area of optoelectronic devices. It can be grown lattice matched onto InP and $In_{0.47}Ga_{0.53}As$ with x=0.52, the room temperature energy band gap of $Al_{0.48}In_{0.52}$ being 1.46eV [6.1]. The conduction band discontinuity for a InGaAs/AlInAs heterojunction is ~0.5eV [6.2] compared with only 0.23eV for the InGaAs/InP heterojunction. The former system, therefore, provides a better confinement of carriers and is more suited for quantum well structures. To date, many structures have been fabricated using InGaAs/AlInAs, e.g. double heterostructure lasers emitting at 1.55μm [6.3], modulation doped structures (HEMTs) with 77K mobilities >170,000 $cm^2V^{-1}s^{-1}$ [6.4] and rib optical waveguides [6.5]. Furthermore, AlInAs can also be used as a buffer layer and Schottky-assist for FETs in InGaAs [6.6-6.7].

So far, AlInAs has been grown mainly by MBE. Growth using LPE is difficult because of the large difference in the distribution coefficients between aluminium and indium [6.8], leading to difficulties in controlling the composition of the alloy. Growth of AlInAs is particularly suitable by MBE since it involves only one group V source (type I alloy) and therefore the composition of the alloy is simply controlled by the relative proportions of the incident Al and In fluxes. Nevertheless, many problems still remains which have rendered AlInAs a less well understood material system than InGaAs or AlGaAs. For instance, the existence of

a large difference in the thermal stability between InAs and AlAs means that the upper limit to the growth temperature is governed by the least stable binary component (InAs in this case). The temperature used for growing AlInAs is normally below 600°C in order to avoid significant loss of indium from the growth surface. At these temperatures, however, involatile aluminium oxide(s) is formed on the growth front via interaction with oxygenated species in the growth chamber such as CO and CO_2 [6.9], resulting in a large quantity of unwanted deep level impurities being incorporated into the epitaxial layer. On the other hand, it is known that the mobility of aluminium increases with temperature which in turn would be expected to reduce the concentration of traps related to native defects such as vacancies/complex. A compromise must therefore be made in choosing the appropriate conditions when growing AlInAs to achieve the desired layer quality.

In a series of papers, Cheng et al. [6.10-6.12] have demonstrated successfully the doping of AlInAs using Si and Sn for n-type and Be for p-type layers. Free-carrier concentrations of $\geq 10^{19} cm^{-3}$ were achieved for both n-type and p-type dopants. Thus, doping does not appear to be a problem in AlInAs grown by MBE. So far, the growth and properties of undoped AlInAs have not been addressed in a systematic fashion. In this chapter, the results of a series of study of AlInAs epitaxial layers grown by MBE at BTRL under different conditions are presented. Various characterisation techniques have been employed to explored the relationship between the properties of the grown layers and their growth conditions. Although this chapter is concerned with undoped AlInAs, some of the samples were lightly doped with Si to avoid the layer becoming semi-insulating.

6.2 Growth Details

Both Fe- and S-doped InP substrates were used in the growth. They were purchased from different manufacturers including MCP, Sumitomo, ICI and Nippon. The specifications for the substrates from each manufacturer were identical. The substrates, two inches in diameter, were firstly subjected to a chemo-mechanical polish using a bromine-methanol solution, to produce a damage-free surface. These polished wafers were then place in a storage unit for subsequent growth. Before the substrate was introduced into the MBE system, it was degreased, cleaned and etched. The procedure used was as follows;

a) degrease in organic solvent; acetone followed by trichloroethylene and finally propanol,
b) leave in conc. H_2SO_4 for 3 to 5 minutes, and wash with DI water,
c) leave in conc. HNO_3 for about 10 minutes at room temperature to form a thin oxide layer, and wash with DI water,
d) place in 40% HF for 30 seconds to remove the oxide, and finally
e) rinse with DI water and spin dry.

Directly after the 'wet' chemical etching process, the substrate was introduced into the fast entry loadlock in which the pressure was then reduced by a rotary pump. The substrate was next transferred into the preparation chamber where it was heated to about 100°C for 30 minutes to remove any residual moisture and volatile species remaining on the surface. Finally, the substrate was transported into the main UHV growth chamber. The background pressure in the growth chamber, being dominated by As_4 molecules, was usually about 10^{-6} mbar with the arsenic cell hot and

shutter closed. At this stage, the substrate has a very thin surface oxide (~ a few monolayers) and a weak arsenic stabilised (2x4) RHEED surface reconstruction was quickly observed on heating when the substrate was mounted using an indium-less sample holder. However, if the substrate was mounted onto the holder with metallic indium then the As-(2x4) RHEED pattern required a longer time to be observed, indicating the presence of a thicker layer of oxide. The arsenic background flux was found to be sufficient to stabilise the substrate in the thermal cleaning process during which the substrate was heated to 500°C; the time taken for the oxide to desorb was typically 1-2 minutes (complete removal of the oxide was indicated by the RHEED pattern changing from spotty to a sharp As-(2x4) pattern). The epitaxial layers described in this chapter were grown with indium mounted substrates.

The MBE system used here has an arsenic Knudsen cell with a source capacity of 1kg. This would last for approximately six months of normal, continuous usage. Operating temperatures of 300-350°C were used to produce significant As_4 flux which was dissociated to an As_2 flux in the cracking zone (T_{crk}=800-900°C) situated in front of the Knudsen cell. The arsenic charge from various manufacturer was found not to affect the overall quality of the grown layers, but marked variations between batches from the same manufacturer were observed. This is in direct contrast to the results found by Martin et al. for phosphorus [5.13]. The group III fluxes (Al,In and Ga) are generated by standard Knudsen cells, each with a volume of 16cc. The Knudsen cell for aluminium was normally kept at an idling temperature of ~800°C to prevent solidification of the aluminium and subsequent fracturing of the pBN crucible.

The epitaxial layers described in this chapter were

grown at substrate temperatures in the range of 500-600°C. At temperatures above 600°C, Davies et al. [6.14] found that a significant amount of indium starts to desorb from the growth surface, causing difficulties in controlling the precise composition and leading to lattice mismatched layers. The loss of indium at high substrate temperatures can be suppressed by an increase in the arsenic overpressure, but this is accompanied by an increase in the free carrier density associated with impurities originated from the arsenic charge [6.15]. However, this is a very weak effect $\sim P(As_4)^{1/4}$ and therefore is not a practical route to the growth of AlInAs at high substrate temperatures. An alternative method to offset the indium loss is to supply an excess of indium flux during growth [6.16]. Scott et al. have used this approach for the ternary alloy InGaAs and produced epitaxial layers with very good electrical and optical characteristics [6.5]. The loss of a substantial amount of indium is undesirable because it would affect the lattice matching between the hetero-junctions. Another factor which affects lattice matching is the use of an incorrect combination of the group III fluxes during growth. The degree of lattice mismatch can be easily detected by X-ray techniques, as will be shown later.

The various AlInAs layers grown in the series with their corresponding substrate temperature, arsenic cell temperature, silicon cell temperature, layer thickness and the morphology are tabulated in table 6.1. The layer thickness is estimated from the growth rate used. All of the epitaxial layers were grown with a thin capping layer of GaAs (~10-50Å) to avoid surface oxidation. The samples were characterised by different techniques including double crystal X-ray diffractometry, low temperature PL, phase contrast microscopy, SEM, Hall effect measurement and DLTS.

Tabel 6.1 The growth parameters used for the growth of AlInAs with their surface morphology and layer thicknesses.

Sample No.	Growth Temp(°C)	Arsenic Cell Temp.(°C)	Silicon Cell Temp.(°C)	Layer Thickness(μm)	Morphology
MV398	520	443	960	2.3	smooth
MV403	530	453	960	2.0	smooth
MV400	540	443	960	2.2	rough
MV402	550	453	960	2.2	rough
MV401	560	443	960	2.3	rough
MV411	580	448	-	1.4	shiny (rough edges)
MV407	580	448	920	1.4	shiny
MV409	580	453	-	1.1	shiny
MV408	580	453	860	1.4	shiny
MV406	580	453	920	1.4	shiny
MV404	580	453	960	2.0	shiny
MV405	600	453	960	1.4	shiny

6.3 Thermodynamic Prediction of Indium Desorption at High Substrate Temperatures

In the MBE growth of AlInAs, the indium atoms evaporate from the growth surface at a faster rate than their aluminium counterparts. This behaviour may be understood by the relative bond strengths of the binaries; In-As (36.0kcal/mol) and Al-As (62.0 kcal/mol), i.e. almost a factor of two difference. When the substrate temperature is sufficiently high, the amount of indium loss from the epitaxial layer can be detected by techniques such as Auger depth profiles [6.17,6.18] and X-ray diffraction (as will be shown in section 6.4.2.1). The temperature at which the onset of indium loss occurs can be estimated thermodynamically using the method described by Heckingbottom for the AlGaAs system [6.19]. Consider the equilibrium reaction path for the growth of InAs:

$$InAs(s) = In(g) + \tfrac{1}{2}As_2(g) \quad \ldots\ldots\ldots\ldots\ldots\ldots (6.1)$$

where the subscripts (s) and (g) correspond to the solid and gas phases respectively.

The equilibrium constant for this equation is then given by

$$K = P(In)\ P(As_2)^{1/2} / a(InAs) \quad \ldots\ldots\ldots\ldots\ldots\ldots (6.2)$$

where P represents pressure, a denotes activity which is unity for pure substance.

One may regard the ternary alloy as a mixture of the two binaries, i.e. $Al_xIn_{1-x}As = xAlAs + (1-x)InAs$. The activity of AlAs is considered to be unity since all the Al condenses for temperatures below 700°C. Thus only the InAs activity is required. It is assumed that a(InAs) is given by its concentration, similar to that for GaAs [6.19], i.e. $a(InAs) = (1-x)$

Thus for x=0.48, and equation (6.2) reduces to

$$K=2.1\,P(In)\,P(As_2)^{1/2} \quad \ldots\ldots\ldots\ldots\ldots\ldots\ldots\ldots (6.3)$$

The value of K is calculated from the experimental data given in reference [6.19], which is found to be given by

$$K = \exp(24.76 - 4.71\times10^{4}/T) \quad \ldots\ldots\ldots\ldots\ldots\ldots (6.4)$$

Using equations 6.3 and 6.4, the equilibrium pressure of indium can therefore be calculated for a particular arsenic pressure. Comparing the computed indium pressure with the actual indium flux supplied yields the amount of indium desorbing from the surface. Figure 6.1 shows the calculated result for two different As_2 overpressures (3×10^{-6} & 1×10^{-5} torr). It is apparent that significant indium loss occurs at temperatures >540°C. A change in the As_2 pressure from 3×10^{-6}torr to 1×10^{-5}torr can be seen to increase the normalised growth rate (corresponding to decrease in the indium desorption rate).

One point needs to be stressed concerning the exact growth temperature at which indium loss becomes substantial. Using sputter Auger profiling on AlInAs, Wood observed a decrease in the indium signal at T_s=560°C [6.18]. On the other hand, Davies et al. reported that indium loss only become significant for T_s>600°C [6.14]. Although the result of Wood et al. is in line with the above thermodynamic prediction, the growth temperatures quoted in existing literature should be regarded cautiously since they vary substantially from one MBE system to another and depend on how the temperature itself is measured.

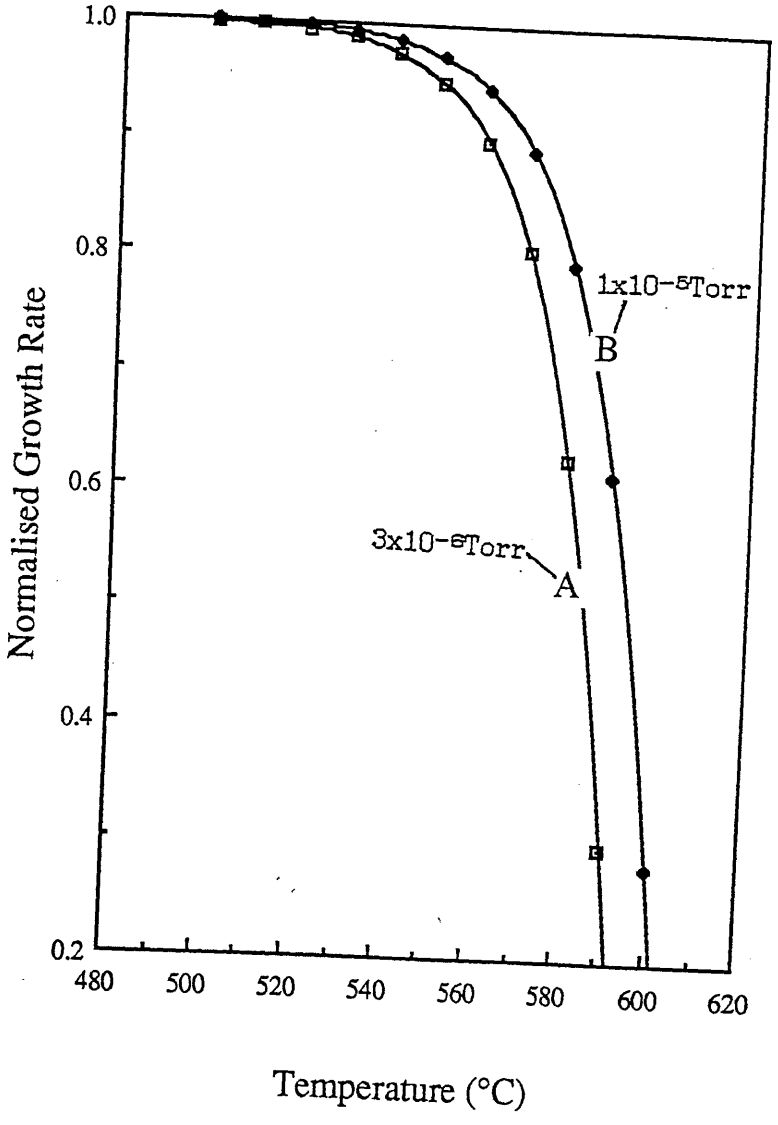

Figure 6.1 The computed normalised growth rate as a function of temperature at an arsenic pressure of $3x10^{-6}$ torr and $1x10^{-5}$ torr.

6.4 Measurement of Lattice Mismatch by X-Ray Techniques

To produce electronic grade material for devices, it is essential to minimise the mismatch of the hetero-junction between the epitaxial layer and its substrate. If the mismatch exceeds a critical value, the lattice distortion will no longer be elastically accommodated and plastic slip will occur producing dislocations that ultimately degrade the electronic and the optical properties of the resultant structure. As mentioned earlier, this mismatch can be caused by either an incorrect combination of group III fluxes and/or by using too high a temperature for growth. X-ray techniques provide a way of measuring the lattice mismatch down to few ten parts per million (ppm). Two different X-ray measurement techniques were used for measuring the mismatch between the grown layer and its substrate: divergent beam (DB) and double crystal diffractometry (DCX). The former has the advantages of being simple and provides a quick feed-back to the growers. The latter method is more accurate, and may provide a quantitative measure (from the spectrum FWHM) of the crystallinity of the material.

6.4.1 Mismatch Determined by Divergent Beam Method

The degree of mismatch for a number of the AlInAs/InP samples was obtained by the divergent beam camera technique. The (004) reflection of the CuKα lines was used throughout and the Bragg reflected beam recorded using typical dental X-ray plates. After developing the exposed plate, two pairs of arcs should be visible, each pair correspond to the $K\alpha_1$ and $K\alpha_2$ lines. The two respective pairs of arcs are related to the substrate and the epitaxial layer. It is normally easy to establish which pair belongs to the substrate since it usually appears sharper than the epitaxial

layer pair. Figure 6.2 shows two typical recorded images on diffraction plates. The lattice mismatch is calculated by measuring the distance between the substrate and the layer arc. However when the layer is of poor structural quality, its associated Bragg arc will appear indistinct (see figure 6.2b); the separation is then measured from the centre of the layer arc to that of the substrate. The measured mismatch is translated into a deviation from the "exact" composition in terms of percentage of indium (1% change of indium content is equivalent to ~700ppm of mismatch). The results for samples MV402, MV407, MV408 and MV411 are shown in table 6.2. Comparison of these results with that deduced from DCX (discussed below) indicate that the DB technique is in very good agreement.

6.4.2 Mismatch Determined by Double Crystal Diffractometry (DCX)

The results of the double crystal X-Ray diffraction measurement on the whole set of AlInAs/InP samples studied are tabulated in table 6.2. On average, the FWHM of the rocking curves for the AlInAs layers is ~35 arc sec., slightly greater than for the InP substrate which suggests it is of fairly good crystalline quality. The raw data of the rocking curves for three of the samples (grown at different T_s) are shown in figure 6.3. These layers, MV400, MV406 & MV405 were grown at 540°C, 580°C & 600°C respectively. The sharp diffraction peak in each of the spectra is from the InP substrate and with a FWHM of ~15 arc secs. On the right of the InP diffraction peak in each of the spectra is the AlInAs diffraction peak with a larger FWHM. This indicates a negative mismatch between the AlInAs and the InP, i.e. the indium content is less than 52%. From figure 6.3, it can be seen that the degree of mismatch becomes larger as T_s

(a)

(b)

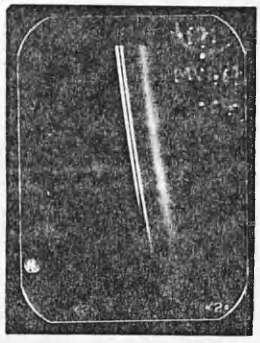

(c)

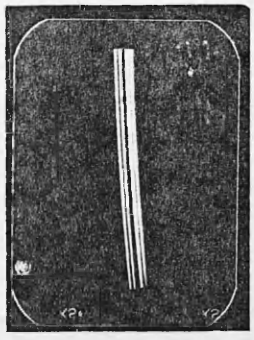

Figure 6.2 Typical diffraction images obtained using the Divergent Beam technique.

Table 6.2 X-ray measurements of the mismatch of AlInAs from the InP substrate.

Sample No.	FWHM (secs) layer	FWHM (secs) substrate	Mismatch (ppm)	I(layer)/I(sub)	Indium (%)	% In by DB
MV398	32	20	-640	1.00	51.4	
MV403	57	20	-1000	0.92	50.8	
MV400	64	12	-280	1.11	51.9	
MV402	102	29	-1100	0.80	50.7	50.8
MV411	40	26	-630	0.73	51.4	51.4
MV407	46	23	-1500	0.74	50.2	50.5
MV409	45	18	-629	0.66	51.4	
MV408	27	29	-1400	0.79	50.3	50.5
MV406	44	12	-1000	0.83	50.8	
MV404	41	28	-1300	1.25	50.4	
MV405	24	33	-1590	0.82	50.0	

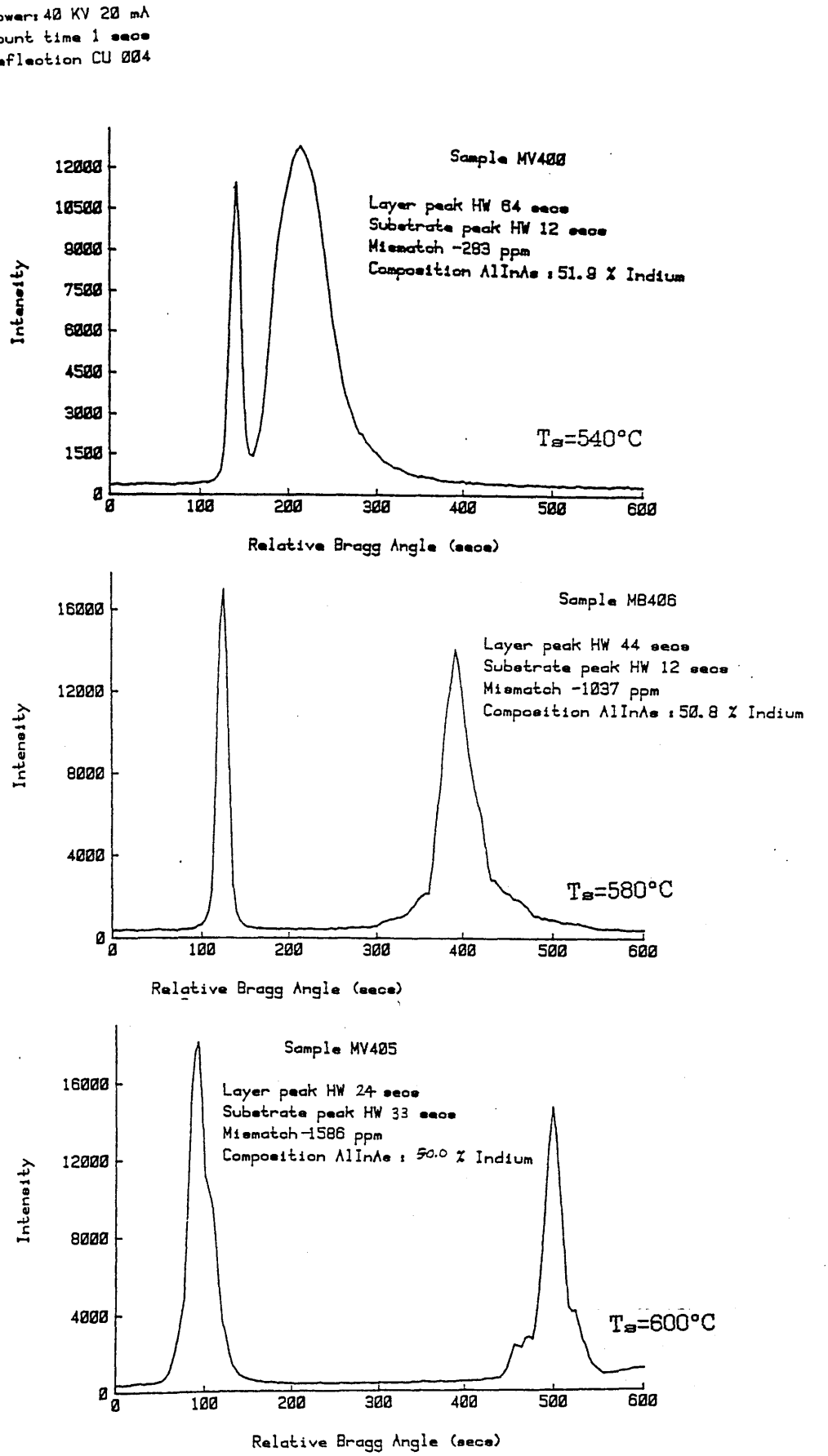

Figure 6.3 The rocking curves for the AlInAs samples grown at temperatures of 540°C, 580°C and 600°C.

increases from 540°C to 600°C, the corresponding indium content decreasing from ~52% to 50%. The trend exhibited here indicates a definite loss of indium at T_s=580°C which is in line with the thermodynamic prediction described in section 6.3. However, it should be remembered that the layers were grown separately and therefore some variation in the incident fluxes can be expected.

6.4.3 Onset of Indium Loss measured by DCX

To avoid the variation of fluxes, a structure may be designed such that only the growth temperature is varied. Although this investigation on AlInAs was not performed, the principle would be the same even though the experiments were carried out on the InGaAs system. Two structures (shown in figure 6.4) were grown separately in the MBE system described in chapter 5, each under a different arsine overpressure. For each structure, the InGaAs was grown at four different temperatures. The first structure MG136 was grown with a arsine flow of 8cc/min and the substrate temperature was varied between 660-720°C (indicated temperature by the substrate thermocouple). The second structure MG138 was grown with a lower arsine flow (3cc/min) and the substrate temperature was changed between 650-690°C (temperature indicated by the substrate thermocouple). The rocking curves for the two structures are shown in figures 6.5(a) and 6.6(a). Distinct diffraction peaks corresponding to the different growth temperatures used are clearly resolved. However, these peaks are much closer together for MG138 (figure 6.6(a)), leading to difficulties in assigning the peak to its corresponding substrate temperature. A theoretical model as described by Halliwell et al. [6.20] can be used to produce a theoretical fit to an experimental rocking curve data, thus alleviating the above

MG136

Arsine Flow Rate=8cc/min

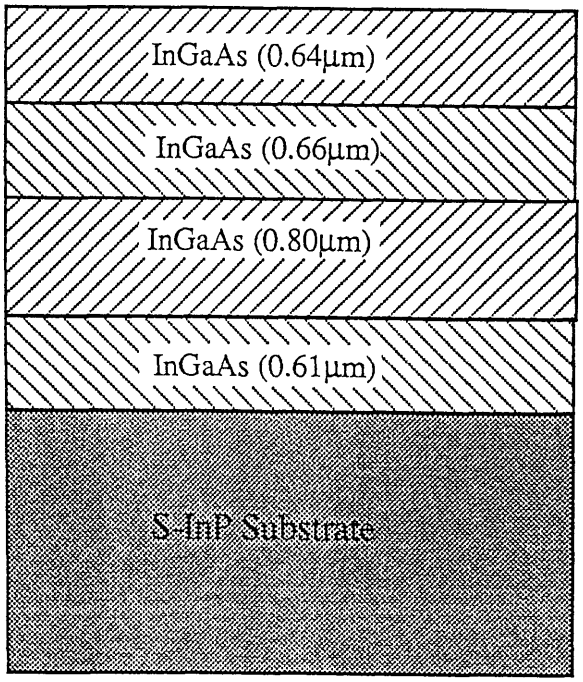

T(sub)=720°C

" =710°C

" =690°C

" =660°C

MG138

Arsine Flow Rate=3cc/min

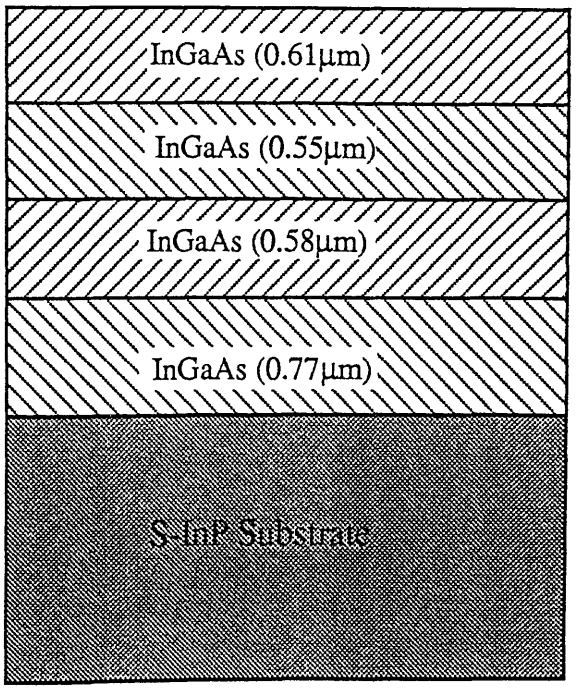

T(sub)=690°C

" =680°C

" =670°C

" =650°C

Figure 6.4 The two structures for studying indium loss at high temperatures.

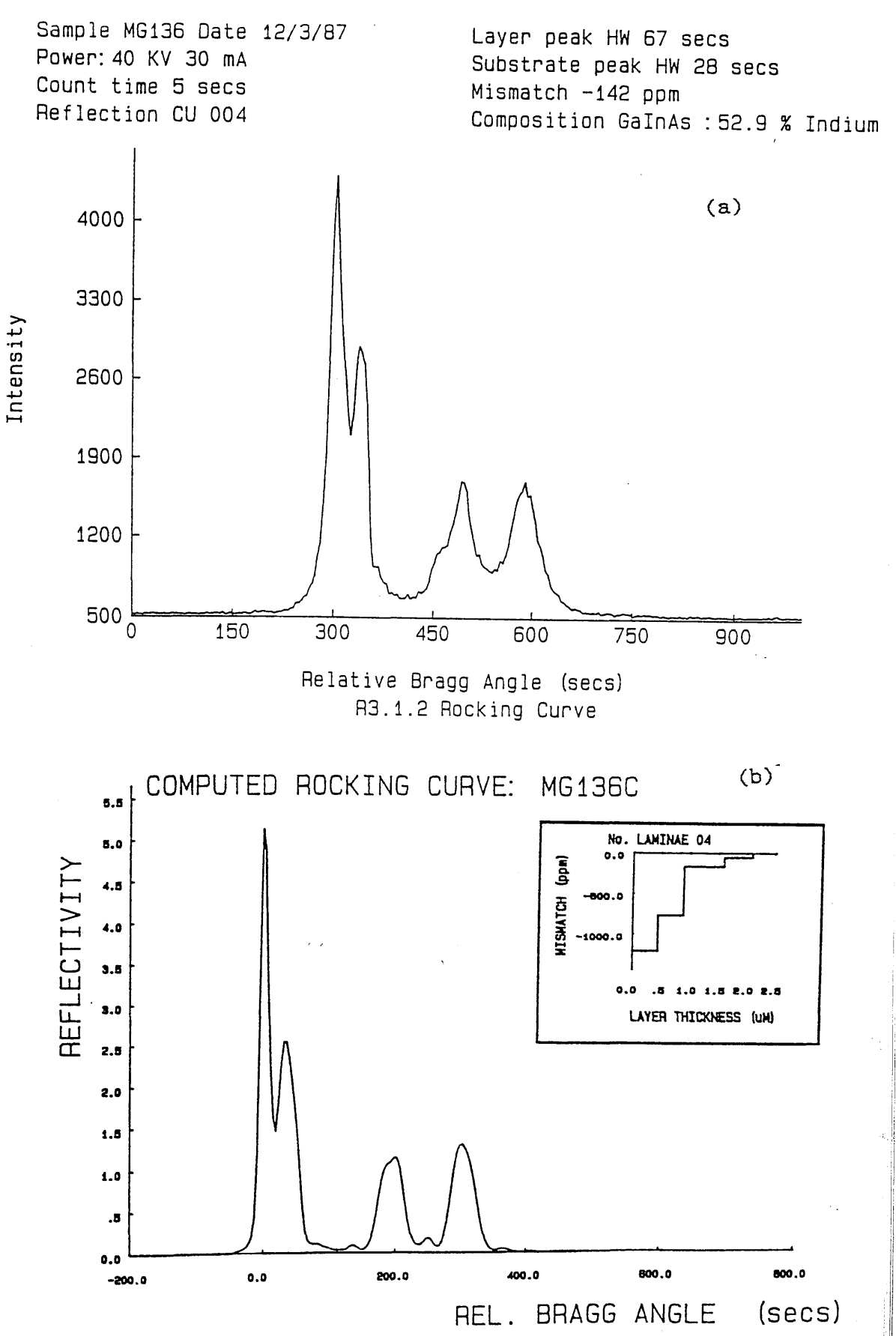

Figure 6.5 (a) The rocking curve of the InGaAs structure MG136 (see figure 6.4). (b) The computed rocking curve using a theory described by Halliwell et al. in reference 6.20.

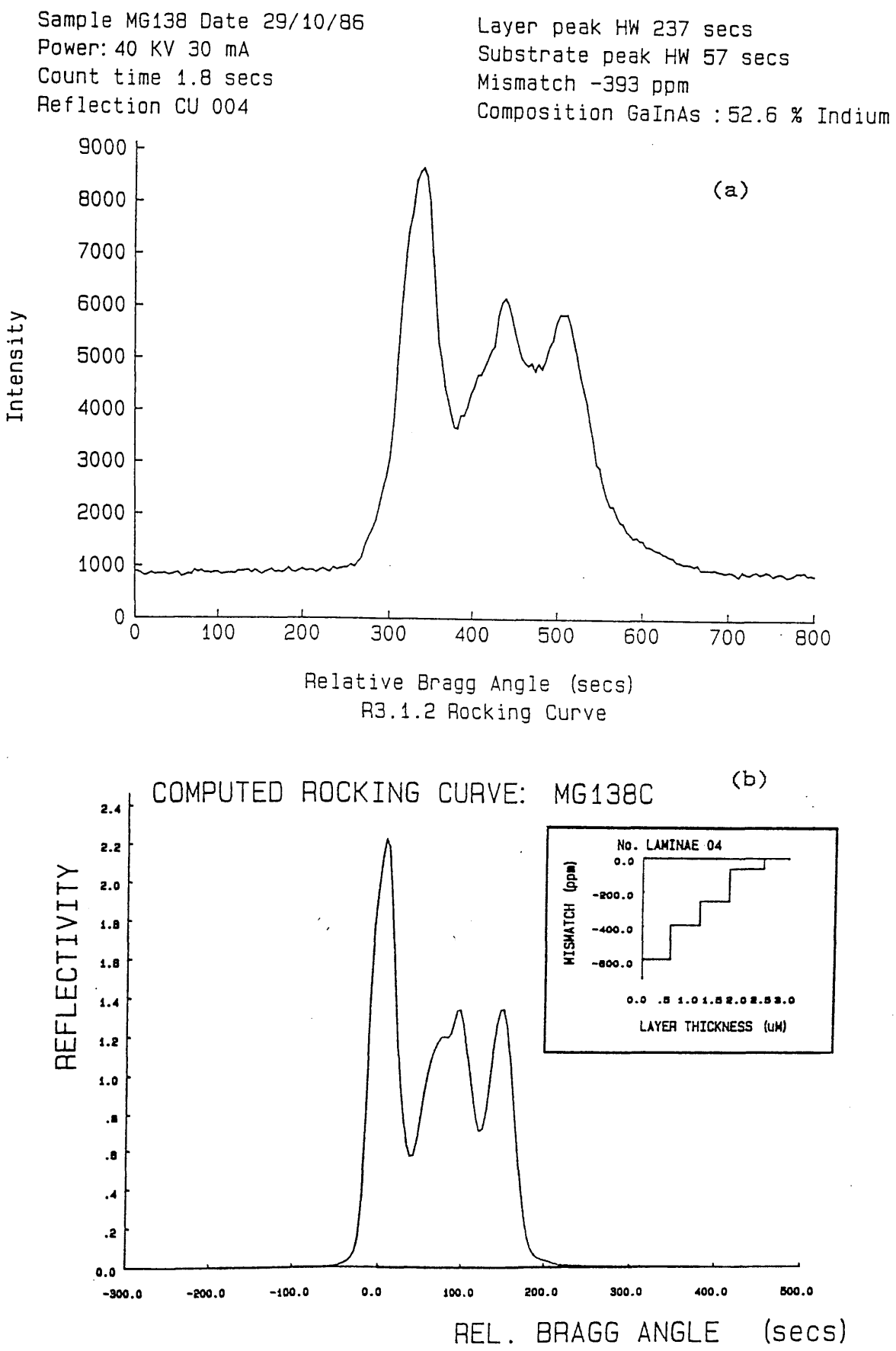

Figure 6.6 (a) The rocking of the InGaAs structure MG138 (see figure 6.4). (b) The computed rocking curve using the theory described by Halliwell et al. in reference 6.20.

problem. The rocking curves for MG136 and MG138 have been computed theoretically and are shown in figures 6.5(b) and 6.6(b) respectively. The insert in these figures are the thickness and mismatch values used in the calculations. Excellent agreement is seen between the experimental and the theoretical rocking curves.

Using the data deduced above, an activation energy for the desorbing indium species may be obtained by plotting the mismatch values against their corresponding substrate temperatures as shown in figure 6.7. The slopes of the graph for MG136 and MG138 are both identical and give an activation energy of -4.4±0.2eV. The shift of the two graphs with respect to temperature indicates that the indium desorbing species is a function of the arsine overpressure, i.e indium desorption may be suppressed by increasing the arsine flow in the case of InGaAs. The activation energy obtained here is the same as that found by Scott et al. (-4.4eV) using sputter Auger depth profiling [6.5], thereby providing further support for the validity of the X-ray theoretical simulation procedures.

The growth temperature at which a significant amount of indium begins to desorb may also be located during growth using RHEED. In the case of InGaAs, the onset temperature corresponds to the surface reconstruction pattern changing from (1x2) to (4x2). Thus, it is possible to control the growth parameters in-situ to prevent substantial loss of indium. In figure 6.8, the phase boundary of InGaAs grown at a growth rate of 1.7 μm/hr is shown. The experimental points in the figure were obtained from many growth runs. Note also the substrate temperatures are indicated values only and not the true growth temperatures. This phase diagram provides a quick reference for growers to keep within the no indium loss regime for a given growth rate (group III fluxes). The principle would again be

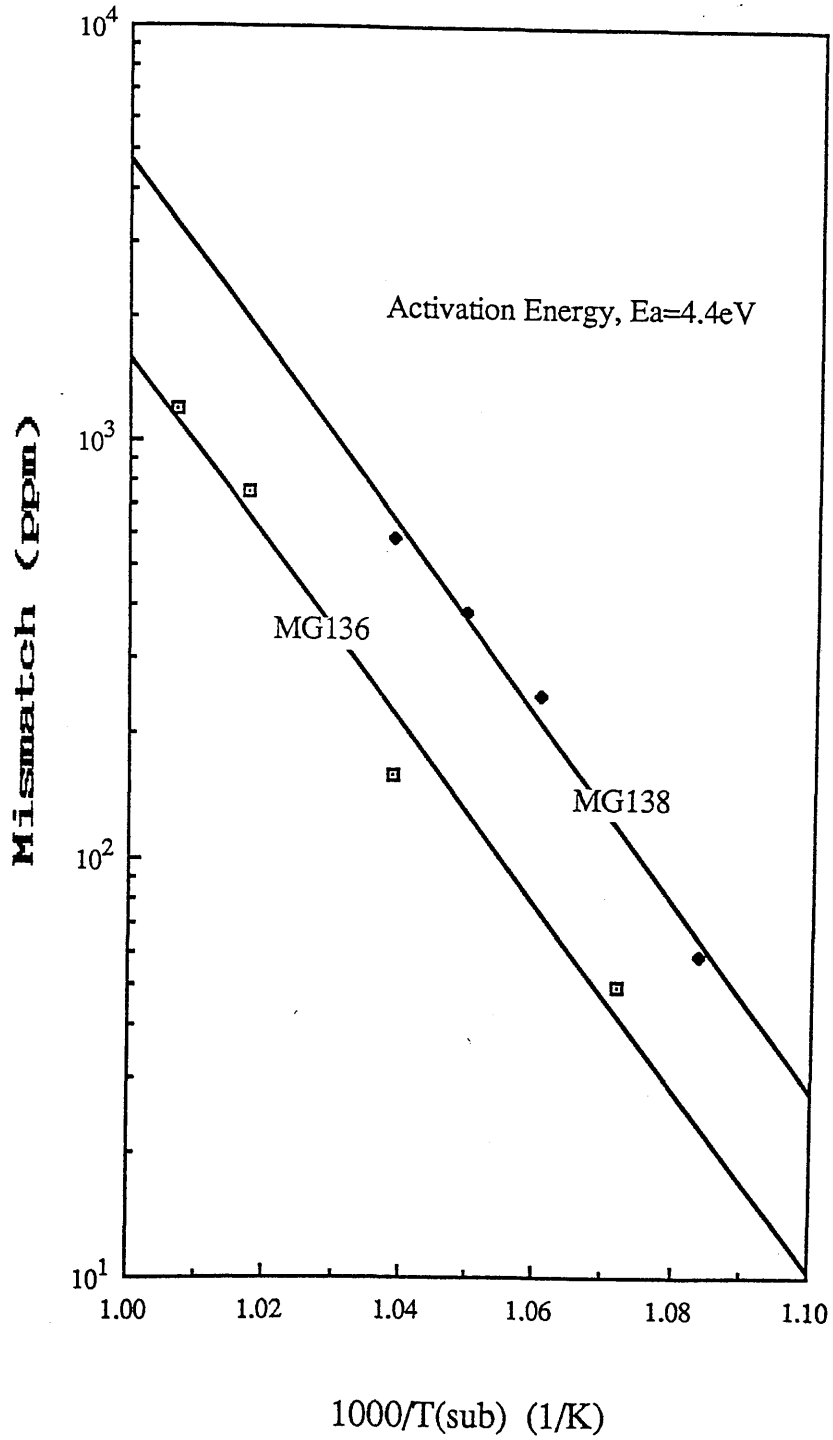

Figure 6.7 The mismatch between the epitaxial InGaAs and the InP substrate as a function of the inverse of substrate temperature. An activation energy of desorption, E_a=4.4eV, is deduced.

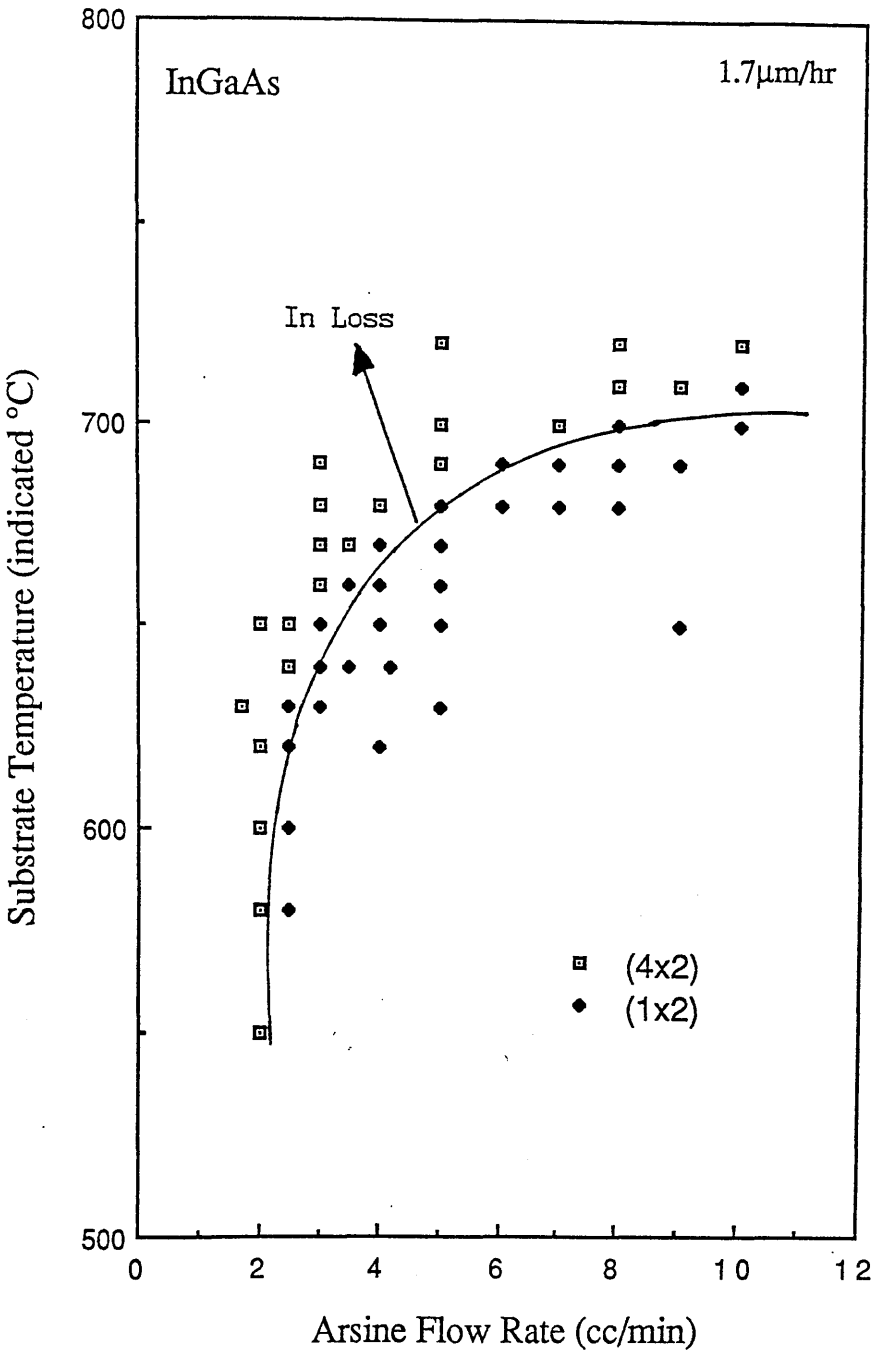

Figure 6.8 Phase diagram of InGaAs obtained by RHEED. The solid line shows the transition to an indium loss region as indicated.

expected to be the same for the loss of indium in AlInAs.

6.5 Surface Morphology

Scott et al. reported the first observation of a so called 'forbidden' temperature window for the growth of AlInAs which results in 'rough' morphology [6.5]. Below and above this temperature region, the surface of the epitaxial layer tends to be smooth and shiny. This 'rough' temperature window occurs between 540° and 580°C as indicated in table 6.1. Phase contrast microscopy and secondary electron microscopy were used to examine the surface features of the samples grown within and outside this forbidden temperature region. The phase contrast micrographs for three AlInAs samples, with the same magnification of 1000x, grown at different temperatures (MV403 at T_s=530°C, MV401 at T_s=560°C, & MV405 at T_s=600°C) are shown in figure 6.9. As the substrate temperature increases, the morphology of the epitaxial layer becomes rough once a critical temperature is reached (540°C in our case). However when the temperature is increased beyond the rough regime, the surface of the epitaxial layer becomes smooth once again (see figure 6.9c).

This surface roughness window (lying within 40°C temperature range) is similar to that observed in the growth of AlGaAs [6.21-6.23] where rough morphology occurs for layers grown between 630° and 690°C, i.e. it occurs 100° higher than AlInAs. The exact mechanism giving rise to this rough morphology feature is still not well understood although several proposals have been put forward. Amongst these are: a much reduced surface mobility of Al compared with Ga in the forbidden T_s range [6.22,6.24], a deficiency of the population of arsenic [6.25], the existence of growth

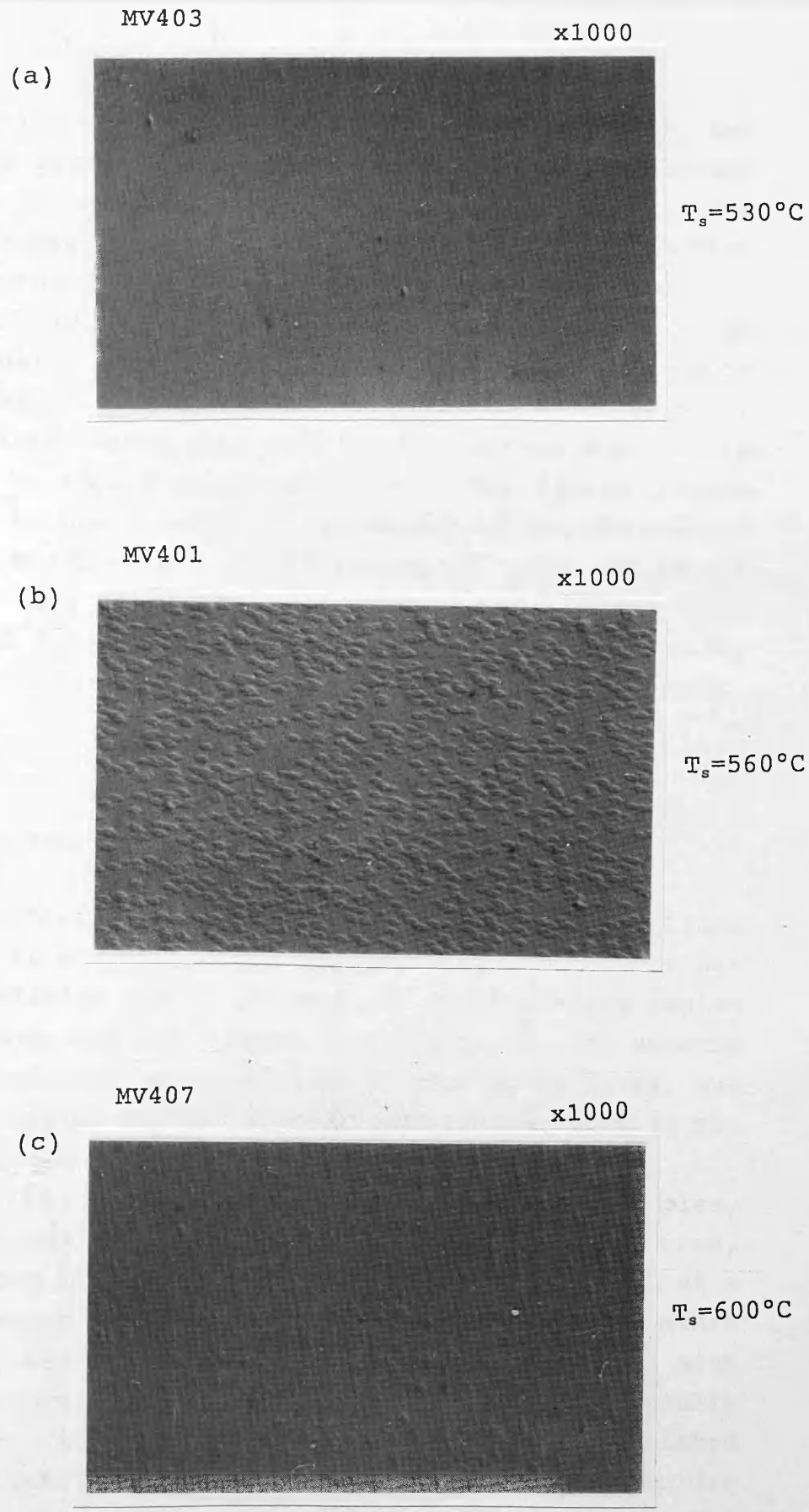

Figure 6.9 Phase contrast micrographs for the AlInAs samples grown at temperatures of 530°C, 560°C and 600°C.

inhibiting impurities (e.g. carbon) [6.26,6.27], and surface segregation of Ga [6.23,6.28,6.29]. Although there is no conclusive evidence at present, the experimental results discussed in the next section favour the surface segregation model.

The morphology of the AlInAs appears to be relatively free of defects. Indeed oval defects associated with MBE growth were not observed on any of the AlInAs layers. The only kind of defect observed is shown in figure 6.10 (a) & (b). The former figure shows the phase contrast micrograph of the defect for sample MV401 with a magnification of 1000x, while the latter is a SEM micrograph of defect for MV406. This kind of defect has also been reported by Kerr [6.30] who attributed it to spitting from the group III cell.

6.6 Low Temperature Photoluminescence

The influence of the morphological feature of AlInAs on its PL properties was studied to determine whether a correlation exists between the rough surface region of growth and the AlInAs PL output. The PL spectra described here were recorded at BTRL by S. Davey, but more detailed optical studies will be described in the next chapter.

The PL spectra for three AlInAs samples, corresponding to three different growth temperatures, are shown in figure 6.11: the samples were grown at a low temperature (530°C), an immediate temperature (540°C) which produced a rough morphology and a high temperature (600°C). The spectra are essentially similar, each has a sharp peak at ~800nm associated with AlInAs and a fairly broad, low intensity shoulder at 830-900nm which was found to be associated with the substrate of InP. The possible recombination

(a)

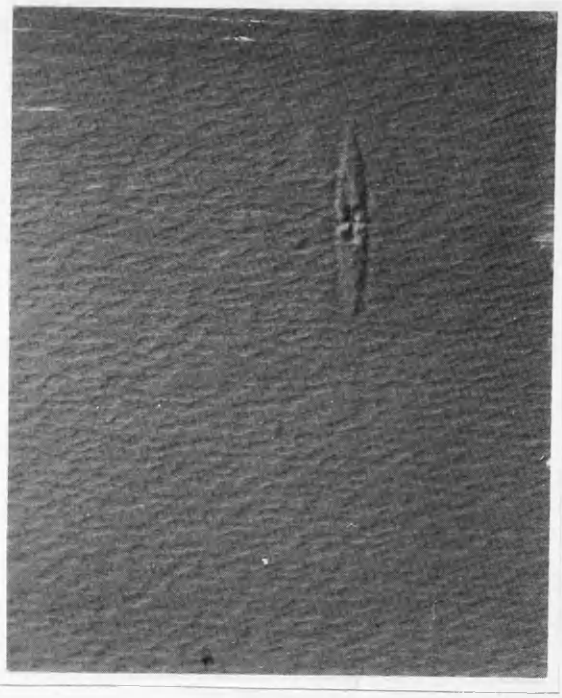

(b)

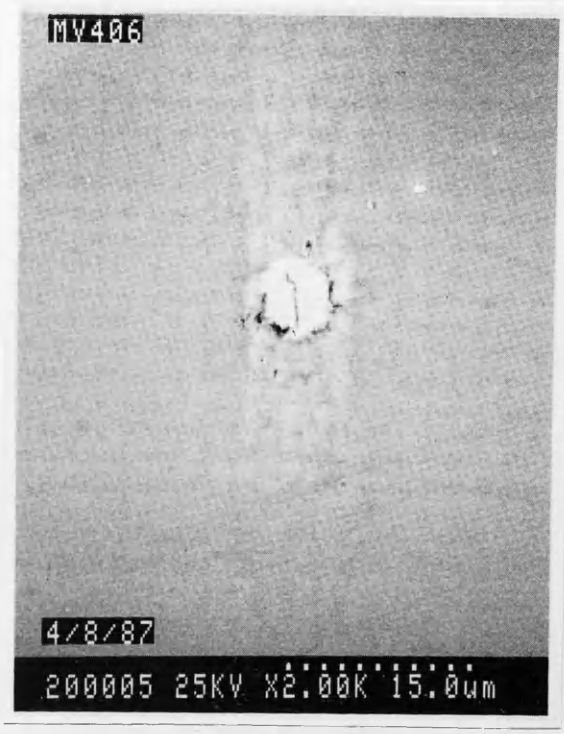

Figure 6.10 (a) Phase contrast micrograph of a typical defect observed on an AlInAs surface. (b) SEM micrograph of a similar defect.

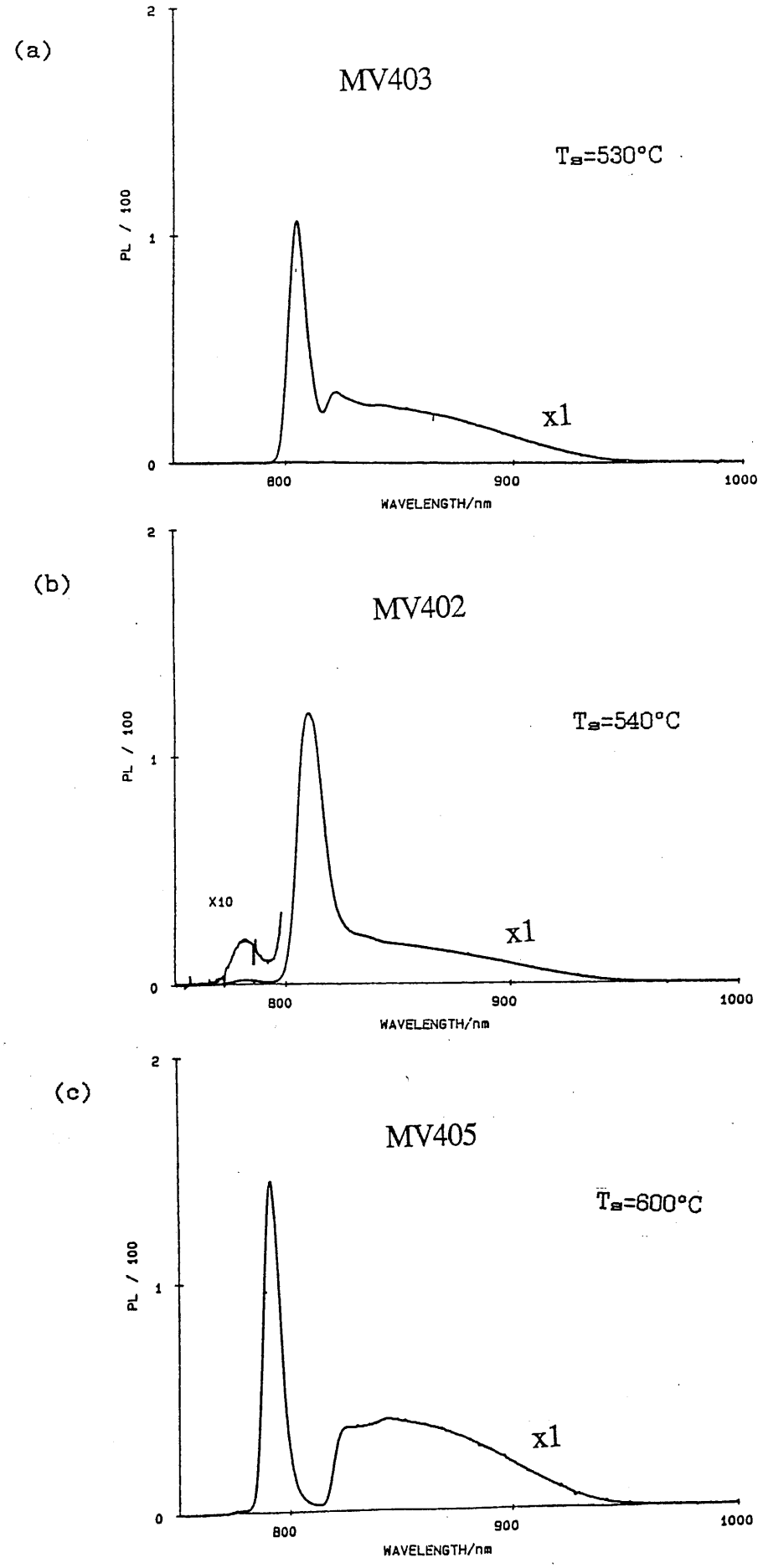

Figure 6.11 4K PL spectra of the AlInAs samples grown at temperatures of 530°C, 540°C and 600°C.

mechanisms giving rise to the AlInAs peak will be discussed in chapter 7. The FWHM of the AlInAs emission peak varied from 14 to 25meV for the series of samples considered, which are amongst the narrowest linewidths observed in this material system. A graph of the FWHM versus the growth temperature have been plotted and is shown in figure 6.12. The PL linewidth is seen to increase within the rough surface window; it increases to a maximum of ~25meV from about 16meV at low and high temperatures. Hence, it is evident that growth of AlInAs in the 'forbidden' temperature window is undesirable if high optical quality material is required.

In addition, a weak intensity emission peak at a higher energy than that of the AlInAs emission was observed in the PL spectrum for the samples grown in the 'forbidden' temperature region. This high energy peak, shown in figure 6.11 (MV402), occurs at 1.5868eV and is ~55 meV above the AlInAs peak. Such emission peak was absent for samples grown outside the 'forbidden' growth window. This suggests its origin is somehow related to the surface of the epitaxial layer. A possible explanation of this emission is due to the diffusion and segregation of the indium atoms forming a different composition of surface layer of AlInAs. This model is similar to the segregation of Ga in AlGaAs proposed by Massies et al. [6.29]. If one considers the PL emission peak of AlInAs corresponds to a measure of its band gap as given by Davies et al. [6.14], then the higher energy peak in figure 6.11 would arise from a layer with a smaller indium molar fraction, in fact it has a 3.5% indium deficient composition from a perfectly matched layer.

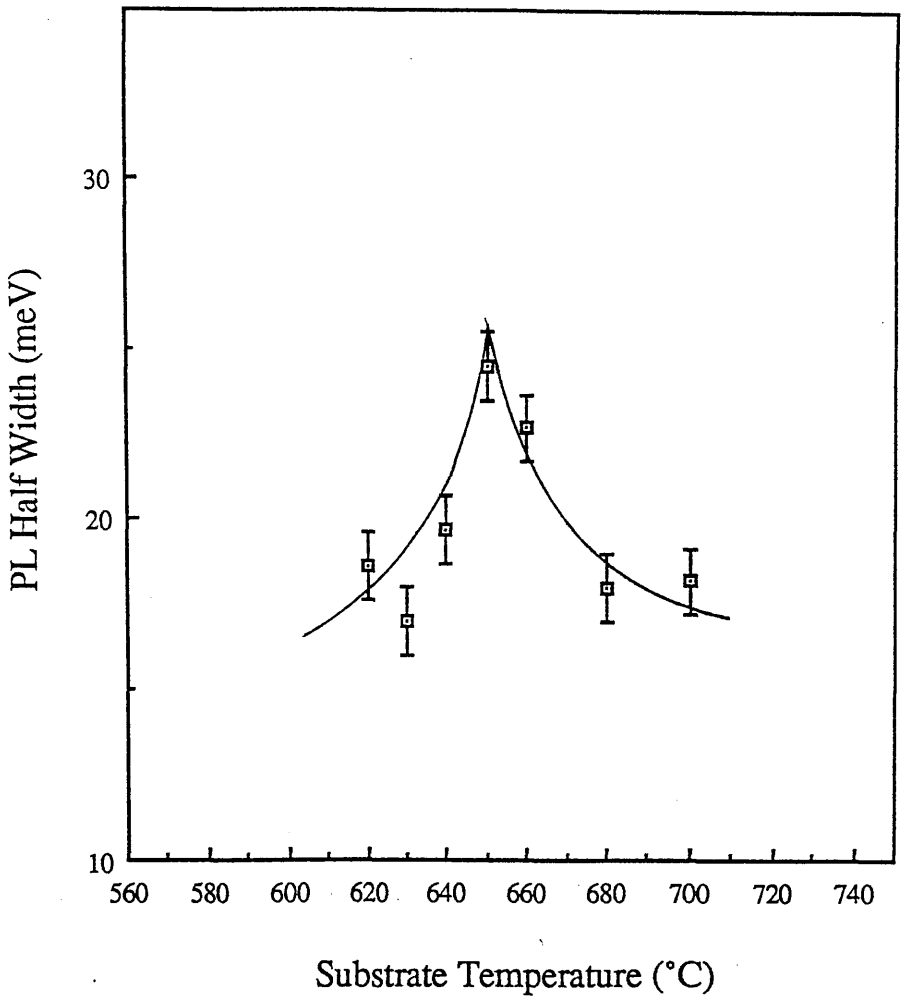

Figure 6.12 AlInAs PL half width as a function of the substrate temperature.

6.7 Deep Level Measurements

The deep level impurities in AlInAs have not been investigated as extensively as in other III-V ternary alloys such as InGaAs and AlGaAs although a small number of reports exist in the literature [6.31-6.33]. The deep traps reported in the literature, however, are not in very good agreement, the only consensus being that the trap concentrations are relatively high $N_S > 10^{15} cm^{-3}$ which is probably due to the low growth temperatures used in the MBE growth [6.34].

It has been seen previously that there is a parallel between AlInAs and AlGaAs in that there exists a 'forbidden' growth window in each case. Hong et al. pursued this further by investigating whether a (D-X) like state is present in AlInAs [6.32]. They have measured a deep electronic level at 350meV below the conduction band edge with a capture cross-section of $10^{-18} cm^{-2}$. The concentration of this trap was shown to depend strongly on the level of Si dopants and AlInAs with this impurity level exhibited persistent photoconductivity. Hong et al. concluded that this is a (D-X) like centre similar to the EL2 trap commonly found in AlGaAs.

The main objectives in the deep levels measurements described here were to establish whether or not a correlation existed between the traps and the surface roughness window, and to study the deep levels as a function of the growth parameters. Both electron and hole traps were considered. The former were measured on Schottky diodes by the standard DLTS technique and the latter were assessed using transparent Schottky diodes by the method known as minority carrier transient spectroscopy (MCTS) [6.35]. The measurements were performed using the Polaron S4600 unit together with a Boonton capacitance meter 72B. The system was controlled by a HP9816 micro-computer and was capable

of scanning from 90 to 450K with the Polaron S4900 cryostat. An AlGaAs solid state laser operating at 850nm was used for the MCTS measurements.

6.7.1 DLTS Measurements

For these measurements, a diode is necessary. To fabricate a Schottky diode, the three stages below were followed:

(I) Before any evaporation onto the semiconductor materials the following degreasing procedure is carried out:

(a) degrease in boiling trichloroethylene for 10mins.,

(b) leave in boiling propanol for 5-10mins,

(c) wash with de-ionised water and blow dry.

The next two stages are deposition of ohmic and Schottky contact and are performed using the following recipes:

(II) Ohmic:-

Evaporate ~2000Å of Au/Sn(2%) and anneal at ~420°C for 60s in forming gas (90%N_2:10%H_2).

(III) Schottky:-

Removal of surface oxide by the chemical etch-

Conc. H_2SO_4 for 45s, followed by

HCl:H_2O (1:1) for 20s.

Deposit ~500Å of Ti and lastly evaporate ~2000Å of Au.

The I-V characteristics of the resultant diodes were close to ideal, with an ideality factor estimated to be 1.1-1.3. The reverse dark current was approximately $2x10^{-7}Acm^{-2}$ at -5V and the reverse breakdown occurred at -25V. The DLTS measurements were performed with the diode at a reverse bias lying within -2 to -10V

and with a fill pulse chosen to completely fill the traps. Spectral scans were usually taken between 90-400K. Up scans (i.e. going from 90 to 400K) as well as down scans (i.e. going from 400 to 90K) were taken to minimise the error introduced by the temperature lag which was found to be 5° between the up and down scans. The average peak position of up and down scans was taken for a particular emission trap.

Two p-n junction diode structures were also used for the DLTS measurements. These are shown schematically below:

MV526	MV530
P^+ GaAs cap	P^+ -GaAs cap
1μm AlInAs($Be=5x10^{17}cm^{-3}$)	0.3μm AlInAs($Be=5x10^{17}cm^{-3}$)
1μm AlInAs($Si=5x10^{16}cm^{-3}$)	1.2μm AlInAs($Si=1x10^{17}cm^{-3}$)
n^+ InP Substrate	n^+ InP Substrate

MV526 was grown at T_s=580°C with As_2 while MV530 was grown at T_s=500°C using As_4. Ohmic contacts on the n+ substrates were formed by Au/Sn and the ohmic contact to the p+ AlInAs was achieved by deposition of 500Å Ti followed by 2000Å Au/Zn. Individual devices were then defined by lithographic patterning. Wet etching was required to remove the Au, Ti and AlInAs in the exposed area in order to form the diodes. The recipes were:

Au - $KI:I:H_2O$ (8g:0.2g:10ml) for 2-3mins.,

Ti - $HF:H_2O$ (1:3) for 60secs.,

AlInAs - $H_2SO_4:H_2O_2:H_2O$ (1:5:60) which has an average etch rate of 1.6 μmhr^{-1} .

A typical DLTS spectrum for a Schottky diode is shown in figure 6.13. It has a broad emission peak at ~210K for a 200/s emission rate window. The spectra

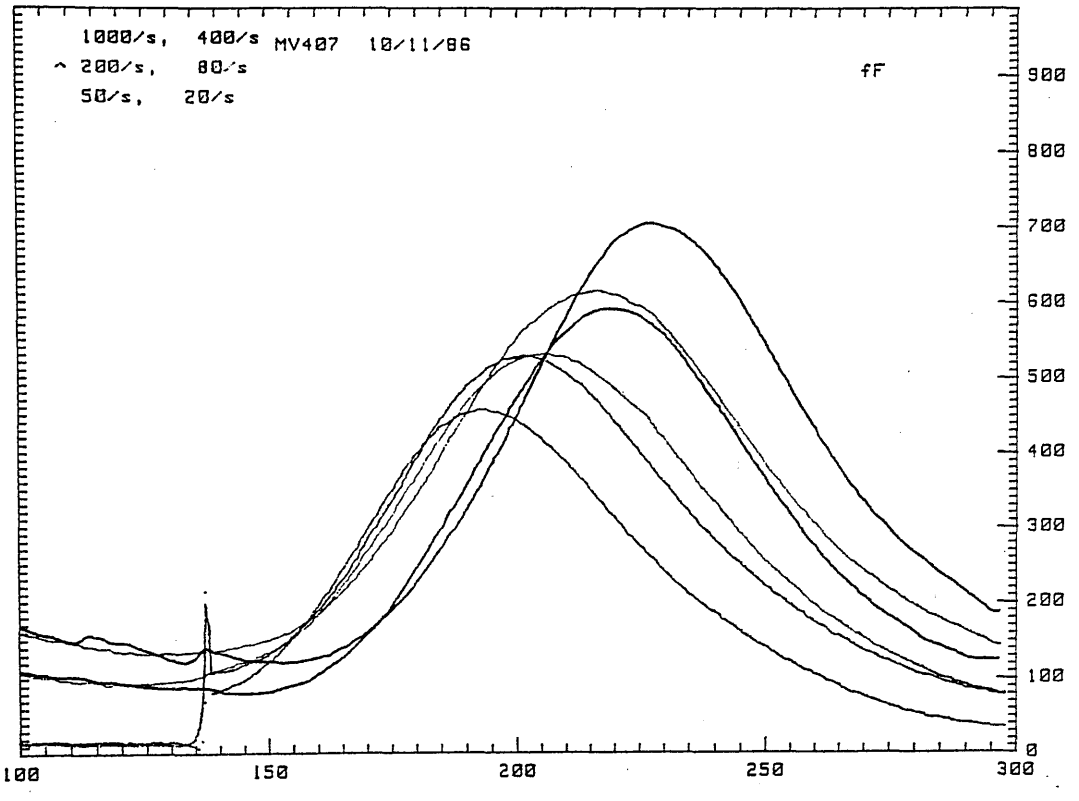

Figure 6.13 A typical DLTS spectrum for AlInAs.

observed for all the samples are similar except that some emission peaks associated with traps at relatively low concentrations (at least an order of magnitude lower) occurred only for samples grown in the surface roughness window. Table 6.3 lists the detected electron and hole traps together with their peak position at 200/s emission rate window, their activation energies, their capture cross-section and their concentrations. The following summarises the observations drawn from the results of the DLTS measurements on the electron traps:

(a) MBE3 and MBE4 are the dominant electron traps in the samples with activation energies of 0.48 and 0.44eV respectively.

(b) MBE0, MBE1 and MBE2 (with their respective activation energies of 0.1eV, 0.13eV and 0.16eV) occur only for layers grown in the rough surface region.

(c) MBE5 (activation energy of 0.61eV) is only detected in the two p-n junction samples (MV526 & MV530). It is the dominant trap in both these samples although MBE3 and MBE4 are also present but at much lower concentrations. The only obvious difference between these samples and the Schottky samples is the presence of Be. Hence MBE5 is tentatively assigned to traps associated with the Be dopant.

(d) the arsenic flux has little influence on the deep levels since it is seen that the DLTS signatures for MV407 & MV406 (grown under nominally same conditions except for different arsenic flux) are much the same in both trap concentration as well as the type of traps.

(e) As shown in table 6.4 the concentration of deep

Table 6.3 The measured electron and hole traps in AlInAs with their activation energies, capture cross-sections and concentrations.

Trap	Peak Position at $e=200s^{-1}$ (K)	Activation energy (meV)	Capture x-section σ_∞ (cm^{-2})	Concentration (cm^{-3}) $x10^{15}$
Electron				
MBE0	100	190	-	~0.3
MBE1	130	-	-	~0.3
MBE2	160	260	$2.2x10^{-17}$	0.2-0.6
MBE3	210	480	$1.5x10^{-16}$	0.3-1.0
MBE4	250	440	$4x10^{-18}$	0.3-1.0
MBE5	345	610	$3.0x10^{-18}$	2.0
Hole				
MBH1	<95	-	-	0.02-0.3
MBH2	170	220	$5.0x10^{-19}$	0.02-1.0
MBH3	290	540	$4.8x10^{-18}$	0.02-0.5

Table 6.4 Results of the AlInAs samples obtained by C-V profiling and PL.

Sample No	N_d-N_a CV (cm^{-3}) x10^{15}	% Indium PL	FWHM (meV) PL	n(300)-n(100) (cm^{-3}) x10^{15}
MV398	>1.0	51.0	18.6	depleted at 300K
MV403	2.5	50.5	17.0	depleted at 300K
MV400	1.5	51.3	19.7	5.0
MV402	8.0	51.0	24.5	5.0
MV401	4.0	51.0	22.7	2.0
MV411	2.0-3.0	50.9	15.4	depleted at 100K
MV407	1.5	50.2	18.3	4.5
MV409	8.0-10.0	50.4	14.6	depleted at 300K
MV408	10.0	49.9	16.9	5.0
MV406	15.0	50.0	16.4	5.0
MV404	22.0	49.8	18.0	3.0
MV405	45.0	49.3	18.2	5.0

levels which freeze out between 300 and 77K is ~$5x10^{15}cm^{-3}$. This would suggest the total trap concentration is ~$5x10^{15}cm^{-3}$ which is in line with the deep level concentrations indicated in table 6.3.

(f) at T_s<540°C deep levels are dominant over the role played by Si and the layers deplete out, indicating the trap concentration must be very high.

(g) at T_s>540°C deep levels are dominant only when no Si is introduced, implying the trap concentration in the layers is lower than those grown at T_s<540°C.

(h) at T_s>580°C the influence of Si doping is greater than deep levels and the layers become more n-type as the Si flux is increased.

(i) the capture cross-section of MBE3 ($\sigma_\infty=1.5x10^{-16}cm^{-2}$) is greater than MBE4 ($\sigma_\infty=4x10^{-18}cm^{-2}$). This can also be seen by using a short filling pulse. Figure 6.14 (a) & (b) show the effect of changing the fill pulse from 10ms to 10μs. The capacitance change for MBE4 is faster than for MBE3, implying MBE3 has a larger capture cross-section. Changing the fill pulse time is often used to separate traps that have a significant difference in their capture cross-sections.

6.7.2 Minority Carrier Transient Spectroscopy (MCTS)

The procedure for the fabrication of a transparent Schottky diode was similar to that for the Schottky diode describe above. Ohmic contact onto the n+ InP substrate was the same as above. For the Schottky, a sheet of titanium of thickness less than 200-300Å was deposited onto the semiconductor layer to provide a transparent contact. Approximately 2000Å of gold was

(a)

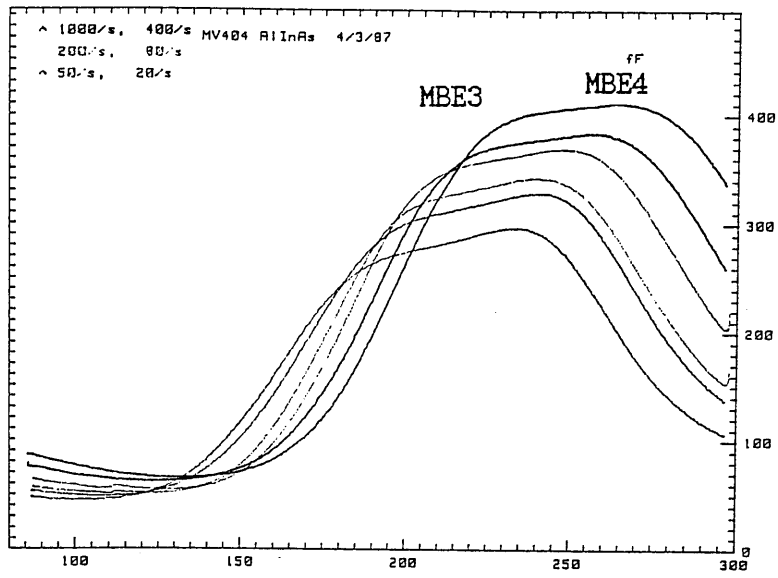

(b)

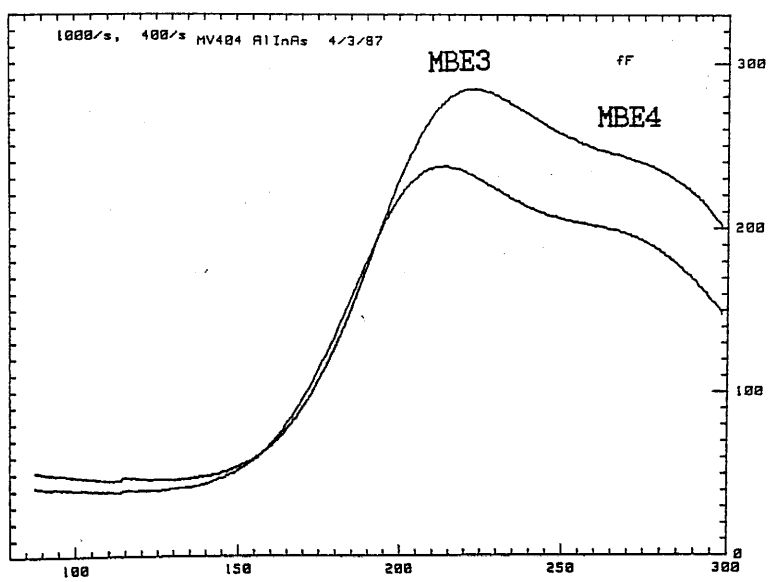

Figure 6.14 (a) DLTS spectrum obtained for a filling pulse of 10ms. (b) DLTS spectrum obtained for a filling pulse of 10μs.

then evaporated onto the titanium sheet. Lithography techniques were then used to define the effective area of the diodes. After exposure and development, the diode area was defined by etching the titanium away in a solution of $HF:H_2O$ (1:3) for 5-10s.

A typical MCTS spectrum is shown in figure 6.15 revealing the three dominant traps (MBH1, MBH2 & MBH3) found in the samples. The lower section of table 6.3 summaries the hole traps observed in AlInAs Schottky samples. MBH2 and MBH3 are at 0.22 and 0.54eV above the valence band edge respectively. The position of the energy level for MBH1 however could not be determined since the emission peaks occurred at or below 95K which suggests it would be <0.2eV above the valence band.

A correlation between the three hole traps and the roughness window was not observed in the samples. It should be noted that these traps are approximately an order of magnitude lower in concentration than the electron traps, which has been observed previously [6.32]. In addition, it was found that sample MV409, which was not deliberately doped with Si, showed substantially reduced hole trap concentrations (in the low $10^{13}cm^{-3}$ range) compared with the other samples in the series. This would suggest that these hole traps might be associated with defects involving the Si dopant. The three hole traps observed in this study do not however appear to correspond to the reported traps in reference [6.32].

6.8 The use of As_2 versus As_4

According to Tsang et al [6.36] there is an improvement in the optical and electrical characteristics for epitaxial layers grown by MBE using As_2 instead of As_4 . Indeed, the series of AlInAs

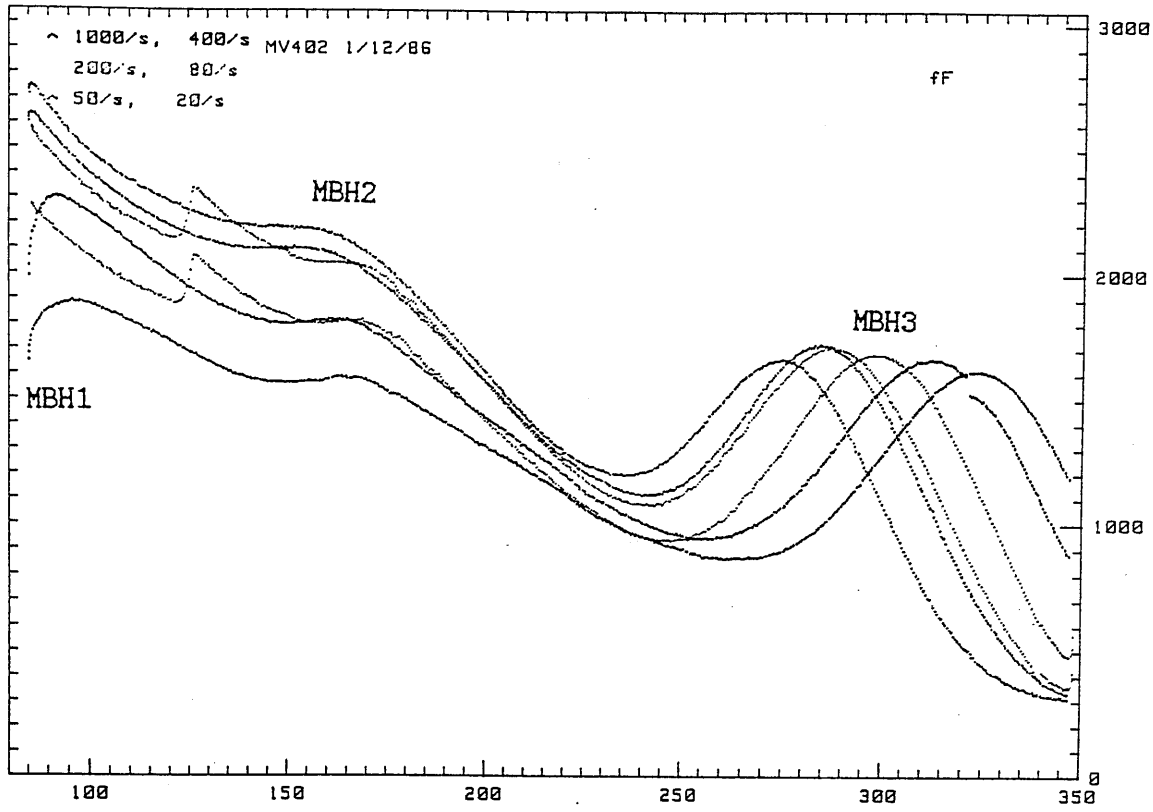

Figure 6.15 A typical MCTS spectrum for AlInAs.

layers in this study, which were grown using As_2, does appear to have very good optical properties; the linewidth of 15meV is the narrowest observed in this material system. However Scott et al. [6.5] found that AlInAs grown using As_2 instead of As_4 did not affect the surface roughness region and also did not influence the temperature at which indium loss becomes significant.

To determine whether As_2 is more advantageous than As_4 , two AlInAs epitaxial layers were grown. The layers were each of 2um thick and were grown under identical conditions except that one was with As_2 (MV662) and the other with As_4 (MV663). Table 6.5 shows the results of the mobility and the 18K PL measurements. It is seen that the layers have similar mobility values both at 300K and 77K, although the values for the layer grown with tetramers are higher by 10%. This is also supported by the 18K PL linewidth values which were found to be 35meV for MV622 and 28meV for MV663. Hence contrary to the general expectation, the use of As_2 did not improve the quality of the layer to any measurable extent. One possible explanation is the total concentration of defects associated with the use of high Al in AlInAs is much more dominant than that induced by the arsenic species.

The mobility values measured in this study compare well with others reported in the literature [6.8, 6.11, 6.27]. Figures 6.16 (a) & (b) show the mobility versus the free carrier concentration plots at 300 and 77K. The 300K mobility of the samples grown by LPE (ref. 6.8) is about a factor of four higher than those grown by MBE. The 77K mobility values of the data presented here do not appear to change from the 300K values, suggesting the importance of alloy contribution to scattering at the temperatures considered [6.32].

Table 6.5 The carrier concentrations, mobilities and the 18K PL FWHM for two AlInAs grown with different arsenic species; MV662 (As_2) and MV663 (As_4).

Sample	Carrier Concentration $x10^{16}(cm^{-3})$		Mobility $(cm^2V^{-1}s^{-1})$		18K PL FWHM (meV)
	300K	77K	300K	77K	
MV662	2.9	2.1	990	945	35
MV663	3.0	2.3	1034	1072	28

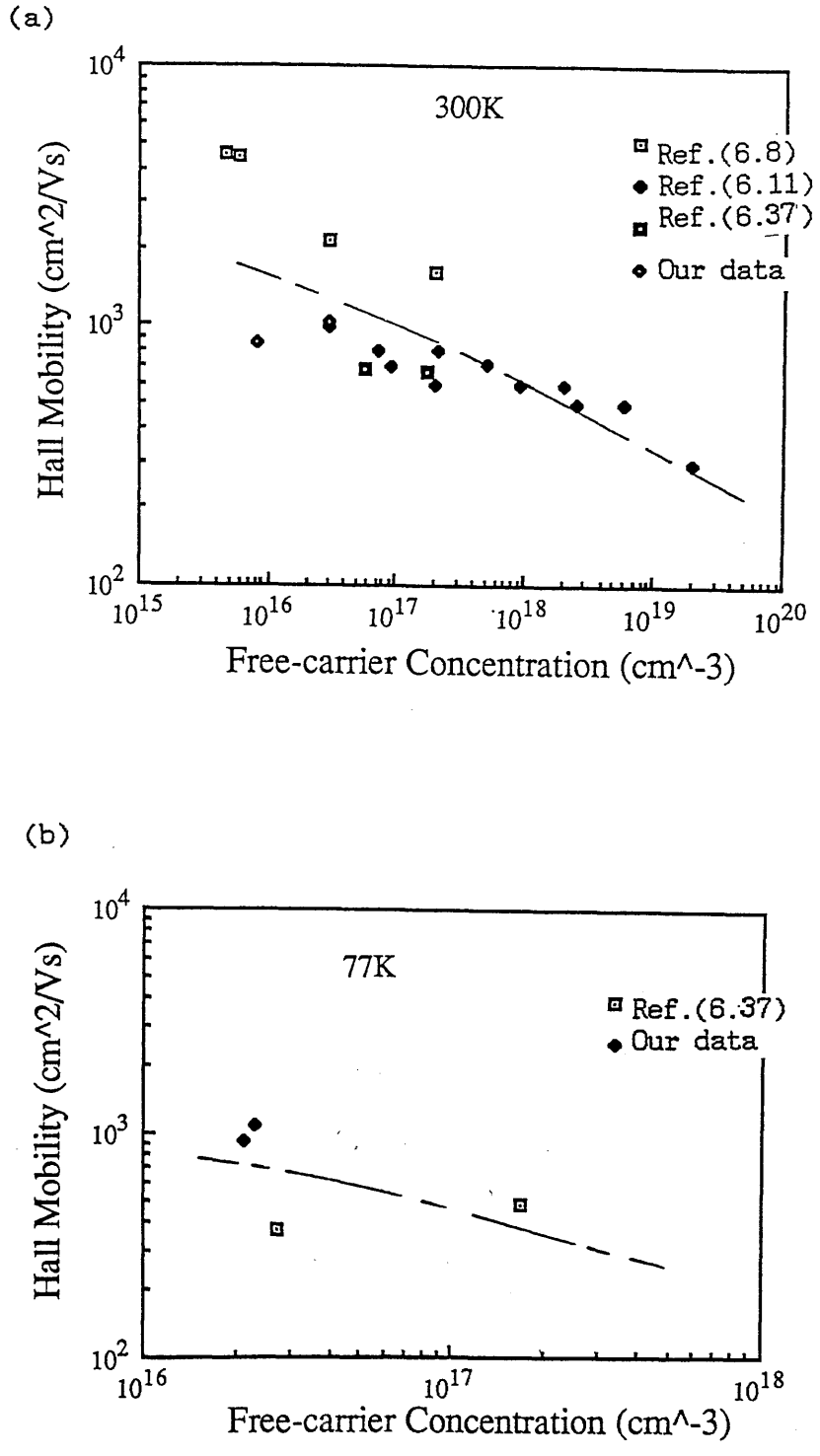

Figure 6.16 Mobility as a function of free-carrier concentration for AlInAs at (a) 300K and (b) 77K. Included in the figures are the results reported by other authors as indicated.

6.9 Conclusion

A series of epitaxial AlInAs layers lattice matched to (100)InP grown under different conditions by MBE has been systematically characterised. They were grown in the temperature range of 500-600°C which was below the onset of indium loss according to Davies et al. [6.14]. The loss of indium may conveniently be detected using the X-ray double crystal diffraction technique and was demonstrated for InGaAs, the activation energy of which was found to be -4.0±0.2eV in excellent agreement with previous value reported by Scott et al. from Auger depth profiling data [6.5].

AlInAs epitaxial layers were found to exhibit a similar 'forbidden' growth temperature window to the growth of AlGaAs. AlInAs grown at temperatures between $530°C<T_s<570°C$ was found to be 'rough' in appearance but 'shiny' outside this temperature window. In the 'rough' temperature regime, deep level measurements revealed the existence of three unique electron traps (MBE0, MBE1 & MBE2). However, these traps were not dominant compared to the two common electron traps (MBE3 & MBE4) found in all AlInAs samples. The total concentration of the electron traps was found to be $\sim 5 \times 10^{15} cm^{-3}$. Unique hole traps associated with the 'rough' temperature window were not detected. The concentrations of the three common hole traps (MBH1, MBH2 & MBH3) observed were found to be influenced by the Si flux. The total concentration of the hole traps was an order of magnitude lower than the electron traps. However, the precise nature of the measured electron and hole traps was not determined.

The epitaxial layers grown in the 'rough' temperature region also showed an increase in the PL linewidths. The FWHM of the emission at 800nm increased by approximately 50% (from ~16meV to 25meV). In addition, a very low intensity emission peak at

~60meV above the normal AlInAs peak was observed only in the 'rough' surface samples. This was attributed to a thin surface layer of AlInAs having a different composition from its bulk caused by the segregation of indium atoms.

Finally, the effect of using different arsenic species (As_2, As_4) for the growth was considered. The experiments revealed little evidence for an improvement in either the optical or electrical characteristics for layers grown with As_2 compared to the layers grown using As_4, contrary to the general expectation.

6.10 References

[6.1] M.R. Lorentz and A. Onton, Proceedings of the 10th International Conference on the Physics of Semiconductors, Cambridge, Massachusetts, 1970 (U.S. Atomic Energy Commission, Washington, D.C.), p.44.

[6.2] P. People, K.W. Wecht, K. Alavi and A.Y. Cho, Appl. Phys. Lett., 43, 118 (1983).

[6.3] K. Alavi, T.P. Pearsall, S.R. Forrest and A.Y. Cho, Electron. Lett., 19, 227 (1983).

[6.4] D.J. Newson, K.F. Berggren, M. Pepper, E.G. Scott and G.J. Davies, J. Phys. C19, L403 (1986).

[6.5] E.G. Scott, D.A. Andrews and G.J. Davies, J. Crystal Growth, 81, 296 (1987).

[6.6] C.Y. Chen, A.Y. Cho, P.A. Garbinski and K.Y. Cheng, IEEE Electron Device Lett., 3, 15 (1982).

[6.7] P. O'Connor, T.P. Pearsall, K.Y. Chang, A.Y. Cho, J.C.M. Hwang and K. Alan, IEEE Electron Device Lett., 3, 64 (1982).

[6.8] T. Tanahashi, K. Nakajima, A. Yamaguchi and I. Umebu, Appl. Phys. Lett., 43, 1030 (1983).

[6.9] K.A. Prior, G.J. Davies and R. Heckingbottom, J. Crystal Growth, 66, 55 (1984).

[6.10] K.Y. Cheng, A.Y. Cho and W.A. Bonner, J. Appl. Phys., 52, 4672 (1981).

[6.11] K.Y. Cheng, A.Y. Cho and W.R. Wagner, J. Appl. Phys., 52, 6328 (1981).

[6.12] K.Y. Cheng and A.Y. Cho, J. Appl. Phys., 53, 4411 (1982).

[6.13] T. Martin, C.R. Stanley, A. Iliadis, C.R. Whitehouse and D.E. Sykes, Appl. Phys. Lett., 46, 995 (1985).

[6.14] G.J. Davies, T. Kerr, C.G. Tuppen, B. Wakefield and D.A. Andrews, J. Vac. Sci. Technol., B2, 219 (1984).

[6.15] G.J. Davies and D.A. Andrews, J. Phys. D: Appl. Phys., 17, L143 (1984).

[6.16] W.T. Tsang, J. Appl. Phys., 52, 3861 (1981).

[6.17] B. Goldstein and D. Szostak, Appl. Phys. Lett., 26, 685 (1975).

[6.18] C.E.C. Wood, D.V. Morgan and L. Rathbun, J. Appl. Phys., 53, 4524 (1982).

[6.31] D.C. Rogers, T.S. Cheng, S.T. Davey, E.G. Scott and D.R. Wood, Presented at the Solid State Conference, Inst. Phys., Imperial College, December 1986.

[6.32] W.P. Hong, S. Dhar, P.K. Bhattacharya and A. Chin, J. Electronic Materials, 16, 271 (1987).

[6.33] P.S. Whitney, W. Lee, C.G. Fonstad, J. Vac. Sci. Technol., B5, 796 (1987).

[6.34] W.P. Hong, S. Dhar, P. Berger, A. Chin and P.K. Bhattacharya, Presented at the 28th Electronic Materials Conference, Amherst, MA, 1986.

[6.35] R. Brunwin, B. Hamilton, P. Jordan and A.R. Peaker, Elect. Lett., 15, 349 (1979).

[6.36] W.T. Tsang, J.A. Ditzenberger and N.A. Olsson, IEEE Electron. Dev. Lett., EDL4 (1983).

[6.37] J. Massies, J.F. Rochette, P. Etienne, P. Delescluse, A.M. Huber and J. Chevrier, J. Crystal Growth, 64, 101 (1983).

[6.19] R. Heckingbottom, J. Vac. Sci. Technol, B3, 572 (1985).

[6.20] M.A.G. Halliwell, J. Juler and A.G. Norman, Inst. Phys. Conf. Ser. No. 67: Microsc. Semicond. Mater. Conf., Oxford, March 1983, 365.

[6.21] H. Morkoc, T.J. Drummond, W. Kopp and R. Fischer, J. Electrochem. Soc., 129, 824 (1982).

[6.22] F. Alexandre, L. Golstein, G. Leroux, M.C. Joncour, H. Thibierge and E.V.K. Rao, J. Vac. Sci. Technol., B3, 950 (1985).

[6.23] R.A. Stall, J. Zilko, V. Swaminathan and N. Schumaker, J. Vac. Sci. Technol., B3, 524 (1985).

[6.24] M. Heiblum, E.E. Mendez and L. Osterling, J. Appl. Phys., 54, 6982 (1983).

[6.25] L.P. Erickson, T.J. Mattord, P.W. Palmberg, R. Fisher and H. Morkoc, Elect. Lett., 19, 632 (1983).

[6.26] R.C. Miller, W.T. Tsang and O. Munteanu, Appl. Phys. Lett., 41, 374 (1982).

[6.27] P.M. Petroff, R.C. Miller, A.C. Gossard and W. Wiegmann, Appl. Phys. Lett., 44, 217 (1984).

[6.28] J. Massies, J.F. Rochette and P. Delescluse, J. Vac. Sci. Technol., B3, 613 (1985).

[6.29] J. Massies, F. Turco and J.P. Contour, Semicond. Sci. Technol., 2, 179 (1987).

[6.30] T. Kerr, PhD Thesis, University of Glasgow, 1984.

[6.31] D.C. Rogers, T.S. Cheng, S.T. Davey, E.G. Scott and D.R. Wood, Presented at the Solid State Conference, Inst. Phys., Imperial College, December 1986.

[6.32] W.P. Hong, S. Dhar, P.K. Bhattacharya and A. Chin, J. Electronic Materials, 16, 271 (1987).

[6.33] P.S. Whitney, W. Lee, C.G. Fonstad, J. Vac. Sci. Technol., B5, 796 (1987).

[6.34] W.P. Hong, S. Dhar, P. Berger, A. Chin and P.K. Bhattacharya, Presented at the 28th Electronic Materials Conference, Amherst, MA, 1986.

[6.35] R. Brunwin, B. Hamilton, P. Jordan and A.R. Peaker, Elect. Lett., 15, 349 (1979).

[6.36] W.T. Tsang, J.A. Ditzenberger and N.A. Olsson, IEEE Electron. Dev. Lett., EDL4 (1983).

[6.37] J. Massies, J.F. Rochette, P. Etienne, P. Delescluse, A.M. Huber and J. Chevrier, J. Crystal Growth, 64, 101 (1983).

CHAPTER 7

Photoluminescence (PL) of $Al_{0.48}In_{0.52}As$ and its Pressure Dependence

7.1 Introduction

The many reports on AlInAs published up till now have placed emphasis primarily on its growth and/or the electrical properties. Detailed studies of the optical behaviour of this material system have been largely avoided, probably because of the lack of material with good photoluminescence efficiency. Compared with other ternary alloys such as AlGaAs and InGaAs, epitaxial layers of AlInAs grown by MBE are of relatively poor quality as indicated by their PL linewidths and Hall carrier mobility. For instance, PL line-widths of 5meV are readily obtained for AlGaAs and InGaAs grown by MBE [7.0] compared to the one of the best value of 15meV for AlInAs reported in existing literature [7.1]. The inferior quality of AlInAs is associated primarily with the low substrate temperature used for growth, which is governed by the least stable of the two binary end members, namely InAs in this case. A low growth temperature also leads to clustering and deep level formation due to the low surface mobility of aluminium, and an increase in the probability of oxygen incorporation which also introduces deep traps into the forbidden band gap of the semiconductor. These effects contribute directly to the homogeneous broadening in the linewidth of the PL emission. Welch et al. have reported the optical characteristics of $Al_{0.48}In_{0.52}As$ as a function of both T_s and III/V flux ratio [7.1]; a FWHM of 15meV was obtained, comparable to those epitaxial layers

discussed in the previous chapter. However, no assignment was made to their observed PL emission peak. Reports by both Wakefield et al. [7.2] and Davies et al. [7.3], on the other hand, assumed the observed emission peak in their cathodoluminescence spectra to be a direct measure of the energy band gap, i.e., band to band transitions.

This chapter is concerned with the detailed nature and behaviour of the PL emission from MBE grown AlInAs. The specimens used were those described in the last chapter. Measurements on the samples were performed as a function of sample temperature and laser excitation intensity. Photoluminescence excitation (PLE) spectra were also taken to provide further evidence on the identity of the recombination processes. Additionally, the dependence of the PL emission on hydrostatic pressure, provided by a diamond anvil cell (DAC), was measured to yield information on the band structure of this ternary system.

7.2 PL Emission Behaviour

The PL spectrum of AlInAs has been briefly described in the previous chapter. Up to now, the associated recombination mechanisms giving rise to the emission lines were not clearly identified. This necessitates a detailed PL investigation. The PL spectra described here were obtained on two different PL setups;. the first being the same as used in the InP work discussed in chapters 2-4 (the system is capable of acquiring a lowest temperature of 15K) and the second system was based on a liquid helium immersion cryostat capable of achieving temperatures down to 1.2K (more details of this PL apparatus can be found in reference 7.4).

7.2.1 Dependence on Sample Temperature

Varying the sample temperature can provide much information to assist with the identification of the PL emission peaks as described in chapter 2 and 4. The emission spectrum of $Al_{0.48}In_{0.52}As$ has been recorded as a function of sample temperature in the range of 1.7K to 90K. A typical set of the PL spectra as a function of temperature for sample MV409 is illustrated in figure 7.1. At low temperatures (T<50K) the spectrum is dominated by an emission peak (labelled A) which is centred at 1.547eV for a temperature of T=1.7K with a FWHM≈16meV. This peak shifts to a lower energy as the temperature increases up to ~50K, and is accompanied by a decrease in its emission intensity. At a temperature of 50K, the intensity of peak A is almost completely quenched and can be barely resolved. Above 50K, a new emission peak (labelled B) centred at 1.550eV appears whose energy is approximately temperature independent. However, the magnitude of this emission peak is relatively weak compared to that of peak A, being approximately x200 smaller at 90K, indicating that its associated recombination process is much less efficient than for peak A.

The energy shift of peak A was examined to see if it follows that of the band gap. The temperature variation of the band gap for AlInAs is assumed to have the form [7.5]

$$E_g(T) = E_o - \alpha T/(\beta + T^2) \quad \ldots\ldots\ldots\ldots\ldots\ldots (7.1)$$

similar to the binary compounds, where E_o is the energy gap at 0K, α is a constant and β is the Debye temperature. The value of β for AlInAs is estimated from a linear interpolation between the Debye temperatures for the binary end members, namely InAs and AlAs. Figure 7.2 shows the experimental data and

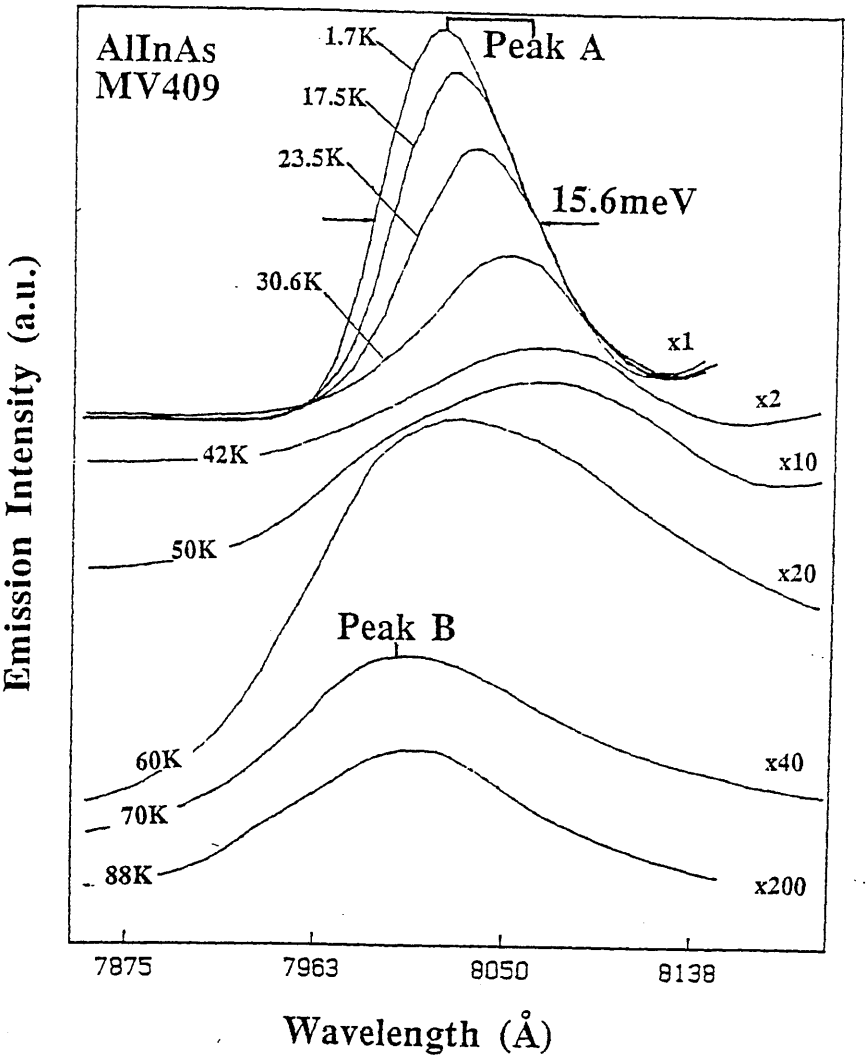

Figure 7.1 Typical PL spectra of AlInAs at various temperatures between 1.7K and 88K.

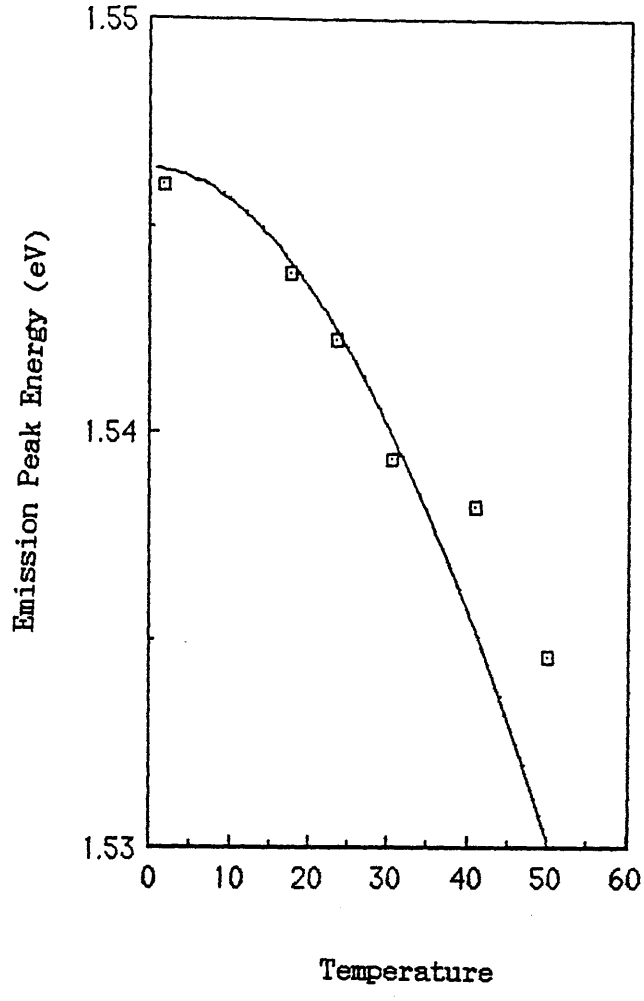

Figure 7.2 Energy peak A as a function of temperature. The solid line is the fitted curve of the band edge temperature dependence using the empirical expression given in reference [7.5].

the graph deduced from the above equation (solid line). The theoretical graph is obtained using α=2.5x10^{-3}eV/K and ß=335K, and shifted so that it falls onto the experimental points for comparison. The shift of peak A therefore appears to follow the variation of the band gap, suggesting an excitonic like transition [7.6]. However, this interpretation must be regarded cautiously since the value of α used in the calculation is about an order of magnitude larger than those for the binary compounds [7.5].

The FWHM of the AlInAs emission peak has been plotted as a function of the sample temperature in the range of 17-43K as shown in figure 7.3. In this temperature region emission peak A is dominant and therefore the linewidth variation can be considered due solely to peak A. The FWHM can be seen to increase with temperature at a faster rate than k_BT (from 17meV at 20K to 30meV at 40K), which might suggest the recombination process involved is non-excitonic. Another possibility which would result in the observed fast rate of increase in the linewidth with temperature is the existence of multiple emission peaks which are not resolved individually. This will be pursued further in section 7.3.

Information concerning the thermal processes in AlInAs can be obtained by measuring the integrated emission intensity as a function of temperature. Figure 7.4 shows the experimental data with the PL spectra of peak A shown in the insert for sample MV408. A theoretical fit of the form which applies to neutral donors [7.7],

$$I(T) \propto 1/[1+C\exp(-E_d/k_BT)] \quad \ldots\ldots\ldots\ldots\ldots\ldots (7.2)$$

where C is a constant and E_d is the binding energy of the donors, is made to the experimental data. The best fit is found for E_d=15±1 meV which is about a factor of

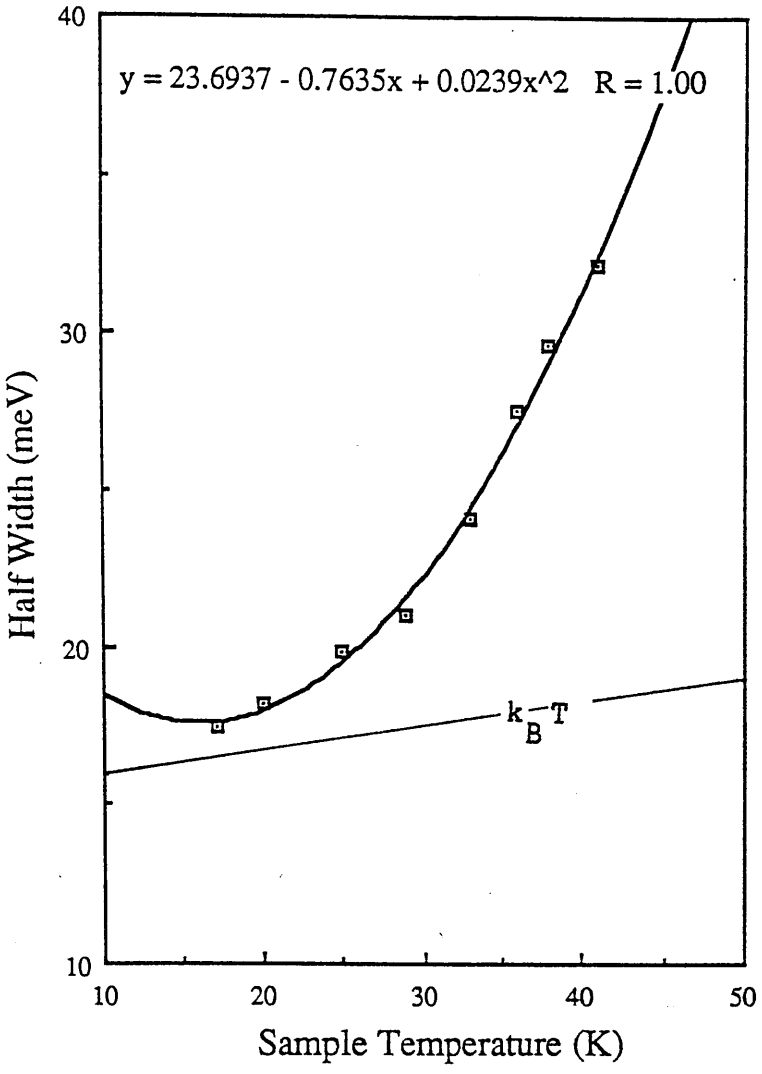

Figure 7.3 The full width at half maximum (FWHM) of the AlInAs emission at temperatures below 50K. The increase in FWHM with temperature is faster than k_BT, indicating emission peak A can not be excitonic like or multiple emission peaks are present.

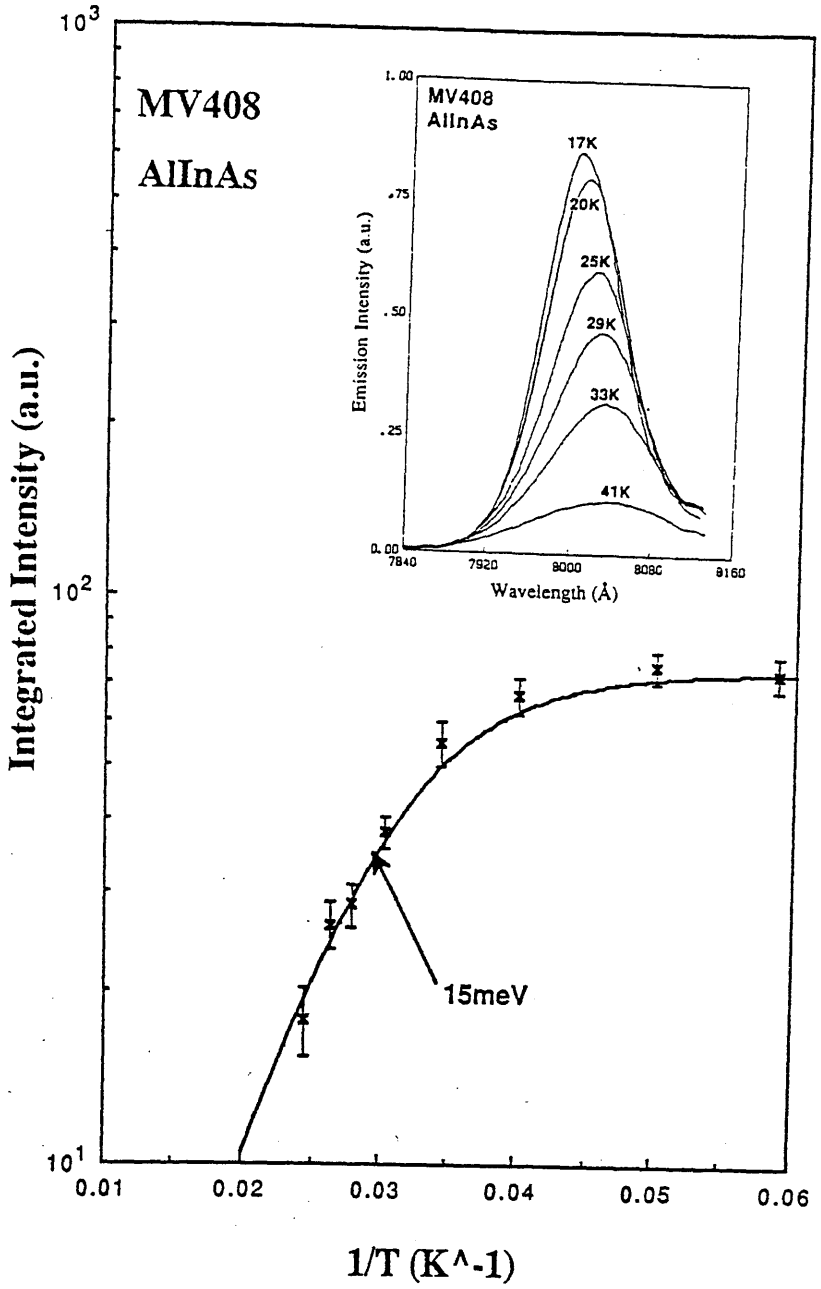

Figure 7.4 The integrated emission intensity as a function of the inverse temperature. The insert shows the PL spectra between 17K and 41K for sample MV408. The solid line in the figure is a theoretical fit to the experimental data using the expression given in equation (7.2), and an activation energy of 15meV is deduced.

two greater than the binding energy of the impurity bound exciton in AlInAs (≈7meV assuming a simple hydrogenic model). This further points to the non-excitonic behaviour of the emission peak A.

7.2.2 Dependence on Laser Excitation

To clarify further the nature of the emission peaks A and B, measurements were performed as a function of the laser excitation intensity at temperatures of 2 and 80K respectively. Figure 7.5 shows the experimental results obtained plotted in log-log form. The incident laser excitation intensity used varied over two orders of magnitude. A linear relationship is found for peak A and peak B with slopes of 0.9 and 1.6±0.2 respectively. According to reference [7.8], the integrated PL emission intensity (I_{out}) is related to the incident laser excitation intensity (P_{ex}^{s}) by the expression:

$$I_{out} \propto P_{ex}^{s} \quad \ldots\ldots\ldots\ldots\ldots\ldots\ldots\ldots\ldots\ldots\ldots\ldots (7.3)$$

where s=1 for exciton related transitions and s=2 for free-carrier recombinations. From figure 7.5, emission peak A appears to be excitonic like. Peak B, on the other hand, is more free-carrier like and may be ascribed to a free-to-bound (e-A°) transition.

7.3 Deconvolution of the 15K PL Emission Spectra

The low temperatures spectra of $Al_{0.48}In_{0.52}As$ under study all exhibit linewidths of about 15meV. Values of this magnitude compare favourably with those reported by other authors. For instance, Hong et al. [7.9]

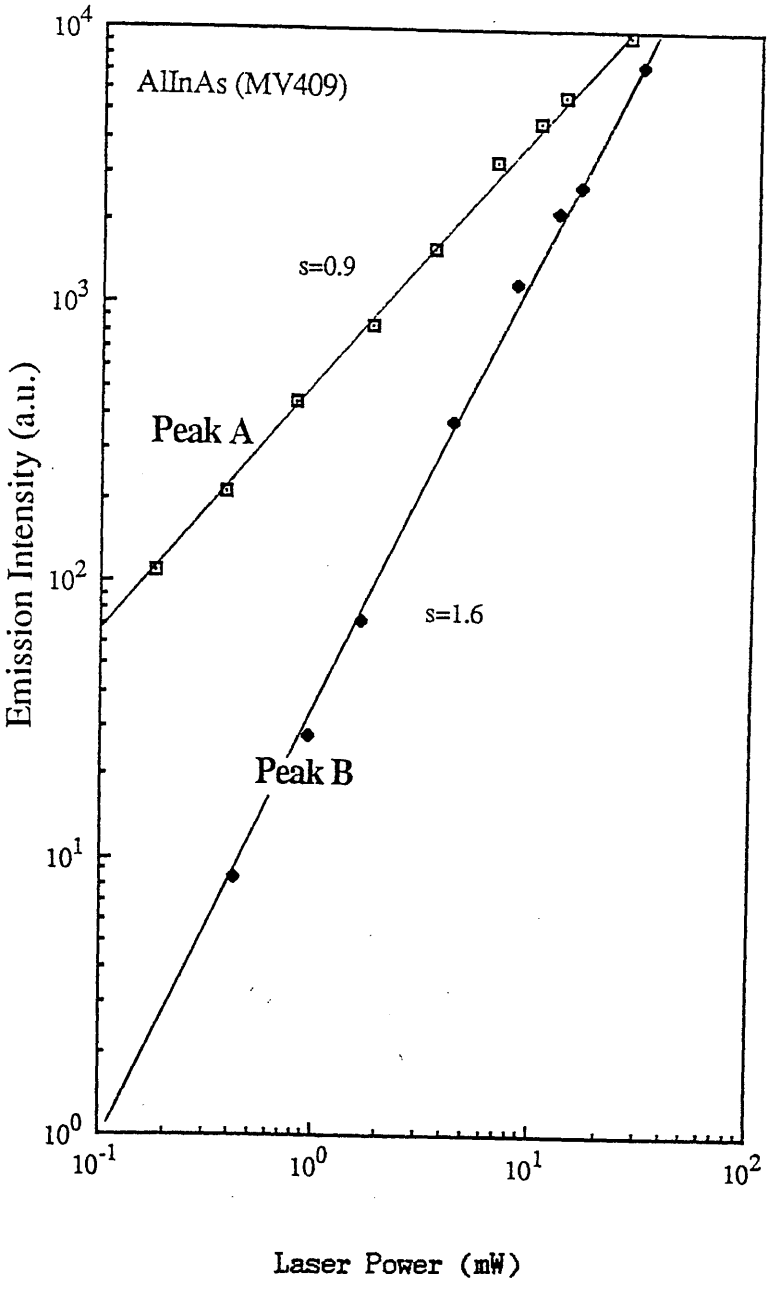

Figure 7.5 The dependence of emission intensity on incident excitation laser intensity for both peak A and B. Peak A is seen to have a near unity slope whereas peak has slope of 1.6, suggesting that the former is more excitonic like and the latter is more free-carrier like.

observed a FWHM of 19meV at 10K, which was believed to be associated with alloy clustering in the crystal. For a perfectly lattice matched and ordered alloy of AlInAs crystal, the excitonic linewidth was calculated to be 4meV. The large linewidth of AlInAs has also been shown to be associated with the poor crystallinity of the lattice [7.1]. Besides the broadening caused by poor crystallinity, any other emissions adjacent to the transition (peak A) would also increase the linewidth to the experimental observed value. In view of this, a curve fitting procedure has been performed on the low temperature AlInAs emission spectra.

Assuming the emission of peak A is given by a Gaussian distribution, the spectrum can effectively be reproduced by two curves as illustrated in figure 7.6 for specimen MV408 at 17K. In this figure, the experimental data are indicated by the crosses while the deconvoluted curves (A and C) and their resultant are shown by the dotted and solid lines respectively. The net sum of the two curves A' and C is seen to be in excellent agreement with the experimental spectrum. Hence, it is proposed that the observed asymmetric lineshape of the low temperature PL emission is caused by the existence of a relatively weak unknown transition (peak C) lying 16meV below the dominant emission peak A.

7.4 Photoluminescence Excitation (PLE) Measurement

Photoluminescence excitation (PLE) measurements were performed on the AlInAs samples to provide additional experimental information on the nature of the emission peaks. The PLE spectra were all taken at 2K with a Styryl 9 dye laser which could be tuned in the range of 800-900nm. Emission peak heights were corrected for

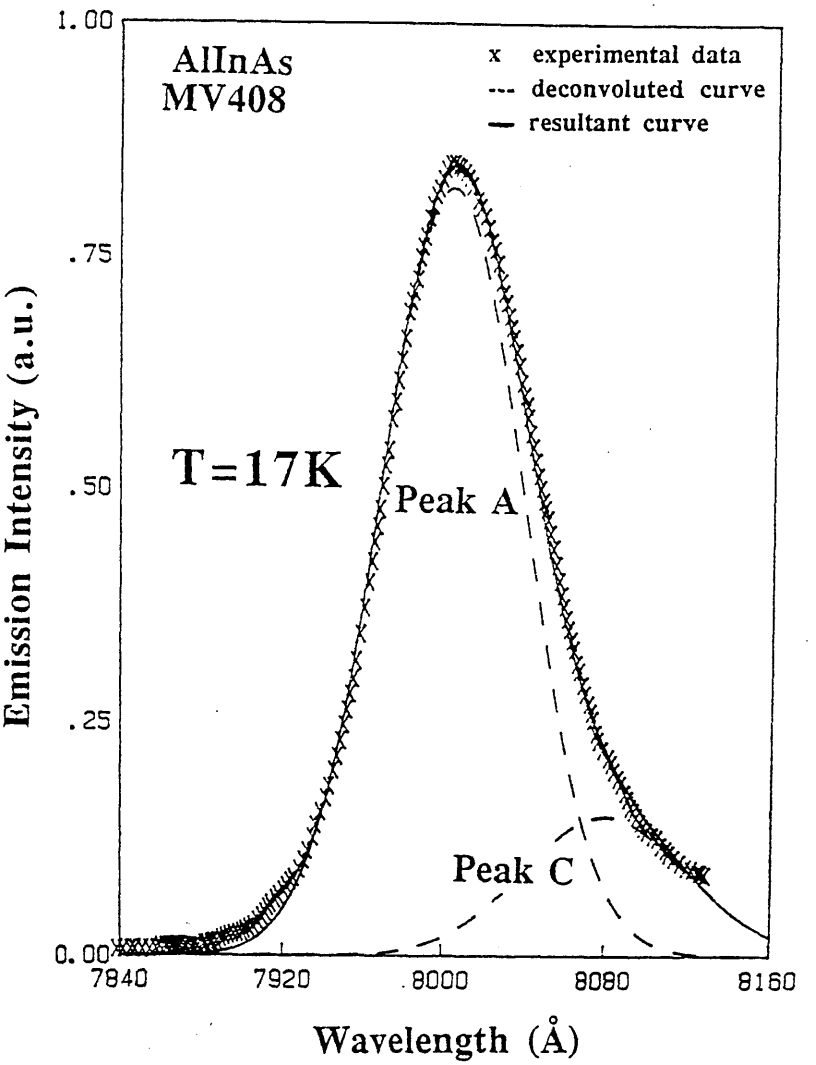

Figure 7.6 The 17K PL emission of AlInAs is deconvoluted into two separate emission peaks assuming they can be described by a Gaussian distribution. Peak A is the dominant emission while Peak C (~13meV below peak A) is comparatively weak.

the wavelength response of the detector. This may be accomplished in two ways :

(a) using neutral density filters to keep the incident laser intensity constant, or

(b) normalising the observed spectrum with respect to the output power of the laser at the respective wavelengths.

Figure 7.7 shows a typical PLE spectrum for sample MV402 with its PL signature. The appearance of a slight shoulder shifted by 36meV from the sensing wavelength of 1.5176eV is observed. This large energy shift strongly indicates that the emission (peak A) centred at 1.5252eV is not due to exciton bound to shallow impurities. The rising edge in the PLE spectrum at about 1.57eV could be the onset of the transition observed by Praseuth et al. [7.10] at 1.62eV which is ascribed here to band-to-band emission.

From the experimental evidence, emission peak A may tentatively be assigned to donor-to-acceptor recombinations $(D^{\circ}\text{-}A^{\circ})_A$ which are the normal transitions paths at low temperatures.

7.5 PL Dependence on Hydrostatic Pressure

When a semiconductor is subjected to the influence of an external applied pressure the lattice of the crystal is compressed, thus resulting in a change in its overall band structure. The PL emission as a function of pressure will therefore provide an indirect access to the band structure. In order to study the effects of pressure on AlInAs and to deduce information about its band structure, experiments were performed with a diamond anvil pressure cell (DAC) which is capable of working pressures of tens of kilobars. This work was performed at the SERC high

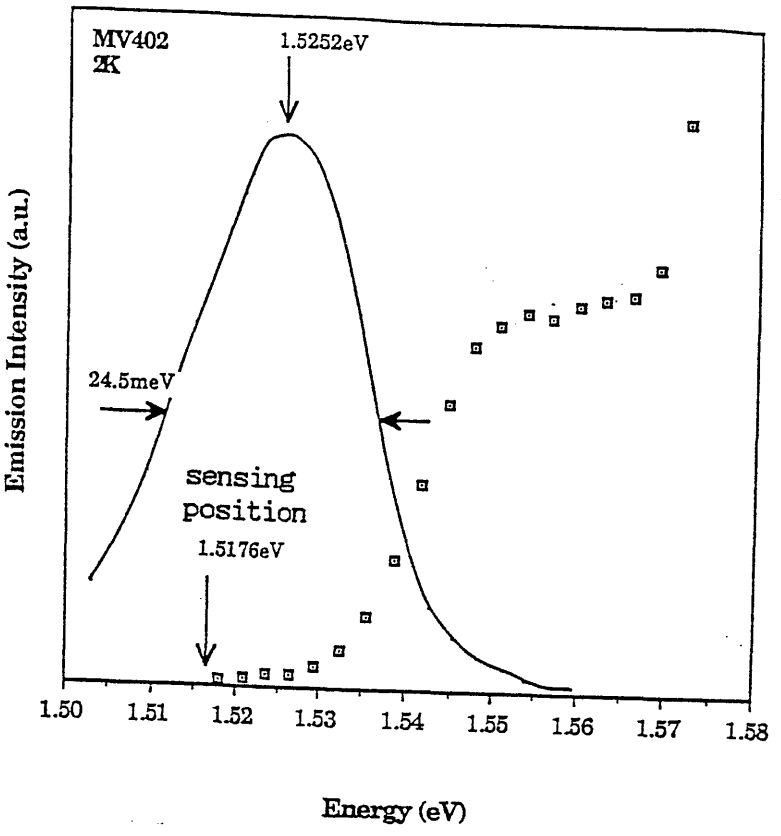

Figure 7.7 A typical PLE spectrum of AlInAs. Included in the figure is the PL spectrum at 2K. The PLE data reveals the presence of emission shoulder shifted by ~35meV from the sensing position at 1.5176eV.

pressure facility at STL Technology, Harlow in Essex. The optical spectra at different pressures were taken by Dr. T.P. Beales at STL.

The basic construction of the DAC used for the experiments is shown in figure 7.8. Essentially, the sample is suspended in a pressure transmitting liquid confined by a steel gasket between the two diamond faces. The liquid used in this study is a mixture of ethanol and methanol (4:1). External mechanical pressure is applied to the diamond supports which induce a large hydrostatic pressure in the fluid. Details of the experimental procedure are given in reference [7.4].

The luminescence experiments as a function of hydrostatic pressure were performed at 80K. Figure 7.9 shows the spectra of a typical AlInAs sample for different pressures below 50 kbar. The sharp emission peak in each of the spectra is due to the fluorescence of ruby chips loaded together with the AlInAs specimen into the DAC. Its energetic position is used as a pressure gauge since the pressure dependence of the ruby emission is well known. Minimal broadening of the ruby line observed in the spectra indicates the presence of 'true' hydrostaticity in the diamond cell. As the pressure is increased, the AlInAs peak moves to a higher energy and its intensity gradually diminishes as it approaches the Γ-X cross-over point at which the semiconductor becomes indirect, resulting in a substantial decrease of PL emission intensity. GaAs [7.11] and InP [7.12] become an indirect gap semiconductor at pressures greater than 35 kbar and 100 kbar respectively. The corresponding pressure at the Γ-X point for AlInAs is expected therefore to lie somewhere between 35-100 kbar since its Γ-X energy separation is 0.6eV (estimated from an interlopation between the binary members), i.e., between the value for GaAs (0.48eV) and InP (0.70 eV). Indeed, from

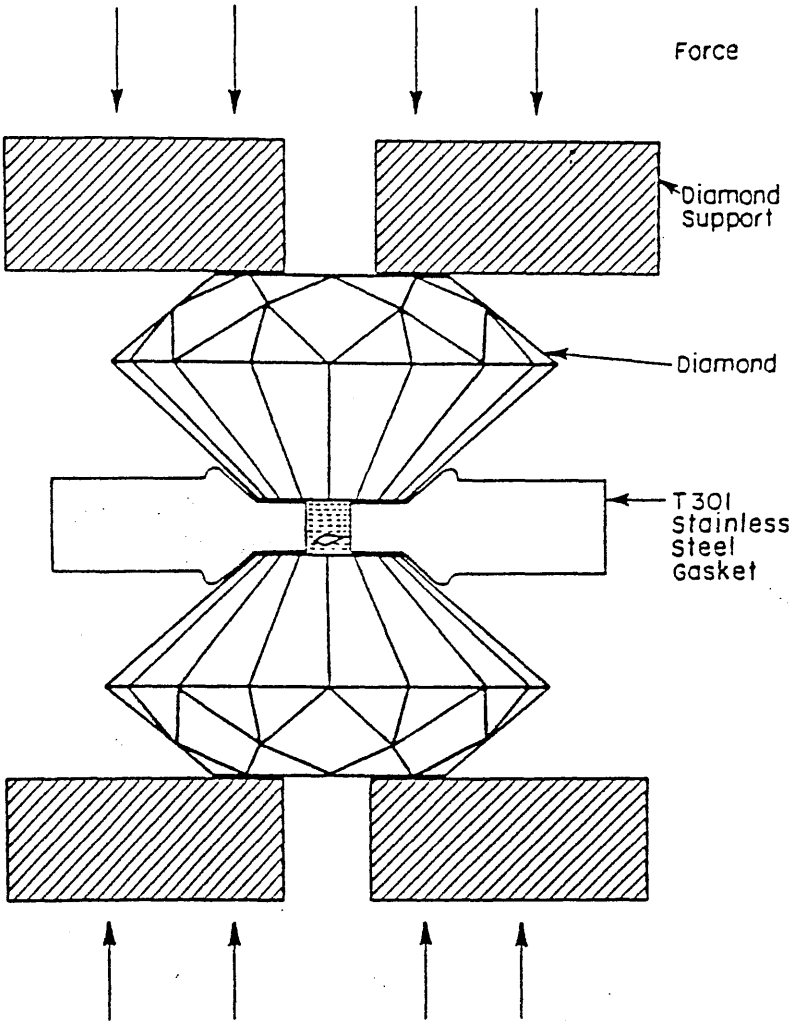

Figure 7.8 A schematic diagram of a diamond anvil cell (DAC). The sample is suspended in a medium confined by the gasket and between the diamond pieces. The pressure is applied externally as shown by the arrows.

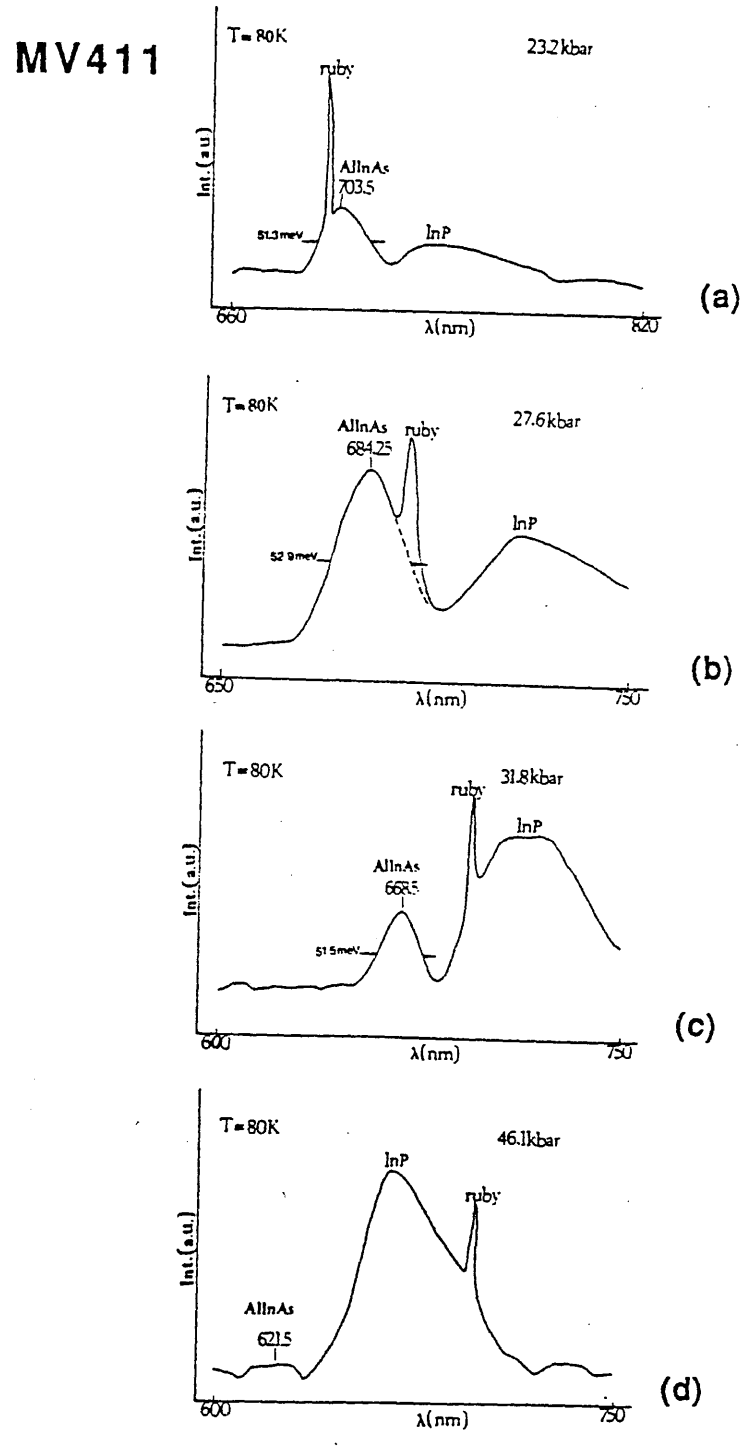

Figure 7.9 The PL spectra of AlInAs at different pressures between 20 kbar and 46 kbar. The sharp emission is from the ruby which acts a reference emission and the negligible broadening of the such line indicates 'true' hydrostaticity in the cell.

figure 7.9 it is seen that the point at which the AlInAs changes from a direct to an indirect gap semiconductor, as evidenced by a quenching of the luminescence, requires a pressure around 50kbar. The low energy part of the emission spectra shown in figure 7.9 is associated with the InP substrate which shifts at a different rate compared to AlInAs. Now, the (e-A°) transition closely follows the band edge variation with pressure since the change in acceptor effective mass is negligible [7.13]. The position of the (e-A°) peak can therefore be used as a measure of the change of the band gap as function of pressure. The shift of the AlInAs energy position has been plotted as a function of the pressure as shown in figure 7.10. A least squares fit has been applied to the experimental data yielding a sublinear relationship:

$$E_g = 1.546 + 8.7\times10^{-3}P - 2.76\times10^{-5}P^2 \quad \ldots\ldots\ldots\ldots\ldots (7.4)$$

The quadratic term in this equation arises from the pressure dependence of the nonlinearity in the bulk modulus. This may be seen by considering Murnaghan's equation [7.14] relating the lattice constant a, the pressure P and the bulk modulus B_o:

$$-(\delta a/a_o) = 1 - [(B_o'/B_o)P + 1]^{-1/(3Bo')} \quad \ldots\ldots\ldots\ldots (7.5)$$

where δa is the change in lattice constant relative to the pressure and B_o' is derivative of the bulk modulus with respect to the pressure. The bulk modulus can be obtained directly from reference data or alternatively calculated from the stiffness constants as

$$B_o = (C_{11} + 2C_{12})/3 \quad \ldots\ldots\ldots\ldots\ldots\ldots (7.6)$$

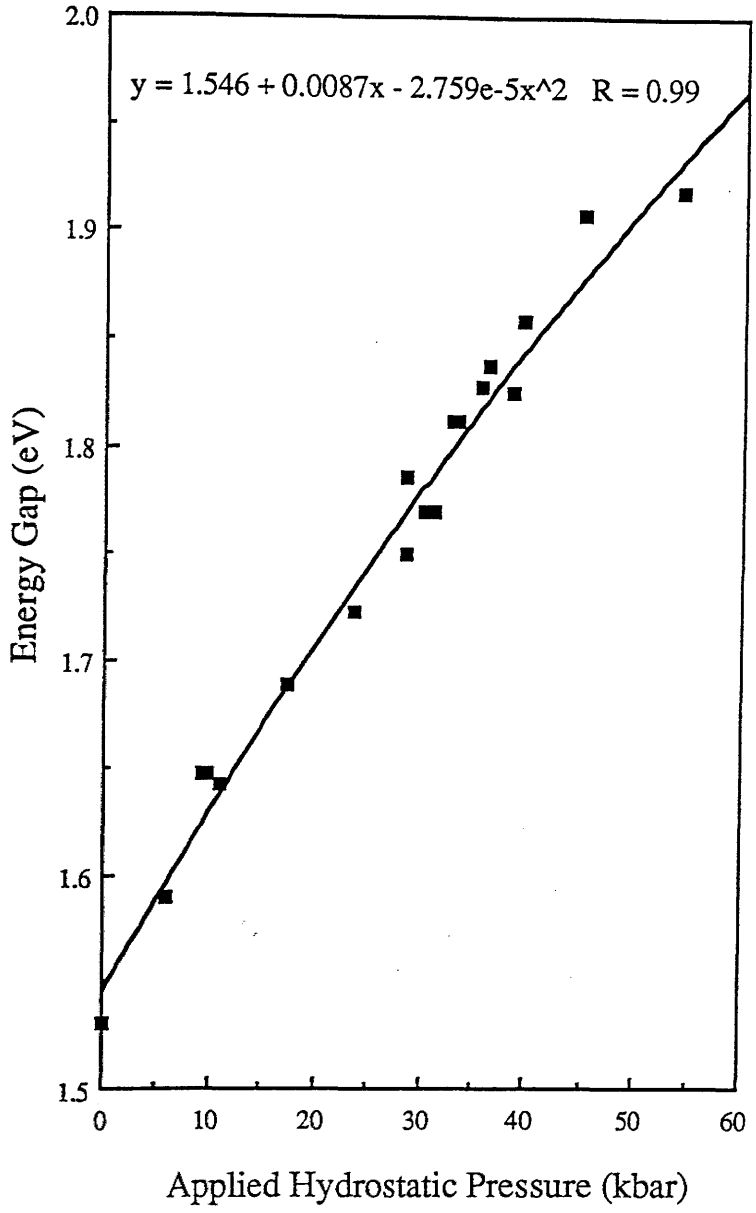

Figure 7.10 The shift of the PL energy position of AlInAs as a function of applied hydrostatic pressure at 80K. The solid line is a least square fit to the data with the equation at the top of the figure, giving a pressure coefficient of 8.7meV/kbar.

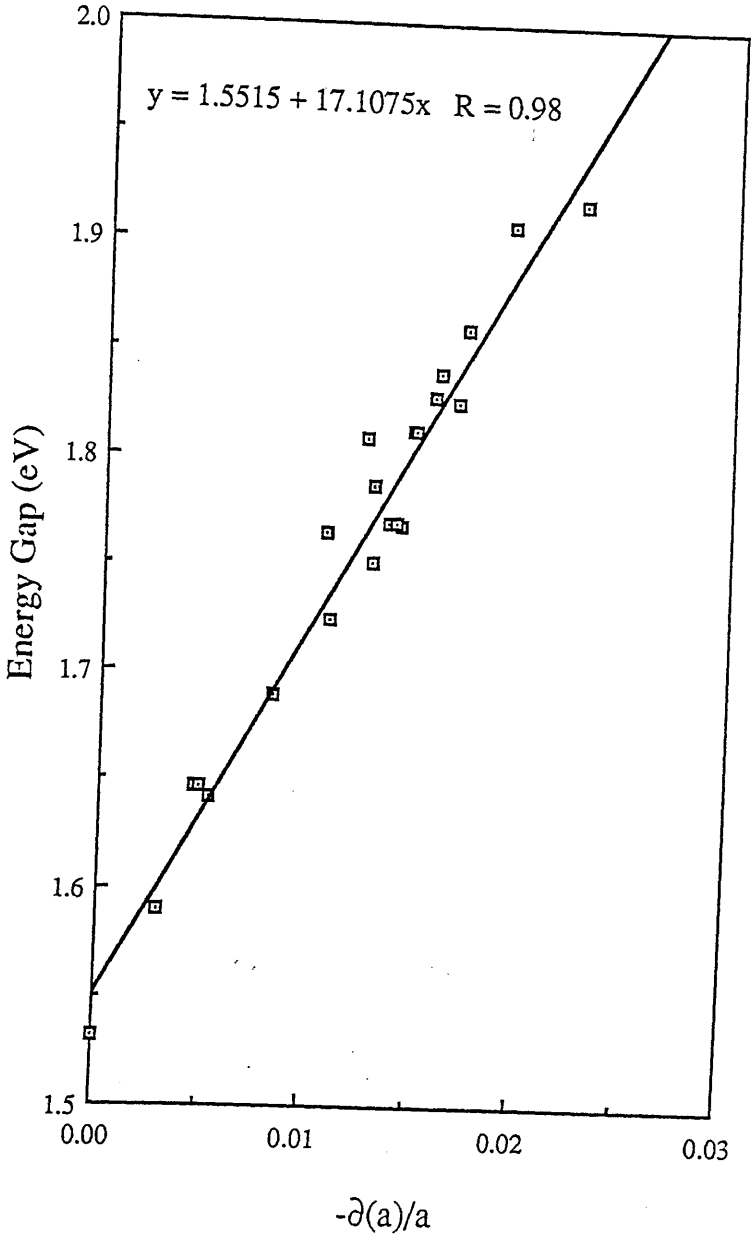

Figure 7.11 The shift of the PL energy position of AlInAs as a function of the fractional change in the lattice constant ($\partial a/a$). The solid line is the least square fit to the data and from its slope an deformation potential of 5.8eV is deduced.

B_o for $Al_{0.48}In_{0.52}As$ is not known experimentally but it is reasonable to use the value obtained by interpolation between the end members of the binary compounds. In the present case, B_o (AlInAs)= 672 kbar and B_o'= 4.5 are used in the calculation. Now the energy band gap is related to the lattice constant by the following equation [7.14]:

$$E_g = E_o + 3\xi(\delta a/a_o) \quad \ldots\ldots\ldots\ldots\ldots\ldots\ldots\ldots (7.7)$$

where ξ is the deformation potential. By plotting the measured energy of the band edge luminescence against $-(\delta a/a_o)$, a straight line graph should be obtained the slope of which can be used to estimate deformation potential. In figure 7.11, ξ is found to be $-(5.7\pm0.3)$eV for AlInAs. This compares favourably with the values obtained for other members in the III-V family; for example People et al. [7.15] measured = $-(7.79\pm0.4)$eV for $Ga_{0.53}In_{0.47}As$ and Muller et al. [7.12] measured $=-(6.35\pm 0.05)$eV for InP.

Finally, it should be noted that the FWHM of the AlInAs emission shown in figure 7.9 remains approximately constant at 50 meV in the range of pressures considered, suggesting an insignificant effect of pressure on the alloy clusters.

7.6 Conclusion

The use of low temperature PL and PLE measurements has revealed the existence of three different recombination processes in the $Al_{0.48}In_{0.52}As$ alloy system. At low temperatures (<50K), the PL spectrum is dominated by donor-to-acceptor transition $(D^\circ\text{-}A^\circ)_A$ centred at 1.52-1.54eV. Deconvolution of the experimental spectra has unmasked a separate emission

at about 16meV below the $(D^{\circ}-A^{\circ})_A$ transition whose origin is not known at present. At high temperatures (>50K), the two low temperature emission peaks are quenched and a third transition peak at ~3meV above the $(D^{\circ}-A^{\circ})_A$ emission appears which is ascribed to free-to-bound transitions $(e-A^{\circ})$.

The behaviour of the AlInAs emission as a function of applied hydrostatic pressure provided by a diamond anvil cell has been investigated. The AlInAs emission shifts to higher energy as the pressure is increased and the emission intensity quenches near the Γ-X cross-over at ~50 kbar. The pressure coefficient for the lowest conduction band has been estimated to be 8.7±0.1meV/kbar at 80K, similar to the values for other III-V compounds. The deformation potential for AlInAs has also been estimated and found to be 5.8± 0.3eV which compares favourably with the values for other III-V material systems.

7.7 References

[7.0] G.W. Wicks, PhD thesis, Cornell University (1981).

[7.1] D.F. Welch, G.W. Wicks, L.F. Eastman, P. Parayanthal and F.H. Pollak, Appl. Phys. Lett., 46, 169 (1985).

[7.2] B. Wakefield, M.A.G. Halliwell, D.A. Andrews and D.R. Wood, Appl. Phys. Lett., 44, 341 (1984).

[7.3] G.J. Davies, T. Kerr, C.G. Tuppen, B. Wakefield and D.A. Andrews, J. Vac. Sci. Technol., B2, 219 (1984).

[7.4] I. Ferguson, PhD Thesis, University of St. Andrews (1989).

[7.5] Y.P. Varshni, Physica, 34, 149 (1967).

[7.6] W.J. Turner, W.E. Reese and G.D. Pettit, Phys. Rev., 136, A1467 (1964).

[7.7] P.J. Dean, Phys. Rev., 157, 655 (1967).

[7.8] Xu Zhongying, Xu Jizong, Ge Weikun, Zheng Baozhen, Xu Junying and Li Yuzhang, Solid State Comm., 61, 707 (1987).

[7.9] W.P. Hong, P.K. Bhattacharya and J. Singh, Appl. Phy. Lett., 50, 618 (1987).

[7.10] J.P. Praseuth, L. Goldstein, P. Henoc, J. Preimot and G. Danan, J. Appl. Phys., 61, 215 (1987).

[7.11] G.D. Pitt and J. Lees, Phys. Rev., B2, 4144 (1970).

[7.12] H. Muller, R. Trommer, M. Cardona and P. Vogl, Phys. Rev., B21, 4879 (1980).

[7.13] D.J. Wolford and J.A. Bradley, Solid State Comm., 53, 1069 (1985).

[7.14] F.D. Murnaghan, Proc. Nat. Acad. Sci., U.S.A., 30, 244 (1944).

[7.15] R. People, A. Jayaraman, K.W. Wecht, D.L. Sivco, A.Y. Cho, Appl. Phys. Lett., 52, 2124 (1988).

CHAPTER 8

Conclusions and Future Work

High quality undoped InP grown by solid source MBE was achieved by optimising the three basic growth parameters: growth rate, substrate temperature and flux ratio. The epitaxial layers were normally n-type due to contamination in the red phosphorus starting material. The best layer obtained to date had a 77K Hall mobility of $42,500 cm^2V^{-1}s^{-1}$ with a free-carrier concentration $(N_D-N_A)=2.5x10^{15}cm^{-3}$. The PL spectrum of this sample recorded at 17K has a (D°X) half-width of <4meV and is dominated by excitonic recombinations near the band edge. Futher improvement of layer quality lies in the purification of the starting sources, in particular the red phophorus, or the use of alternate sources with less contamination by impurities.

The role of sulphur in InP was studied using an electrochemical Knudsen source. The experimental results are explained by a kinetic model proposed by Wood et al. [3.10] in conjunction with a thermodynamic analysis to explain the effects at high substrate temperatures. It was found that sulphur is an ideal dopant in InP at growth temperatures below 500°C, and above which the desorption of In_2S becomes significant. Future work will involve an investigation of the doping behaviour of selenium in InP since in the case of GaAs, the onset of desorption of selenium is about 30° above that of sulphur.

An initial attempt was made at producing p-type material using magnesium whilst growing InP under the optimised conditions previously determined. However,

the properties of the doped samples were found to be comparable to the undoped InP, indicating that either the sticking coefficient of magnesium is very low or it is electrically inactive in the sample. Further work would be to perform SIMS measurements on these samples to verify if magnesium has indeed been incorporated.

The electrical and optical properties of the MOMBE InP grown at BTRL were measured. The samples were found to be comparable to the best InP grown by solid source MBE. This is encouraging since they were the first samples produced when the system started to handle gas sources. Future works in this area include characterising samples grown at a much later date when the system environment has improved, and developing an understanding of the growth processes using the modulated beam techniques.

The optical and electrical properties of $Al_{0.48}In_{0.52}As$ were also characterised. The first observed region of rough surface for this ternary material system when grown at substrate temperatures between 530° and 570°C was correlated with an increase in the PL linewidths and the presence of unique electron traps measured by DLTS. Future work in this material system is to grow at temperatures >600°C and offset the loss of indium by increasing the incident indium or decreasing the gallium flux, thus ensuring layers lattice-matched to the InP substrate.

List of Publications

(1) D.C. Rogers, T.S. Cheng, S.T. Davey, E.G. Scott and D.R. Wood, Presented at the 'Solid State Conference', Institute of Physics, Imperial College, December 1986.

(2) V.M. Airaksinen, T.S. Cheng and C.R. Stanley, J. Cryst. Growth, 81,332 (1987).

(3) V.M. Airaksinen, T.S. Cheng and C.R. Stanley, J. Cryst. Growth, 84,241 (1987).

(4) I. Ferguson, T.S. Cheng, C.M. Sotomayor-Torres, T. Beales and E.G. Scott, Presented at the 'Solid State Conference', Institute of Physics, University of Bristol, December 1987. "Photoluminescence of Molecular Beam Epitaxially (MBE) Grown AlInAs under Hydrostatic Pressure"

(5) D.A. Andrew, T.S. Cheng, D.R. Wood and G.J. Davies, Presented at the 'Recent Developments in the Growth and Characterisation of III-V Semiconductors', Institute of Physics, Electronics Group, London, January 1988. "The Growth of High Quality InP from Metalorganic Sources by Molecular Beam Epitaxy (MOMBE)"

(6) T.S. Cheng, V.M. Airaksinen and C.R. Stanley, J. Appl. Phys., 64, 6662 (1988).

(7) I.T. Ferguson, T.P. Beales, T.S. Cheng, C.M. Sotomayor-Torres and E.G. Scott, Semicond. Scien. & Tech., 4, 243 (1989).